

Unlimited distribution.

An Electromagnetic Vorticity Meter

by Thomas B. Sanford, James A. Carlson, and Mark D. Prater

Technical Report
APL-UW TR 9503
November 1995

Contract N00039-91-C-0072

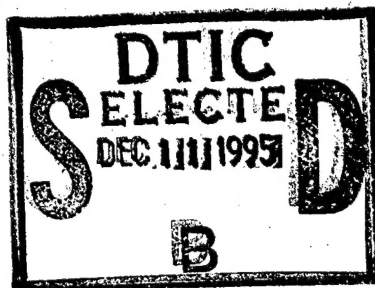
19951206 070

NOV 10 1995

Unlimited distribution.

An Electromagnetic Vorticity Meter

by Thomas B. Sanford, James A. Carlson, and Mark D. Prater

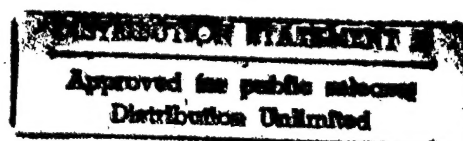


Technical Report
APL-UW TR 9503
November 1995



Applied Physics Laboratory University of Washington
1013 NE 40th Street Seattle, Washington 98105-6698

Contract N00039-91-C-0072

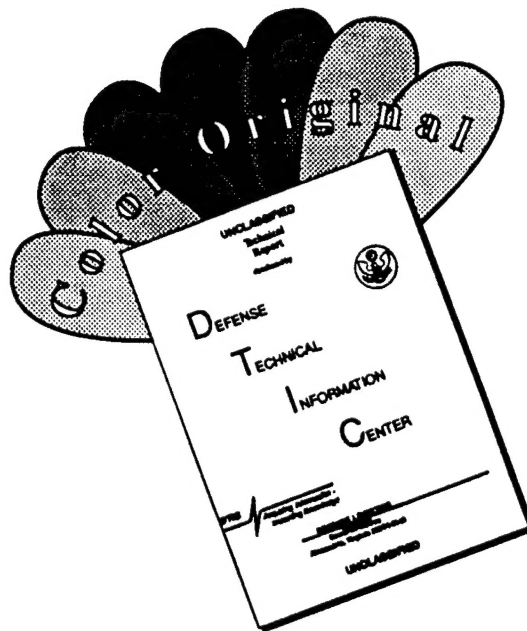


Acknowledgments

This project was supported by Kenneth Ferer of the Tactical Oceanography Warfare Support Program, situated at NRL-SSC, addressing the requirements of the Oceanographer of the Navy.

Accession For	
NTIS GRA&I	<input checked="checked" type="checkbox"/>
DTIC TAB	<input type="checkbox"/>
Unannounced	<input type="checkbox"/>
Justification	
By	
Distribution	
Availability Codes	
Dist	Avail and/or Special
A-1	

DISCLAIMER NOTICE



THIS DOCUMENT IS BEST QUALITY AVAILABLE. THE COPY FURNISHED TO DTIC CONTAINED A SIGNIFICANT NUMBER OF COLOR PAGES WHICH DO NOT REPRODUCE LEGIBLY ON BLACK AND WHITE MICROFICHE.

TABLE OF CONTENTS

	<i>Page</i>
1. Introduction	1
1.1 What is Vorticity?	1
1.2 Need for Vorticity Observations	2
2. Concept and Operating Principles	4
2.1 Concept of EMVM	4
2.2 Governing Equations	4
2.3 Measurement Approach.....	5
2.3.1 2-D case: Flow and magnetic field uniform in z direction	6
2.3.2 3-D case: Uniform rotary flow in dipole magnetic field.....	8
2.4 Modeling.....	11
2.4.1 Uniform flow	12
2.4.2 Solid-body rotation	17
2.5 Response Function for Sensor	25
2.6 Relationships Between Electric Field and Velocity Components for 2-D Sensor	30
3. Earlier Instruments.....	34
3.1 First EMVM.....	34
3.2 Second EMVM.....	37
3.3 Third EMVM.....	40
3.4 Fourth EMVM.....	46
3.5 Experiences with Tow Bodies	56
3.5.1 C Mk 1 tow body	56
3.5.2 GW fairing	57
3.5.3 Seasoar tow body	58
3.5.4 Comparison of Seasoar and GW fairing performance	58
3.5.5 Seasoar problems and manufacturer repairs and upgrades	63
4. Design, Construction, Use, and Evaluation of the Fifth EMVM.....	66
4.1 Design Goals	66
4.2 Construction	68
4.2.1 Electrode array	68
4.2.2 Splitter plate	71
4.2.3 Magnets.....	72
4.2.4 Underwater electronics, optical links, batteries, and cabling ...	73
4.2.5 Pressure vessels, housings, and structures	78
4.2.6 Shipboard electronics.....	80

4.3 Performance Evaluation	81
4.3.1 Sensitivity and self-noise in APL test tank	81
4.3.2 Summary of low signals in Puget Sound experiments (upper bound on noise)	83
5. Observations of Vorticity in Puget Sound	84
5.1 Point Jefferson	84
5.2 Blakely Rock and Blakely Harbor	89
5.3 Restoration Point and Decatur Reef	107
5.4 Toliva Shoal	119
5.5 Horizontal	121
6. References	129

LIST OF FIGURES

	<i>Page</i>
Figure 2.1. Measurement scheme for determining $\Delta^2\phi/\Delta x^2$, the x component of $\nabla^2\phi$	5
Figure 2.2. Three-dimensional finite-difference approximation of $\nabla^2\phi$	7
Figure 2.3. Typical noise level associated with input amplifier using Analog Devices OP-27 integrated circuit operational amplifiers	9
Figure 2.4. Magnetic field produced by an electric current in a thin coil.....	13
Figure 2.5. The potential field ϕ generated by uniform flow in the presence of the magnetic fields shown in Figure 2.4	16
Figure 2.6. Vector plots of the electric current density \mathbf{J} produced by a uniform flow.....	18
Figure 2.7. Contours of the head factor Hd	19
Figure 2.8. The potential field ϕ generated by flow in solid-body rotation in the presence of the magnetic field shown in Figure 2.4.....	24
Figure 2.9a. Four geometric cases of a vortex overlapping the sensor head	27
Figure 2.9b. The area, A , enclosed by a circle, a chord, and the centerline perpendicular to the chord is $x \sqrt{r^2 - x^2} + x^2 \sin^{-1}(x/r)$	27
Figure 2.10. An example of one initial condition for the MATLAB program that calculates the response of the sensor to different spatial distributions of vorticity	28
Figure 2.11. Theoretical spatially averaged amplitude response of the EMVM sensor to an isolated vortex, where r_v/r_s is the ratio of the radius of the vortex to the radius of the sensing area.....	29
Figure 2.12. Electrode geometry.....	30
Figure 3.1. Block diagram of the electronics for the first version of the EMVM	35
Figure 3.2. First EMVM sensor	36
Figure 3.3. Test facility used for the first version of the EMVM.....	36
Figure 3.4. Second version of the EMVM	37
Figure 3.5. Tri-axial configuration of the second version of the EMVM.....	38
Figure 3.6. Block diagram of the electronics for the second version of the EMVM.....	39

Figure 3.7.	Test facility used for the second version of the EMVM	40
Figure 3.8.	Block diagram of the electronics for the third version of the EMVM	41
Figure 3.9.	Third version of the EMVM.....	43
Figure 3.10.	Tripod-mounted EMVM (three-axis open sensor)	44
Figure 3.11.	Data taken with tripod-mounted three-axis open sensor with and without the shroud	45
Figure 3.12.	Vorticity measurements with a diver creating a disturbance upstream of the EMVM (three-axis open sensor)	47
Figure 3.13.	Vorticity data taken while the third version of the EMVM was slowly rotated (three-axis open sensor)	48
Figure 3.14.	Time integral of one rotation of the tripod-mounted sensor	49
Figure 3.15.	The fourth version of the EMVM mounted in a support frame for use on the seafloor	49
Figure 3.16.	Block diagram of the electronics of the fourth version of the EMVM.....	51
Figure 3.17.	Time series of horizontal velocity and vertical vorticity from EMVM deployment south of Point Jefferson in Puget Sound	54
Figure 3.18.	Power spectrum of vorticity for sensor operated in still water in an electrically isolated test tank	55
Figure 3.19.	Power spectrum of vorticity for sensor oscillated in pure rotation in a still-water test tank at a frequency of 2×10^{-2} Hz.....	55
Figure 3.20.	C Mk 1 tow body as received from the Naval Coastal Systems Center in 1984.....	56
Figure 3.21.	Vorticity meter hanging from the tow bridle, in normal operating configuration	57
Figure 3.22.	Seasoar oceanographic tow body	59
Figure 3.23.	Time series of yaw rate, pitch angle, and roll angle obtained while the Seasoar was being towed in Puget Sound at various speeds	61
Figure 3.24.	Time series of yaw rate, pitch angle, and roll angle of the EMVM with GW fairing being towed at 2.5 kn.....	61
Figure 3.25.	Comparison of yaw-rate spectra for the Seasoar tow body and GW fairing	62
Figure 3.26.	Comparison of pitch spectra for the Seasoar tow body and GW fairing	62

Figure 3.27.	Comparison of roll spectra for the Seasoar tow body and GW fairing	63
Figure 3.28.	Yaw-rate spectrum for the Seasoar vehicle towed at 6.5 kn.....	64
Figure 4.1.	The splitter plate and ceramic straws of the fifth version of the EMVM.....	67
Figure 4.2.	Block diagram of the electronics for the fifth version of the EMVM.....	69
Figure 4.3.	Map of the magnetic field of the fifth version of the EMVM, under a 1-A excitation current.....	72
Figure 4.4.	Schematic diagram of preamplifier electronics for one of three single-axis channels.....	74
Figure 4.5.	Total noise, referred to the input, for three candidate EMVM preamplifiers as a function of source impedance	75
Figure 4.6.	Straight-line transfer function of V/F converters and deviation from a straight-line fit.....	77
Figure 4.7.	The first, all-steel tripod used to place the EMVM near the bottom..	79
Figure 4.8.	All-plastic tripod with fifth version of the EMVM attached	80
Figure 4.9.	Fifth version EMVM noise levels in still water.....	82
Figure 4.10.	Power spectrum of vorticity for data taken in a quiet location in Puget Sound on 14 December 1990	83
Figure 5.1.	Map of Puget Sound with EMVM field operations marked as large dots.....	85
Figure 5.2.	Time series of data from a deployment off Point Jefferson showing random intermittent spikes.....	86
Figure 5.3.	Comparison of spectra obtained during two different deployments of the EMVM on a tripod in Puget Sound	87
Figure 5.4.	Comparison of spectra obtained from the EMVM when two different electrode port configurations were used: one flush mounted and one at the ends of ceramic straws.....	88
Figure 5.5.	Comparison of spectra obtained from the EMVM with the electromagnet turned on and with it turned off	89
Figure 5.6.	Data taken with the EMVM deployed on a tripod at a depth of 15 m in Blakely Harbor	90
Figure 5.7.	Data from the EMVM towed with the GW fairing on 16 April 1991 in the wake of Blakely Rock.....	92

Figure 5.8.	Tide heights at Restoration Point for 16–18 April 1991	93
Figure 5.9.	Vorticity variance along ship's track computed at 20-s intervals for data collected from 2120–2143 UTC on 16 April 1991	94
Figure 5.10.	Vorticity variance along ship's track computed at 20-s intervals for data collected from 2146–2220 UTC on 16 April 1991	94
Figure 5.11.	Vorticity variance along ship's track computed at 20-s intervals for data collected from 2223–2256 UTC on 16 April 1991	95
Figure 5.12.	Vorticity variance along ship's track computed at 20-s intervals for data collected from 2258–2328 UTC on 16 April 1991	95
Figure 5.13.	Vorticity variance along ship's track computed at 20-s intervals for data collected from 2331–2352 UTC on 16 April 1991	96
Figure 5.14.	Vorticity variance along ship's track computed at 20-s intervals for data collected from 2355–0017 UTC on 16–17 April 1991	96
Figure 5.15.	Vorticity variance along ship's track computed at 20-s intervals for data collected from 0020–0042 UTC on 17 April 1991	97
Figure 5.16.	Vorticity variance along ship's track computed at 20-s intervals for data collected from 0044–0111 UTC on 17 April 1991	97
Figure 5.17.	Comparison of vertical vorticity spectra from active and quiet regions of Puget Sound near Blakely Rock	98
Figure 5.18.	Time series of vertical vorticity on a tow with the GW fairing on 17 April 1991	98
Figure 5.19.	Vorticity variance along ship's track computed at 20-s intervals for data collected from 1728–1748 UTC on 17 April 1991	100
Figure 5.20.	Vorticity variance along ship's track computed at 20-s intervals for data collected from 1750–1806 UTC on 17 April 1991	100
Figure 5.21.	Vorticity variance along ship's track computed at 20-s intervals for data collected from 1808–1846 UTC on 17 April 1991	101
Figure 5.22.	Vorticity variance along ship's track computed at 20-s intervals for data collected from 1848–1932 UTC on 17 April 1991	101
Figure 5.23.	Vorticity variance along ship's track computed at 20-s intervals for data collected from 1935–2014 UTC on 17 April 1991	102
Figure 5.24.	Vorticity variance along ship's track computed at 20-s intervals for data collected from 2017–2054 UTC on 17 April 1991	102
Figure 5.25.	Two spectra of vertical vorticity data collected in Blakely Harbor ...	103

Figure 5.26.	Time series data from a tow on 12 June 1991.....	103
Figure 5.27.	Tide heights and average current for Restoration Point on 12–14 June 1991.....	104
Figure 5.28.	Vertical vorticity variance computed at 20-s intervals for data collected on 12 June 1991.....	105
Figure 5.29.	Time series data from a tow on 13 June 1991.....	106
Figure 5.30.	Vertical vorticity variance for data from 13 June 1991 taken during a time when the tidal flow was weak	106
Figure 5.31.	Vertical vorticity variance for data from 13 June 1991 taken during the time of maximum flood tide.....	107
Figure 5.32.	Blowup of one particular event in relation to signals observed during the entire day of towing.....	108
Figure 5.33.	Time series of vertical vorticity data for 10 July 1991	109
Figure 5.34.	Tide heights and average currents for Restoration Point during 10–12 July 1991.....	110
Figure 5.35.	Ship's track and drogue buoy tracks in areas of high vertical vorticity activity near Restoration Point.....	111
Figure 5.36.	Vertical vorticity data from the first half of 10 July 1991.....	112
Figure 5.37.	Vertical vorticity data from the second half of 10 July 1991.....	113
Figure 5.38.	Time series of vertical vorticity data from 11 July 1991	113
Figure 5.39.	Vertical vorticity variance at 20-s intervals for data from 11 July 1991	114
Figure 5.40.	Nine along-track plots of vertical vorticity along a line just south of Restoration Point.....	115
Figure 5.41.	Nine along-track plots of rms vorticity calculated for 20-s intervals	116
Figure 5.42.	Data from pass 1 (top panel, Figure 5.39) formed into 100-m along-track averages and displayed as a single point	117
Figure 5.43.	Vertical rms vorticity data from the 1000-m and 1100-m segments of Figure 5.39 plotted for each pass	118
Figure 5.44.	Contour plot of equal rms vertical vorticity versus distance (x) and time (y)	118
Figure 5.45.	Ship's track around Toliva Shoal in Puget Sound in August 1991	120
Figure 5.46.	Time series of vertical vorticity data for 28 August 1991	121

Figure 5.47.	First circle of Toliva Shoal, 1800–1850 UTC	128
Figure 5.48.	Second circumnavigation of Toliva Shoal, 1850–1940 UTC.....	123
Figure 5.49.	Third circumnavigation of Toliva Shoal, 1940–2030 UTC.....	124
Figure 5.50.	Fourth circumnavigation of Toliva Shoal, 2030–2106 UTC	125
Figure 5.51.	Azimuthal distribution of vertical vorticity variance (s^{-2}).....	126
Figure 5.52.	Data acquired with the EMVM sensor aligned so that the sensitive axis was horizontal	127
Figure 5.53.	Data acquired with the EMVM sensor aligned so that the sensitive axis was horizontal	128

ABSTRACT

The Electromagnetic Vorticity Meter (EMVM) directly measures small-scale vorticity in the ocean using the principles of electromagnetic induction. The scientific motivation for developing the EMVM, the design concept, and the theory of operation are discussed. Complete descriptions are given of the instrument's design, construction, and performance through several evolutions of the sensor, and extensive observations are presented of sensor performance during laboratory and field tests. The tests demonstrate a vorticity noise level of 10^{-3} s^{-1} .

1. INTRODUCTION

An instrument and technique have been developed for the direct measurement of small-scale ocean vorticity. This report reviews the theory on which the instrument, called the Electromagnetic Vorticity Meter, or EMVM, is based, describes its evolution and testing from 1982 to the present, and presents results obtained during laboratory and field tests.

Section 1 defines vorticity and discusses its importance in oceanography. Section 2 describes the concept and operating principles of the EMVM, including detailed equations explaining its operation. Section 3 contains detailed descriptions of the first four versions of the instrument, and Section 4 describes the fifth version. Finally, the results of vorticity observations conducted with the EMVM in Puget Sound are given in Section 5.

1.1 What is Vorticity?

Vorticity is a property of the physical state of a fluid. Qualitatively, it is the spin or swirl of a fluid parcel. Mathematically, it is the curl of velocity, $\nabla \times \mathbf{v}$. Measuring the full vector vorticity is a formidable task. The curl is composed of nine derivatives, although only six are independent for divergence-free flow.

Vorticity is fundamentally important in fluid mechanics and particularly important in physical oceanography. Because few processes generate or dissipate it, once there, it can be long lived. In fact, some theories treat vorticity as a conserved quantity that does not change as the fluid moves. In addition, because of its organized motion (i.e., swirl), it stands out from the general background motions. Often the description of a particular flow feature is most simply stated in terms of the vorticity distribution and dynamics.

In the open, undisturbed ocean, only boundary friction from wind at the surface or drag at the bottom and mixing (often caused by breaking internal waves) can impart vorticity. This characteristic is evident from the momentum equations for irrotational (i.e., high-frequency) internal waves:

$$u_t = -p_x/\rho + F \quad (1.1)$$

and

$$v_t = -p_y/\rho + G, \quad (1.2)$$

where u and v are the horizontal velocity components, p and ρ are the pressure and density functions, F and G are the nonlinear and forcing terms, and the subscripts denote differentiations. Cross differentiation of the momentum equations yields

$$(v_x - u_y)_t = G_x - F_y. \quad (1.3)$$

The quantity $v_x - u_y$ is the vertical component of the curl of velocity, i.e., the vertical component of vorticity. In the absence of nonlinearities and forcing (i.e., $F = G = 0$), the

vertical vorticity should be small or zero. High-frequency internal waves have little vertical vorticity, and lower-frequency ones have vertical components that are less than the planetary value (denoted as f or the Coriolis parameter, $\approx 10^{-4} \text{ s}^{-1}$ at mid-latitudes).

Thus, mapping the vorticity distribution can yield information about what dynamic processes a water parcel has experienced. In studying ocean mixing, for example, one of the difficulties is distinguishing normal, ambient structures that are not undergoing significant stirring from structures that appear similar but are undergoing active stirring and dissipation. One difference is that mixing events contain large contributions from small-scale vorticity.

1.2 Need for Vorticity Observations

Vorticity plays an important role in the cascades of energy between the large scales of generation and the smaller scales over which energy dissipation occurs. Vortical motion is possibly the explanation behind much of the variability observed in the ocean that cannot be assigned to internal waves. On mesoscales, say tens of kilometers, vorticity is the most important dynamic variable in physical oceanography. Features such as ocean eddies often exhibit vorticity comparable to the planetary value, but at scales of a meter and less the principal signals are due to mixing and nonlinear processes.

Historically, there has been a need to measure small-scale vorticity for general studies of turbulence as well as specifically for oceanography. Saffman (1981) claims that "the invention of an accurate non-intrusive, fine-resolution vorticity meter would be of inestimable value..." while Müller et al. (1986) state that in order to test recent theories of oceanic finestructure, "we need to develop techniques to measure potential vorticity on small scales."

Too little is known about the vorticity field. This situation results from technical difficulties in observing vorticity, not from a conscious intent to ignore it. Müller (1984) says, "The vortical mode also exists at scales traditionally associated with internal waves. This basic fact has been somewhat repressed in the oceanographic community." He argues that small-scale vortical structures exist and may be responsible for the noninternal-wave "finestructure" invoked to explain moored current and temperature measurements. (The part of the observed current and temperature variance that does not conform to behavior required of linear internal waves has been denoted as finestructure.) Müller states that we need to learn how to measure potential vorticity, which is a measure of the ratio of absolute vorticity to the effective depth of the vortex. (Absolute vorticity is the sum of planetary and relative vorticity.)

Another justification for conducting this development is that measurements of velocity and vorticity are vitally important to understanding the role of motions at scales of 1–10 m. Gargett et al. (1981) report a change in the slope of vertical shear spectra at about 10-m vertical wavelength. The horizontal wavelengths associated with this

spectral "knee" are not known. The region spans a gap between internal waves with low vertical wavenumbers and motions with high vertical wavenumbers governed by turbulence and viscous dissipation. New ocean observations, perhaps of vorticity, are needed to understand more about the structure and physics of this region. In addition, Müller makes the point that the vortical mode is needed to generate a complete description of the internal wave regime.

Lin and Pao (1979) have demonstrated in laboratory experiments that stratification inhibits vertical motion. Thus a stratified fluid quickly exhibits quasi two-dimensional motion in the form of horizontal vortices which have vertical vorticity. Their collapse occurs on the order of six buoyancy periods. One hypothesis is that, regardless of the initial spectrum, there will be an inverse cascade of vorticity variance. Thus, if there is no additional generation of vorticity, the overall variance levels will decrease, but the remaining energy will move to lower wavenumbers.

Finally, because the natural background of small-scale vorticity is expected to be small, observations of enhanced levels may indicate an unnatural, artificial source. The torque needed to spin up a vortex about the vertical axis is not easily provided within the upper ocean. Wind stress or water moving past a surface are potential sources, and vorticity is a definitely a signature of wave instability and breakdown.

In spite of the advantages of directly measuring vorticity, no sensor with that capability at appropriate length scales and useful accuracy had been developed. This deficiency was addressed through the development and use of the Electromagnetic Vorticity Meter.

In order for the EMVM to be scientifically useful, it must have a noise level significantly below the expected ambient level of vorticity in the open ocean. It is possible to estimate the energy levels of the current finestructure and infer the needed sensor performance. From observations during the Internal Wave Experiment (IWEX), where the presumption of finestructure was first invoked (Briscoe, 1975), the nonlinear contamination is estimated to be about 1 cm/s rms at high frequency (~ 1 cph). A simple model for the relative vorticity of a circular vortex of peak speed 1.4 cm/s and radius L to that speed is

$$\zeta = \frac{2 \times 1.4}{L} \times 10^{-2} \text{ s}^{-1} . \quad (1.4)$$

The factor of two comes from the contributions of both velocity components. In IWEX, the coherence at high frequency dropped rapidly at less than 10-m separations, so L must be around 10 m or less. Then ζ would be about 0.003 s^{-1} , a level slightly higher than demonstrated sensor performance.

2. CONCEPT AND OPERATING PRINCIPLES

2.1 Concept of EMVM

The EMVM operates on the principles of motional induction which govern the electric fields induced as water moves through a magnetic field. These principles are the basis of the conventional electromagnetic current meter which generates a magnetic field and measures the potential differences between spaced electrodes. In this case, only the first derivatives of the potential field are observed. In the EMVM, we measure the first ($\nabla\phi$) and second ($\nabla^2\phi$) derivatives of the electric potential field. The first differences yield the usual linear velocity components; the second provide the determination of a component of water vorticity.

The first mention of measuring $\nabla^2\phi$ to estimate a component of small-scale vorticity appears to be by Grossman et al. (1957). Baker (1971) described the construction and use of a "vortex probe" based on the two-dimensional Laplacian of the potential field. Tsinober et al. (1987) described a very small (≈ 1 mm) probe used to study turbulence in salt water. They reported good success with the method and offered the following list of advantages:

- It offers the possibility of distinguishing between velocity components because of the vector nature of the basic relation and the sensitivity to the direction of the flow.
- It is linear and does not require any calibration procedure (in fact, no calibration procedure can be applied to this method).
- It is insensitive to the physical properties of the fluid medium.
- It yields an instantaneous measure of quantities fluctuating in time, i.e., its response time is extremely small.
- It operates in flows of a complex nature, and it allows the determination of the separation and reattachment points and the moment and position of the turbulence onset or relaminization.
- It can be used in nonisotropic turbulence for determining the spectral interval where the turbulence becomes locally isotropic by using high-pass filters and checking if the relations between turbulence components are valid.

2.2. Governing Equations

The governing equation for the motionally induced potential differences in seawater is

$$\nabla\phi = \mathbf{v} \times \mathbf{B} - \mathbf{J}/\sigma, \quad (2.1)$$

where ϕ is the electrostatic potential, \mathbf{v} is the water velocity, \mathbf{B} is the magnetic field, \mathbf{J} is the electric current density, and σ is the electrical conductivity (assumed constant). The

EMVM works by measuring the electric field induced by the vorticity of seawater in a magnetic field. The magnetic field induced by \mathbf{J} is assumed to be negligible and the external magnetic field to be uniform and stationary. Since $\nabla \cdot \mathbf{J} = 0$, then, by taking the divergence of Eq. (2.1), we obtain

$$\nabla^2 \phi = \nabla \cdot (\mathbf{v} \times \mathbf{B}) = \mathbf{B} \cdot \boldsymbol{\omega} - \mathbf{v} \cdot \nabla \times \mathbf{B} \quad (2.2)$$

where $\boldsymbol{\omega}$ is the vorticity of the water (i.e., $\nabla \times \mathbf{v}$). The last term in Eq. 2.2 can be shown to be small compared with the next-to-last term, and can be ignored. The magnetic field produced by the EMVM is unidirectional or symmetrical about an axis, so that only one component of the vorticity is obtained. Thus

$$\nabla^2 \phi \approx B_3 \omega_3 \quad (2.3)$$

where the subscript 3 denotes the component parallel to the magnetic field, which in the instrument's usual configuration will be vertical. If we can measure $\nabla^2 \phi$ and know \mathbf{B} , then we can determine the component of vorticity parallel with \mathbf{B} .

2.3 Measurement Approach

We have no sensor for measuring $\nabla^2 \phi$ directly, but we can estimate it by a finite-difference scheme. An array of electrodes is used to sense voltages that result from vorticity in the presence of an applied magnetic field. In its simplest configuration, the instrument measures the x component of $\nabla^2 \phi$ (i.e., $\partial^2 \phi / \partial x^2$), as shown in Figure 2.1. The voltages across three collinear electrodes are measured. Each outer electrode is referenced to the center (ground) electrode, resulting in the signed voltages shown. The output of

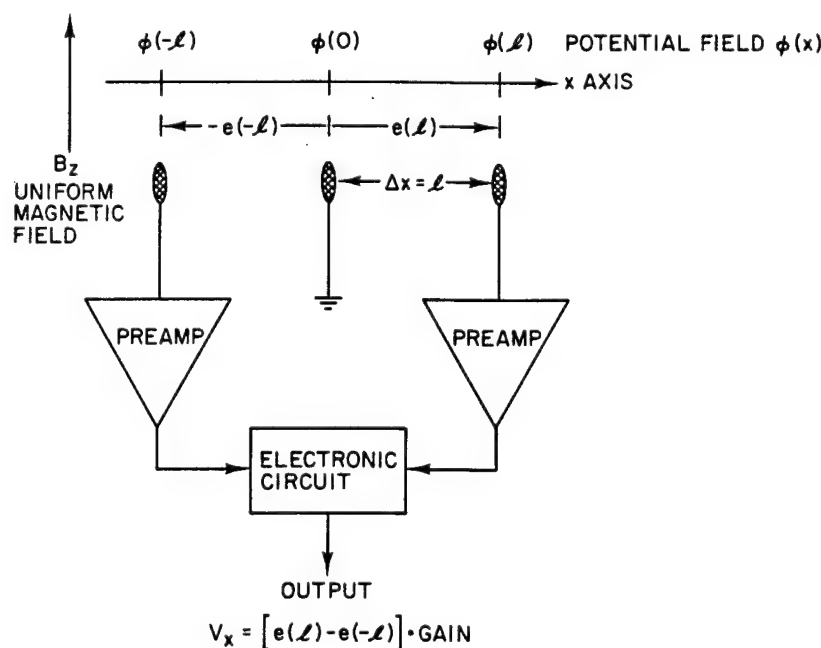


Figure 2.1. Measurement scheme for determining $\Delta^2 \phi / \Delta x^2$, the x component of $\nabla^2 \phi$.

the electronics circuit is the difference in the voltages between the electrode arms. Thus the device is insensitive to a uniform electric field such as that caused by a uniform flow of water or the lateral translation of the sensor through the surrounding seawater. Rather, a voltage will arise only if the seawater has a relative rotary motion. It makes no difference whether the sensor or the water rotates.

The measured voltages can be expressed in terms of the potential ϕ . This potential difference is given as (refer to Figure 2.1)

$$e(l) = \phi(l) - \phi(0) \quad (2.4)$$

and

$$-e(-l) = \phi(-l) - \phi(0). \quad (2.5)$$

The finite difference approximation of $\partial^2 \phi / \partial x^2$ is given by

$$\frac{\Delta^2 \phi}{\Delta x^2} = \frac{\phi(l) + \phi(-l) - 2\phi(0)}{l^2}. \quad (2.6)$$

This can be expressed in terms of the measured voltages as

$$\frac{\Delta^2 \phi}{\Delta x^2} = \frac{e(l) - e(-l)}{l^2}. \quad (2.7)$$

Thus the approximation for $\partial^2 \phi / \partial x^2$ in terms of the output V_x is

$$\frac{\partial^2 \phi}{\partial x^2} = \frac{V_x}{l^2 \times \text{Gain}}. \quad (2.8)$$

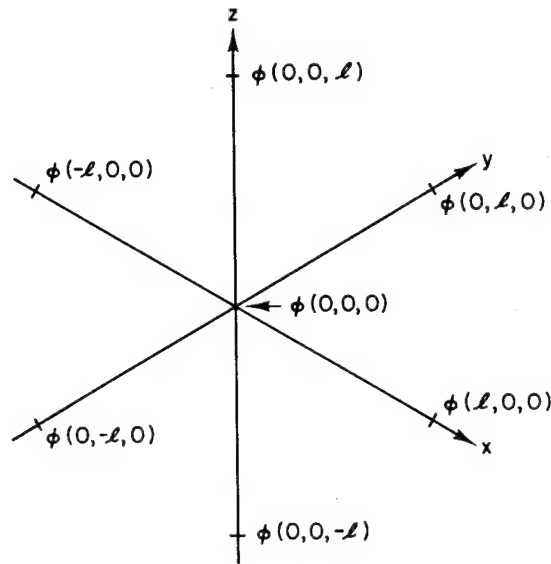
This analysis can be extended to the generalized three-dimensional case in which three independent measurements are made and combined to yield a three-dimensional approximation of $\nabla^2 \phi$. Figure 2.2 illustrates this process.

2.3.1 2-D Case: Flow and magnetic field uniform in z direction

Consider the case of a body of seawater in solid-body rotation about its vertical axis in a uniform vertical magnetic field. A cylindrical coordinate system is used (r, θ, z) . Denote the rotation rate as $\frac{1}{2}\omega_z$ (the $\frac{1}{2}$ is there because the rotation rate is twice the vorticity for solid-body rotation). This situation is equivalent to rotating an electromagnetic sensor in stationary seawater in the presence of the vertical magnetic field, a method used to evaluate our EMVM. For rotation about the $r = 0$ axis, the horizontal velocity in solid-body rotation is $\frac{1}{2}\omega_z r \hat{1}_\theta$, where θ is the angle in the cylindrical coordinate system (positive CCW from x axis). The electric potential function from Eq. 2.1 is

$$\phi(r, \theta) = \int_0^r (\frac{1}{2}B_z \omega_z r - J_r / \sigma) dr. \quad (2.9)$$

The absence of vertical variations in the magnetic field or flow structure means that J_z and $\partial J_z / \partial z$ are zero. Continuity of electric current requires then that $\partial J_r / \partial r$ is also zero. Axial symmetry requires that $J_r = 0$ at $r = 0$. Hence, $\mathbf{J} = 0$ everywhere. Then,



$$\begin{aligned}
 \nabla^2 \phi(x,y,z) &\approx \phi(\ell,0,0) + \phi(-\ell,0,0) + \phi(0,\ell,0) + \phi(0,-\ell,0) + \phi(0,0,\ell) + \phi(0,0,-\ell) \\
 &\quad - 6\phi(0,0,0) / \ell^2 \\
 &\approx \left[\{e(\ell,0,0) - e(-\ell,0,0) + e(0,\ell,0) - e(0,-\ell,0) + e(0,0,\ell) - e(0,0,-\ell)\} \right] / \ell^2 \\
 &\approx \left(\frac{V_x}{G_x} + \frac{V_y}{G_y} + \frac{V_z}{G_z} \right) / \ell^2
 \end{aligned}$$

Figure 2.2. Three-dimensional finite-difference approximation of $\nabla^2 \phi$.

$$\phi(r, \theta) = \frac{1}{4} B_z \omega_z r^2. \quad (2.10)$$

A set of three electrodes, equally spaced on a line in the horizontal plane and located at $r-l$, r , and $r+l$ would sense an average difference voltage of

$$\begin{aligned}
 \frac{\phi(r+l, \theta) + \phi(r-l, \theta) - 2\phi(r, \theta)}{2} &= \frac{1}{8} B_z \omega_z [(r+l)^2 + (r-l)^2 - 2r^2] \\
 &= \frac{1}{4} B_z \omega_z l^2.
 \end{aligned} \quad (2.11)$$

It can be shown that any three equally spaced electrodes on a line in the horizontal plane would yield the same voltage regardless of orientation or reference to the origin of the arbitrary coordinate system. An easy way to confirm this is to consider a triplet of orthogonal electrodes positioned so that the center electrode is at $r=0$. Each axis contributes the same difference voltages, and this condition does not change as the electrode array is moved away from the origin.

A second horizontal axis would, therefore, observe the same voltage. Thus, a two-axis unit would measure an *average* voltage of $\frac{1}{4} B_z \omega_z l^2$. A set of three electrodes equally spaced along the vertical axis will sense zero potential difference and contribute nothing to the sum obtained with two sets of electrodes oriented horizontally, say along the x and y axes. Hence, a sensor with two axes in the horizontal plane would observe an *average* voltage of $\frac{1}{4} B_z \omega_z l^2$. An average voltage is used so that the observed potential does not increase linearly with the number of sensor axes.

2.3.2 3-D Case: Uniform rotary flow in dipole magnetic field

Consider the case of an infinite volume of seawater in solid-body rotation about the vertical (z) axis in a vertical dipole magnetic field. This is a realistic example which simulates what an EMVM (with its own dipole magnetic field) would observe in a patch of vorticity with a spatial scale that is large compared with that of the sensor. Also, it corresponds to the rotation of an EMVM that produces its own dipole magnetic field in a comparatively large tank, such as was done in the laboratory to check the instrument's performance. More complex magnetic fields can be constructed by superposition from this elemental solution.

The symmetry of the problem places constraints on electric current paths. For example, the electric currents must be antisymmetric about the $z = 0$ plane (i.e., mirror images). Consider the line in the z direction that passes through the origin. For a volume in solid-body rotation about this line, the vertical electric currents must change sign at the origin. That is, the currents are an odd function with respect to z . This fact can be seen by considering the induction terms along the z axis. The induction term, $\mathbf{v} \times \mathbf{B} \cdot \hat{\mathbf{1}}_z$, is zero on the z axis. Hence,

$$\phi(0) - \phi(-\infty) = - \int_{-\infty}^0 J_z dz \quad (2.12)$$

and

$$\phi(0) - \phi(\infty) = \int_0^{\infty} J_z dz. \quad (2.13)$$

Because the magnetic field is of finite size, it is necessary that the potential be a constant at infinity; that is, $\phi(\infty)$ must be the same value as $\phi(-\infty)$. It is convenient to take this value to be zero. The only form for J_z that will satisfy the above expression is for it to be an odd function of z . In this way, the potential at the origin is the same regardless of whether the integration toward the origin is along the positive or the negative z axis. Another consequence is that the electric currents converging on the origin along the z axis are compensated by electric currents flowing outward on the x - y plane. Thus the horizontal current along the x axis must also be an odd function of x and of the opposite sign as that for z . That is, if J_z is positive for $z > 0$, then J_x must be negative for $x > 0$. The induction term, $\mathbf{v} \times \mathbf{B} \cdot \hat{\mathbf{1}}_x$, integrates to zero along the line from infinity to the origin. Hence it makes no contribution to the potential at the origin.

The consequence is that integrating from infinity along the z axis yields a potential at the origin that is of opposite sign to that obtained by integration along the x axis. The potential at the origin must be independent of the path of integration. The only way for the potential to be independent of the path of integration is for J_x to be zero on the x axis, for J_y to be zero on the y axis, and for J_z to be zero on the z axis. This argument does not exclude electric currents flowing in other parts of the space, but a formal solution given later demonstrates that $\mathbf{J} = 0$ everywhere. Hence, there can be no electric currents flowing as a consequence of solid-body rotation in a dipole magnetic field. The result is that for vorticity the electric current field is zero.

A vorticity of 0.1 s^{-1} corresponds to a voltage of approximately 25 nV over 5-cm arms in a 10^{-4} T (1 G) magnetic field. The greatest difficulties in detecting such a small signal are due to the drift of the electrode offset voltages, electrode noise, and the $1/f$ behavior of electronic noise. Figure 2.3 shows the spectrum of the noise associated with the electrodes and electronics. The $1/f$ behavior of the electronic noise makes the detection of low-frequency vorticity difficult.

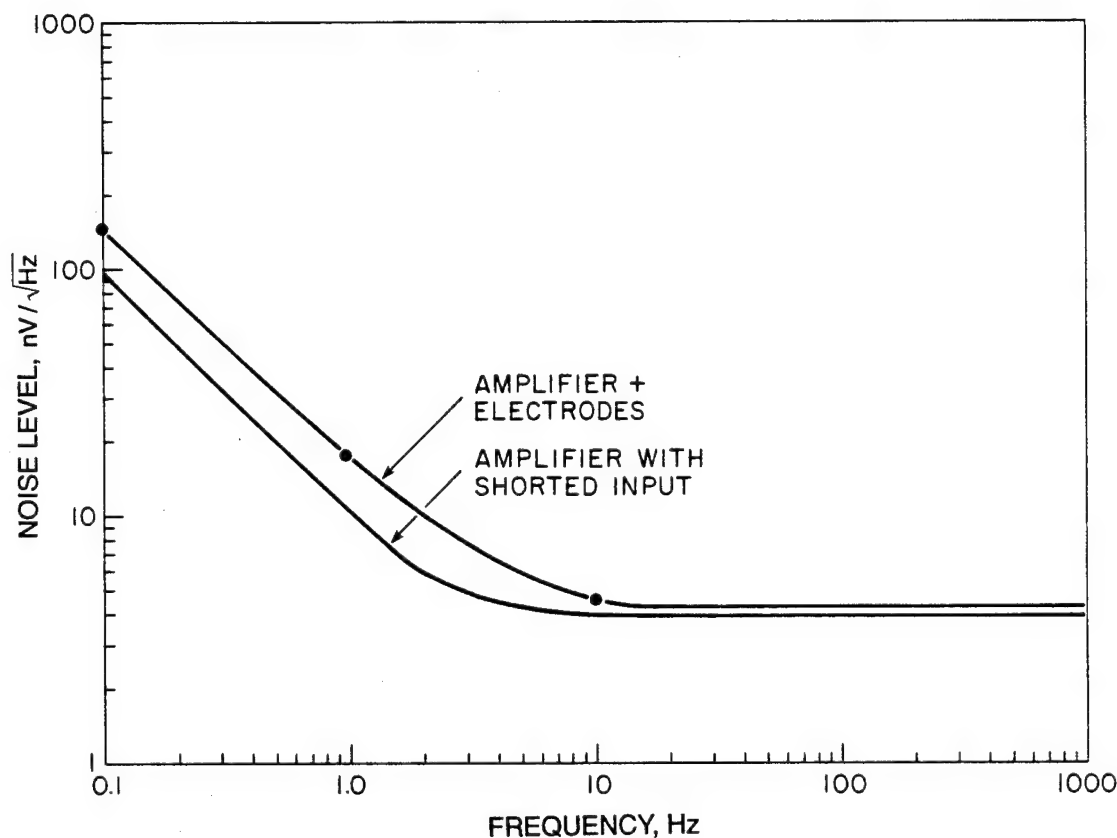


Figure 2.3. Typical noise level associated with input amplifier using Analog Devices OP-27 integrated circuit operational amplifiers. This configuration is similar to that used for the first, second, and third versions of the EMVM.

A more formal derivation of the finite-difference equations can be based on Gauss's theorem. Assume that the vorticity and magnetic field are axially symmetric about the vertical axis, for example, solid-body rotation in a vertical dipole magnetic field. According to Eq. 2.2, $\nabla^2 \phi = \mathbf{B} \cdot \boldsymbol{\omega}$. Integrating this equation over the volume V and applying Gauss's theorem yields

$$\int_A \nabla \phi \cdot \hat{\mathbf{n}} dA = \int_V \mathbf{B} \cdot \boldsymbol{\omega} dV, \quad (2.14)$$

where $\hat{\mathbf{n}}$ is the unit vector normal to the surface A . Consider a body that is a right circular disk of radius R in the horizontal or x - y plane and thickness dz centered about $z = 0$. The left-hand integral can be expressed in terms of contributions from the surface at $r = R$ and from the top and bottom areas:

$$\int_A \nabla \phi \cdot \hat{\mathbf{n}} dA = \int_{A_R} \partial \phi / \partial r dA + \int_{A_{\text{top}}} \partial \phi / \partial z dA + \int_{A_{\text{bot}}} \partial \phi / \partial z dA. \quad (2.15)$$

The contributions from the top and bottom surfaces cancel because of the assumed symmetry of the flow and of the magnetic field about the vertical axis. The potential and radial derivative at R can be expressed in terms of MacLaurin series which can be manipulated to yield

$$\partial \phi(r) / \partial r = \frac{2}{r} [\phi(r) - \phi(0)] - \partial \phi / \partial r|_0 + \frac{r^2}{6} \partial^3 \phi / \partial r^3|_0 + \text{higher order terms}. \quad (2.16)$$

From the earlier analysis, we know that $\phi(r) = \frac{1}{4} \mathbf{B} \cdot \boldsymbol{\omega} r^2$. The term $\partial \phi / \partial r|_0$ is zero, and the third- and higher-order derivatives are zero (and will be small in general for vorticity patterns that are larger than the sensor). Thus we obtain

$$\int_{A_R} [\phi(R) - \phi(0)] dA = \frac{R}{2} \int_V \mathbf{B} \cdot \boldsymbol{\omega} dV \cdots \quad (2.17)$$

Dropping the higher-order terms and expressing the integrals as averages gives

$$\langle \phi(R) - \phi(0) \rangle_{A_R} = \frac{\frac{1}{2} V R}{A_R} \langle \mathbf{B} \cdot \boldsymbol{\omega} \rangle_V, \quad (2.18)$$

where $\langle \rangle_{A_R}$ represents an average over the surface A_R and $\langle \rangle_V$ represents an average over the volume V .

The ratio of the volume (i.e., $V = \pi R^2 dz$) to the area (i.e., $A_R = 2\pi R dz$) of the disk-shaped body is $\frac{1}{2} R$; thus Eq. 2.18 becomes

$$\langle \phi(R) - \phi(0) \rangle_{A_R} = \frac{R^2}{4} \langle \mathbf{B} \cdot \boldsymbol{\omega} \rangle_V. \quad (2.19)$$

For a thin disk ($dz \ll R$), the "volume" average is more nearly an average over the surface between the origin and the radius R , and the "surface" area is more nearly an average around the circumference at the radius R . If electrodes are added off the x - y plane, the volume changes as does the bounding surface.

The simplest approximation of a spherical array is six electrodes at distances of $\pm R$ on the x , y , and z axes and one reference electrode at the origin. The corresponding area and volume are for the sphere of radius R about the origin. Recall that the vertical potential gradient is zero, and electrodes separated in that direction make no contribution to the average. Therefore, the average potential difference is $2/3$ that of a single axis. The volume average of $\mathbf{B} \cdot \boldsymbol{\omega}$ times the ratio of volume to area is $1/3 R^2 \mathbf{B} \cdot \boldsymbol{\omega}$. Hence, for the 2-D case where the volume integral is trivial,

$$\langle \phi(R) - \phi(0) \rangle_{A_R} = \frac{R^2}{4} \langle \mathbf{B} \cdot \boldsymbol{\omega} \rangle_V, \quad (2.20)$$

in confirmation of Eq. 2.19.

The utility of the vertical electrodes appears when flow is not two-dimensional and perpendicular to the axis of \mathbf{B} .

We interpret our measurements in terms of the integral expression because it explicitly accommodates spatially variable \mathbf{B} and $\boldsymbol{\omega}$. In summary, the average potential from a set of equally distributed electrodes (minus the potential at the origin of the array) is interpreted as equal to the average scalar product of magnetic field and vorticity. We use the robust relationship given in Eq. 2.19 for converting average electric potential differences into a component of the average vorticity parallel to the known applied magnetic field.

2.4 Modeling

Section 2.3 derived expressions between potential measurements and vorticity with a minimum of mathematical complexity. In this section, analytical solutions are derived for uniform flow and uniform solid-body rotation. In this analysis, we will assume that the magnetic field is generated by a thin coil. Using the assumptions made earlier, the governing equations are

$$\nabla \phi = \mathbf{v} \times \mathbf{B} - \mathbf{J} / \sigma \quad \text{and} \quad \nabla^2 \phi = \mathbf{B} \cdot \nabla \times \mathbf{v}. \quad (2.21)$$

The goal is to develop analytical expressions for ϕ and \mathbf{J} based on specified forms of \mathbf{B} and \mathbf{v} .

The magnetic field vector \mathbf{B} produced by an electric current (I) in a thin coil of radius a can be expressed as two infinite series of Legendre polynomials in a spherical coordinate system (r, θ, γ). The first is for the domain within a sphere defined by the coil (denoted hereafter as the "inner" region),

$$B_r = -\frac{\mu I}{2a} \sum_{n \text{ odd}}^{1 \text{ to } \infty} (-1)^{\frac{n+1}{2}} (n+1) \Pi \left[\frac{n}{n+1} \right] \left[\frac{r}{a} \right]^{n-1} P_n(\cos \theta) \quad (2.22a)$$

$$B_\theta = \frac{\mu I}{2a} \sum_{n \text{ odd}}^{1 \text{ to } \infty} (-1)^{\frac{n+1}{2}} \frac{(n+1)}{n} \Pi \left[\frac{n}{n+1} \right] \left[\frac{r}{a} \right]^{n-1} P_n^1(\cos \theta) \quad (2.22b)$$

and for the domain beyond the coil sphere (the "outer" region),

$$B_r = -\frac{\mu I}{2a} \sum_{n \text{ odd}}^{1 \text{ to } \infty} (-1)^{\frac{n+1}{2}} (n+1) \prod \left[\frac{n}{n+1} \right] \left[\frac{a}{r} \right]^{n+2} P_n(\cos\theta) \quad (2.22c)$$

$$B_\theta = -\frac{\mu I}{2a} \sum_{n \text{ odd}}^{1 \text{ to } \infty} (-1)^{\frac{n+1}{2}} \prod \left[\frac{n}{n+1} \right] \left[\frac{a}{r} \right]^{n+2} P_n^1(\cos\theta), \quad (2.22d)$$

where μ is the magnetic permeability and P_n and P_n^1 are Legendre and associated Legendre polynomials, respectively. The product term here will denote $\frac{1}{2}$ for $n=1$, $\frac{1}{2} \cdot \frac{3}{4}$ for $n=3$, etc. Only the values of n used in the summation (here n being odd only) will be used in the product term. The magnetic field computed by Eq. 2.22 is displayed in Figure 2.4.

The boundary conditions are (1) that ϕ is bounded at the origin, (2) that ϕ is zero at infinity, and (3) that the radial components of the $\nabla\phi$ and \mathbf{J} vectors are continuous across the boundary between the inner and outer regions. We will now examine the solution for two simple flow regimes.

2.4.1 Uniform flow

Assume a flow of uniform horizontal velocity (U), with no vertical component or variation. Then

$$\mathbf{v} = U \hat{i} = U \sin\theta \cos\gamma \hat{r} + U \cos\theta \cos\gamma \hat{\theta} - U \sin\gamma \hat{\gamma}. \quad (2.23)$$

For uniform flow, the velocity field is irrotational ($\nabla \times \mathbf{v} = 0$), so the problem reduces to solving for the Laplacian of the potential, $\nabla^2\phi = 0$, with the conditions

$$(r = a) \phi_i = \phi_o \quad \text{and} \quad (r = a) \left[\mathbf{v} \times \mathbf{B} - \nabla\phi \right]_i \hat{r} = \left[\mathbf{v} \times \mathbf{B} - \nabla\phi \right]_o \hat{r}, \quad (2.24)$$

where the subscripts i and o denote inner and outer regions, respectively. First, we will examine the radial component of $\mathbf{v} \times \mathbf{B}$ in order to deal with the second boundary condition. In spherical coordinates,

$$\mathbf{v} \times \mathbf{B} = -v_\gamma B_\theta \hat{r} + v_\gamma B_r \hat{\theta} + (v_r B_\theta - v_\theta B_r) \hat{\gamma}. \quad (2.25)$$

For the inner region,

$$(\mathbf{v} \times \mathbf{B}) \hat{r} = \frac{U\mu I}{2a} \sum_{n \text{ odd}}^{1 \text{ to } \infty} (-1)^{\frac{n+1}{2}} \frac{(n+1)}{n} \prod \left[\frac{n}{n+1} \right] \left[\frac{r}{a} \right]^{n-1} \sin\gamma P_n^1; \quad (2.26a)$$

for the outer region,

$$(\mathbf{v} \times \mathbf{B}) \hat{r} = -\frac{U\mu I}{2a} \sum_{n \text{ odd}}^{1 \text{ to } \infty} (-1)^{\frac{n+1}{2}} \prod \left[\frac{n}{n+1} \right] \left[\frac{a}{r} \right]^{n+2} \sin\gamma P_n^1. \quad (2.26b)$$

The second boundary condition (at $r = a$) can then be written as

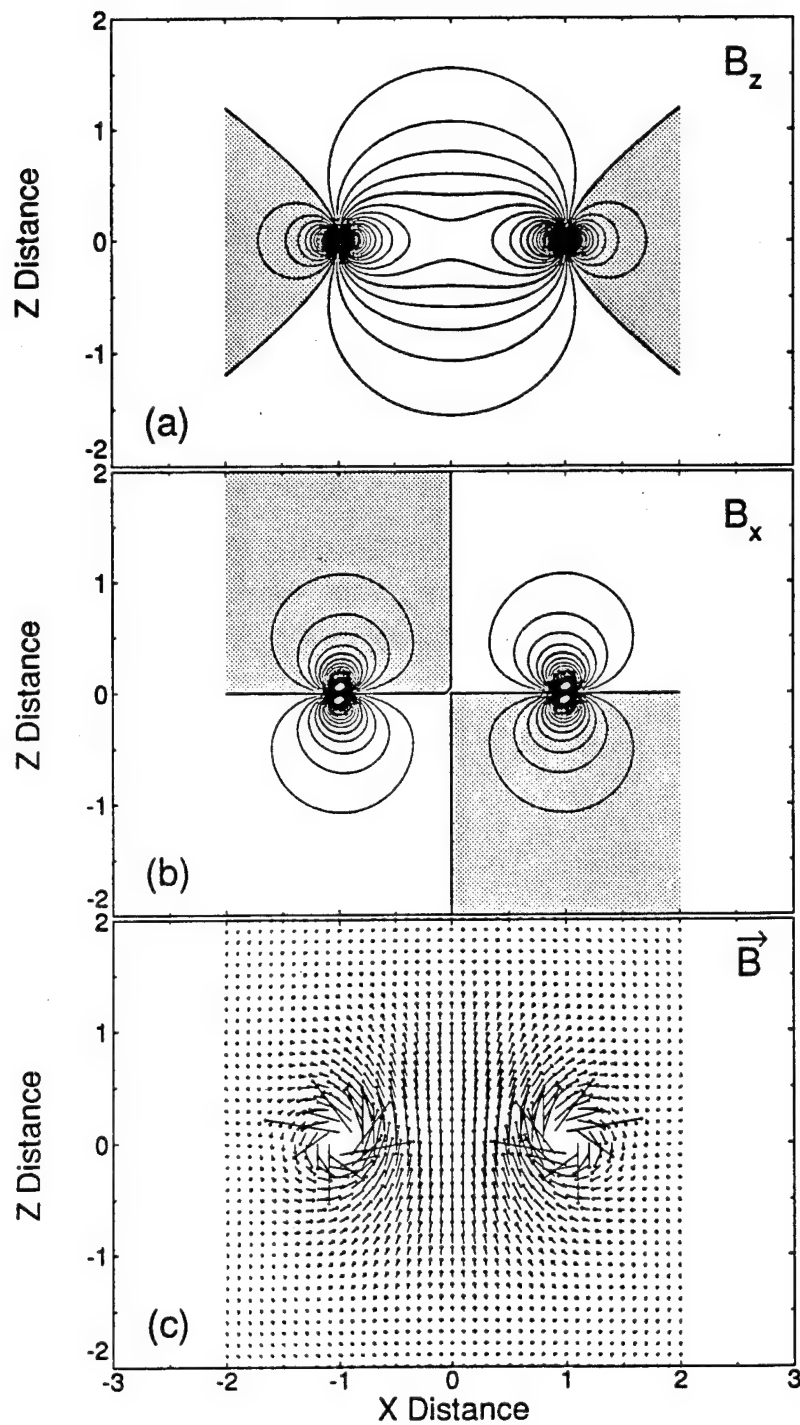


Figure 2.4. Magnetic field produced by an electric current in a thin coil. Distances are normalized by a , the radius of the coil. The current is running counterclockwise through the coil, as viewed from above. The field has been transformed into a x - z coordinate system. The contour values and scales are arbitrary, and gray shading denotes negative values. (a) Contours of the vertical component of \mathbf{B} . (b) Contours of the horizontal component of \mathbf{B} . (c) Vectors of \mathbf{B} . Note that the vectors are nearly uniform in both direction and magnitude near the center of the coil.

$$\frac{\partial \phi_i}{\partial r} = \frac{\partial \phi_o}{\partial r} + \frac{U\mu I}{2a} \sum_{n \text{ odd}}^{1 \text{ to } \infty} (-1)^{\frac{n+1}{2}} \frac{(2n+1)}{n} \Pi \left[\frac{n}{n+1} \right] \sin \gamma P_n^1. \quad (2.27)$$

The general solution for the inner region is

$$\phi_i = \sum_{n=0}^{\infty} \sum_{m=0}^{\infty} \left[\frac{r}{a} \right]^n \left[C_{mn}^i Y_{mn}^e + S_{mn}^i Y_{mn}^0 \right], \quad (2.28)$$

where C and S are as yet undetermined coefficients and

$$Y_{mn}^e = P_n^m(\cos \theta) \cos m\gamma \quad \text{and} \quad Y_{mn}^0 = P_n^m(\cos \theta) \sin m\gamma \quad (2.29)$$

are spherical harmonics. In a similar manner, the general solution for the outer region is

$$\phi_o = \sum_{n=0}^{\infty} \sum_{m=0}^{\infty} \left[\frac{a}{r} \right]^{n+1} \left[C_{mn}^o Y_{mn}^e + S_{mn}^o Y_{mn}^0 \right]. \quad (2.30)$$

So, the first boundary condition can be expressed as

$$\sum_{n=0}^{\infty} \sum_{m=0}^{\infty} \left[C_{mn}^i Y_{mn}^e + S_{mn}^i Y_{mn}^0 \right] = \sum_{n=0}^{\infty} \sum_{m=0}^{\infty} \left[C_{mn}^o Y_{mn}^e + S_{mn}^o Y_{mn}^0 \right], \quad (2.31)$$

while the second boundary condition gives

$$\begin{aligned} \sum_{n=0}^{\infty} \sum_{m=0}^{\infty} \frac{n}{a} \left[C_{mn}^i Y_{mn}^e + S_{mn}^i Y_{mn}^0 \right] = & - \sum_{n=0}^{\infty} \sum_{m=0}^{\infty} \frac{(n+1)}{a} \left[C_{mn}^o Y_{mn}^e + S_{mn}^o Y_{mn}^0 \right] \\ & + \frac{U\mu I}{2a} \sum_{n \text{ odd}}^{1 \text{ to } \infty} (-1)^{\frac{n+1}{2}} \frac{(2n+1)}{n} \Pi \left[\frac{n}{n+1} \right] \sin \gamma P_n^1. \end{aligned} \quad (2.32)$$

After dividing through by a , the last term can be expressed as

$$\frac{U\mu I}{2} \sum_{n \text{ odd}}^{1 \text{ to } \infty} A_{1n} Y_{1n}^0, \quad (2.33)$$

where, for n odd,

$$A_{1n} = (-1)^{\frac{n+1}{2}} \frac{(2n+1)}{n} \Pi \left[\frac{n}{n+1} \right] \quad \text{and} \quad Y_{1n}^0 = \sin \gamma P_n^1. \quad (2.34)$$

Since the only external constraint on our problem comes from the $\mathbf{v} \times \mathbf{B}$ portion of the boundary condition, and it contains only Y_{1n}^0 terms, we can reduce our boundary conditions to

$$\sum_{n=0}^{\infty} S_{1n}^i Y_{1n}^0 = \sum_{n=0}^{\infty} S_{1n}^o Y_{1n}^0 \quad (2.35a)$$

and

$$\sum_{n=0}^{\infty} n S_{1n}^i Y_{1n}^0 = - \sum_{n=0}^{\infty} (n+1) S_{1n}^o Y_{1n}^0 + \frac{U\mu I}{2} \sum_{n \text{ odd}}^{1 \text{ to } \infty} A_{1n} Y_{1n}^0. \quad (2.35b)$$

Equating similar degrees of Y_{1n}^0 and setting all even degrees of S_{1n} to zero, we obtain

$$S_{1n}^i = S_{1n}^o \quad \text{and} \quad n S_{1n}^i = -(n+1) S_{1n}^o + \frac{U\mu I}{2} A_{1n}. \quad (2.36)$$

We now have two equations and two unknowns, which yield

$$S_{1n}^i = S_{1n}^o = \frac{U\mu I}{2} \frac{A_{1n}}{(2n+1)}. \quad (2.37)$$

The expressions for the potential ϕ in the inner and outer regions are then

$$\phi_i = \frac{U\mu I}{2} \sum_{n \text{ odd}}^{1 \text{ to } \infty} (-1)^{\frac{n+1}{2}} \frac{1}{n} \prod \left[\frac{n}{n+1} \right] \left[\frac{r}{a} \right]^n \sin \gamma P_n^1 \quad (2.38a)$$

and

$$\phi_o = \frac{U\mu I}{2} \sum_{n \text{ odd}}^{1 \text{ to } \infty} (-1)^{\frac{n+1}{2}} \frac{1}{n} \prod \left[\frac{n}{n+1} \right] \left[\frac{a}{r} \right]^{n+1} \sin \gamma P_n^1. \quad (2.38b)$$

The ϕ field is shown in Figure 2.5. For uniform flow, the potential field has no curvature in the center, and thus no vorticity would be measured. This is expected for uniform flow. However, to infer velocity from $\nabla \phi$, the current density must be known. Equation 2.21 is rewritten as

$$\nabla \phi = \mathbf{v} \times \mathbf{B} \left[1 - \frac{\mathbf{J}/\sigma}{\mathbf{v} \times \mathbf{B}} \right] = \mathbf{v} \times \mathbf{B} (1 - Hd), \quad (2.39)$$

where Hd is a correction, or "head" factor. The above division process expresses the following form: $Hd = \mathbf{J}/\sigma \cdot \hat{i} / (\mathbf{v} \times \mathbf{B}) \cdot \hat{i}$, where \hat{i} is a unit vector in the i th direction. This factor will be computed next.

The three components of the electric current density are

$$\mathbf{J} \hat{r} = \sigma \left[-v_{\gamma} B_{\theta} - \frac{\partial \phi}{\partial r} \right], \quad (2.40a)$$

$$\mathbf{J} \hat{\theta} = \sigma \left[v_{\gamma} B_r - \frac{1}{r} \frac{\partial \phi}{\partial \theta} \right], \quad (2.40b)$$

and

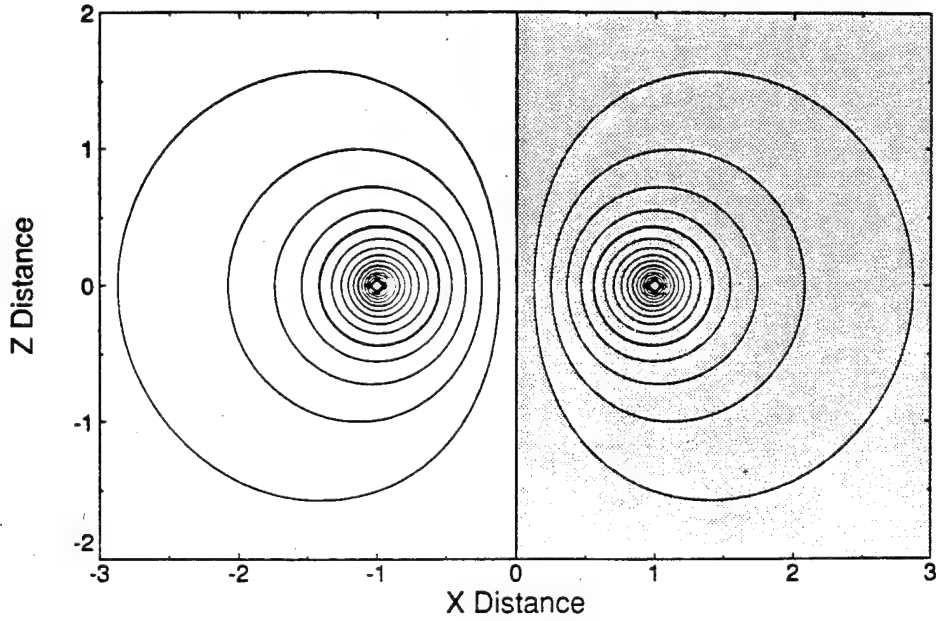


Figure 2.5. The potential field ϕ generated by uniform flow in the presence of the magnetic fields shown in Figure 2.4. The field has been transformed into an x - z coordinate system. Again, gray shading denotes negative values. The view is with the flow coming out of the page. The fine-scale perturbations are an artifact of the Legendre polynomial solution. The contour values are arbitrary.

$$\mathbf{J}\hat{\gamma} = \sigma \left[v_r B_\theta - v_\theta B_r - \frac{1}{r \sin \theta} \frac{\partial \phi}{\partial \gamma} \right]. \quad (2.40c)$$

Using the above expressions for \mathbf{B} , \mathbf{v} , and ϕ and simplifying, we obtain

$$\mathbf{J}_i \hat{r} = \frac{\sigma U \mu I}{2a} \sum_{n \text{ odd}}^{1 \text{ to } \infty} (-1)^{\frac{n+1}{2}} \frac{1}{n} \Pi \left[\frac{n}{n+1} \right] \left[\frac{r}{a} \right]^{n-1} \sin \gamma P_n^1, \quad (2.41a)$$

$$\mathbf{J}_o \hat{r} = \frac{\sigma U \mu I}{2a} \sum_{n \text{ odd}}^{1 \text{ to } \infty} (-1)^{\frac{n+1}{2}} \frac{1}{n} \Pi \left[\frac{n}{n+1} \right] \left[\frac{a}{r} \right]^{n+2} \sin \gamma P_n^1, \quad (2.41b)$$

$$\mathbf{J}_i \hat{\theta} = \frac{\sigma U \mu I}{2a} \sum_{n \text{ odd}}^{1 \text{ to } \infty} (-1)^{\frac{n+1}{2}} \Pi \left[\frac{n}{n+1} \right] \left[\frac{r}{a} \right]^{n-1} \sin \gamma \left[(n+1) P_n + \frac{(n+1) P_{n-1}^1 - n \cos \theta P_n^1}{n \sin \theta} \right], \quad (2.41c)$$

$$\mathbf{J}_o \hat{\theta} = \frac{\sigma U \mu I}{2a} \sum_{n \text{ odd}}^{1 \text{ to } \infty} (-1)^{\frac{n+1}{2}} \Pi \left[\frac{n}{n+1} \right] \left[\frac{a}{r} \right]^{n+2} \sin \gamma \left[(n+1) P_n + \frac{(n+1) P_{n-1}^1 - n \cos \theta P_n^1}{n \sin \theta} \right], \quad (2.41d)$$

$$\mathbf{J}_i \hat{\gamma} = \cos \gamma \frac{\sigma U \mu I}{2a} \sum_{n \text{ odd}}^{1 \text{ to } \infty} (-1)^{\frac{n+1}{2}} \Pi \left[\frac{n}{n+1} \right] \left[\frac{r}{a} \right]^{n-1} \left[(n+1) \cos \theta P_n + \frac{(n+1) \sin^2 \theta - 1}{n \sin \theta} P_n^1 \right], \quad (2.41e)$$

and

$$\mathbf{J}_o \hat{\gamma} = \cos \gamma \frac{\sigma U \mu I}{2a} \sum_{n \text{ odd}}^{1 \text{ to } \infty} (-1)^{\frac{n+1}{2}} \Pi \left[\frac{n}{n+1} \right] \left[\frac{a}{r} \right]^{n+2} \left[(n+1) \cos \theta P_n - \frac{n \sin^2 \theta + 1}{n \sin \theta} P_n^1 \right]. \quad (2.41f)$$

The \mathbf{J} fields are plotted in Figure 2.6, while Hd , the ratio of \mathbf{J}/σ and $\mathbf{v} \times \mathbf{B}$, is plotted in Figure 2.7. Near the center of the coil, the values of Hd are nearly uniform at 0.5. Thus the velocity estimated from $\nabla \phi$ measurements alone is only half what exists.

2.4.2 Solid-body rotation

Let us now assume a flow of solid-body rotation, centered about the z axis. For a spherical coordinate system, the vorticity ω of the system is

$$\omega \hat{z} = \omega \cos \theta \hat{r} - \omega \sin \theta \hat{\theta}. \quad (2.42)$$

The problem now is to solve the Poisson equation, $\nabla^2 \phi = \mathbf{B} \cdot \omega$, with the constraints that the potential ϕ is bounded at the origin and is zero at infinity and that the potential as well as the radial component of \mathbf{J} is continuous across the interface between the inner and outer regions. The solution scheme will proceed as follows. First, we will rewrite $\nabla^2 \phi = \mathbf{B} \cdot \omega$ as

$$\nabla^2 (\phi_P + \phi_H) = \mathbf{B} \cdot \omega, \quad (2.43)$$

where $\nabla^2 \phi_P = \mathbf{B} \cdot \omega$ and $\nabla^2 \phi_H = 0$, and the subscripts P and H denote the particular and the homogeneous solutions. We will first solve for ϕ_P , beginning with the right-hand side of our inhomogeneous equation, where, after regrouping terms and simplifying, we obtain

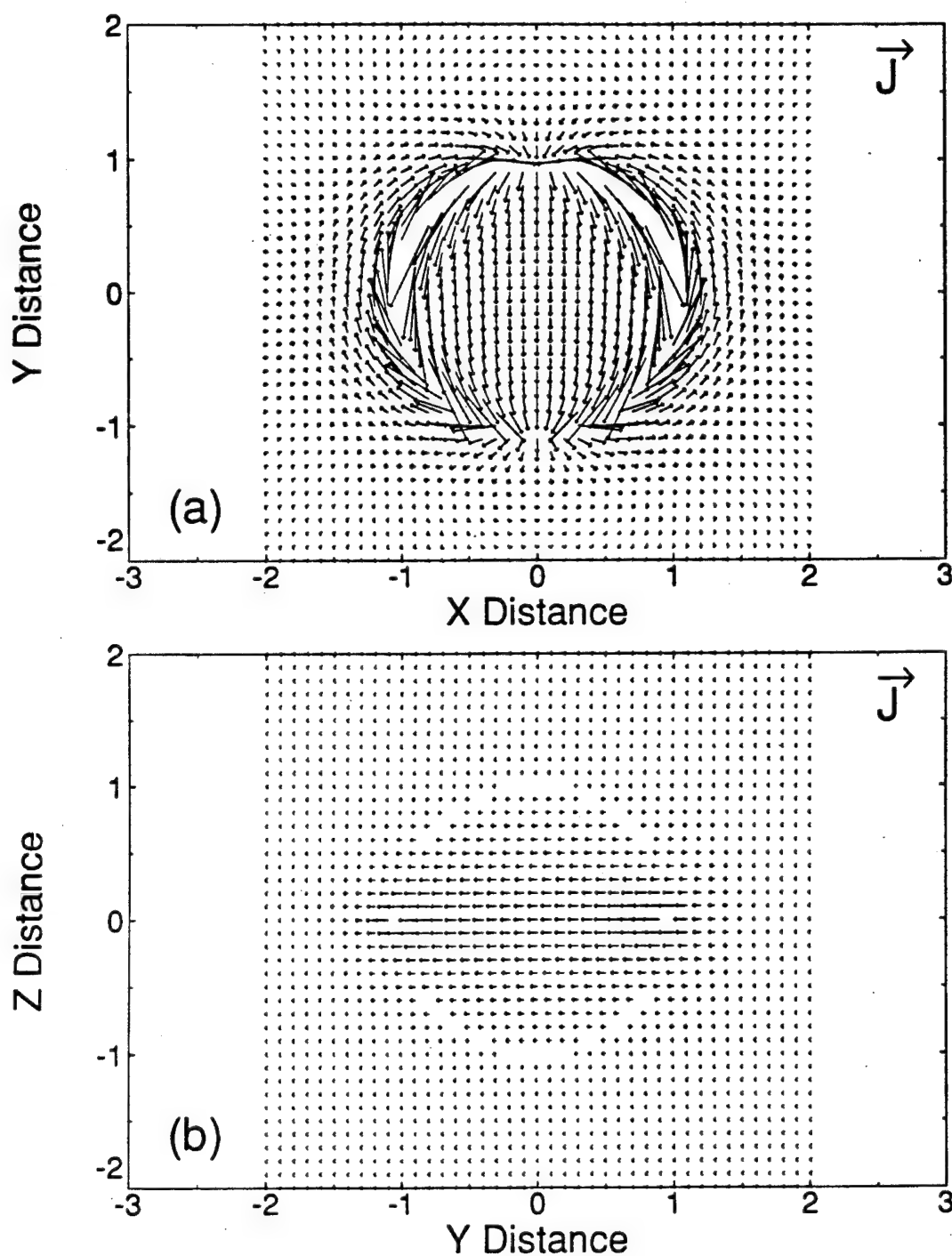


Figure 2.6. Vector plots of the electric current density \mathbf{J} produced by a uniform flow. The fields have been transformed into an x - y - z coordinate system. (a) View in the x - y plane, looking down from above. The uniform flow is from left to right (positive x direction). Within the coil, \mathbf{J} is in the same direction as $\mathbf{v} \times \mathbf{B}$. Since $\nabla \phi = \mathbf{v} \times \mathbf{B} - \mathbf{J}/\sigma$, the value of $\nabla \phi$ is less than expected from $\mathbf{v} \times \mathbf{B}$ alone. (b) View in the y - z plane, looking from the positive x direction. There is no vertical component of \mathbf{J} in this slice.

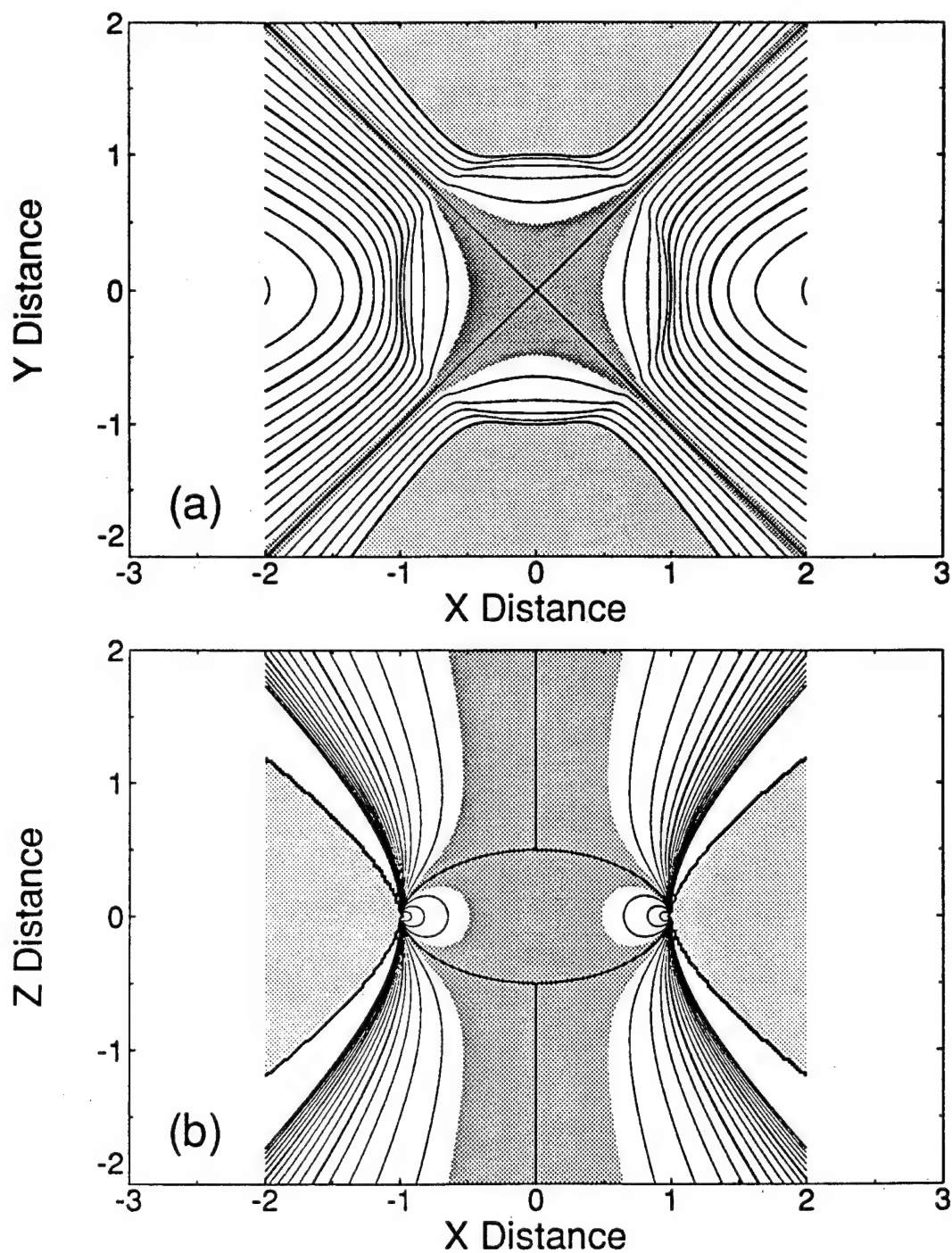


Figure 2.7. Contours of the head factor H_d . The light gray shading denotes negative values (whose contours are not shown), while the dark gray indicates the region where this component of the head factor is between 0.45 and 0.55. (a) Contours in the x - y plane. (b) Contours in the x - z plane. Note that for most of the region within the coil, the head factor is nearly 0.5.

$$\omega \cdot \mathbf{B} = \frac{\omega \mu I}{2a} \sum_{n \text{ even}}^{0 \text{ to } \infty} (-1)^{\frac{n}{2}} (n+1) \prod \left[\frac{n-1}{n} \right] \left[\frac{r}{a} \right]^n P_n. \quad (2.44)$$

The product term is defined here to be equal to 1 when $n = 0$. Since this equation forms the right-hand side of a Poisson equation and contains terms of the form P_n and r/a , we will try a form of ϕ_P that has these same characteristics. Note that the right-hand side has no dependence on the angle γ . So, let

$$\phi_{iP} = \sum_{n=0}^{\infty} C_n \left[\frac{r}{a} \right]^{n+m} P_n(\cos\theta), \quad (2.45)$$

where the C_n are undetermined coefficients and m is a constant power to be determined.

The Laplacian of ϕ in spherical coordinates is

$$\nabla^2 \phi_{iP} = \frac{1}{r^2} \frac{\partial}{\partial r} \left[r^2 \frac{\partial \phi}{\partial r} \right] + \frac{1}{r^2 \sin\theta} \frac{\partial}{\partial \theta} \left[\sin\theta \frac{\partial \phi}{\partial \theta} \right] + \frac{1}{r^2 \sin^2\theta} \frac{\partial^2 \phi}{\partial \gamma^2}. \quad (2.46)$$

If we use the assumed form of the solution, the Laplacian of ϕ_{iP} becomes, after considerable algebra,

$$\nabla^2 \phi_{iP} = \frac{1}{a^2} \sum C_n [2(n+m) + (n+m)(n+m-1) - n(n+1)] \left[\frac{r}{a} \right]^{n+m-2} P_n. \quad (2.47)$$

Now, equating the left-hand side of our Poisson equation with the right-hand side, for $n = 0$, we obtain

$$\frac{C_0}{a^2} [2m + m(m-1)] \left[\frac{r}{a} \right]^{m-2} = \frac{\omega \mu I}{2a}. \quad (2.48)$$

In order that the powers of r cancel on each side of the equation, m is required to equal 2. Thus,

$$\frac{C_0}{a^2} [4 + 2] = \frac{\omega \mu I}{2a} \quad \text{or} \quad C_0 = \frac{\omega a \mu I}{12}. \quad (2.49)$$

Because the right-hand side of our equation is exactly zero for odd values of n , then $C_{n, \text{odd}} \equiv 0$. In general, C_n can be expressed in the form

$$C_n = \frac{\omega \mu I}{2a} (-1)^{\frac{n}{2}} a^2 f(n) = \frac{\omega a \mu I}{2} (-1)^{\frac{n}{2}} f(n), \quad (2.50)$$

where

$$f(n) = \frac{1}{2} \frac{n+1}{(2n+3)} \prod \left[\frac{n-1}{n} \right]. \quad (2.51)$$

So, plugging our value for C_n back into our original expression for ϕ_{iP} , we obtain

$$\phi_{iP} = \frac{\omega a \mu I}{4} \sum_{n \text{ even}}^{0 \text{ to } \infty} (-1)^{\frac{n}{2}} \frac{n+1}{2n+3} \prod \left[\frac{n-1}{n} \right] \left[\frac{r}{a} \right]^{n+2} P_n(\cos\theta). \quad (2.52)$$

Now, let us repeat the previous work, but for $r/a > 1$ outside the thin coil. The left-hand side is now

$$\omega \cdot \mathbf{B} = - \frac{\omega \mu I}{2a} \sum_{n \text{ even}}^{2 \text{ to } \infty} (-1)^{\frac{n}{2}} (n) \prod \left[\frac{n-1}{n} \right] \left[\frac{a}{r} \right]^{n+1} P_n. \quad (2.53)$$

In a manner similar to before, let

$$\phi_{oP} = \sum_{n=0}^{\infty} D_n \left[\frac{a}{r} \right]^{n+m} P_n(\cos\theta). \quad (2.54)$$

The Laplacian then becomes

$$\nabla^2 \phi_{oP} = \frac{1}{a^2} \sum D_n \left[(n+m)(n+m+1) - 2(n+m) - n(n+1) \right] \left[\frac{a}{r} \right]^{n+m+2} P_n. \quad (2.55)$$

Matching terms and realizing that $D_n \equiv 0$ for all odd n and for $n = 0$, then for $n = 2$ we obtain

$$\frac{D_2}{a^2} [(2+m)(3+m) - 2(2+m) - 2(2+1)] \left[\frac{a}{r} \right]^{2+m+2} = \frac{\omega \mu I}{2a} \left[\frac{a}{r} \right]^3. \quad (2.56)$$

In order that the powers of r cancel on each side of the equation, m is required to equal -1 . Thus

$$\frac{D_2}{a^2} [2 - 2 - 6] \left[\frac{a}{r} \right]^3 = \frac{\omega \mu I}{2a} \left[\frac{a}{r} \right]^3, \quad (2.57)$$

or

$$D_2 = - \frac{a^2}{6} \frac{\omega \mu I}{2a} = - \frac{\omega a \mu I}{12}. \quad (2.58)$$

In general, D_n can be expressed in the form

$$D_n = - \frac{\omega \mu I}{2a} (-1)^{\frac{n}{2}} a^2 g(n) = - \frac{\omega \mu a I}{2} (-1)^{\frac{n}{2}} g(n), \quad (2.59)$$

where

$$g(n) = - \frac{1}{2} \frac{n}{(2n-1)} \prod \left[\frac{n-1}{n} \right]. \quad (2.60)$$

So, finally,

$$\phi_{oP} = \frac{\omega a \mu I}{4} \sum_{n \text{ even}}^{0 \text{ to } \infty} (-1)^{\frac{n}{2}} \frac{n}{2n-1} \Pi \left[\frac{n-1}{n} \right] \left[\frac{a}{r} \right]^{n-1} P_n(\cos\theta). \quad (2.61)$$

Since the inner and outer particular solutions of the potential (ϕ_{iP} and ϕ_{oP}) do not match at the interface $r = a$, we will add a solution of Laplace's equation such that the combined potential (homogeneous and particular solutions) is continuous. As an additional constraint, we will force the induced current density to be continuous across the interface as well.

For the inner region, the solutions are

$$\phi_{iP} = \frac{\omega a \mu I}{4} \sum_{n \text{ even}}^{0 \text{ to } \infty} (-1)^{\frac{n}{2}} \frac{n+1}{2n+3} \Pi \left[\frac{n-1}{n} \right] \left[\frac{r}{a} \right]^{n+2} P_n(\cos\theta) \quad (2.62a)$$

and

$$\phi_{iH} = \sum_{n=0}^{\infty} A_n \left[\frac{r}{a} \right]^n P_n(\cos\theta), \quad (2.62b)$$

where A_n will be determined to satisfy the boundary condition.

For the outer region, the solutions are

$$\phi_{oP} = \frac{\omega a \mu I}{4} \sum_{n \text{ even}}^{0 \text{ to } \infty} (-1)^{\frac{n}{2}} \frac{n}{2n-1} \Pi \left[\frac{n-1}{n} \right] \left[\frac{a}{r} \right]^{n-1} P_n(\cos\theta) \quad (2.63a)$$

and

$$\phi_{oH} = \sum_{n=0}^{\infty} B_n \left[\frac{a}{r} \right]^{n+1} P_n(\cos\theta). \quad (2.63b)$$

where B_n will be determined to satisfy the boundary condition. Now, we must ensure that the potentials match at the interface, or

$$(\phi_{iP} + \phi_{iH})_{r=a} = (\phi_{oP} + \phi_{oH})_{r=a}. \quad (2.64)$$

For n even, we match degrees of Legendre polynomials, so

$$\begin{aligned} A_n + \frac{\omega a \mu I}{4} (-1)^{\frac{n}{2}} \frac{n+1}{2n+3} \Pi \left[\frac{n-1}{n} \right] \\ = B_n + \frac{\omega a \mu I}{4} (-1)^{\frac{n}{2}} \frac{n}{2n-1} \Pi \left[\frac{n-1}{n} \right], \end{aligned} \quad (2.65)$$

or

$$A_n = B_n + \frac{\omega a \mu I}{4} (-1)^{\frac{n}{2}} \frac{(2n+1)}{(2n-1)(2n+3)} \Pi \left[\frac{n-1}{n} \right]. \quad (2.66)$$

Next, we ensure that the radial derivatives match at the interface. From the governing equation, we have

$$\mathbf{J} = \sigma(\mathbf{v} \times \mathbf{B} - \nabla \phi). \quad (2.67)$$

So, to ensure that the radial component of \mathbf{J} is continuous, we have the constraint that

$$\left[(\mathbf{v} \times \mathbf{B})_i - \frac{\partial}{\partial r} (\phi_{iP} + \phi_{iH}) \right]_{r=a} \hat{r} = \left[(\mathbf{v} \times \mathbf{B})_o - \frac{\partial}{\partial r} (\phi_{oP} + \phi_{oH}) \right]_{r=a} \hat{r}. \quad (2.68)$$

Our model flow is solid-body rotation with vorticity ω ; thus it has an angular rate of $\omega/2$ and a velocity of

$$\mathbf{v} = \frac{\omega}{2} (r \sin \theta) \hat{\gamma}. \quad (2.69)$$

So

$$\mathbf{v} \times \mathbf{B} = -v_\gamma B_\theta \hat{r} + v_\gamma B_r \hat{\theta}. \quad (2.70)$$

The radial component of $\mathbf{v} \times \mathbf{B}$ for the two regions can be written

$$(\mathbf{v} \times \mathbf{B})_i \hat{r} = \frac{\omega \mu I}{4} \sum_{n \text{ even}}^{0 \text{ to } \infty} (-1)^{\frac{n}{2}} \frac{(4n^3 + 8n^2 + n - 2)}{(2n-1)(2n+3)} \Pi \left[\frac{n-1}{n} \right] P_n \quad (2.71a)$$

$$(\mathbf{v} \times \mathbf{B})_o \hat{r} = -\frac{\omega \mu I}{4} \sum_{n \text{ even}}^{0 \text{ to } \infty} (-1)^{\frac{n}{2}} \frac{(4n^3 + 4n^2 - 3n - 1)}{(2n-1)(2n+3)} \Pi \left[\frac{n-1}{n} \right] P_n. \quad (2.71b)$$

Now, matching degrees of Legendre polynomials across the interface,

$$-n A_n = (n+1) B_n - \frac{\omega a \mu I}{4} (-1)^{\frac{n}{2}} \frac{(2n+1)(2n^2 + 2n - 1)}{(2n-1)(2n+3)} \Pi \left[\frac{n-1}{n} \right]. \quad (2.72)$$

Now we have two equations and two unknowns. Using Eq. 2.66 and Eq. 2.72, we obtain

$$A_n = \frac{\omega a \mu I}{4} (-1)^{\frac{n}{2}} \frac{n}{(2n-1)} \Pi \left[\frac{n-1}{n} \right] \quad (2.73a)$$

and

$$B_n = \frac{\omega a \mu I}{4} (-1)^{\frac{n}{2}} \frac{(n+1)}{(2n+3)} \Pi \left[\frac{n-1}{n} \right]. \quad (2.73b)$$

All the odd degrees of A_n and B_n are exactly zero. The final forms of the inner and outer homogeneous solution are

$$\phi_{iH} = \frac{\omega a \mu I}{4} \sum_{n \text{ even}}^{0 \text{ to } \infty} (-1)^{\frac{n}{2}} \frac{n}{(2n-1)} \Pi \left[\frac{n-1}{n} \right] \left[\frac{r}{a} \right]^n P_n \cos(\theta) \quad (2.74a)$$

and

$$\phi_{oH} = \frac{\omega a \mu I}{4} \sum_{n \text{ even}}^{0 \text{ to } \infty} (-1)^{\frac{n}{2}} \frac{(n+1)}{(2n+3)} \Pi \left[\frac{n-1}{n} \right] \left[\frac{a}{r} \right]^{n+1} P_n \cos(\theta). \quad (2.74b)$$

Finally, combining the homogeneous and the particular solutions of the potential results in

$$\phi_i = \frac{\omega a \mu I}{4} \sum_{n \text{ even}}^{0 \text{ to } \infty} (-1)^{\frac{n}{2}} \frac{n+1}{2n+3} \Pi \left[\frac{n-1}{n} \right] \left[\frac{r}{a} \right]^{n+2} \left[P_n - P_{n+2} \right] \quad (2.74c)$$

and

$$\phi_o = \frac{\omega a \mu I}{4} \sum_{n \text{ even}}^{0 \text{ to } \infty} (-1)^{\frac{n}{2}} \frac{n}{2n-1} \Pi \left[\frac{n-1}{n} \right] \left[\frac{a}{r} \right]^{n-1} \left[P_n - P_{n-2} \right]. \quad (2.74d)$$

The potential field ϕ for the velocity field in solid-body rotation is shown in Figure 2.8.

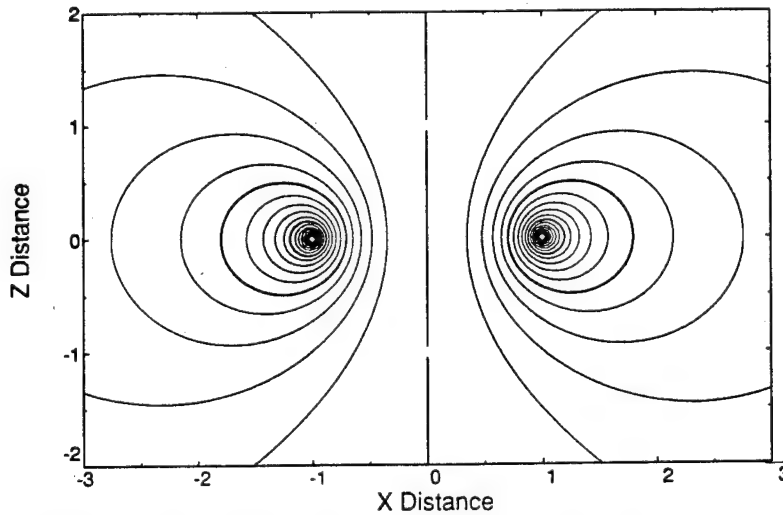


Figure 2.8. The potential field ϕ generated by flow in solid-body rotation in the presence of the magnetic field shown in Figure 2.4. The field has been transformed into an x - z coordinate system. Again, contour values are arbitrary. The view is with the flow coming into and out of the page. Unlike for uniform flow, ϕ here is everywhere positive.

To compute the induced electric currents, we plug our expressions for \mathbf{v} , \mathbf{B} , and ϕ into our governing equation vector expression of $\sigma(\mathbf{v} \times \mathbf{B} - \nabla \phi)$, and obtain

$$\begin{aligned} \mathbf{J} = & \frac{\sigma \omega \mu I}{4} \sum_{n \text{ even}}^{0 \text{ to } \infty} (-1)^{\frac{n}{2}} \Pi \left[\frac{n-1}{n} \right] \left[\frac{r}{a} \right]^{n+1} \\ & \left[\sin \theta P_{n+1}^1 - \frac{(n+1)(n+2)}{2n+3} \left[P_n - P_{n+2} \right] \right] \hat{r} \\ & + \sin \theta \frac{\sigma \omega \mu I}{4} \sum_{n \text{ even}}^{0 \text{ to } \infty} (-1)^{\frac{n}{2}} \frac{n+1}{2n+3} \Pi \left[\frac{n-1}{n} \right] \left[\frac{r}{a} \right]^{n+1} \\ & \left[(2n+3) P_{n+1} + \left[P'_n - P'_{n+2} \right] \right] \hat{\theta}. \end{aligned} \quad (2.75)$$

It can be shown that both the terms in brackets are *identically* zero. Thus, the current density \mathbf{J} is zero in the inner region when the flow is in solid-body rotation.

Now, for the outer region, the vector addition of $\sigma(\mathbf{v} \times \mathbf{B} - \nabla \phi)$ yields

$$\begin{aligned} \mathbf{J} = & \frac{\sigma \omega a \mu I}{4} \sum_{n \text{ even}}^{2 \text{ to } \infty} (-1)^{\frac{n}{2}} \Pi \left[\frac{n-1}{n} \right] \left[\frac{a}{r} \right]^n \\ & \left[\sin \theta P_{n-1}^1 + \frac{n(n-1)}{2n-1} \left[P_n - P_{n-2} \right] \right] \hat{r} \\ & - \sin \theta \frac{\sigma \omega \mu I}{4} \sum_{n \text{ even}}^{2 \text{ to } \infty} (-1)^{\frac{n}{2}} \frac{n}{2n-1} \Pi \left[\frac{n-1}{n} \right] \left[\frac{a}{r} \right]^n \\ & \left[(2n-1) P_{n-1} - \left[P'_n - P'_{n-2} \right] \right] \hat{\theta}. \end{aligned} \quad (2.76)$$

Again, both the terms in brackets are *identically* zero. Thus, the current density \mathbf{J} is zero in the outer region.

2.5 Response Function for Sensor

As shown earlier in Section 2.3.2, the EMVM determines the area average of vorticity in the circle encompassing a 2-D electrode array. An isolated vortex, say of magnitude Ω_v and radius r_v , completely within the sensing area will produce an apparent vorticity of $\Omega_v(r_v^2/r_s^2)$, where r_s is the radius of the electrode configuration. Thus, the amplitude response function for the sensor is unity for vortices with a size much larger than r_s and decreases as (r_v^2/r_s^2) for small vortices. The power response of the sensor exhibits a

falloff of the form f^{-4} (or k^{-4} , if the frequency scale is converted to wavenumber using Taylor's hypothesis, $f = kU$).

For vortices with a size the same order of magnitude as that of the sensor, the response is determined by the average amount of overlap of the vortex and the sensing area. The computation of overlap area depends on the relative sizes of the two circles ($r_v < r_s$ or $r_v > r_s$) and on the overlap geometry (barely intersecting or broadly overlapping). There are four cases for overlapping circles, as depicted in Figure 2.9a. Suppose the sensor is located at the origin, while the vortex is centered at $x = x_0, y = 0$. The points of intersection of the two circles are $x_i \pm y_i$, where

$$x_i = \frac{r_s^2 - r_v^2 + x_0^2}{2x_0} \quad (2.77)$$

and

$$y_i = \sqrt{r_s^2 - \frac{r_s^2 - r_v^2 + x_0^2}{2x_0}^2} \quad (2.78)$$

Let T_s be the area within the sensor circle on the vortex side of the chord connecting the points of intersection (see Figure 2.9b) and T_v be the area within the vortex circle on the sensor side of the same chord. As shown in Figure 2.9b, the area, A , enclosed by a circle, a chord, and the centerline perpendicular to the chord is

$$A = x\sqrt{r^2 - x^2} + r^2 \sin^{-1} \left[\frac{x}{r} \right] \quad (2.79)$$

Therefore, when $x_i > 0$,

$$T_s = \frac{\pi}{2} r_s^2 - x_i \sqrt{r_s^2 - x_i^2} - r_s^2 \sin^{-1} \left[\frac{x_i}{r_s} \right] \quad (2.80)$$

When $x_i < 0$, the last case shown in Figure 2.9a,

$$T_s = \frac{\pi}{2} r_s^2 + (-x_i) \sqrt{r_s^2 - (-x_i)^2} + r_s^2 \sin^{-1} \left[\frac{-x_i}{r_s} \right], \quad (2.81)$$

which simplifies to the identical expression for $x_i > 0$ in Eq. 2.80. Likewise, for T_v , when $x_0 > x_i$,

$$T_v = \frac{\pi}{2} r_v^2 - (x_0 - x_i) \sqrt{r_v^2 - (x_0 - x_i)^2} - r_v^2 \sin^{-1} \left[\frac{x_0 - x_i}{r_v} \right] \quad (2.82)$$

For the one case where $x_0 < x_i$,

$$T_v = \frac{\pi}{2} r_v^2 + (x_i - x_0) \sqrt{r_v^2 - (x_i - x_0)^2} + r_v^2 \sin^{-1} \left[\frac{x_i - x_0}{r_v} \right], \quad (2.83)$$

which reduces to the $x_0 > x_i$ case. In all cases, the total overlap area is $T_s + T_v$.

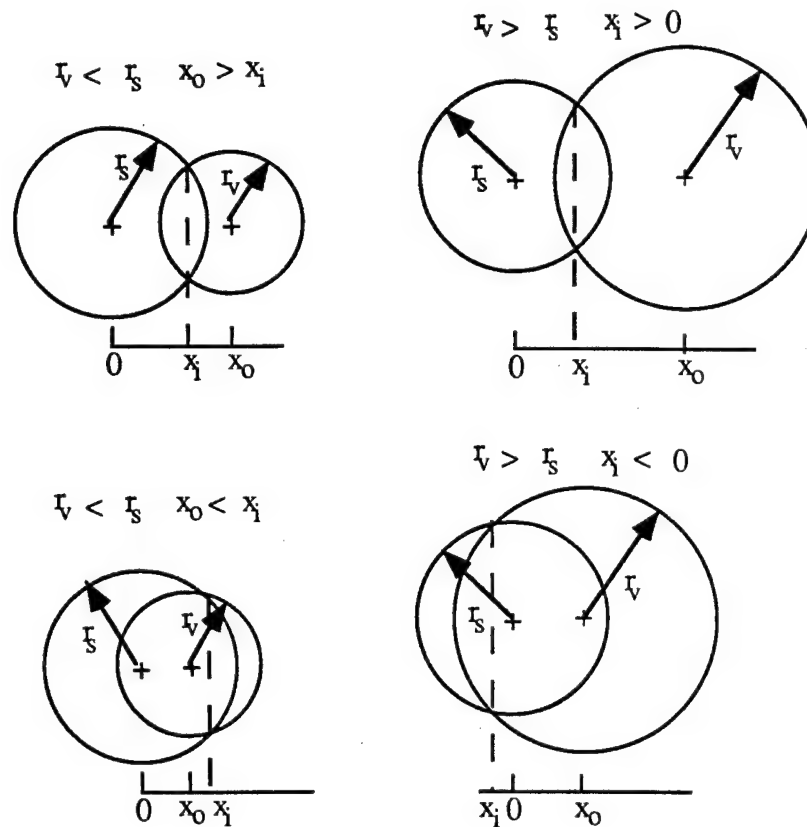


Figure 2.9(a). Four geometric cases of a vortex overlapping the sensor head. The cases are distinguished by the relative size of the circles and the amount of overlap.

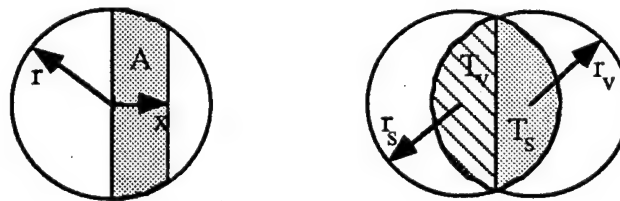


Figure 2.9(b). The area, A , enclosed by a circle, a chord, and the centerline perpendicular to the chord is $x \sqrt{r^2 - x^2} + x^2 \sin^{-1}(x/r)$. The overlap area of the sensing area and a vortex of the same size is $T_v + T_s$, where $T_s = \pi r_s^2/2 - [x_i \sqrt{r_s^2 - x_i^2} + x_i^2 \sin^{-1}(x_i/r_s)]$, where x_i is the horizontal distance from the center of the sensor head to the point of intersection. Likewise, $T_v = \pi r_v^2/2 - [(x_0 - x_i) \sqrt{r_v^2 - (x_0 - x_i)^2} + (x_0 - x_i)^2 \sin^{-1}[(x_0 - x_i)/r_v]]$, where x_0 is the center of the vortex relative to the center of the sensor.

A MATLAB program was written which computes the average effect of a vortex centered at all possible locations on an equi-dimensional grid with separations of r_s/NV , where NV is the number of vortices in the interval $(0, r_s + r_v)$. An example of the positions occupied in the first quadrant when NV is 18 and $r_v < r_s$ is shown in Figure 2.10. When $r_v \ll r_s$, for example, the response will be about r_v^2/r_s^2 minus the effect induced by some of the vortices being on the rim of the sensor so that only a fraction of their area overlaps the sensor's area. Because the area expressions assume the vortex is centered on the x axis, a vortex at each quantized location in x and y is expressed in a rotated coordinate system such that its center is located on the x axis. The overlapping area is computed for each vortex using $T_s + T_v$ as expressed above. Owing to symmetry, it is necessary to average only over a 45° section of the sensor. This was iterated for a range of vortex sizes, and the result is shown in Figure 2.11.

It is possible to check the algorithm against an analytic solution for the special case where the vortex radius equals that of the sensor. As two circles of the same radius, R , pass over one another, the total overlap area, A , is twice the overlap area of one circle on the other.

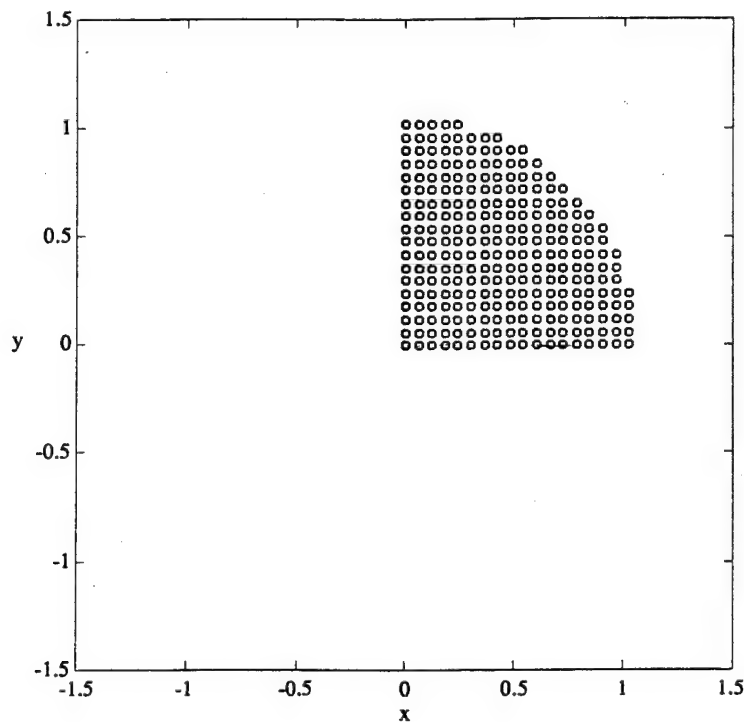


Figure 2.10. An example of one initial condition for the MATLAB program that calculates the response of the sensor to different spatial distributions of vorticity. In this example, the positions and sizes of the analyzed vortices are shown for the first quadrant only, where $NV = 18$ and $\delta x = \delta y = r_s/NV$.

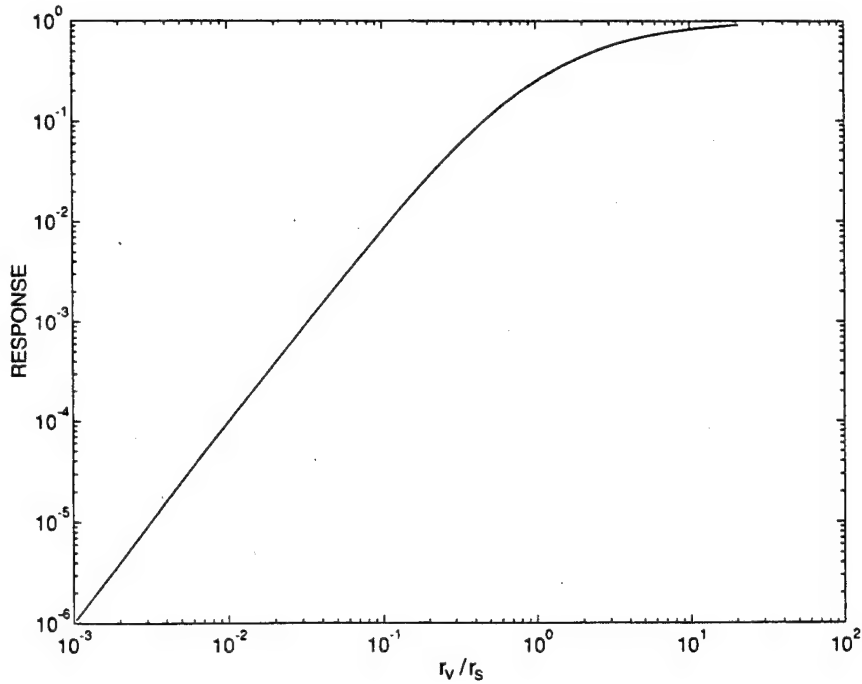


Figure 2.11. Theoretical spatially averaged amplitude response of the EMVM sensor to an isolated vortex, where r_v/r_s is the ratio of the radius of the vortex to the radius of the sensing area. For vortices much larger than the sensor, the response approaches unity. For vortices much smaller than the sensor, the response approaches $(r_v/r_s)^2$.

$$A = 2T_s = \pi R^2 - 2r \sqrt{R^2 - r^2} - 2R^2 \sin^{-1} \left[\frac{r}{R} \right]. \quad (2.84)$$

The average area overlap, \bar{A} , can be determined by integrating the above expression over the grid of possible vortex positions resulting in overlap (in this case, a circle of radius $2R$) and dividing by the area of that grid. That is,

$$\bar{A} = \frac{1}{4\pi R^2} \int_{-2R}^{2R} \int_{-2R}^{2R} A(x,y) dx dy = \frac{1}{\pi R^2} \int_0^{2R} \int_0^{2R} A(x,y) dx dy. \quad (2.85)$$

Transforming to polar coordinates,

$$\bar{A} = \frac{1}{\pi R^2} \int_0^{\frac{\pi}{2}} \int_0^{2R} A(r, \Theta) r dr d\Theta, \quad (2.86)$$

where Θ is the azimuthal angle. However, since $A(r, \Theta) = A(r)$,

$$\bar{A} = \frac{1}{2R^2} \int_0^{2R} A(r) r dr. \quad (2.87)$$

After integration,

$$\begin{aligned} \bar{A} &= \pi R^2 - \frac{4}{R^2} \left[-\frac{1}{4} r(R^2 - r^2)^{1.5} + \frac{1}{8} R^2 r \sqrt{R^2 - r^2} + \frac{R^4}{8} \sin^{-1}\left(\frac{r}{R}\right) \right]_0^{2R} \\ &\quad - 4 \left[\left[\frac{r^2}{2} - \frac{R^2}{4} \right] \sin^{-1}\left[\frac{r}{R}\right] + \frac{r}{4} \sqrt{R^2 - r^2} \right]_0^{2R} \\ &= \pi R^2 - \frac{1}{4} \pi R^2 - \frac{1}{2} \pi R^2 = \frac{1}{4} \pi R^2. \end{aligned} \quad (2.88)$$

Normalized to the sensor head radius, πR^2 ,

$$\frac{\bar{A}}{\pi R^2} = 0.25. \quad (2.89)$$

A value of 0.25 agrees with Figure 2.11 for $r_v/r_s = 1$; that is, the expected response for a unit vortex with its center randomly placed in and around the sensor circle is 0.25 s^{-1} . Of course, when the vortex and sensing area completely coincide, the response is 1; however, the response goes to zero as the displacement between the centers of the two circles goes to $2R$.

2.6 Relationships Between Electric Field and Velocity Components for 2-D Sensor

A 2-D EMVM sensor head consists of five electrodes connected by tubing to five locations above a permanent magnet. The geometry is shown in Figure 2.12. The voltages induced by flow between the center electrode and each outer electrode are measured. The four independent voltages allow the determination of an equal number of

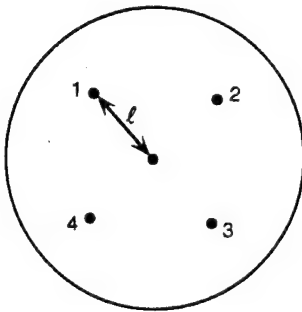


Figure 2.12. Electrode geometry. Electrode sites are numbered 1–4 starting from the upper left facing the sensor with the magnetic field component pointing out of the page.

flow characteristics. One can choose which quantities to compute, such as velocity and two gradient terms. The potential gradient in the water induced by a flow \mathbf{U} through a magnetic field \mathbf{B} is

$$\nabla\phi = \mathbf{U} \times \mathbf{B} - \mathbf{J}/\sigma, \quad (2.90)$$

where ϕ is the electric potential, \mathbf{J} is the electric current density, and σ is the electrical conductivity of the seawater.

Consider a right-hand coordinate system with x and U positive to the left, y and V positive into the figure, and z and W positive up. (This z is not the z used in altitude but one referenced to sensor head.) For a magnetic field of B (positive in direction out of the sensor, i.e., out of the figure) and velocity components of U and W , the potentials (e_1, \dots, e_4) at the ends of the electrode lines are

$$\frac{\sqrt{2}}{l} e_1 = BU_1 - BW_1 - \frac{J_{x1}}{\sigma} - \frac{J_{z1}}{\sigma} \quad (2.91a)$$

$$\frac{\sqrt{2}}{l} e_2 = -BU_2 + BW_2 + \frac{J_{x2}}{\sigma} + \frac{J_{z2}}{\sigma} \quad (2.91b)$$

$$\frac{\sqrt{2}}{l} e_3 = BU_3 + BW_3 + \frac{J_{x3}}{\sigma} - \frac{J_{z3}}{\sigma} \quad (2.91c)$$

$$\frac{\sqrt{2}}{l} e_4 = -BU_4 - BW_4 - \frac{J_{x4}}{\sigma} + \frac{J_{z4}}{\sigma}, \quad (2.91d)$$

where l is the magnitude of the distance vector \mathbf{l}_i between the center and ends of individual electrode tubes, $e_i = \nabla\phi \cdot \mathbf{l}_i$, B is the magnitude of the magnetic field (assumed to be uniform over the sensor), U_i and W_i are the velocity components across each electrode line, and J_{xi} and J_{zi} are the electric current density components along each electrode line.

A difficulty is that no independent measurement of \mathbf{J}/σ is obtained. That is, measuring $\nabla\phi$ along a given vector line (\mathbf{l}) and knowing \mathbf{B} is not enough to uniquely determine \mathbf{U} (Shercliffe, 1962). What is determined by the potential measurements is the difference between the source term $\mathbf{U} \times \mathbf{B}$ and the response term \mathbf{J}/σ . Because the induction is a linear problem, the response is proportional to the source. If the full magnetic field and flow are known, this response function can be computed. Usually, it is determined empirically from calibrations in a tow tank or flume. Both methods have been applied in this work. The interpretation equation used is

$$\nabla\phi \cdot \mathbf{l} = \Delta\phi = C \mathbf{U} \times \mathbf{B} \cdot \mathbf{l}. \quad (2.92)$$

From theory and experiment, we determined that the head factor, C (denoted as Hd earlier), is equal to 0.5 for flow perpendicular to the applied magnetic field.

Now, if we write Eq. 2.92 along the z axis,

$$BU - \frac{J_z}{\sigma} = CBU. \quad (2.93)$$

Similarly, for the x axis,

$$BW - \frac{J_x}{\sigma} = CBW. \quad (2.94)$$

Hence, the combinations of e_1 and e_3 yield

$$\frac{\sqrt{2}}{CBl}(e_3 - e_1) = (W_3 + W_1) + (U_3 - U_1) \quad (2.95)$$

and

$$\frac{\sqrt{2}}{CBl}(e_3 + e_1) = (U_3 + U_1) + (W_3 - W_1), \quad (2.96)$$

where U_i and W_i are spatially averaged velocity components along the i th electrode line. The combinations of e_2 and e_4 yield

$$\frac{\sqrt{2}}{CBl}(e_2 - e_4) = (W_2 + W_4) - (U_2 - U_4) \quad (2.97)$$

and

$$\frac{\sqrt{2}}{CBl}(e_2 + e_4) = -(U_2 + U_4) + (W_2 - W_4). \quad (2.98)$$

The four independent voltages can be combined to determine four flow characteristics. The four that are computed are two velocity components, one vorticity component, and a strain component. The relations are

$$\frac{\sqrt{2}}{4CBl}(e_1 - e_2 + e_3 - e_4) = \frac{U_1 + U_2 + U_3 + U_4}{4} \equiv U, \quad (2.99)$$

$$-\frac{\sqrt{2}}{4CBl}(e_1 - e_2 - e_3 + e_4) = \frac{W_1 + W_2 + W_3 + W_4}{4} \equiv W, \quad (2.100)$$

$$-\frac{e_1 + e_2 - e_3 - e_4}{2CBl^2} = \quad (2.101)$$

$$\begin{aligned} & \frac{\frac{1}{2}(W_1 + W_3) - \frac{1}{2}(W_2 + W_4) - \frac{1}{2}(U_1 + U_4) - \frac{1}{2}(U_2 + U_3)}{l\sqrt{2}} \\ &= \frac{\partial W}{\partial z} - \frac{\partial U}{\partial x} = 2 \frac{\partial W}{\partial z}, \end{aligned}$$

$$\frac{e_1 + e_2 + e_3 + e_4}{Bl^2} = \quad (2.102)$$

$$\frac{\frac{1}{2}(U_1 + U_3) - \frac{1}{2}(U_2 + U_4) - \frac{1}{2}(W_1 + W_4) + \frac{1}{2}(W_2 + W_3)}{l\sqrt{2}}$$

$$= \frac{\partial U}{\partial z} - \frac{\partial W}{\partial x} = \Omega_y.$$

These relations assume that the same velocity components estimated at the intersection of orthogonal lines are equal. The following relations were used in the Eqs. 2.99 and 2.100:

$$(W_1 + W_2) - (W_3 + W_4) = 0 \quad (2.103)$$

and

$$(U_1 + U_2) - (U_3 + U_4) = 0. \quad (2.104)$$

In addition, the 2-D form of the continuity equation was invoked in Eq. 2.101. There is a subtle point that should be made about the absence of the head factor in the expression for vorticity: There is no head factor for vorticity; vorticity does not induce any electric currents, so $C = 1$ (as shown analytically in Section 2.4.2). The basis for this can be seen by summing the expressions for the individual electrode voltages in terms of velocity components and electric currents. The sum of the latter forms an expression of the form $\nabla \cdot \mathbf{J}/\sigma$, which is zero. This fact would have been clear if the individual terms such as J_{xi} and J_{zi} were retained. This was not done in the interest of simplifying the expressions.

3. EARLY INSTRUMENTS

Early EMVMs used a synchronous demodulation scheme to separate the signal from the noise by modulating the magnetic field and applying narrow frequency-band signal processing to the induced voltages. The magnetic field was changed in a sinusoidal or square-wave modulation from positive to negative values at a frequency that was higher than the dominate electrode drift. The electrode voltages were synchronously demodulated at the magnetic chopping rate. This section describes the first four versions of the EMVM.

3.1 First EMVM

The initial EMVM was built in 1982. The electronics were based on a modified circuit board from an expendable current profiler, or XCP (Sanford et al., 1982). A block diagram of the electronics and processing is shown in Figure 3.1. The electrode voltages were broadband amplified with a gain, G_1 , of 250; they were then combined, high-pass filtered, and further amplified by a gain, G_2 , of 200. This approach and the subsequent voltage-to-frequency (V/F) conversions paralleled those used in the XCP. However, the modified electronics were susceptible to ambient 60-Hz noise related to grounding of test and auxiliary equipment. This effect was minimized by isolating the electronics through the use of a fiber-optic data link and battery power.

The simple uniaxial sensor (Figure 3.2) consisted of silver/silver-chloride electrodes surrounded by agar. The length of the electrode arms on each side was approximately 2.5 cm. The test facilities are shown in Figure 3.3. External Helmholtz coils were used to supply a known vertical magnetic field at a specified frequency. Vorticity was generated by an impeller-driven, rigid-lid tank. The sensor assembly was sealed into the tank, with the electrical connections extending up through the rigid lid. Though providing only an approximation to solid-body rotation, the impeller system was judged adequate for the initial phase of investigation. Because the electronic circuitry was sensitive to variations in vorticity, not steady-state vorticity, the impellor was driven by a variable-speed motor. By varying the speed of the motor in a controlled way, known variations in the angular rotation rate were produced. These tests were performed in mid-September 1982.

This initial phase verified the concept of measuring the vorticity-induced electric field in the manner envisioned. However, the detected signals were two to three times less than the expected values. This deviation may have been due to inadequacies of the simple sensor. The tubular shape of the sensor disrupted both the flow field and the resulting electric field. The magnetic field was not uniform throughout the entire flow volume. The effects of the insulating tank walls were not understood. Finally, the fluid was not in truly solid-body rotation, and the vorticity was therefore difficult to quantify.

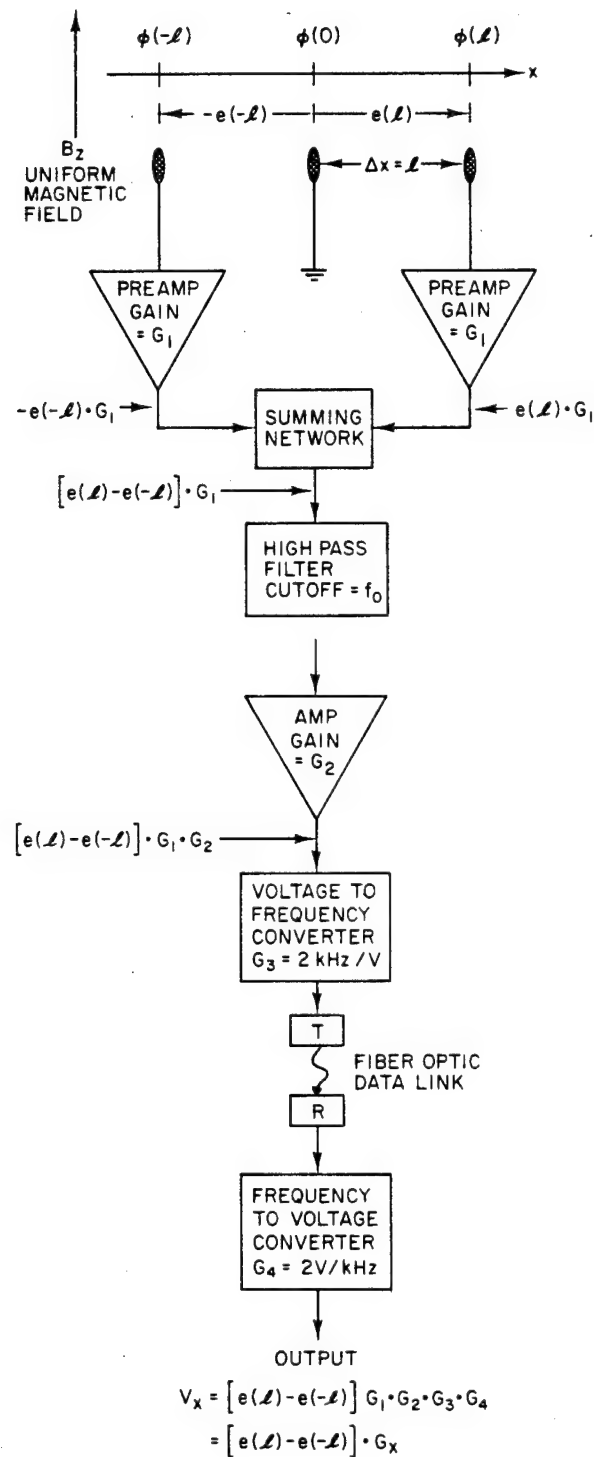


Figure 3.1. Block diagram of the electronics for the first version of the EMVM.

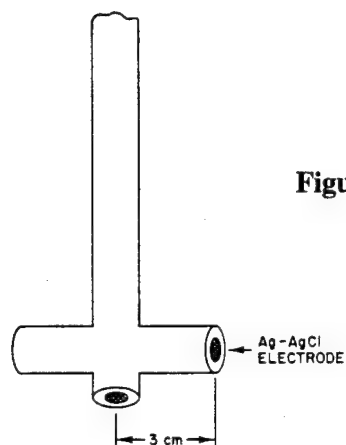


Figure 3.2. First EMVM sensor.

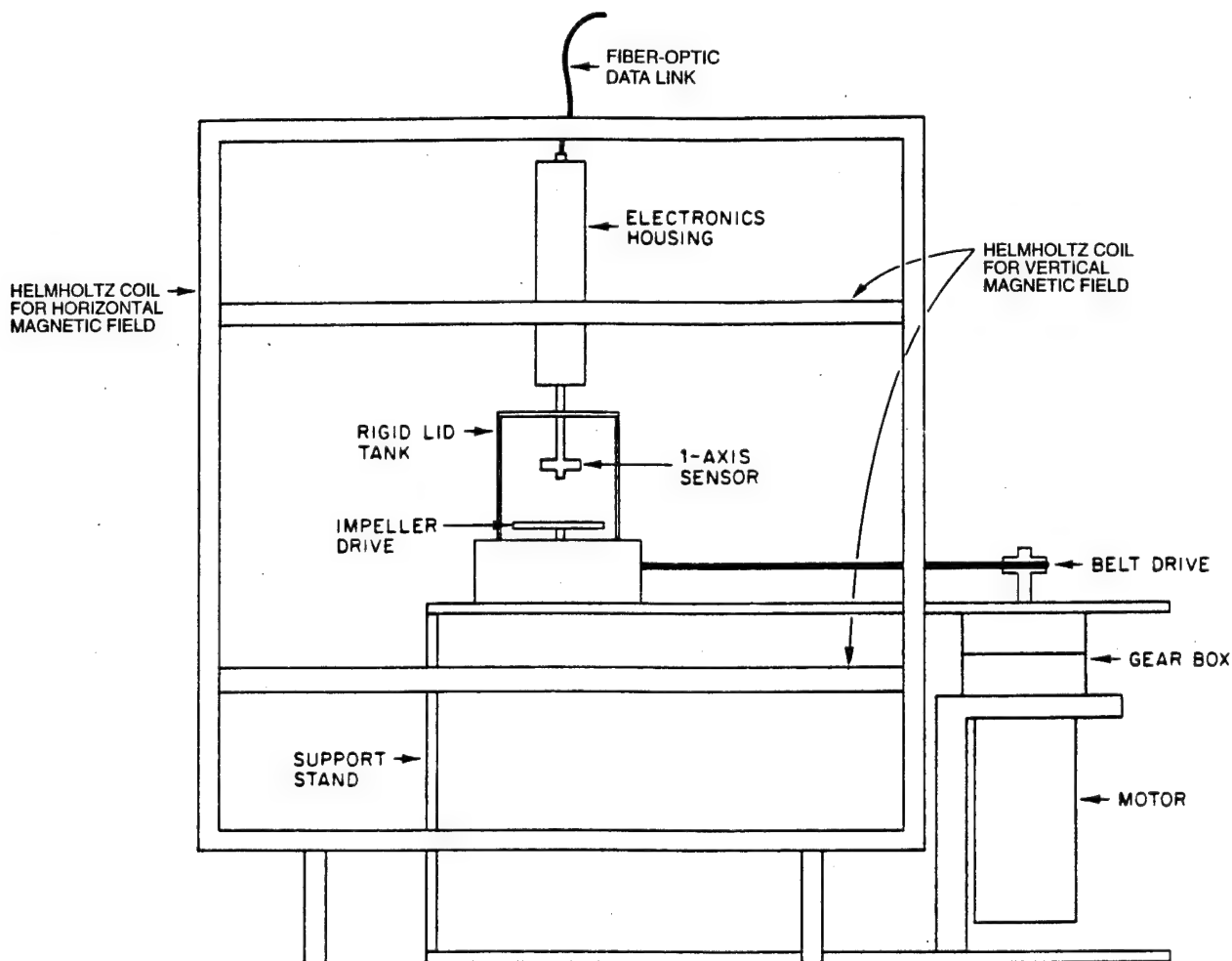


Figure 3.3. Test facility used for the first version of the EMVM.

The sensitivity of the first instrument was limited by the strength of the magnetic field generated by the Helmholtz coils. The maximum magnetic field available was 0.3 to 0.4×10^{-4} T. Moreover, the magnetic field was external and not part of a more compact sensor. A projection of the sensitivity was used as the basis for the design refinements incorporated in later versions. Detection of a vorticity signal of 10^{-1} s^{-1} (corresponding to a rotation period of 2 min) was thought possible using a magnetic field of 10^{-3} T.

3.2 Second EMVM

The next stage of development was to increase the sensitivity of the vorticity meter and to incorporate the source of the magnetic field into the sensor head. The steps included improving the electronics and processing scheme and making a three-dimensional measurement. A test facility was built to generate low-level vorticity in the form of solid-body rotation. This second version of the vorticity sensor was completed on 1 December 1982.

A major problem with using a rapidly changing magnetic field is that it induces large voltages. A time-varying magnetic field acting on a residual loop area produces inductive coupling. In the first version of the vorticity meter, the magnetic field was distributed over a relatively large volume by the Helmholtz coils (see Figure 3.3). In the second version (Figure 3.4), the magnetic field was provided by a coil in the sensor itself. This confined the influence of the magnetic field to a smaller volume, which facilitated isolation of the electronics.

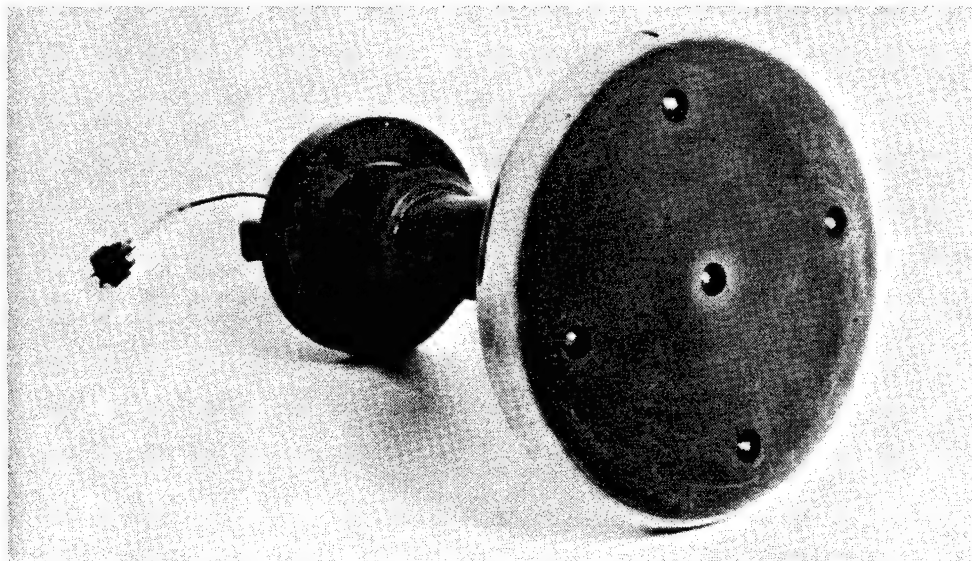


Figure 3.4. Second version of the EMVM. The magnetic field is provided by a coil in the sensor itself.

Most of the residual loop area was in the electrical connections between the electrodes and the electronics. However, the magnitude of the undesired signal was relatively low because of the low magnetic field and the large signal provided by the vorticity. At the large magnetic field level needed to detect small vorticity, such a level of continuous induction noise is intolerable.

This sensor was therefore improved and expanded to make a three-axis measurement, as shown in Figure 3.5. The radial symmetry minimized interference with the electric field. The disc shape was intended to give the least disturbance to the flow field. The coil axis was fixed parallel to that of the z coordinate, so all measurements were of the z component of vorticity.

To minimize the problem of electronic noise caused by induction coupling, the drive coil on the sensor was modulated with a square-wave signal. This confined the induction coupling to short noise spikes (delta functions) superimposed on an otherwise low noise output. A blanking procedure was then used to eliminate these noise spikes from the output. The scheme is illustrated in Figure 3.6. The track-and-hold circuit was driven by the blanking generator, and a lock-in amplifier was used to sample the output synchronously with the magnetic field modulation.

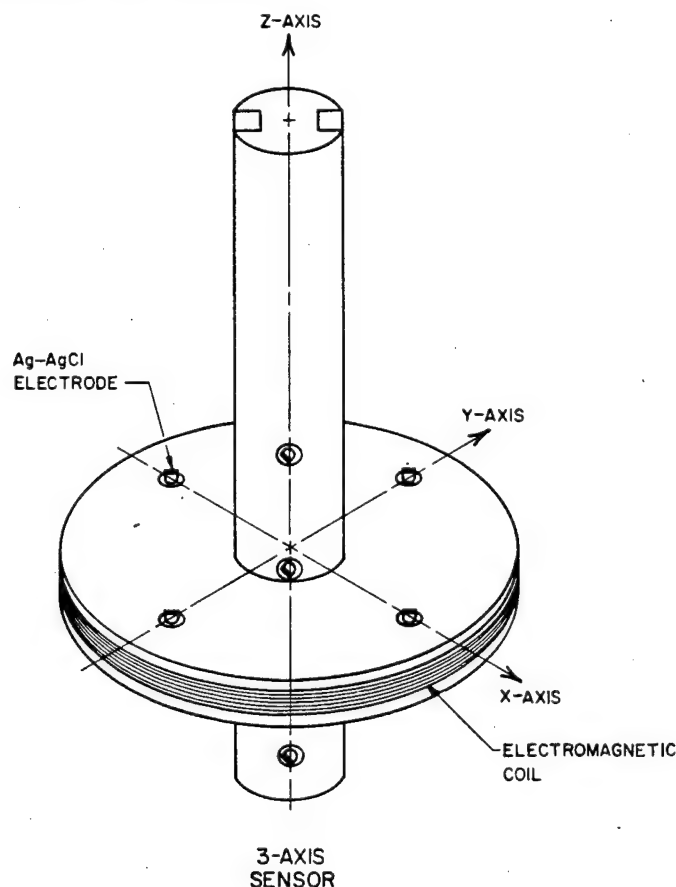


Figure 3.5. Tri-axial configuration of the second version of the EMVM.

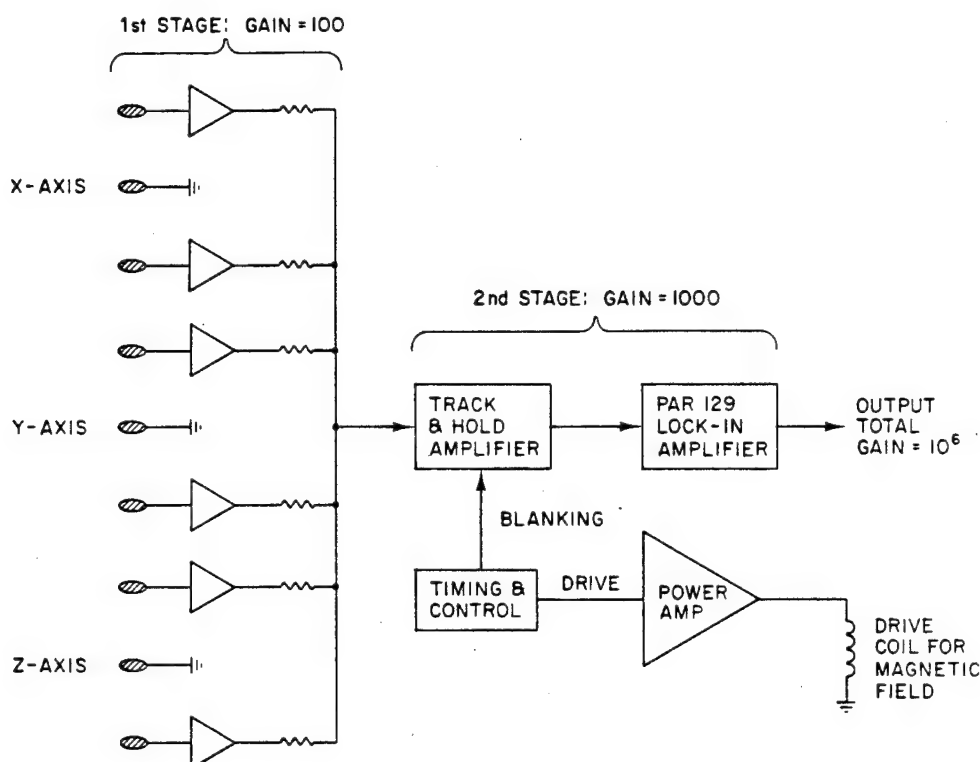


Figure 3.6. Block diagram of the electronics for the second version of the EMVM.

Because of our increased sensitivity, we needed a new facility to impart a known amount of vorticity into the water surrounding the sensor. In February 1983, we constructed a tank that could be rotated slowly on a lazy-Susan base. After some time, this rotating tank would spin the water up into solid-body rotation. Blades were attached to the walls of the tank to speed up this process. The instrument was mounted so that the sensor was in the center of the tank, where it would be surrounded by water that was in solid-body rotation. The period of rotation of the water was the same as that of the tank and could be varied over a wide range. This facility, shown in Figure 3.7, had a lower vorticity limit of 0.1 s^{-2} .

In July 1983, we improved the sensitivity by changing the input preamplifiers from Precision Monolithics OP-10s to PMI OP-227s. This decreased the input noise from about $10 \text{ nV}/\sqrt{\text{Hz}}$ to about $3.5 \text{ nV}/\sqrt{\text{Hz}}$. We also tried driving the coil at higher currents to increase the strength of the magnetic field. The drive levels for the three-axis disc sensor were then of the order of 30 G peak to peak. Tank tests on this sensor indicated development had progressed to the point where we had exceeded our sensitivity goal of 0.1 s^{-1} . The measured noise level in still water was 0.02 s^{-1} rms over the band 0.01–1 Hz. We achieved this level by decreasing the noise level of the electronics to 12 nV rms over a 1-Hz bandwidth. This represents approximately 5 nV rms per amplifier for the six amplifiers used (one for each electrode), which equals the manufacturer's

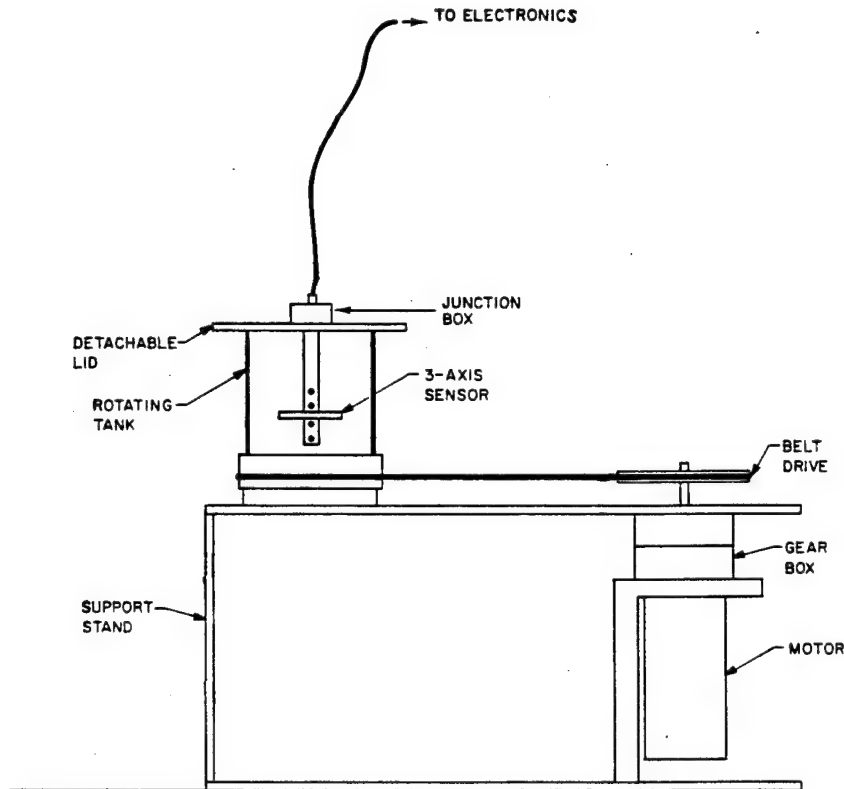


Figure 3.7. Test facility used for the second version of the EMVM.

specification for this device. This noise level was achieved only when the impedance connected across the amplifiers inputs was $1000\ \Omega$ or less. To obtain this low impedance, we used silver/silver-chloride electrodes and relatively large connecting ports out to the point of measurement. These electrodes exhibited very low impedance for their size and had stable and small self-potentials.

3.3 Third EMVM

In August 1983, we constructed an underwater housing for the EMVM electronics using thick-walled PVC pipe. The sensor was attached to one of the endcaps, and the wiring for signals and power was brought out through an underwater connector. In September 1983, we constructed a new deck box that could interface to a 1000-ft underwater tow cable. The new deck box provided a 16-bit parallel interface to an HP-9845 computer. A computer program was written to perform the synchronous demodulation and graphics display of the data.

A block diagram of the drive and signal processing electronics is shown in Figure 3.8. The magnetic field was modulated and applied at a 15-Hz rate. The modulation was square wave, and the voltage spikes induced were ignored. The 15-Hz commutation frequency was chosen because it was a subharmonic of 60 Hz, which greatly decreased our sensitivity to power-line pickup. It was also high enough so that $1/f$ noise from the amplifiers was not a problem.

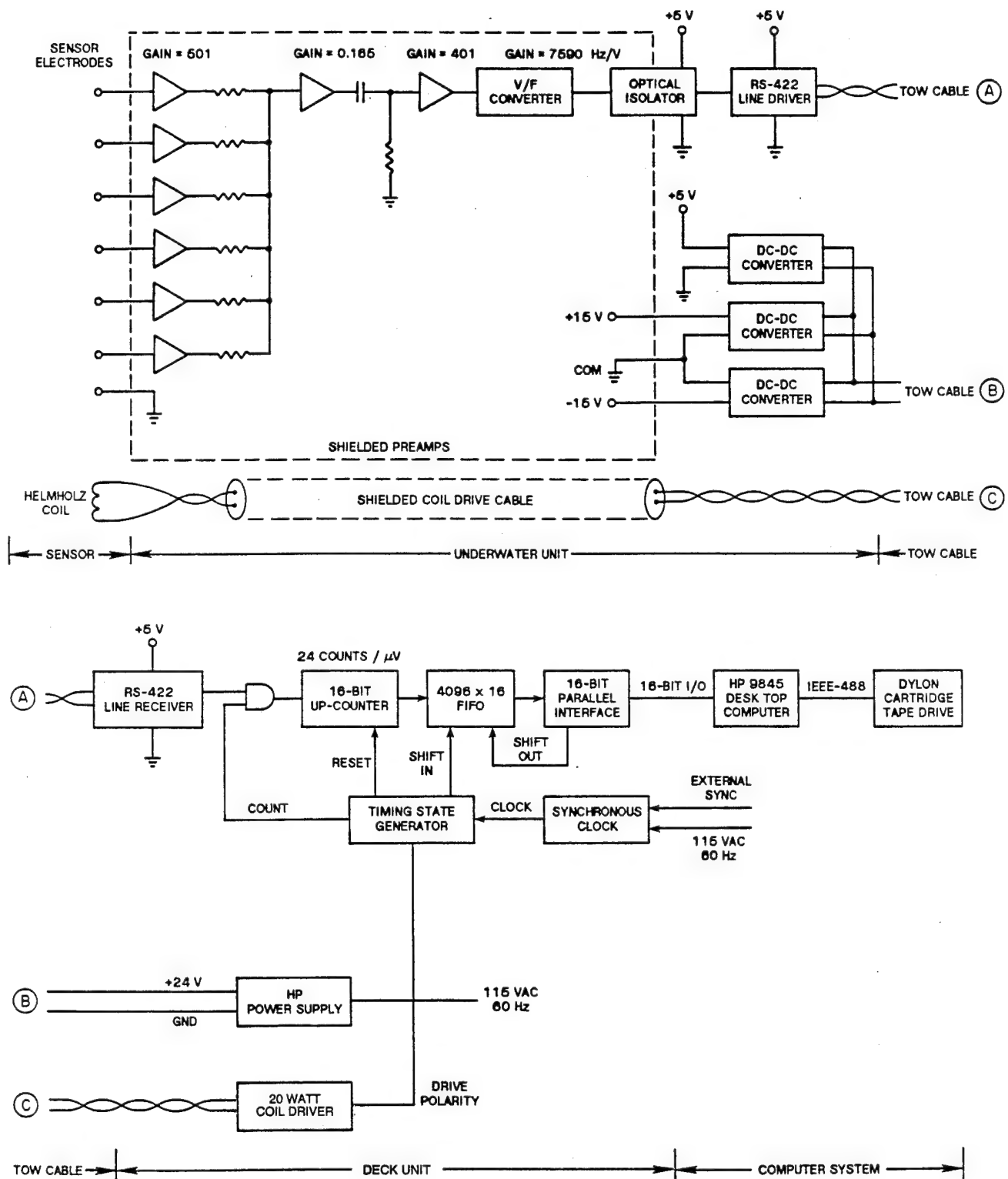


Figure 3.8. Block diagram of the electronics for the third version of the EMVM.

Our deck box performed two basic functions: driving the coil at the 15-Hz commutation frequency and synchronously demodulating the sensor signals. The synchronous demodulation was performed by counters that were allowed to count up during the part of the coil drive cycle after the switching transients had died out. The counters were then read and reset during the blanking periods when the switching transient was present. Several different counting schemes were switch selectable from the front panel. The best results were obtained when one coil was driven at 15 Hz, the counters counted for 1/60 s, and the blanking interval was 1/60 s.

The first field tests of the integrated system were conducted from the APL acoustics barge in October 1983. For these tests, the sensor and electronics were attached to the ram mounted in the center of the vessel. However, the noise level was very large because of 60-Hz interference. (The ac current distribution on the vessel appears to have numerous leaks into the surrounding seawater.) As a result, nanovolt-level measurements were not easily performed. An attempt was made to avoid 60-Hz interference by installing the sensor and electronics on a fiberglass boat towed by the barge. Power and data were conveyed by a multiconductor cable. The 60-Hz noise was much less, but we observed high noise levels due to the vigorous motion of the light boat in the wake of the barge. Because our intent was to determine more about the low-noise performance, we decided to install the system on a platform on the bottom of Puget Sound for the noise tests. At the same time, we decided to develop a new sensor with the goal of reducing the disturbance of the flow past the sensor.

The new sensor was completed on 9 January 1984. This sensor, shown in Figure 3.9, consisted of electrodes mounted on long struts extending into the flow. This orientation presents the least disturbance to the flow, assuming the sensor is aligned with the oncoming velocity as on a towed body. The magnetic field was provided by Helmholtz coils surrounding the sensing volume. Although this configuration induced less interference with the ambient flow, the magnetic field strength was less since the coils were rather far away from the electrodes.

In February 1984, we installed the new system on a tripod platform off Pier C in Shilshole Bay in Seattle and collected several hours of observations. The goals of the experiment were to determine the *in situ* noise of the system and to verify the calibration. The equipment is shown in Figure 3.10. A plastic garbage can was used to shroud the sensor for the noise tests; it did not interfere with the sensor but excluded any velocity and vorticity signals from entering the sensing volume. An example of the data obtained with and without the shroud is presented in Figure 3.11. The variables presented are, from top to bottom, vorticity, the x and y components of velocity, the x and y components of acceleration (from a separate sensor), and the carrier frequencies of the five FM data channels. The velocity measurements are obtained from the same information used to compute vorticity, except that the electrode differences are added, rather than

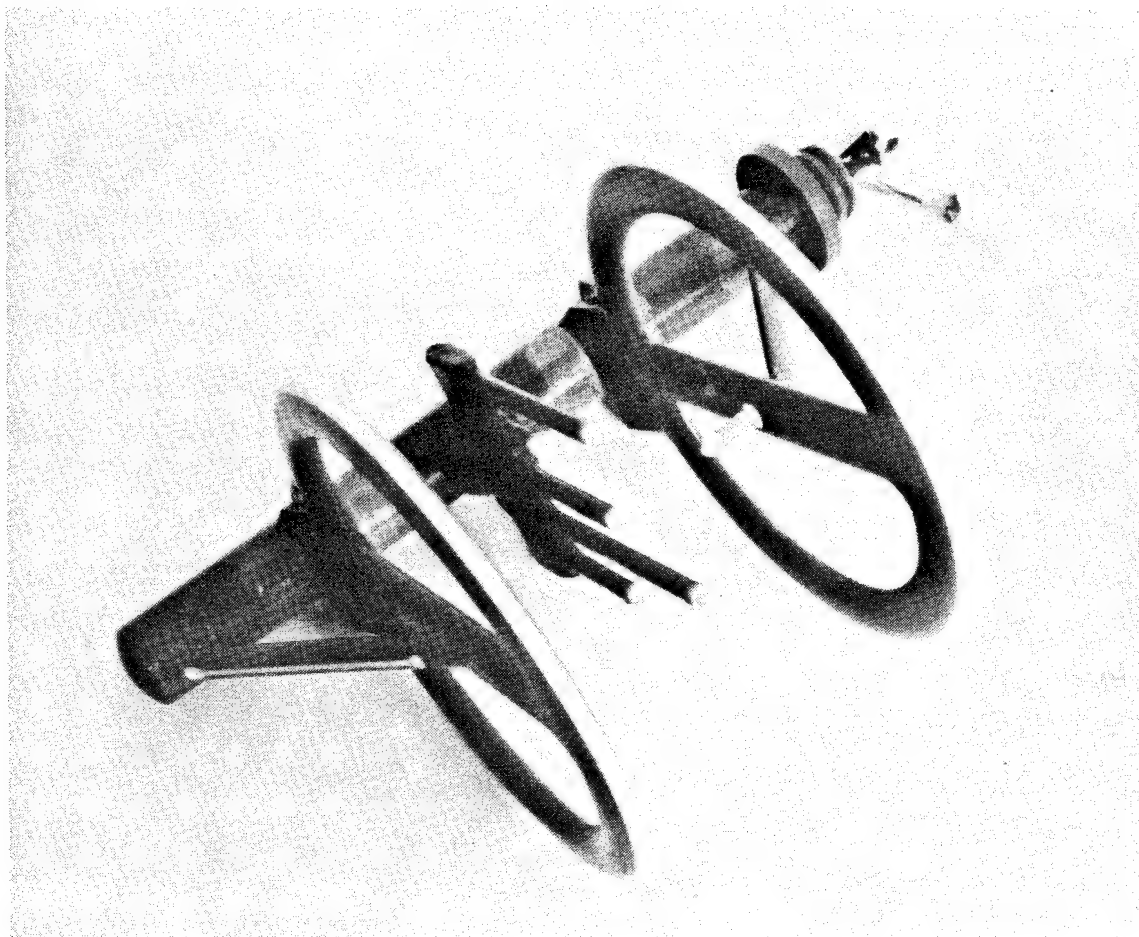


Figure 3.9. Third version of the EMVM. This version is a three-axis sensor with Helmholtz coils for field modulation.

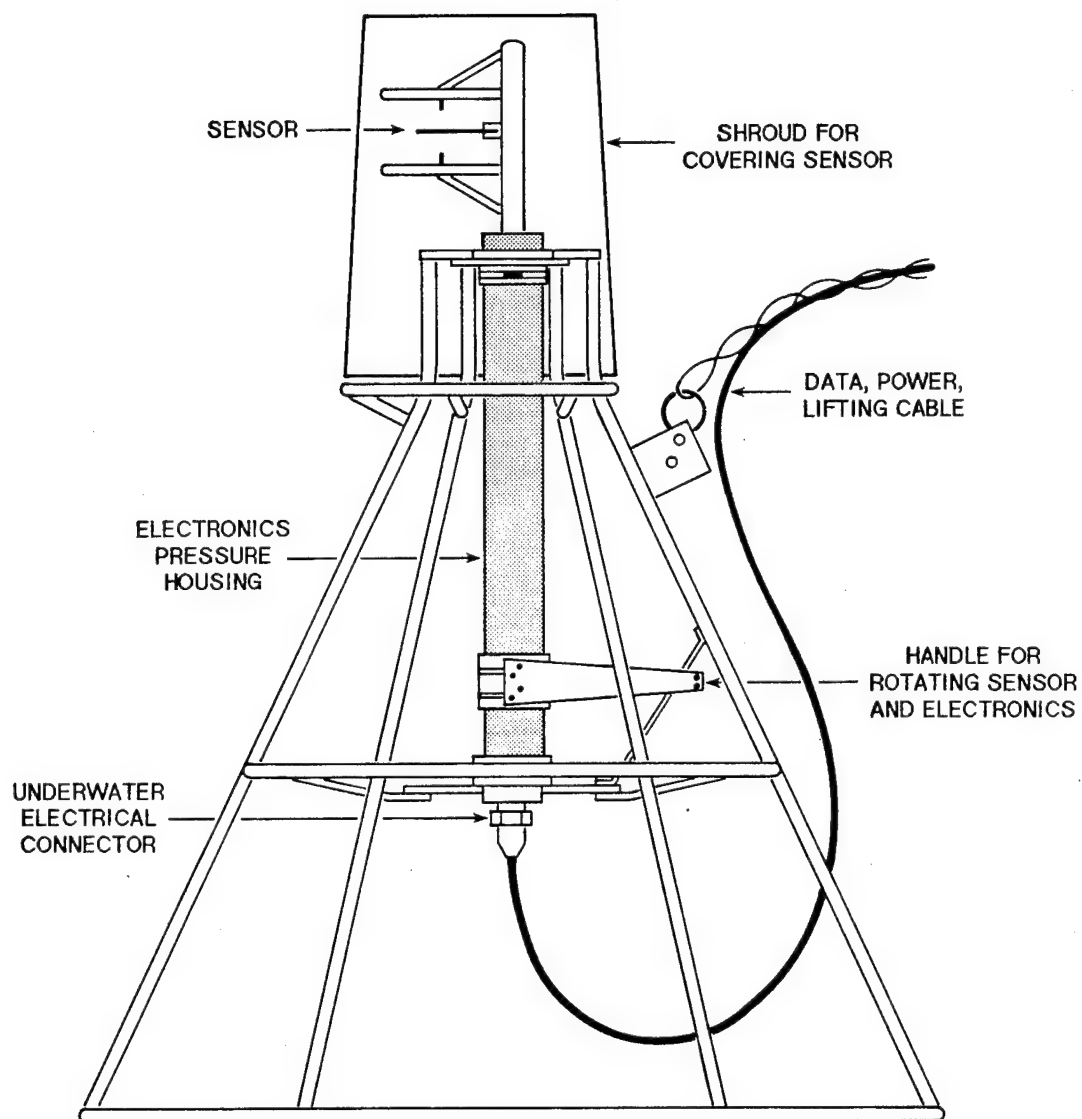
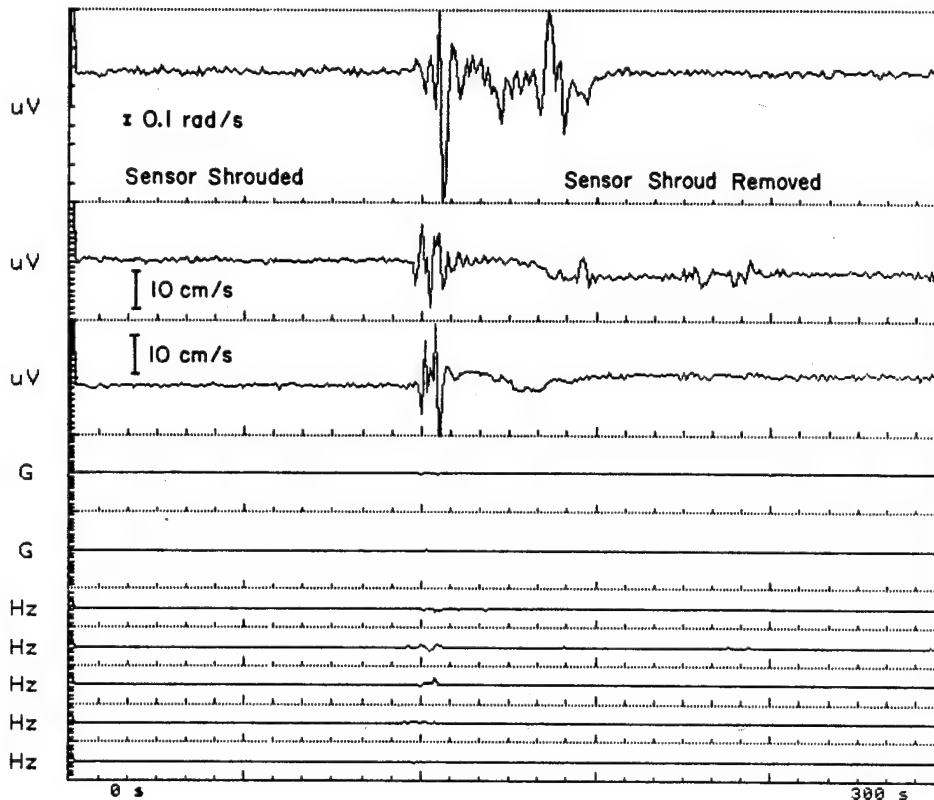


Figure 3.10. Tripod-mounted EMVM (three-axis open sensor).

PROG=VMPB3J
 INPUT FILE=TEST28...UNIT MOORED OFF PIER C SHILSHOLE SENSOR SHROUD REMOVED

TRACK # 1

DUMP TIME=03:14:09:42:02



```
*****
*VORTICITY *
*****
PLOT LIMITS= 0 uV TO 1 uV
BASELINE FREQUENCY PLOT LIMITS= 5000 Hz TO 95000 Hz
*****
*EMCM X *
*****
PLOT LIMITS=-20 uV TO 0 uV
BASELINE FREQUENCY PLOT LIMITS= 5000 Hz TO 95000 Hz
*****
*EMCM Y *
*****
PLOT LIMITS= 10 uV TO 30 uV
BASELINE FREQUENCY PLOT LIMITS= 5000 Hz TO 95000 Hz
*****
*ACCEL X *
*****
PLOT LIMITS=-.1 uV TO .1 uV
BASELINE FREQUENCY PLOT LIMITS= 5000 Hz TO 95000 Hz
*****
*ACCEL Y *
*****
PLOT LIMITS=-.1 uV TO .1 uV
BASELINE FREQUENCY PLOT LIMITS= 5000 Hz TO 95000 Hz
Nav= 30
DISPLAYED DATA ARE 1 SECOND AVERAGES
```

Figure 3.11. Data taken with tripod-mounted three-axis open sensor with and without the shroud.

differenced, and expressed as velocity. The accelerations were monitored to ensure that the platform was not being moved or disturbed by the flow. This figure illustrates the performance in the field. The noise level is about $3 \times 10^{-2} \text{ s}^{-1}$. Note that the vorticity level seemed to be about the same with or without the shroud. Note also that the x velocity channel observes some disturbances that are not seen in vorticity. This is one of the major benefits of this sensor—it responds to vorticity, not just some isolated velocity disturbance. Figure 3.12 shows another example of vorticity measurements from the platform, in this case, with a diver creating a disturbance upstream from the sensor. There is a sizable vorticity signature, whereas there is little or no disturbance in the velocity channels. Compare this example with the previous figure.

It is not possible to generate vorticity structure of known size and strength. Having divers swim upstream of the sensor hardly constitutes a calibration of the system. We therefore mounted the sensor and electronics in such a way that both could be rotated through a known angle (see handle in Figure 3.10). In this case, the time integral of the vorticity is just twice the rotation angle. An example of slow rotation over a duration of about 10 s is shown in Figure 3.13; the vorticity is shown in the top panel and the velocity components in the next two panels. There is a local current of about 3 cm s^{-1} that changes sign on the y current sensor as the unit is rotated. The time integral of one of these rotations is displayed in Figure 3.14. The area is 1.9 rad, or 110° , the angle through which the sensor was in fact rotated. This agrees with the results of similar laboratory experiments.

3.4 Fourth EMVM

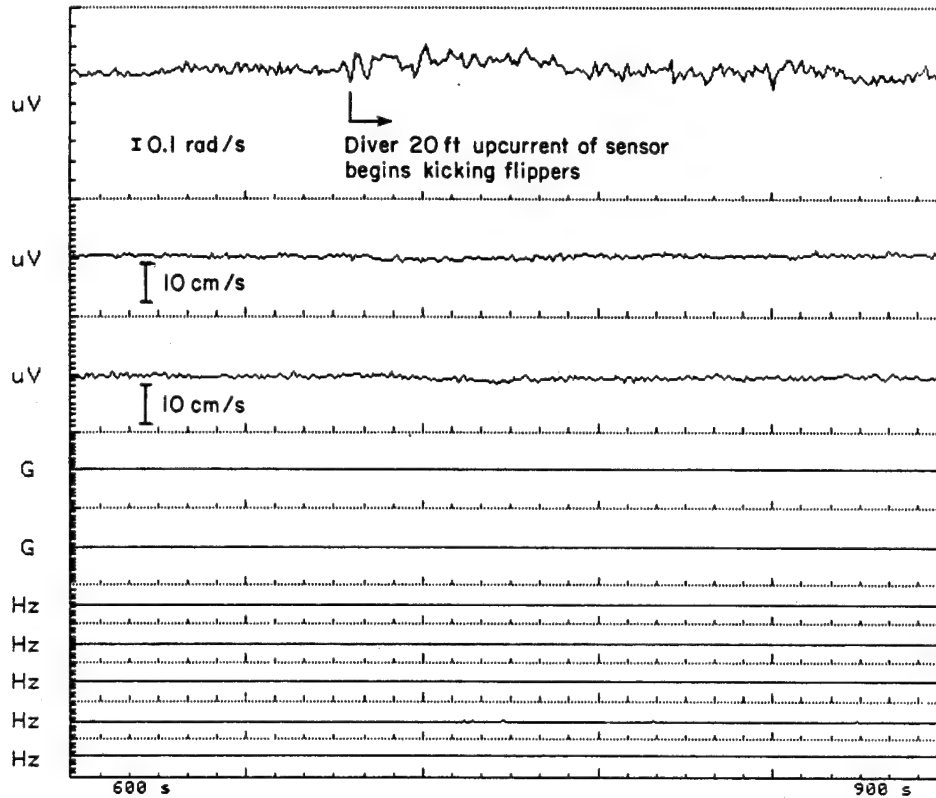
It was realized that, to make an order of magnitude improvement in the sensor sensitivity, the size of the sensor would have to substantially increase. Figure 3.15 shows the fourth configuration of the instrument while placed in a support frame for use on the seafloor. The EMVM itself was just under 2 m long and about 0.5 m in diameter. In this version, the electronics were housed in a larger pressure case which allowed a new high-power coil driver to operate underwater. In addition, a new data transmission technique was used to send the data over the underwater cable. The underwater unit also grew to accommodate additional sensors such as a compass and pitch, roll, and yaw-rate sensors. The magnetic field was generated by Helmholtz coils, producing a field flux density of 50 G (50×10^{-4} tesla). A block diagram of the electronics is shown in Figure 3.16. The EMVM was previously operated by means of a HP-9845 computer. New software allowed us to use an HP-9020 computer, giving faster acquisition, more powerful real-time processing, and a color graphics display.

First tests of the completed instrument were performed in a test tank at APL in the spring of 1985. During that year, numerous laboratory experiments were performed to calibrate the EMVM and determine the noise levels, and a new "paddle-type" sensor was

PROG=VMPB3J
 INPUT FILE=TEST30...UNIT MOORED OFF PIER C SHILSHOLE DIVERS WILL GENERATE VORTICITY

TRACK # 3

DUMP TIME=03:17:11:26:36



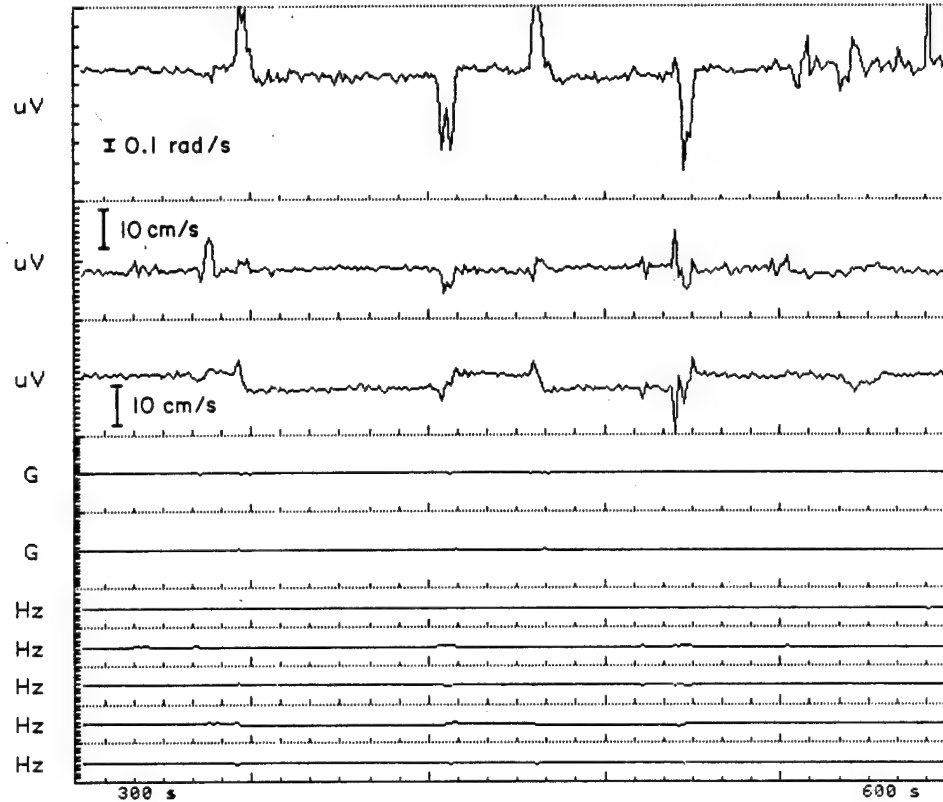
```
*****
*VORTICITY *
*****
PLOT LIMITS= 0 uV TO 1 uV
BASELINE FREQUENCY PLOT LIMITS= 5000 Hz TO 95000 Hz
*****
*EMCM X *
*****
PLOT LIMITS=-20 uV TO 0 uV
BASELINE FREQUENCY PLOT LIMITS= 5000 Hz TO 95000 Hz
*****
*EMCM Y *
*****
PLOT LIMITS= 10 uV TO 30 uV
BASELINE FREQUENCY PLOT LIMITS= 5000 Hz TO 95000 Hz
*****
*ACCEL X *
*****
PLOT LIMITS=-.1 uV TO .1 uV
BASELINE FREQUENCY PLOT LIMITS= 5000 Hz TO 95000 Hz
*****
*ACCEL Y *
*****
PLOT LIMITS=-.1 uV TO .1 uV
BASELINE FREQUENCY PLOT LIMITS= 5000 Hz TO 95000 Hz
Nav= 30
DISPLAYED DATA ARE 1 SECOND AVERAGES
```

Figure 3.12. Vorticity measurements with a diver creating a disturbance upstream of the EMVM (three-axis open sensor).

PROG=VMPB3J
 INPUT FILE=TEST28...UNIT MOORED OFF PIER C SHILSHOLE SENSOR SHROUD REMOVED

TRACK # 1

DUMP TIME=03:14:09:46:14



```
*****
*VORTICITY *
*****
PLOT LIMITS= 0 uV TO 1 uV
BASELINE FREQUENCY PLOT LIMITS= 5000 Hz TO 95000 Hz
*****
*EMCM X *
*****
PLOT LIMITS=-20 uV TO 0 uV
BASELINE FREQUENCY PLOT LIMITS= 5000 Hz TO 95000 Hz
*****
*EMCM Y *
*****
PLOT LIMITS= 10 uV TO 30 uV
BASELINE FREQUENCY PLOT LIMITS= 5000 Hz TO 95000 Hz
*****
*ACCEL X *
*****
PLOT LIMITS=-.1 uV TO .1 uV
BASELINE FREQUENCY PLOT LIMITS= 5000 Hz TO 95000 Hz
*****
*ACCEL Y *
*****
PLOT LIMITS=-.1 uV TO .1 uV
BASELINE FREQUENCY PLOT LIMITS= 5000 Hz TO 95000 Hz
Nav= 30
DISPLAYED DATA ARE 1 SECOND AVERAGES
```

Figure 3.13. Vorticity data taken while the third version of the EMVM was slowly rotated (three-axis open sensor).

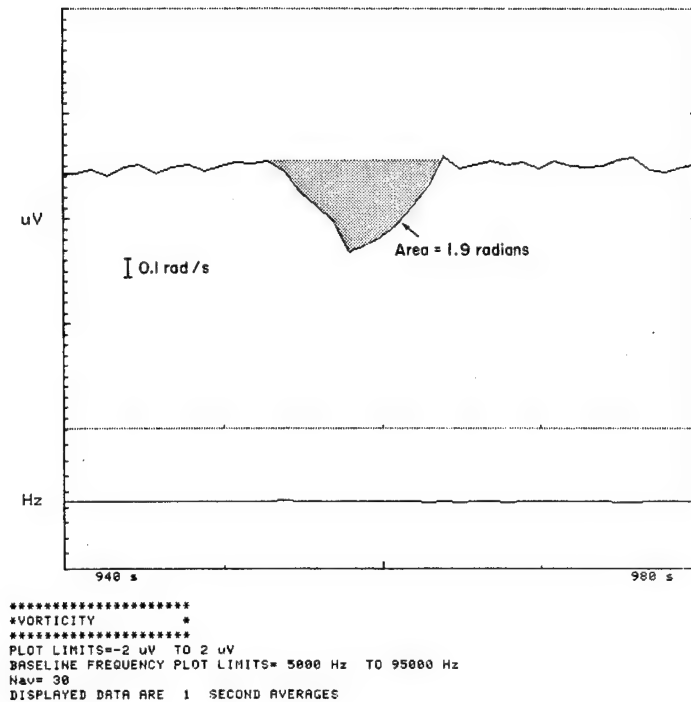


Figure 3.14. Time integral of one rotation of the tripod-mounted sensor.

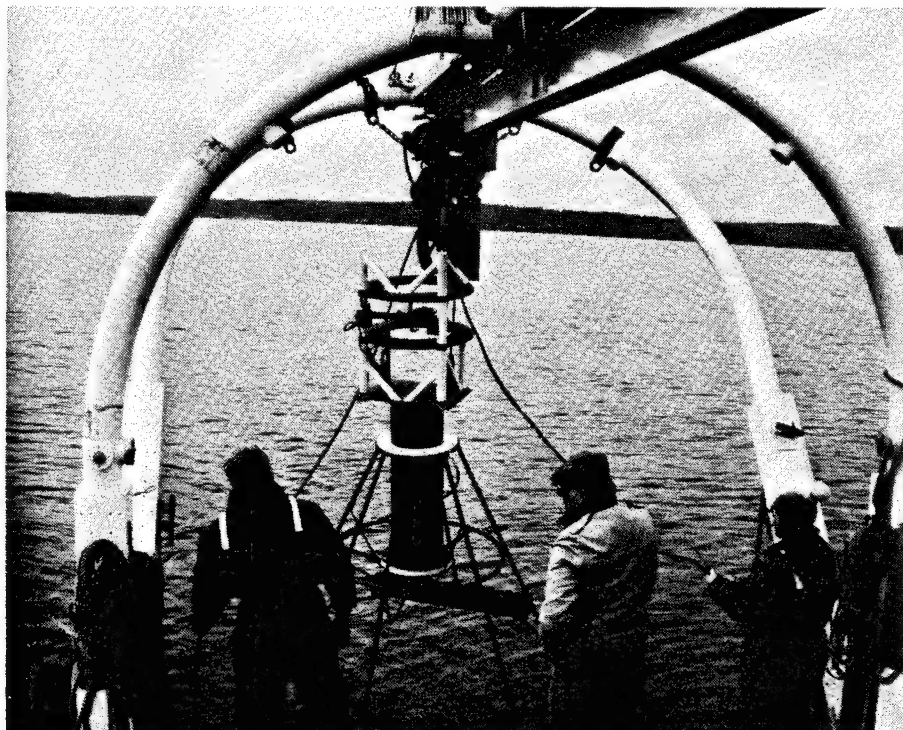
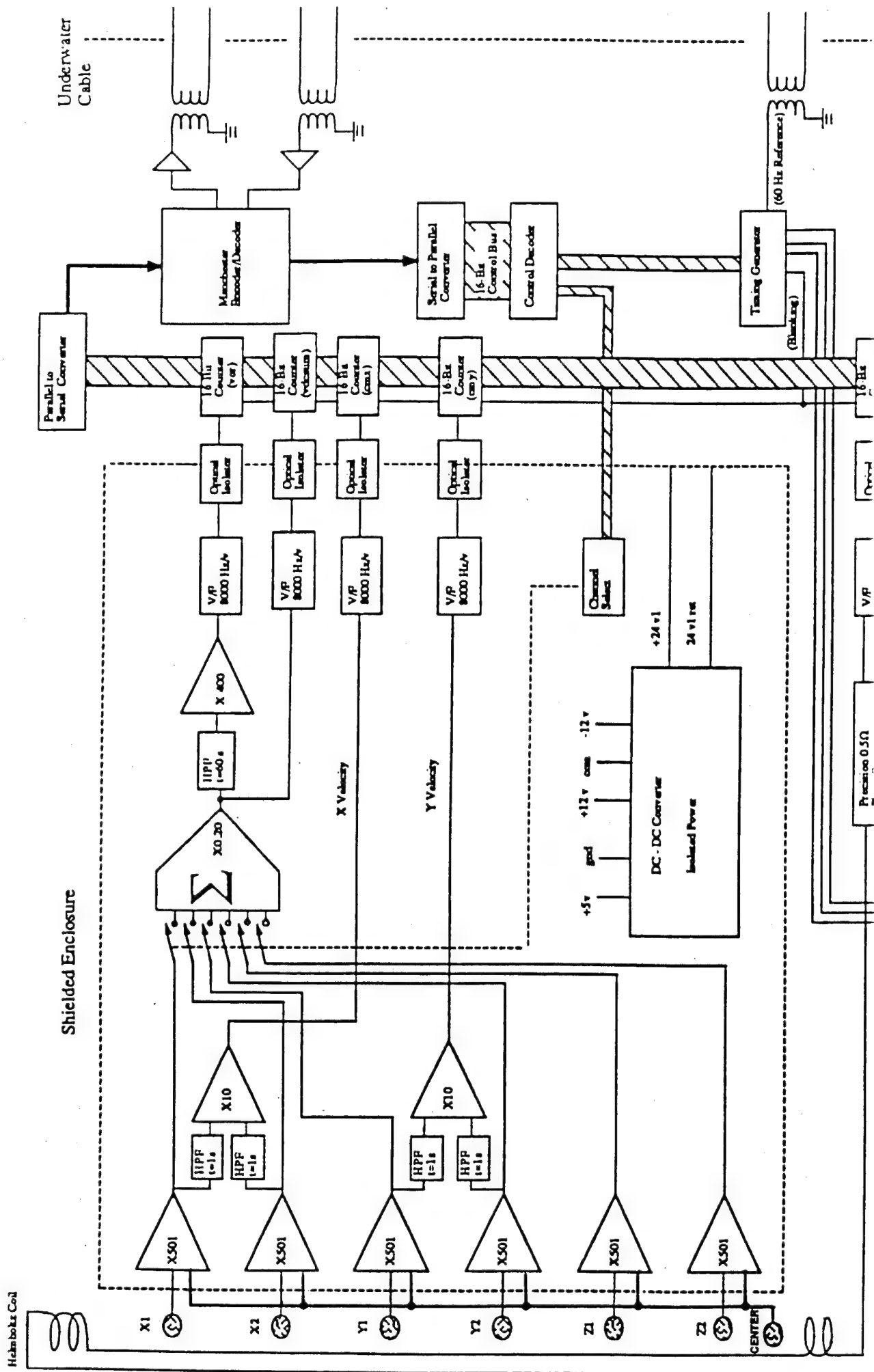
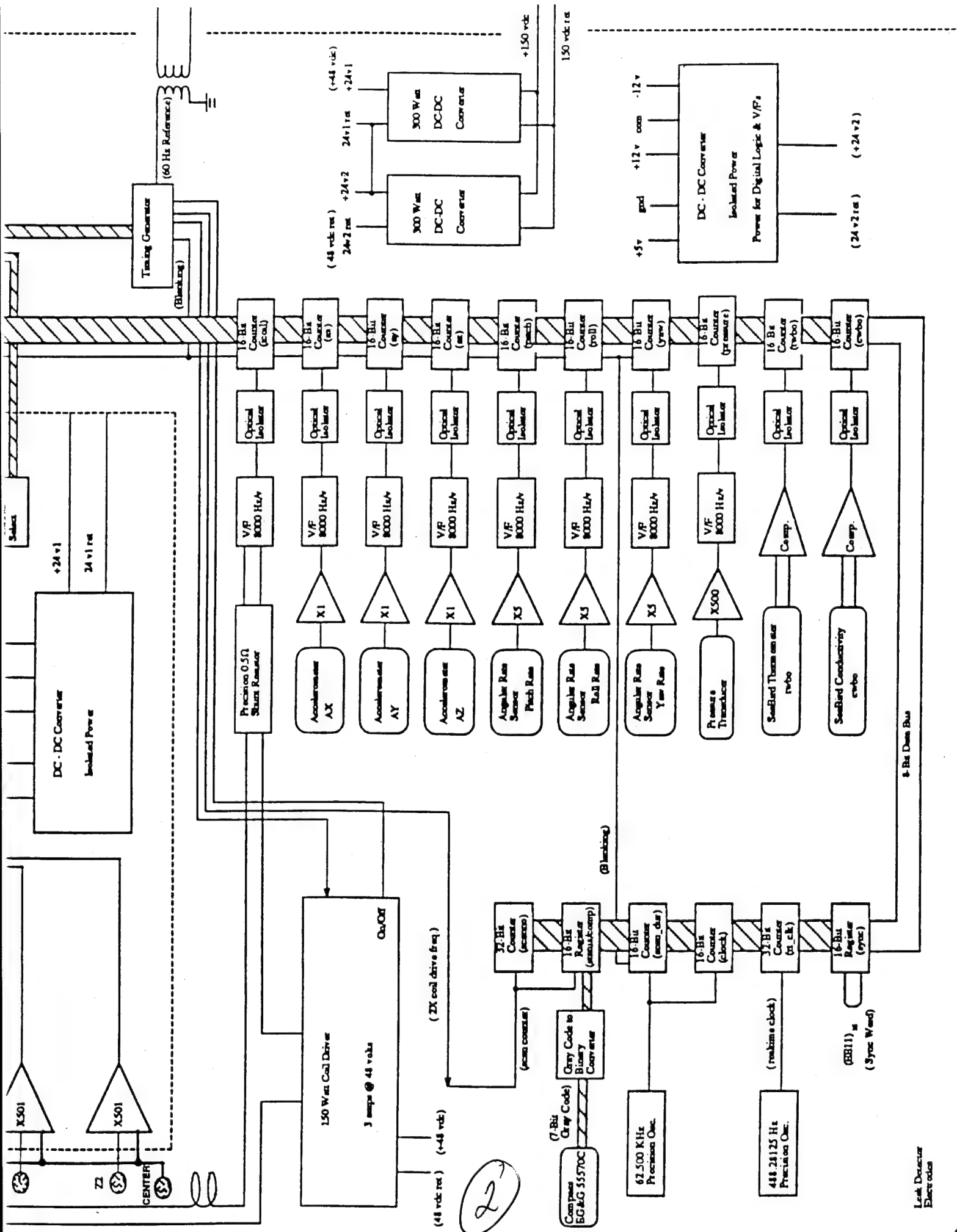


Figure 3.15. The fourth version of the EMVM mounted in a support frame for use on the seafloor.

1





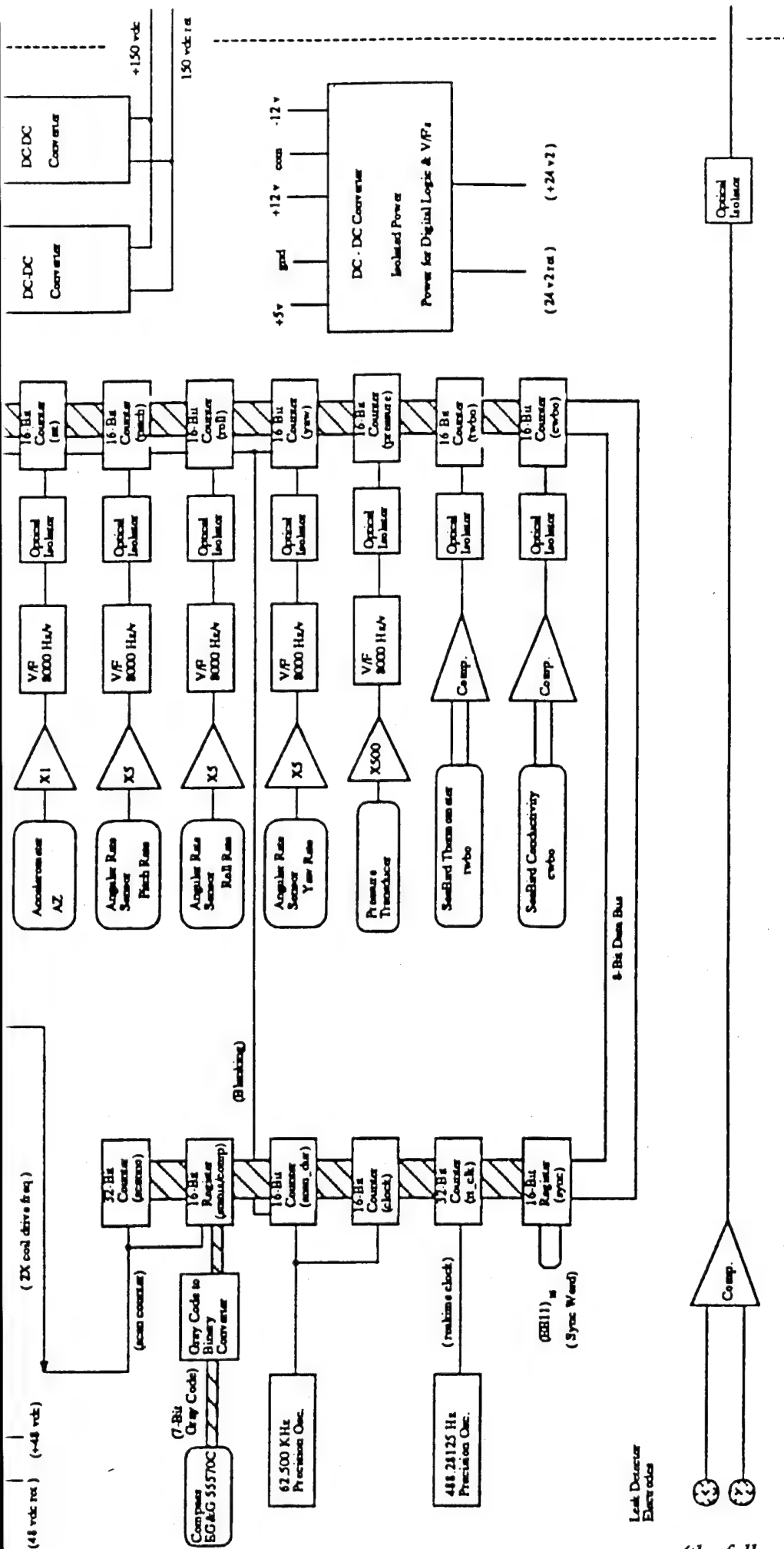


Figure 3.16. Block diagram of the electronics of the fourth version of the EMVM. This version added optical isolation to the shielded front-end electronics and 16 auxiliary data channels. The RS-422 data link used in the tow cable was replaced with a bi-directional, asynchronous, serial, Manchester-encoded data link. This type of data link allowed the use of transformer coupling at each end of the tow cable for added isolation.

constructed during the summer of 1985. This was a three-axis sensor with the measurement ports arranged on the upper and lower surfaces of a thin disc. The electrodes and measurement ports for the vertical axis were supported on "horns" which protruded up from the rear perimeter of the disc.

On 28 February 1986, this EMVM was field tested south of Port Jefferson in Puget Sound in about 15 m of water. The deployment served as an engineering test of the instrument as well as an opportunity to obtain a time series of vorticity in a tidal regime. The instrument was placed on the bottom in a support frame with the help of divers. The site was fairly level, with a smooth, sandy bottom. While in the support frame, the vorticity and current sensors were 2 m above the bottom. Apparent vorticity was generated by the divers slowly rotating the EMVM, providing a means to check calibration as well as to determine a "zero" for the current measurements.

After the divers left the water, a 3-hour time series of vertical vorticity and horizontal velocity was obtained (Figure 3.17). The coordinates were rotated so that velocities were displayed in a "flood-ebb" reference. The EMVM recorded 1.5 hours on either side of lower low-water, and about 2 hours before and 1 hour after the slack water before flood tide. The vorticity level was about 0.08 s^{-1} peak to peak for data sampled at 0.5-s intervals. Just before slack tide, the vorticity levels became very erratic, in part because of the tidal current turning and approaching the EMVM from an oblique angle. The divers descended again and rotated the EMVM into the current. The vorticity signal leveled off at about 0.40 s^{-1} peak to peak after the adjustment.

On 27 March 1986, another test of the EMVM was made in Puget Sound, this time 2 n.mi. north of Shilshole Bay; again the sensor was mounted on a tripod in 15 m of water. The test consisted of two trials, each about 50 min long. The first was at the time of the maximum flood tidal current in the middle of Puget Sound (0.25 m/s); the second was during a decelerating tidal current averaging about 0.19 m/s . These values were estimated from the 1986 NOAA tidal current tables for the Pacific Coast of North America. The actual velocities measured by the EMVM were about 6 cm/s . The two trials compared two different electromagnetic field sensors. The first, the same type used in the February test, was disk shaped whereas the second was finger shaped. It was hoped that the finger-shaped sensor would be less intrusive than the disk-shaped sensor and thus would create less contamination.

Further testing was undertaken in the laboratory to establish reference levels of self-noise under the quietest conditions possible. For the laboratory tests, the instrument was suspended so that the magnetic coils and the sensors were immersed in a salt-water-filled plastic tank. The tank water was electrically isolated from the floor and all surrounding objects. Velocity and vorticity were simulated by oscillating the instrument, using a small motor and a pivot arm. First, the arm was placed to the side of the EMVM to simulate the vorticity seen by the EMVM when it was moving in pure rotation in still

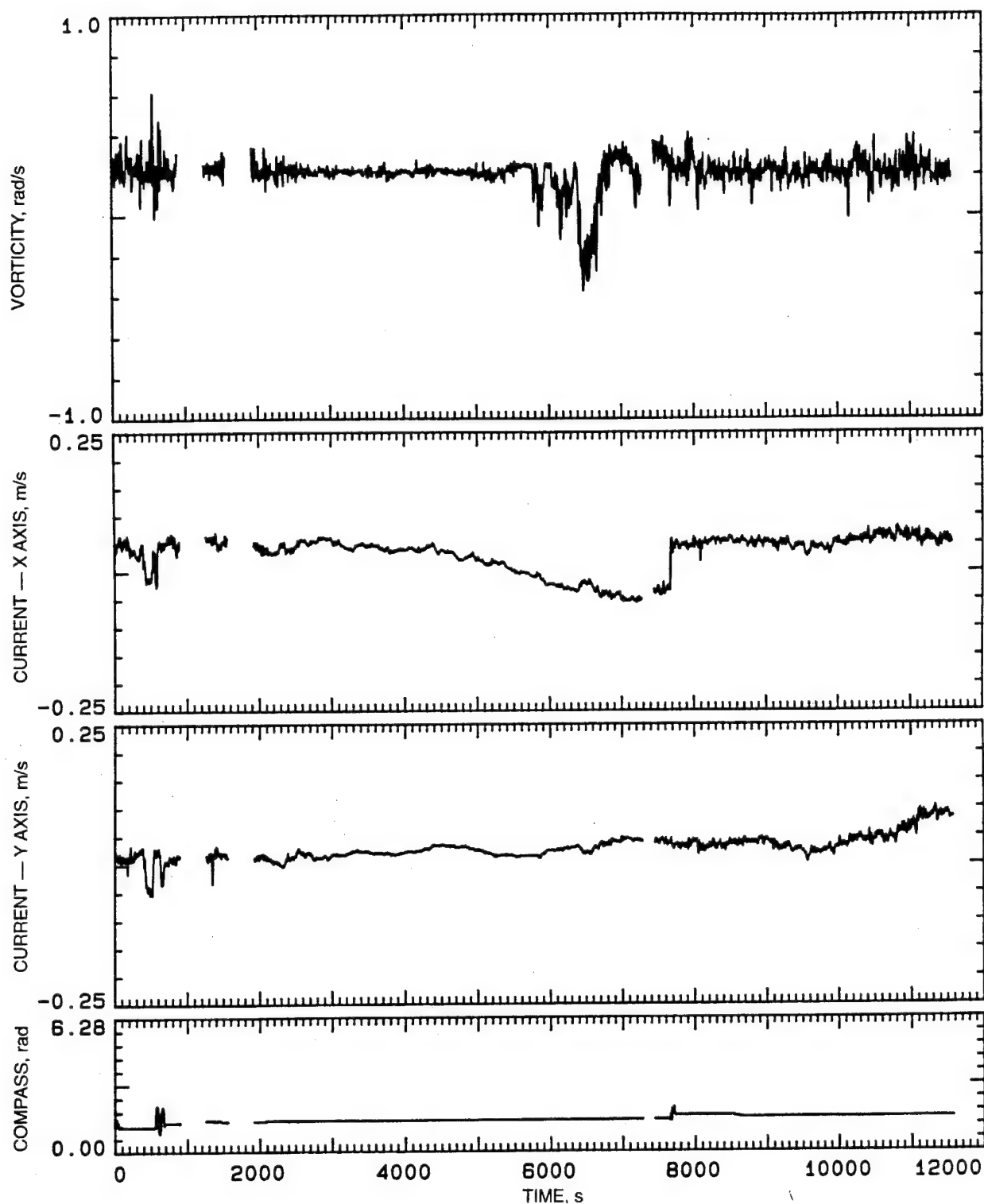


Figure 3.17. Time series of horizontal velocity and vertical vorticity from EMVM deployment south of Point Jefferson in Puget Sound.

water. Then the arm was moved to the center of the EMVM to simulate the velocity while the instrument was in pure translation through the water. In a quiescent tank with no instrument motion, the spectral levels of vorticity variance were $10^{-6} \text{ s}^{-2}/\text{Hz}$ (Figure 3.18), and the energy levels were $6 \times 10^{-7} \text{ s}^{-2}/\text{Hz}$. When the instrument was set up for oscillation at a specified period, the level of the vorticity variance spectra remained at $10^{-6} \text{ s}^{-2}/\text{Hz}$ (Figure 3.19) except for the spectral band around the oscillation frequency.

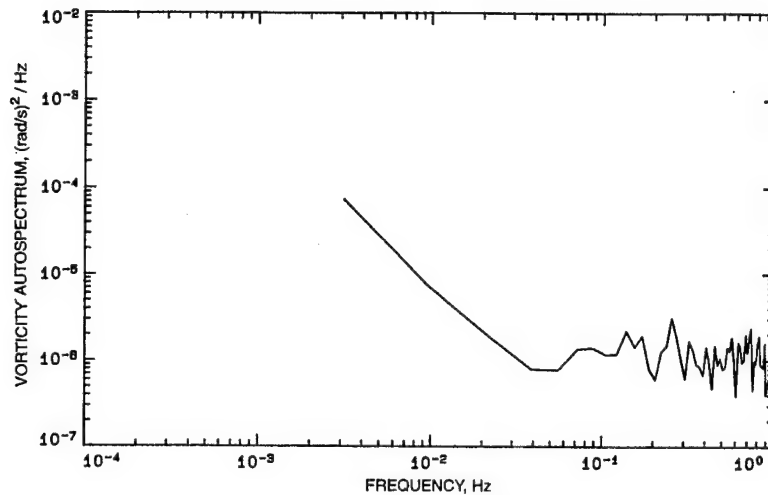


Figure 3.18. Power spectrum of vorticity for sensor operated in still water in an electrically isolated test tank. A noise floor of $10^{-6} \text{ (rad/s)}^2/\text{Hz}$ is reached at frequencies above $5 \times 10^{-2} \text{ Hz}$. Below $5 \times 10^{-2} \text{ Hz}$, the noise power increases 100 times for every decade decrease in frequency.

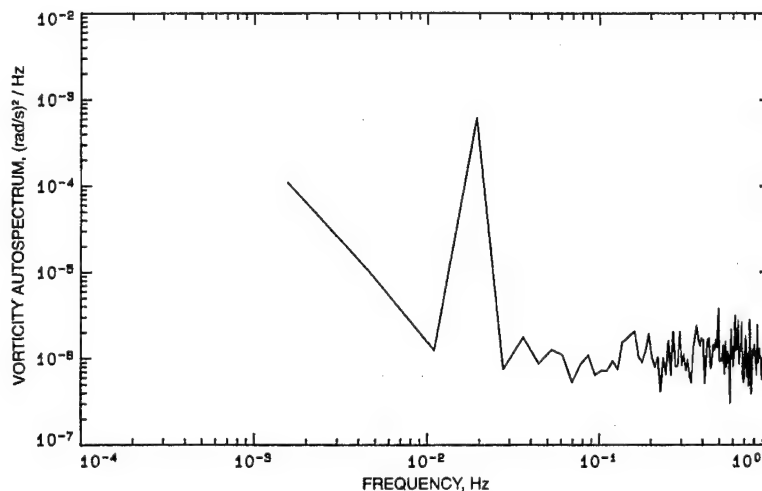


Figure 3.19. Power spectrum of vorticity for sensor oscillated in pure rotation in a still-water test tank at a frequency of $2 \times 10^{-2} \text{ Hz}$. The noise floor remains unchanged, with the dominant signal at the oscillation frequency.

3.5 Experiences with Tow Bodies

Soon after the first successful EMVM tests on a tripod early in 1984, we wanted to install the instrument on a vehicle for towing. We investigated existing tow bodies and found two that might meet our requirements. One was the system used by the Navy known as the C Mk 1. The other was the commercial version of the Batfish, known as Seasoar. The former could be had on loan; the latter cost over \$50,000. Initially, we sought to use the former; ultimately, we purchased the latter.

3.5.1 C Mk 1 tow body

In the spring of 1984, we received a C Mk 1 towed vehicle on loan from the Naval Coastal Systems Center. Figure 3.20 shows the unit as received. The depressor wings have a total wingspan of about 5 ft. The central body is a fiberglass pressure case with an outside diameter of about 9 in. The bottom-following electronics with pitch and roll stabilization utilize about one-half of the available internal volume. The sidescan sonar sys-

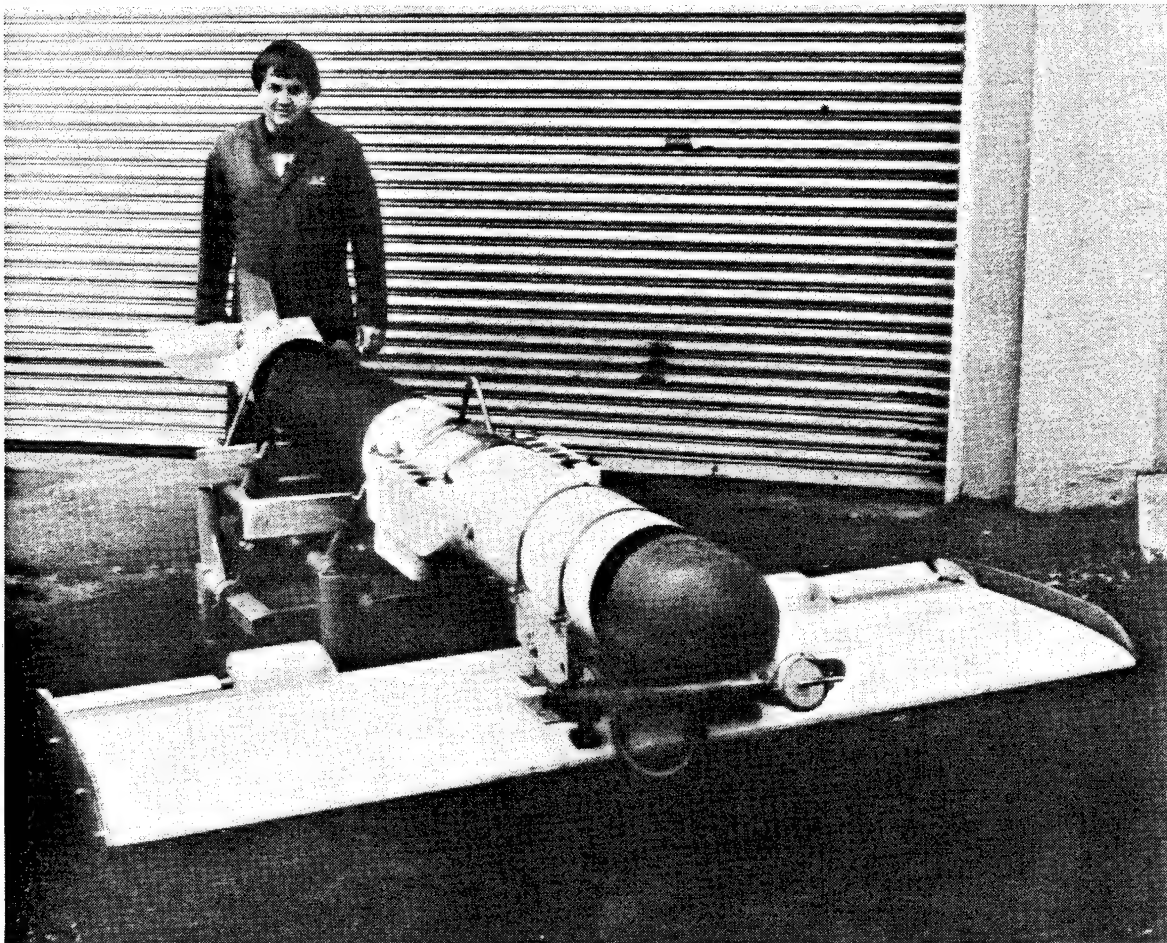


Figure 3.20. C Mk 1 tow body as received from the Naval Coastal Systems Center in 1984.

tem takes up another one-third of the available volume, leaving a small space forward near the nose for an auxiliary payload. The internal electronic circuits utilized vacuum tubes which made them obsolete. We were able to find replacement tubes, so we used the existing electronics rather than building solid-state replacements. As received, the electronics were designed to fly the vehicle at a constant height off the bottom. The bottom-following circuitry was modified to allow the vehicle to fly at a controlled depth, and the APL winch used for towed targets was modified to accommodate the C Mk 1's tow cable. Several test tows were made in April 1984 in Lake Washington to evaluate the dynamic stability of the vehicle. Because of the large surface area of the depressor wings, large transient loads were applied to the winch, cable, and wooden deck plates of the towing vessel. The C Mk 1 was able to fly at a constant depth, although pitch stability was obtained only under fair weather conditions. The tow characteristics drifted slowly over time, and upon retrieval it was found that the fiberglass wings were filling with water.

3.5.2 GW Fairing

During the spring of 1987, we designed and constructed a fiberglass fairing for the vorticity meter which allowed the whole instrument to be towed underwater. This was done rather than use the C Mk 1 vehicle because the C Mk 1 would have been unable to accommodate the additional volume and weight of EMVM version 4. Figure 3.21 shows the instrument out of the water hanging from the towing bridle. The orientation of the

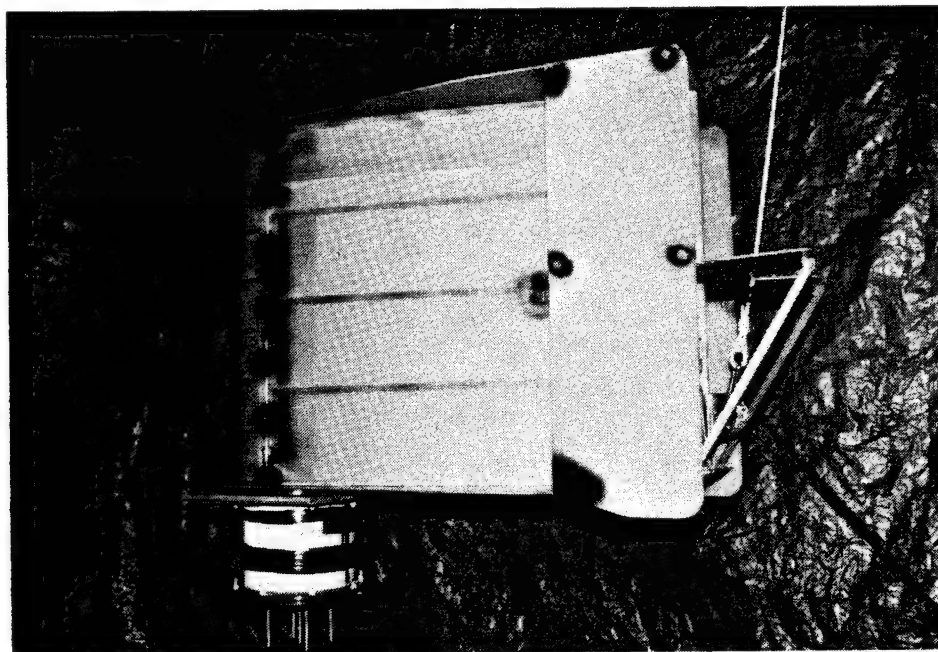


Figure 3.21. Vorticity meter hanging from the tow bridle, in normal operating configuration. The fiberglass fairing designed by G. Welsh (GW fairing) is prominent.

instrument shown in this photograph is the normal operating configuration. The pressure case of the EMVM is in essence the leading edge of an airfoil which is towed in an upright orientation by a bridle attached to the the upper endcap of the instrument. The height of the airfoil is 36 in. Above and below this wing section are flat flow-splitting plates which taper from a width of 16 in. at the leading edge to 24 in. at the trailing edge. At the rear are adjustable elevators which are used to trim the tow body for level flight at the nominal tow speed. The electromagnet coil and array of sensor measurement tubes extend below the lower flow-splitting plate of the fairing. The first test tows of this instrument were accomplished in June 1987 in Puget Sound. Minor tweaking of the bridle attachment point and elevator angle resulted in a stable towed instrument. However, the roll stability was greatly affected by the tow speed. At tow speeds above 3 kn, the instrument/fairing combination began to roll back and forth with amplitudes of $\pm 15^\circ$ or more at a period of a few tens of seconds. This behavior limited the tow speed to less than 3 kn.

3.5.3 *Seasoar tow body*

The Seasoar vehicle was purchased from Chelsea Instruments Ltd., U.K., in July 1988 as a replacement for the C Mk 1. Figure 3.22 shows the Seasoar vehicle as shipped from Chelsea Instruments. This particular vehicle was chosen on the basis of a comparison study commissioned by the Naval Ocean Research and Development Activity which showed that the Seasoar was superior in several categories of performance. For our application, the reported low vehicle vibration levels and low yaw rates were key specifications. Because of the high cost of this unit and its foreign manufacture, the time required to purchase and take delivery of this device was almost 1 year. By the time the Seasoar was received, we were successfully using the GW fairing and obtaining good results with our field observations in Puget Sound.

3.5.4 *Comparison of Seasoar and GW fairing performance*

The Seasoar tow body was tested in Lake Washington on 24 April 1991 for 1 hour and again on 25 April for 2 hours. Tow speeds ranged from 3.5 kn to about 5 kn maximum. Because the water depth was at most 200 ft, only 150–175 ft of cable were payed out. Enough experience was gained from these tests to warrant testing in Puget Sound at higher speeds and with more tow cable extended. On 29 April 1991, the Seasoar was deployed from APL's R/V *Miller* in Puget Sound for 5.5 hours. The maximum tow speed was 7.5 kn, and the performance of the Seasoar was evaluated with various amounts of tow cable payed out.

The fiberglass fairing designed by G. Welsh and used to tow the EMVM since 1987 was most recently used during 16–18 April 1991 for tows through the wake of Blakely Rock. The tow speed found most effective for this work was about 2.5 kn. At higher tow speeds, the EMVM pitched down such that the flow-splitting plate was flying with a 0° to -5° angle of attack. This evidently caused some flow separation at the leading edge, as a large increase in random noise was observed in the vorticity data.

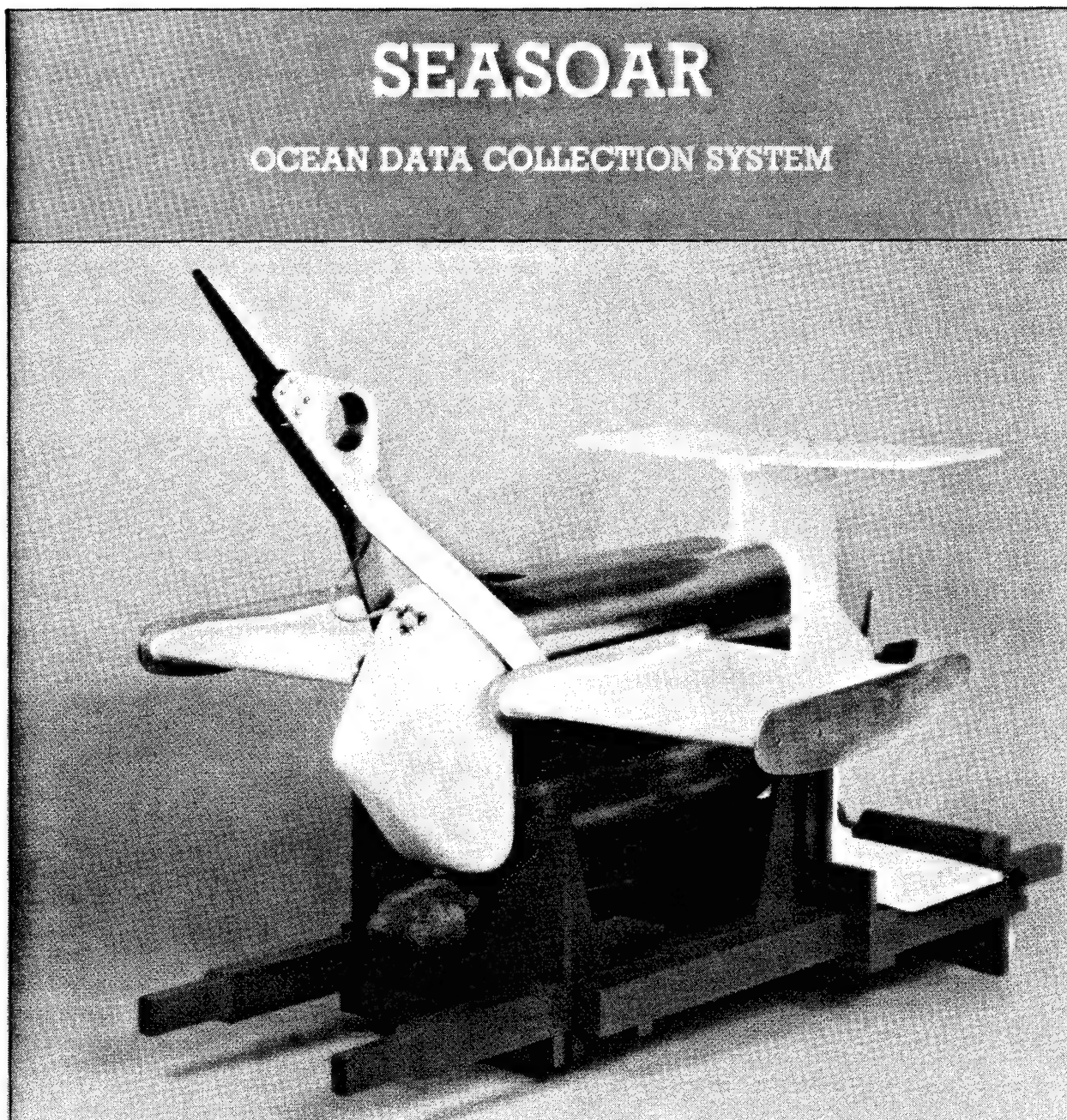


Figure 3.22. Seasoar oceanographic tow body. The wing angle can be changed dynamically via an internal hydraulic actuator. The actuator extracts its power from the passing seawater using a small propeller assembly coupled to a hydraulic pump. This system allows the tow body to be controlled remotely; it can be ordered to dive, surface, or fly at a prescribed depth.

To evaluate the performance of the towed underwater vehicles, a special self-contained sensor and data-acquisition package was constructed to collect data on vehicle dynamics. This system consisted of a pressure vessel 6 in. in diameter and 22 in. long housing a suite of three accelerometers mounted orthogonally to each other, one three-axis magnetometer, one two-axis angular rate sensor (providing pitch rate and yaw rate), and a pressure transducer for depth measurement. These sensors were anti-alias filtered at 5 Hz and sampled at 10 Hz with a 10-bit digitizer. The digital data were buffered by a TattleTale Model 5 microcomputer system and sent up the tow cable as an asynchronous bit-serial data stream at 9600 baud. The serial data were optically coupled at each end of the cable, and the power to the sensor package was isolated from the ship power by dc-dc converters. This eliminated the dc ground loop path allowing electric currents to flow down the tow cable, through the sensor package, and back up through the seawater to the towing vessel.

Given the sensitivity of the fourth EMVM to static pitch angles and the inherent sensitivity to yaw rate, it is these parameters, along with roll angle stability, that have been analyzed for both vehicles. Figure 3.23 shows time series for yaw rate, pitch angle, and roll angle for the Seasoar while it was being towed in Puget Sound at a depth of 70 m with 170 m of cable winched out. The added vertical lines indicate the times when the tow speed was changed. The tow speed started at 3.5 kn and was increased in 0.5-kn increments up to a final to speed of 6.5 kn. At 6.5 kn, the Seasoar vehicle becomes less stable, exhibiting larger roll excursions of $\pm 4^\circ$. Also at 6.5 kn, the yaw rate becomes active, indicating the vehicle is fishtailing with a maximum rate of 0.05 s^{-1} . Figure 3.24 is a similar time series for the GW fairing while it was being towed at a depth of 10 m with about 30 m of cable out. The GW fairing shows much less roll stability, with excursions of $\pm 5^\circ$. This is probably due to the tow cable attachment point being located at the top of the body, about 0.5 m above the center of mass of the combined tow body and sensor package. The pitch stability is similar to that of Seasoar, with maximum excursions of $\pm 2^\circ$.

Figure 3.25 compares Seasoar and GW fairing yaw-rate spectra. The solid line is the spectrum for data taken with the GW fairing towed at 2.5 kn; the dotted line is for data taken with the Seasoar towed at 3.5 kn. Below 0.1 Hz, the Seasoar vehicle exhibits yaw rates an order of magnitude lower than those for the GW fairing. The GW fairing seems to have an energy peak at a 20-s period. For frequencies above 0.2 Hz, both tow bodies have similar yaw rates. The Seasoar spectrum is quite a bit noisier at high frequencies because it is realized from a single 200-s time series. The GW fairing spectrum, on the other hand, is the average of 17 spectra, each based on a 200-s time series. It is therefore difficult to compare the two spectra at the high frequency end. Figures 3.26 and 3.27 are similar plots for the pitch and roll data. Again, the solid line is the spectrum for the GW fairing and the dotted line is for the Seasoar.

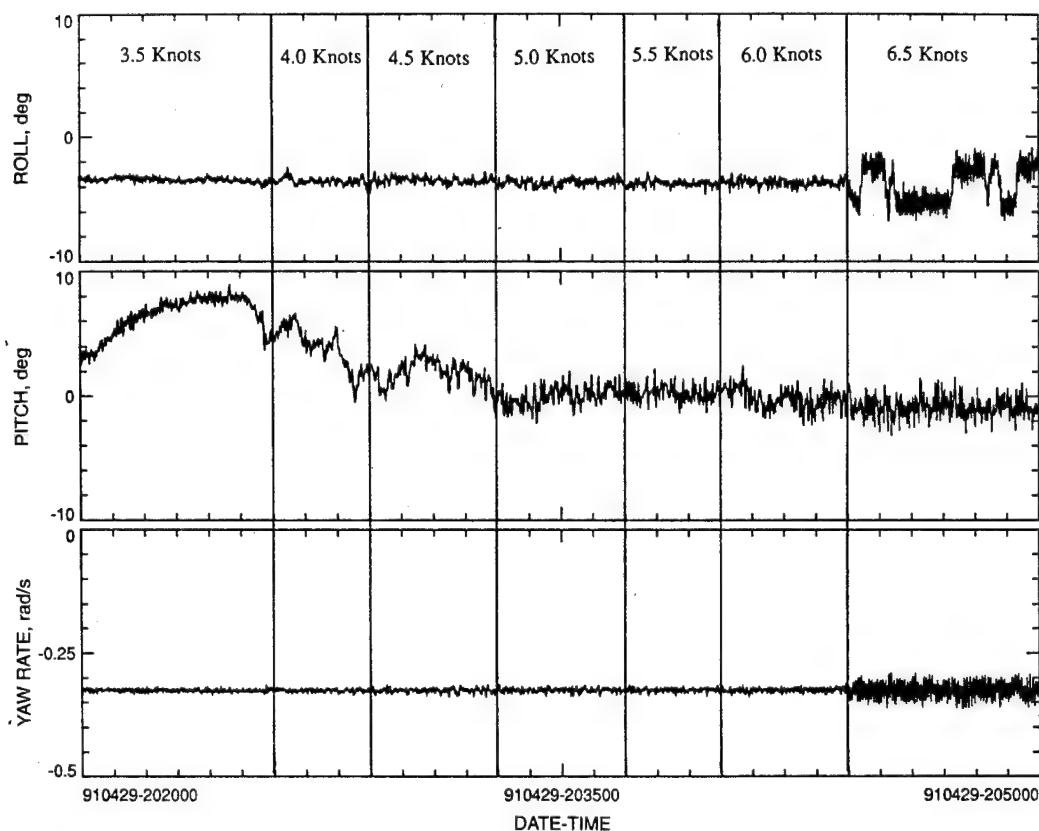


Figure 3.23. Time series of yaw rate, pitch angle, and roll angle obtained while the Seasoar was being towed in Puget Sound at various speeds. Time scale is in two-digit units indicating, from left to right, year, month, day - hour, minutes, seconds.

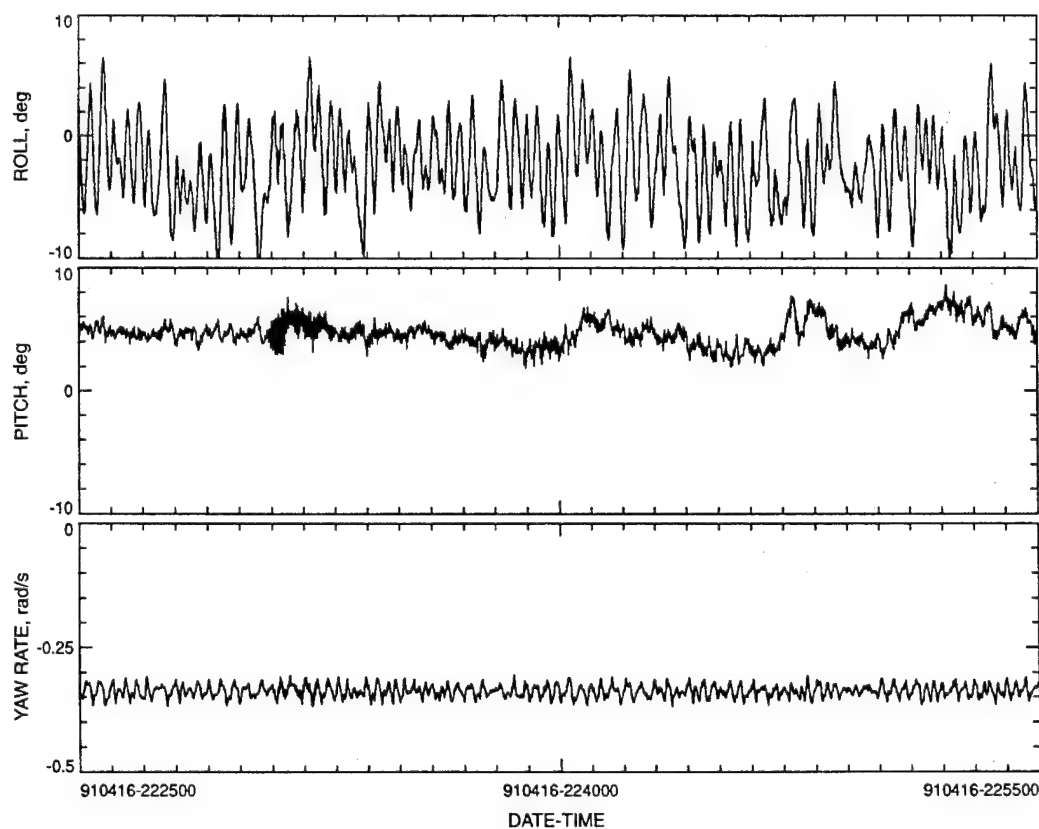


Figure 3.24. Time series of yaw rate, pitch angle, and roll angle of the EMVM with GW fairing being towed at 2.5 kn. Time scale as in Figure 2.23.

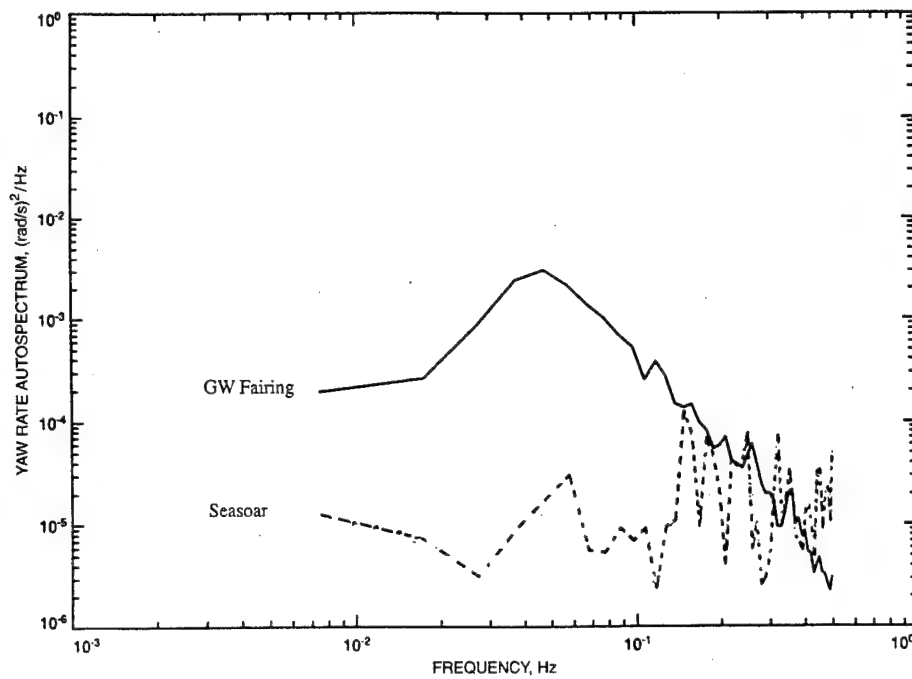


Figure 3.25. Comparison of yaw-rate spectra for the Seasoar tow body and GW fairing.

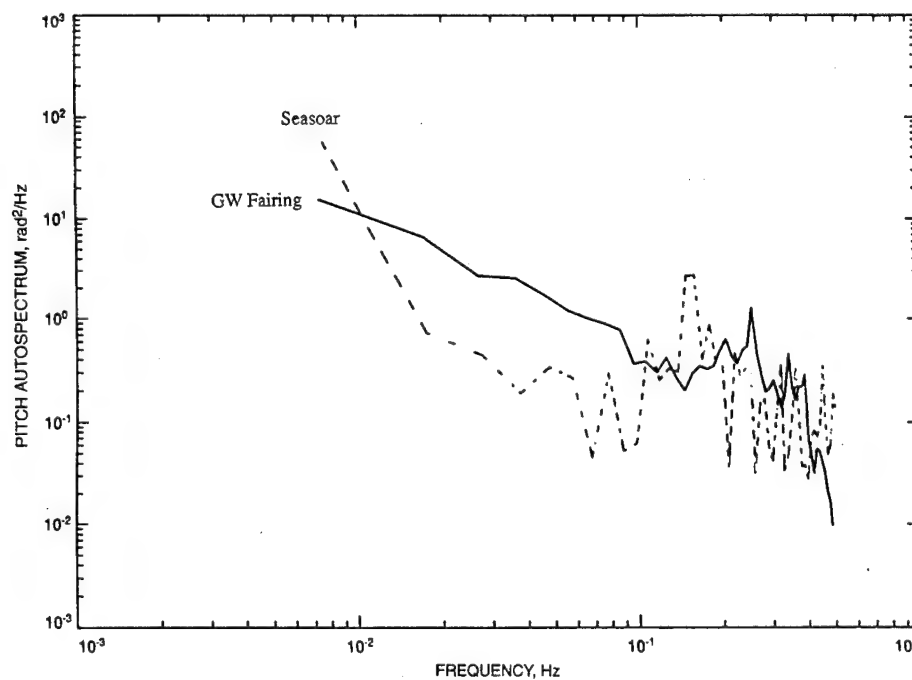


Figure 3.26. Comparison of pitch spectra for the Seasoar tow body and GW fairing.

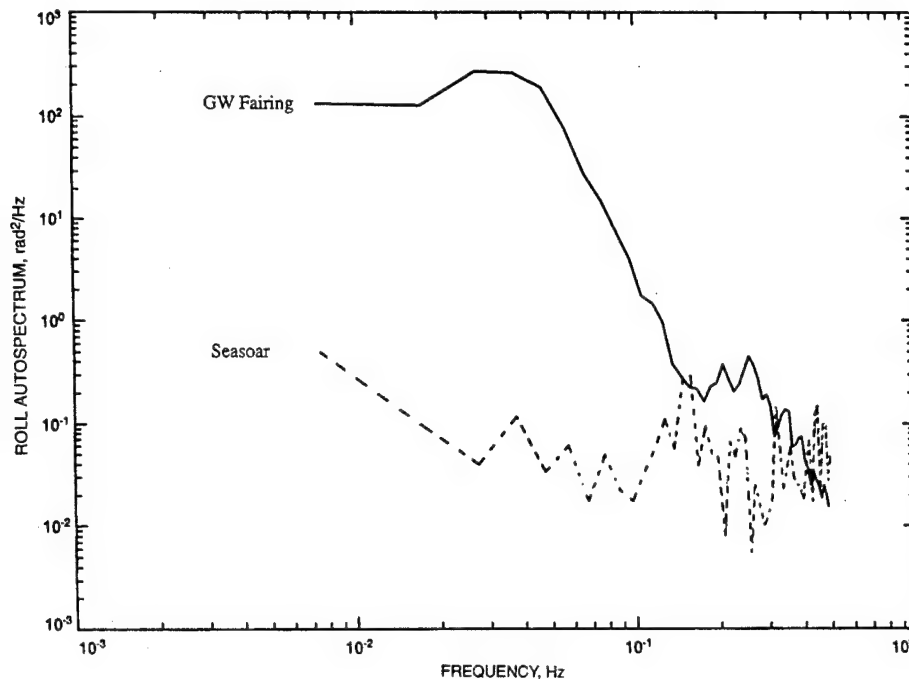


Figure 3.27. Comparison of roll spectra for the Seasoar tow body and GW fairing.

Figure 3.28 shows the yaw-rate spectrum for Seasoar when the vehicle was being towed at 6.5 kn. Note the large-amplitude yaw oscillation at about 0.19 Hz. This yaw-rate amplitude would make the Seasoar unacceptable for use with the EMVM at this tow speed.

In conclusion, the Seasoar outperforms the GW fairing at low tow speeds in all three categories of comparison (yaw rate, pitch angle, and roll angle). At tow speeds below 3.5 kn, however, the Seasoar vehicle becomes unstable in depth keeping owing to insufficient hydraulic pressure to activate the wing. At tow speeds above 6 kn, the Seasoar again becomes unstable and exhibits excessive yaw rates and roll rates. Since the instability is narrowband at 0.19 Hz and this frequency is fairly low compared with the resonant frequencies of the control surfaces on the Seasoar, it may be due to a dynamic interaction of the tow body with the tow cable. It may be possible to damp out this yaw oscillation with an appropriate cable fairing or a longer length of cable payed out. In its present configuration, the GW fairing cannot be trimmed to maintain positive pitch angle for tow speeds above 2.7 kn, limiting its use to tow speeds of 2.5 kn or lower.

3.5.5 Seasoar problems and manufacturer repairs and upgrades

After only 8 hours of towing, the Seasoar became sluggish in its response to control signals from the deck box. In addition, control settings that had been previously determined were no longer appropriate. We decided to bring the Seasoar back up on deck for

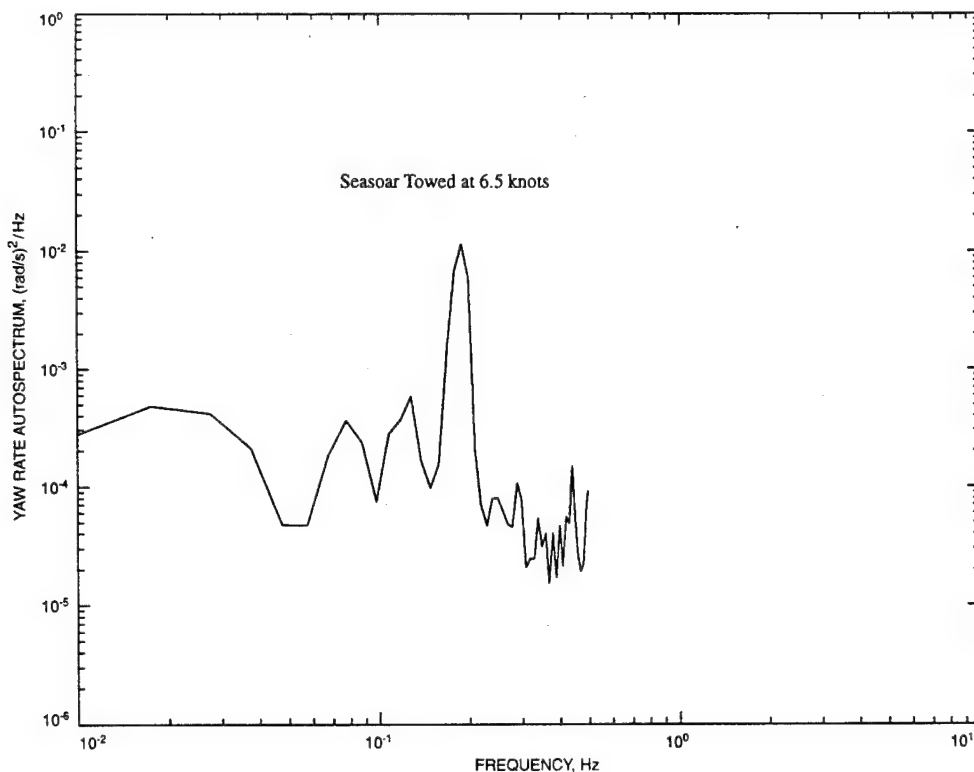


Figure 3.28. Yaw-rate spectrum for the Seasoar vehicle towed at 6.5 kn.

a visual inspection. At first glance nothing seemed to be wrong; however, when the propeller was turned by hand, we noticed an excessive amount of radial play in the rear bearing for the propeller shaft. We returned the unit to the laboratory for a closer inspection.

We removed the propeller from the tail shaft. There was no significant play between the propeller and the shaft. The shaft did have lateral bearing play, so we decided to remove the hydraulic unit from the vehicle. With the unit removed from the vehicle, we drained the rear tail-shaft housing. Approximately 600 ml of fluid was drained from the housing. It was a frothy mixture of oil and salt water with a slightly greenish tint. Some brownish to black particles settled out of the solution. The most obvious problem was that the Teflon tail shaft bearing was free to spin inside the PVC housing. The bearing measured 1.170 in. long with an outside diameter of 0.740–0.745 in. The inside diameter of the bearing measured 0.500–0.501 in. Both of the lip seals showed wear and tearing on their inside diameters. After the lip seals were removed, it was possible to measure the diameter of the hole that receives the Teflon tail-shaft bearing. The inside diameter of the hole measured 0.750 in. We have concluded that the bearing was always free to wobble in the PVC housing while the tail shaft was spinning. This could cause the lip seals to fail owing to the large amount of lateral shaft movement.

In further examining the PVC rear housing, we noticed that there was cracking adjacent to two of the helicoil inserts. One of these cracks extended radially inward across the O-ring face seal surface. This was another potential source of seawater intrusion into the oil-filled cavity. The 0.132-in. diameter (cross section) O-ring that provided the seal between the PVC housing and the flanged stainless steel endcap was examined and found to be in perfect condition, as was the 0.120 in. deep by 0.156 in. wide O-ring groove in the stainless endcap. The design, however, allows for only a 10% compression of the O-ring. O-ring manufacturers recommend 16% to 23% compression for a static face-seal gland. The O-ring was therefore another potential source of seawater intrusion.

In conclusion, the Seasoar developed serious mechanical problems after only 8.5 hours of operation. These problems were repaired, but a redesign of the rear bearing assembly was required for increased reliability. In addition, a redesign of the rear face seal between the PVC housing and the stainless steel endcap was recommended. Other users of the Seasoar had reported similar problems, and Chelsea was making modifications to increase the reliability of the vehicle. Moreover, the present EMVM was too large to install on the Seasoar.

We therefore decided to postpone further tow-body work in favor of focusing on improving sensor performance. This decision lead to construction of a fifth version of the EMVM.

4. DESIGN, CONSTRUCTION, USE, AND EVALUATION OF THE FIFTH EMVM

We sought to implement a number of needed improvements in a new system while retaining as much of the main electronics as possible. The design concentrated on a new sensor unit, but one physically and electrically isolated from the main electronics. Most of what was learned about earlier versions was incorporated into the new sensor, electrode array, and magnet.

4.1. Design Goals

The principal design goals were to

- eliminate the electric measurements along the axis of the magnetic field
- produce less disturbance and be more symmetric to the flow
- protect the electrodes for better noise performance
- construct the sensor out of plastic
- separate the sensor from the main electronics
- isolate the sensor head with optical-fiber data links and batteries
- keep flow away from the magnet except in the region of measurement
- incorporate a permanent magnet into the sensor.

One important change was the decision to forgo 3-D measurements. The electrodes along the axis of the magnet were not providing an important signal in the situations encountered, such as in the laboratory tests. It was decided to concentrate on an array of five electrodes in the x - y plane, normal to the principal axis of the magnet. The individual voltages between each outer electrode and the central reference electrode were recorded. This arrangement permitted us to compute velocity components normal to the magnet's axis and the vorticity aligned with the axis. One reason for this design was to eliminate asymmetry in the sensor. Earlier designs had structures that disturbed the flow and might have produced different results, depending on the orientation of the incoming flow. In seeking to achieve symmetry in the sensor, we were responding to problems that were not predominantly from the lack of symmetry but from a tendency for the V/F converters to influence each other. Nonetheless, we continued to improve symmetry even after the V/F problem was identified and corrected because the goal seemed appropriate on general principles.

The most noticeable design change was making the measurements above a smooth circular plate (see Figure 4.1). The circular plate has a tapered leading edge to reduce turbulence and is intended to slide through the relative flow with little angle of attack. Ceramic straws are used to connect the electrodes to the point where the potential is to be sampled. The electrodes are enclosed in chambers beneath the surface of the plate,

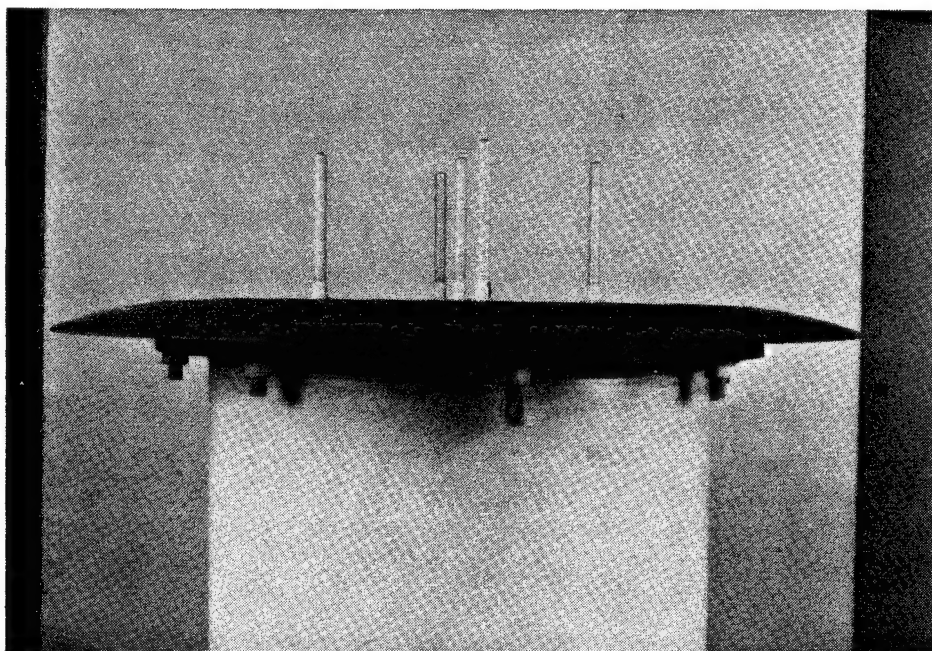


Figure 4.1. The splitter plate and ceramic straws of the fifth version of the EMVM.

called a splitter plate. A seawater-filled ceramic tube in a screw-in fitting electrically connects the electrode to the point of measurement. The electrode chamber and ceramic straw are filled with a solution of agar and seawater. The resulting jello-like substance is electrically conducting and avoids problems from air bubbles entrapped in tubes filled with just seawater. The encapsulation of the electrodes is intended to damp the temperature fluctuations and eliminate the salinity changes experienced by the electrodes. With a sensitivity of about $300 \mu\text{V}/^\circ\text{C}$ between similar electrodes at different temperatures, it is important to reduce this effect in the bandwidth of interest.

The electrode cups and straws are 4 in. apart on the plate and arranged in the form of a plus sign. The straws are 4.5 in. long and of the smallest diameter possible for the flow conditions. The splitter plate, electrode plenum, and magnet chamber are constructed of plastic to reduce electrical noise from corrosion currents.

The electromagnet is housed behind the splitter plate and electrode plenum. It is placed within a plastic enclosure to contain any stray currents which might leak from the potted magnet winding and to reduce flow directly on the coil, which might produce strong, erratic signals. The size, power, inductance, and amount of time needed for the inductive spike to decay required that we operate at lower frequency. For the most part, this version was operated at frequencies of 0.5 to 1 Hz. This chamber is also designed to hold the permanent magnet constructed of barium ferrite ceramic. It is open to the seawater. The magnets are kept in place by packing with glass microbeads. The intention is to keep the magnet from moving with respect to the electrodes and cables and thereby inducing spurious voltages.

Experiences with earlier instruments had demonstrated problems with ground loops and other inadvertent paths, even high-impedance ones, between circuits. It was decided that the way to guarantee adequate isolation was to operate the electronics on batteries and use optical data links. It was impossible to power the electromagnet on batteries, but it was possible to isolate the magnetic coils electrically from the preamplifiers and other sensor electronics. Moreover, this scheme allowed the sensor to be located separately from the main electronics, easing difficulties in placing the sensor on carriages and operating it in a test tank.

The low-noise preamplifiers, V/F converters, optical-fiber drivers, and batteries are installed in a short electronics rack. This rack is housed in an aluminum pressure vessel that is of the same material and diameter as the main electronics tube but is only 21 in. long. This chamber contains the essential electronics, batteries, and optical-link components and supports through-hull connectors for recharging the batteries and attaching the optical fibers. The data links and magnet power are connected to the main electronics package which remains outside the test tank in the laboratory or on the boat when making field observations. (See Figure 4.2 for a block diagram of the electronics.)

The design achieved many of the goals but presents some difficulties. The straws are fragile and contribute a rather high impedance to the circuits. This high impedance results in significant Johnson noise and additional voltages resulting from the preamplifier bias current and/or current noise. However, the AD 743 amplifiers have voltage and current noise characteristics that are favorable for this application.

4.2 Construction

4.2.1 *Electrode array*

In previous sensors, the electrodes were placed close to the measurement points. This kept the inter-electrode impedances low, but at the same time the thermal environment of the electrodes was not well controlled. In the new design, each electrode is housed in a thick-walled plastic housing with a 0.5-in. inside diameter and a 1-in. outside diameter. These housings are threaded on one end and have an O-ring seal so that they can be installed and removed easily. The underwater cable connecting the electrode to the preamplifier is sealed to the electrode housing with polyurethane potting compound. As a result of testing various electrodes, it was determined that silver/silver-chloride electrodes from In Vivo Metrics Inc. gave the best performance. We use ceramic tubes filled with a sodium-chloride solution to connect the electrode chambers to the measurement points above the splitter plate. The ends of these tubes must be colinear and equally spaced for a given measurement axis. The tubes are removable to allow replacement in case of damage. An aluminum-oxide ceramic was chosen for its dimensional stability, great stiffness, and high electrical insulation resistance. The ceramic tubes are glued to a threaded insert using a jig which assures that all the tube assemblies will be interchangeable. Dimensional tolerances are such that, when the threaded inserts with tube are screwed into the splitter plate from the side opposite the electrodes, the tips of the

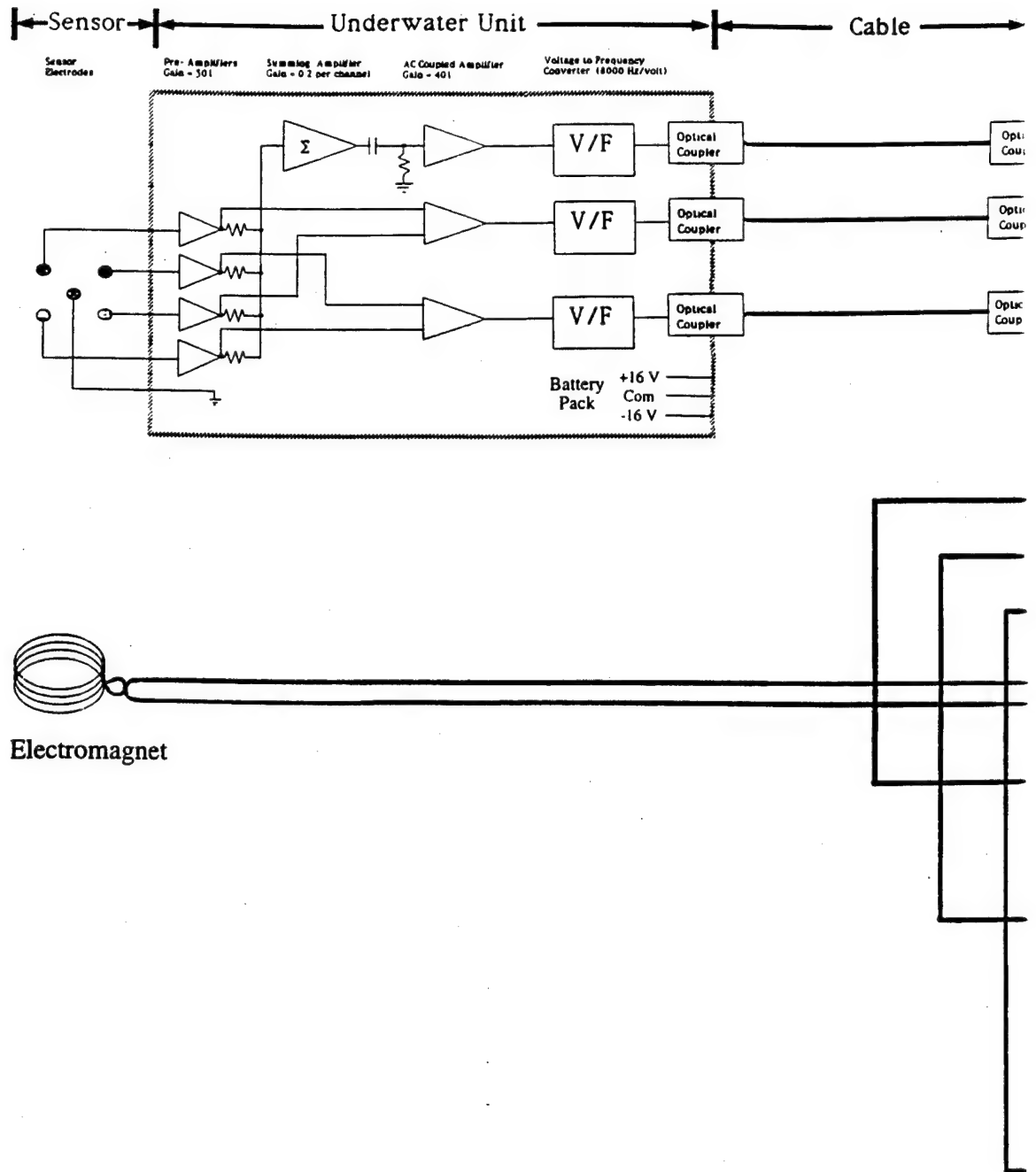


Figure 4.2. Block diagram

①

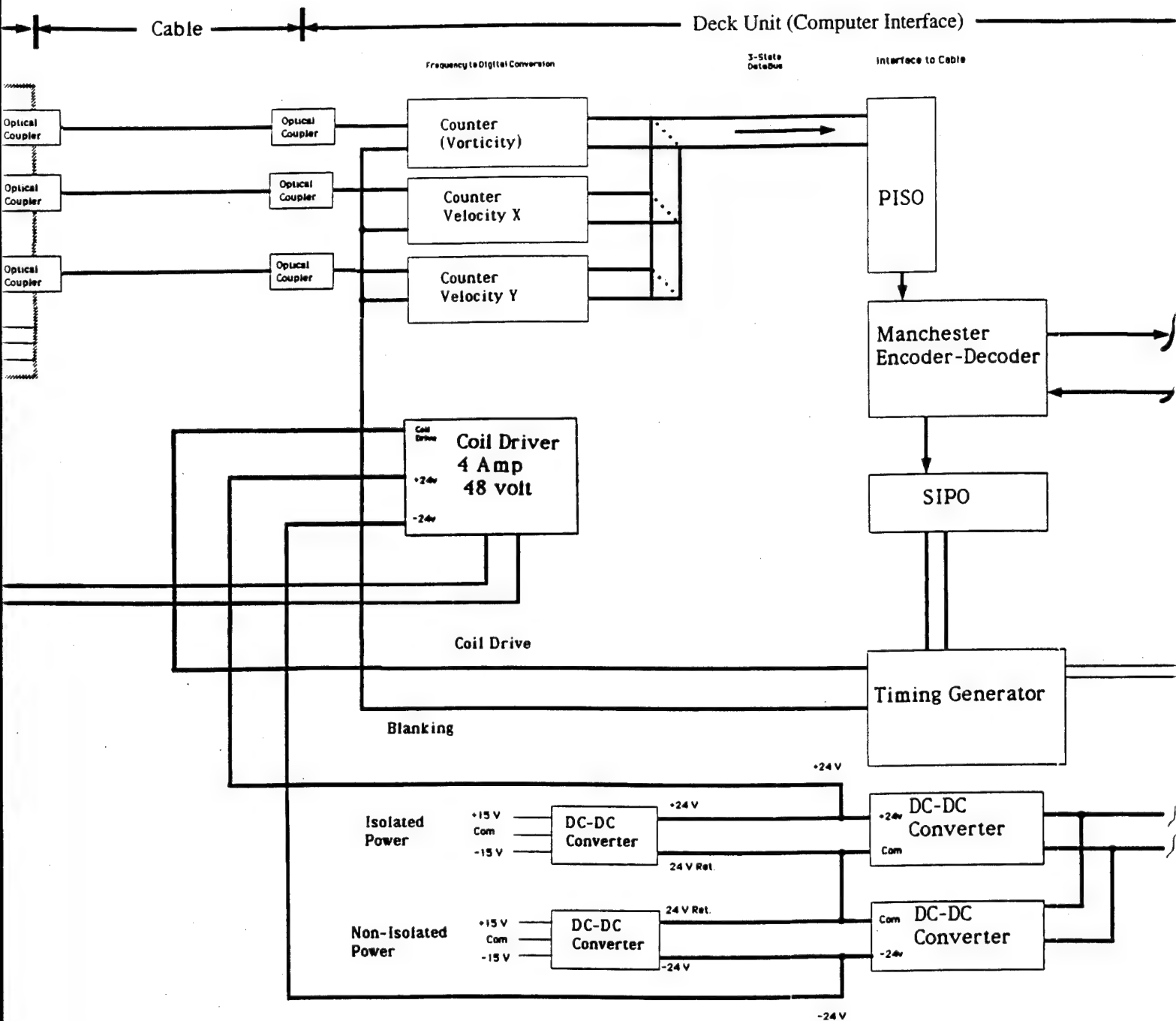
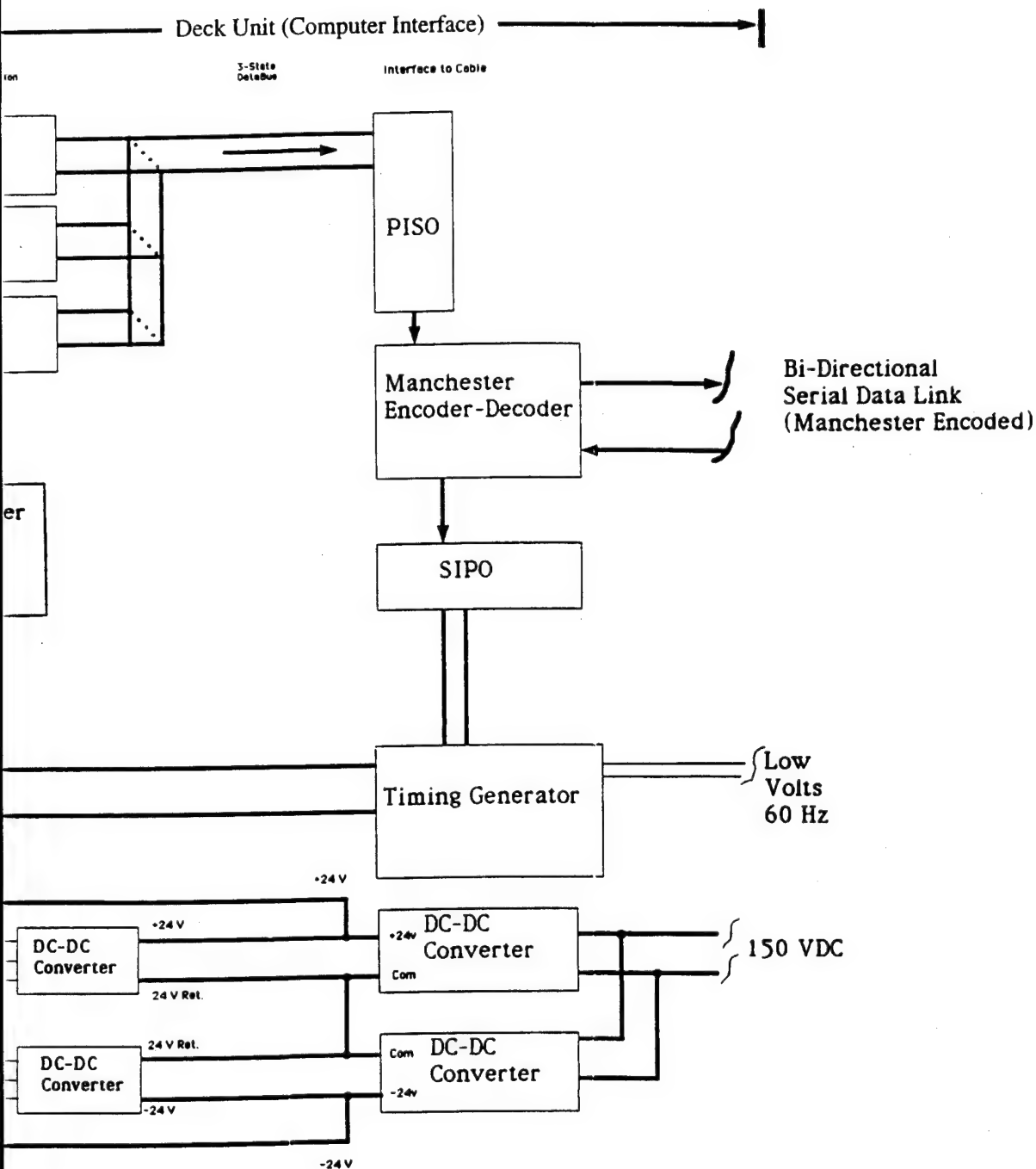


Figure 4.2. Block diagram of the electronics for the fifth version of the EMVM.



the fifth version of the EMVM.

3

ceramic tubes are aligned and equally spaced within ± 0.005 in. To reduce the Johnson noise associated with the resistance of the salt-water bridge formed within the ceramic tubes, we filled them with a water solution of saturated sodium chloride gelled with agarose. The resistance of this solution is about three times lower than that of standard seawater.

Agarose is a polysaccharide isolated from agar, which is derived from marine red algae. We purchase this product as a dry white powder from FMC BioProducts, Rockland, Maine. The agarose is added to the sodium-chloride solution in the amount of 2% by weight. The mixture is stirred, starting at room temperature, and slowly raised to 100°C. After boiling for about 10 min, the solution becomes clear and will gel when cooled to room temperature. The warm, ungelled solution is workable for many minutes when kept on a warm hot plate. The saturated solution forms a salt-crystal skin on the surface if exposed to air owing to evaporation of water. We cover the mixing container to impede evaporation and open it only to extract the ungelled solution as needed.

The procedure for filling the electrode chambers and ceramic tubes was developed over a period of time and is designed to eliminate problems associated with trapped bubbles. After mounting the electrode chambers to the backside of the splitter plate, we fill the electrode chambers with a saturated solution of sodium chloride (no agarose). Next a partial vacuum is drawn from the front side of the splitter plate. This draws the bubbles out from the screw threads and other crevices in the electrode chamber. After the bubbles are removed, the ceramic tubes with their threaded inserts are installed. A chamber filled with a saturated sodium-chloride solution is placed over each ceramic tube and, with the tip of the tube within the solution, a partial vacuum is again drawn. At this point any trapped air, either in the threads or in the sodium-chloride solution, is drawn out through the open end of the ceramic tube. The heated, ungelled agarose and saturated sodium-chloride solution is then inserted into the ceramic tubes with a hypodermic syringe. This must be done carefully so that additional bubbles are not created inside the tube. The ungelled material is injected while the syringe needle is withdrawn slowly and, after cooling, forms a solid plug of gelled electrolyte inside the ceramic tube. The object of this procedure is to produce a bubble-free salt bridge within the tube. While not affecting performance in the test tank, small bubbles collapse under pressure when the instrument is operated in the field. The repeated pressure cycling works the gelled plug loose from inside the ceramic tubes and causes the sensor to fail.

4.2.2 *Splitter plate*

What we refer to as the splitter plate is a flow-splitting plate 20 in. in diameter and 3/4 in. thick. Within the outer 3 in. of the plate's radius, the thickness tapers from 3/4 in. to 0 in., leaving a sharp edge at the outer circumference. The taper is approximately parabolic from the front surface to the back surface, which remains flat out to the edge. The plate is machined from PVC sheet stock. Fiberglass studs glued into blind holes on the back side provide the means for securing the sensor to a plastic flange attached to the coil housing.

4.2.3 Magnets

The electromagnet used with this sensor is a solenoid consisting of 1500 turns of #16 AWG copper wire. The wire was wound on a fiberglass mandrel chucked in a lathe set to turn very slowly. After winding, the coil assembly was potted in electronics grade epoxy potting compound selected for its low water absorption. The epoxy used was Dexter Hysol RE2039/HD3561 mixed in the ratio of 100 parts RE2039 to 30 parts HD3561 by weight. Because the curing process is highly exothermic, castings where the weight of the epoxy is greater than 500 g are not recommended. The encapsulation of the magnet coil required three separate pours. For each pour, the individual components were first debubbled using a vacuum, and after mixing a final vacuum debubbling was performed. The material was then poured into the mold holding the coil and mandrel. The outer diameter of the coil is 11.5 in., the inner diameter is 8.00 in., and the length is 4.00 in. The resistance of the coil is $15.8\ \Omega$, and the inductance is 0.597 H. This coil produces a magnetic field with a strength of 9.5 G/A at a distance of 8.75 in. from the center of the coil, which coincides with the center of our sensor tube array. A map of the magnetic field is found in Figure 4.3. The coil has a time constant (L/R) of 38 ms, which limits the upper frequency at which it can be driven. The maximum frequency of operation is about 2 Hz when using square-wave excitation and requiring that the field remain constant during at least 75% of the cycle.

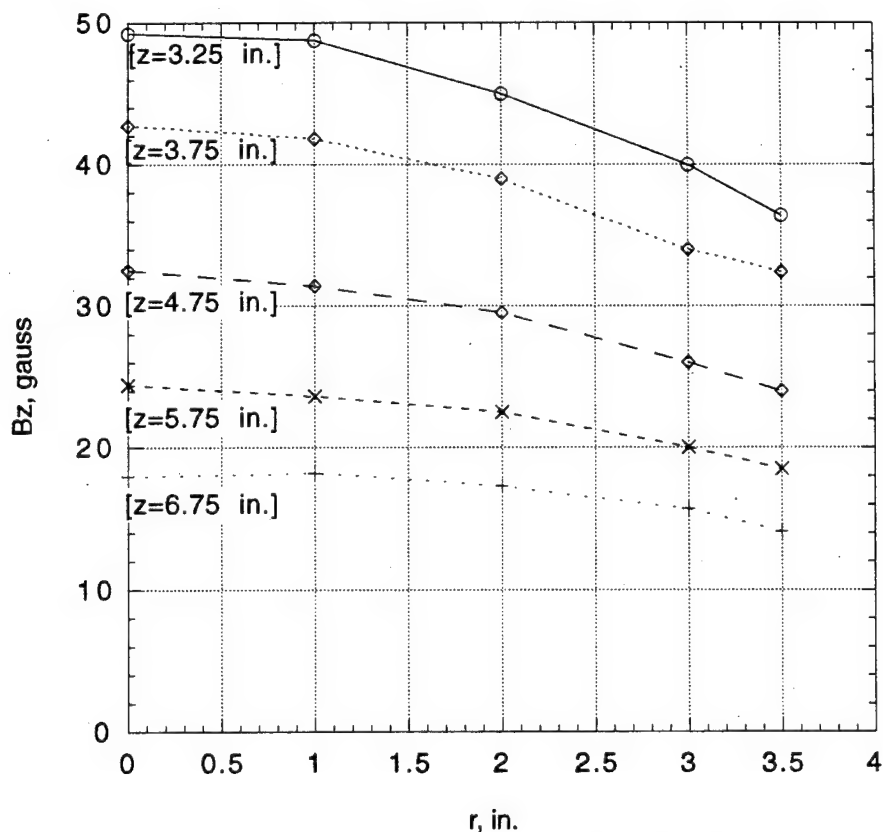


Figure 4.3. Map of the magnetic field of the fifth version of the EMVM, under a 1-A excitation current.

The permanent magnet was assembled from four $6 \times 4 \times 1$ in. ceramic magnets of commercial manufacture. The magnetic material is a sintered barium ferrite ceramic with a magnetic remanence of 2200 G. These magnets are magnetized along their thin dimension, yielding pole faces that are 6×4 in. The maximum field strength measured at the pole face is about 1100 G. This is about half the textbook value for the remanence of this material. The edges exhibited the strongest fields, and the center of the pole face dipped to about 900 G. The magnets were glued together with epoxy (Emmerson & Cummings Ecco Bond 286) which has a very high (2500 psi) shear strength. The individual magnets were held together with wooden clamps while the epoxy was curing. The final result was a magnet $6 \times 8 \times 2$ in. with pole faces 6×8 in. This magnet assembly was placed in a mold whose outside diameter was the same as that of the electromagnet. The magnet was then potted in an epoxy potting compound (Dexter Hysol RE2039/HD3561, 100:30 by weight) to protect it from corrosion. This permanent magnet assembly produces about 140 G at the center of the sensor tube array.

4.2.4 *Electronics, optical links, batteries, and cabling*

The electronics are now separated into three main parts. The computer interface that was used with the previous versions of the instrument remains the same. What had been the underwater cable on the previous version is now much shorter and is a deck cable. The large pressure case that housed the underwater electronics in most of previous versions now sits on the deck. The low-noise preamplifiers and their associated V/F converters have been removed to their own small pressure case. Also inside this small case are a ± 16 -V battery pack and fiber-optic cable drivers and receivers. The fiber-optic cable drivers place four channels of FM data on the underwater fiber-optic cable: One channel for vorticity, two for orthogonal velocity, and one for a low-gain dc-coupled average of the outer four electrode potentials with respect to the center electrode. (The latter is a diagnostic channel used to check the electrodes.) A single fiber-optic receiver provides a synchronization signal for blanking the output of the preamplifier during the switching transient when the electromagnet is used.

The low-noise preamplifiers are the single most important part of the instrument since they determine the noise floor below which the data are no longer visible. A schematic diagram of the preamplifier for a single axis is shown in Figure 4.4. The configuration is a standard three operational-amplifier implementation. The input amplifiers (AD 743s) were chosen for their combination of low voltage noise and low current noise. Since the impedance of the sensor source is about 5000Ω , the amplifier needs this combination of properties to be effective. A comparison of the noise voltage densities of this and some of the alternative amplifiers considered is shown in Figure 4.5. The comparison is somewhat unfair to the Keithley 181 since the noise shown for the other operational amplifiers is for a single amplifier, not an instrumentation configuration. The AD 743 has the lowest total noise at 1 Hz for source impedances greater than 3000Ω . We chose Intersil ID-100 dual diodes for the input overload protection circuitry because of their extremely low leakage current (100 fA). This low current

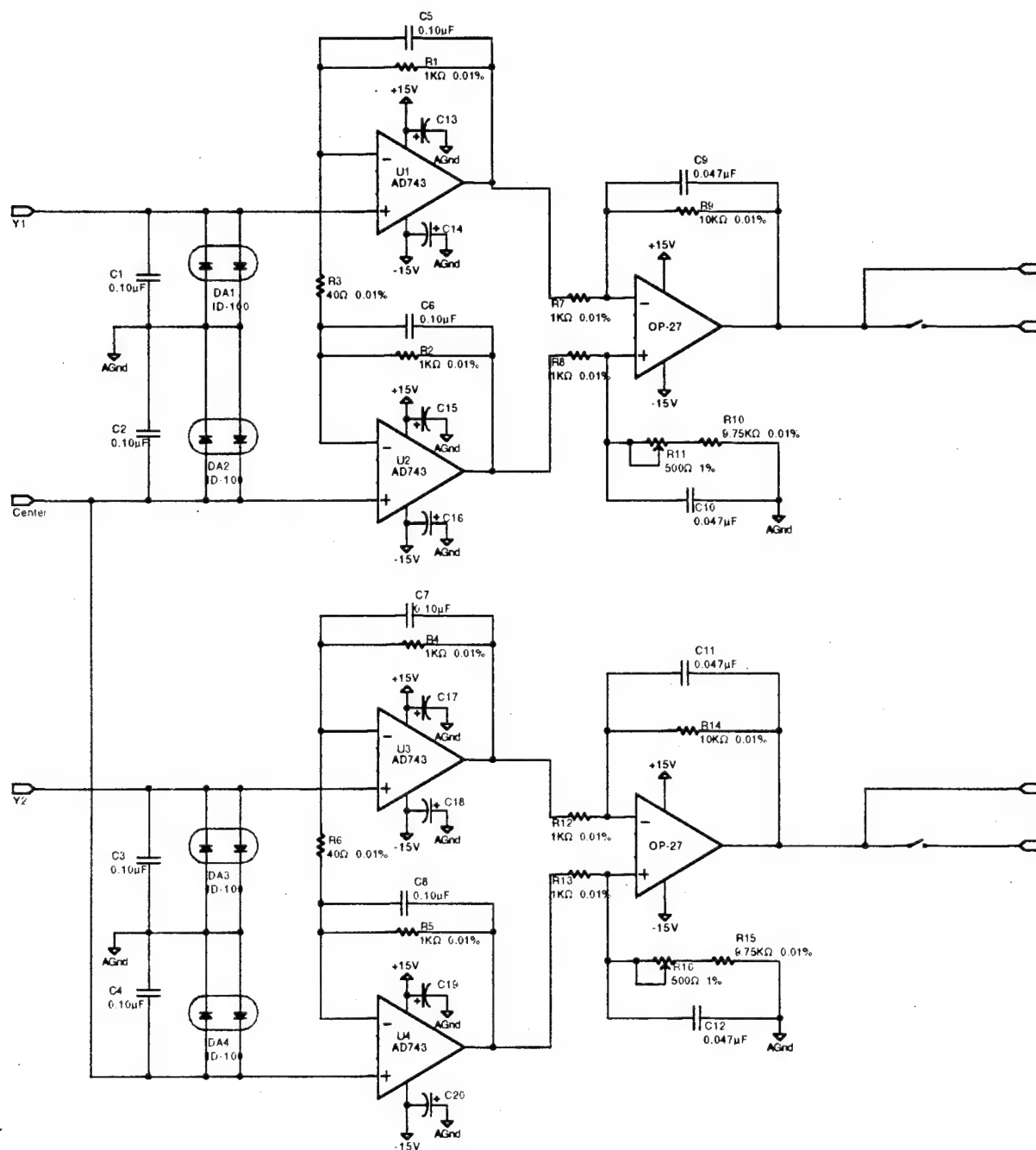


Figure 4.4. Schematic diagram of preamplifier electronics for one of three single-axis channels. Analog Devices AD743 amplifiers were chosen because of their combined low voltage noise and low current noise specifications. The input protection diodes were chosen for their extremely low leakage currents. The potentiometers are adjusted for maximum common-mode rejection at 60 Hz.

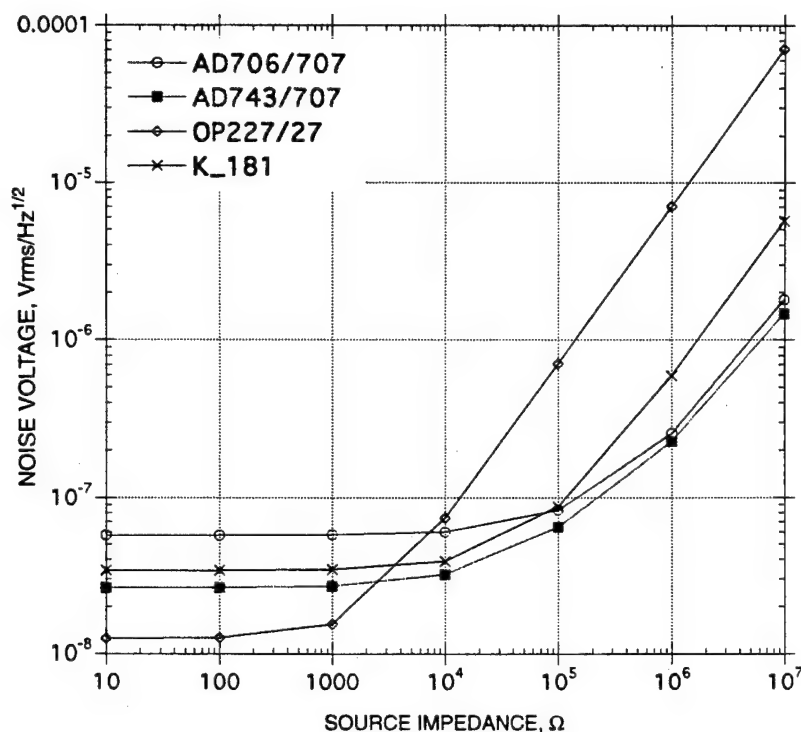


Figure 4.5. Total noise, referred to the input, for three candidate EMVM preamplifiers as a function of source impedance. The source impedance of the EMVM sensors typically ranges from 5×10^3 to $1 \times 10^4 \Omega$.

flowing through the source impedance generates less than 300 pV, well below the voltage noise of the input amplifiers. Provision is made for adjusting the dc common-mode rejection with a balance potentiometer in the second stage. The velocity-induced signals are equal and opposite in sign at the input to amplifiers Y1 and Y2 (see Figure 4.4), and we require these to cancel out for the vorticity calculation. This means that the gains of preamplifiers Y1 and Y2 must be the same. We want to observe vorticity-induced signals that are as small as 1×10^{-4} times the velocity-induced signals. The gain balance required between channels is therefore 1 part in 10^4 . To provide the required gain matching and stability, we have used precision Vishay resistors with a tolerance of 0.01% and a temperature coefficient of 2 ppm/°C. We have chosen a relatively low value of 510 for the overall preamplifier gain so that we can accommodate the large voltages (10 mV) produced by the combination of electrode offset potentials and velocity-induced signals.

The amplified signals are next presented to track-and-hold amplifiers. These amplifiers are synchronized with the coil drive of the electromagnet and hold the preamplifier output starting 16.66 ms before the switching transient and lasting for 150 ms thereafter. The amplifier then switches back and tracks the preamplifier output for the rest of the time. This has the effect of blanking the switching transient from the

next stage, which for vorticity is a summing amplifier and a final, ac-coupled amplifier with a gain of 400. With the switching transient removed, the ac amplifier can be coupled at a much lower frequency. We use a simple one-pole high-pass filter with a corner frequency of 0.05 Hz. For velocity, the output of the track-and-hold amplifiers is ac coupled to differencing amplifiers with a much lower gain. The gain of the differencing amplifiers is only 10 so that the large signals (1 mV per meter per second) present at the electrodes can be accommodated.

The amplified vorticity signals and the two orthogonal velocity channels are next applied to V/F converters. The choice of converters is critical, since a great deal of our earlier problems can be traced to the abnormal but subtle behavior of the previous V/F converters. Our previous problems appeared to be a slight cross-coupling of the velocity and vorticity measurements. It turned out that the output frequency of the converters previously used (Burr Brown VFC 320s) was pulled very slightly toward the operating frequency of the adjacent V/F converter. The effect was small and subtle and proved difficult to correct with the circuit-board layout already in place. Because space is at a premium, it was not possible to separate the converters enough physically to eliminate the problem completely. Our new circuits use VFC 100 integrated circuits also from Burr Brown. The VFC 100 uses a completely different conversion technique. The converter requires an external clock which sets the full-scale frequency to one-half the clock frequency. In addition, output-frequency pulse transitions are forced to coincide with clock transitions. This introduces a considerable amount of phase jitter in the output; as a result, the instantaneous frequency may not be correct, but after many cycles the average frequency is correct. We utilize a single system clock to drive all four V/F converters so that all four converters have outputs with transitions that are synchronous with the same clock. Under these conditions, the converters are not able to influence an adjacent channel, since their output transitions are occurring either at the same time or at times when the adjacent converter is not sensitive. Operating at a clock frequency of 150 kHz, the converters have a center frequency of 37.5 kHz and a deviation of 7.5 kHz/V. The linearity is excellent. The upper panel of Figure 4.6 shows the straight-line transfer function of the converter as measured. The lower panel shows the deviation from a straight-line fit. The deviation is less than 2 Hz from nominal for the entire 70-kHz range.

The output of the V/F converters is a frequency-modulated signal in the 5–75 kHz band. Each of these signals is applied to a fiber-optic cable driver which modulates a 660-nm LED which in turn illuminates the cable fiber. There are five fiber-optic cables, one for each of the three data channels and one for the synchronization/blanking signal. Each cable consists of a plastic fiber 1 mm in diameter and a plastic jacket with an outside diameter of 2 mm. The fiber-optic cable, drivers, and receivers are manufactured by the Hewlett Packard Co. and sold under the name Versatile Link. These components were chosen because of their low cost and their suitability for our low data rates and relatively short distances. Our previous experience with the instrument determined that optical isolation of our underwater sensor unit and the rest of the electronics from the hull of the towing ship was essential.

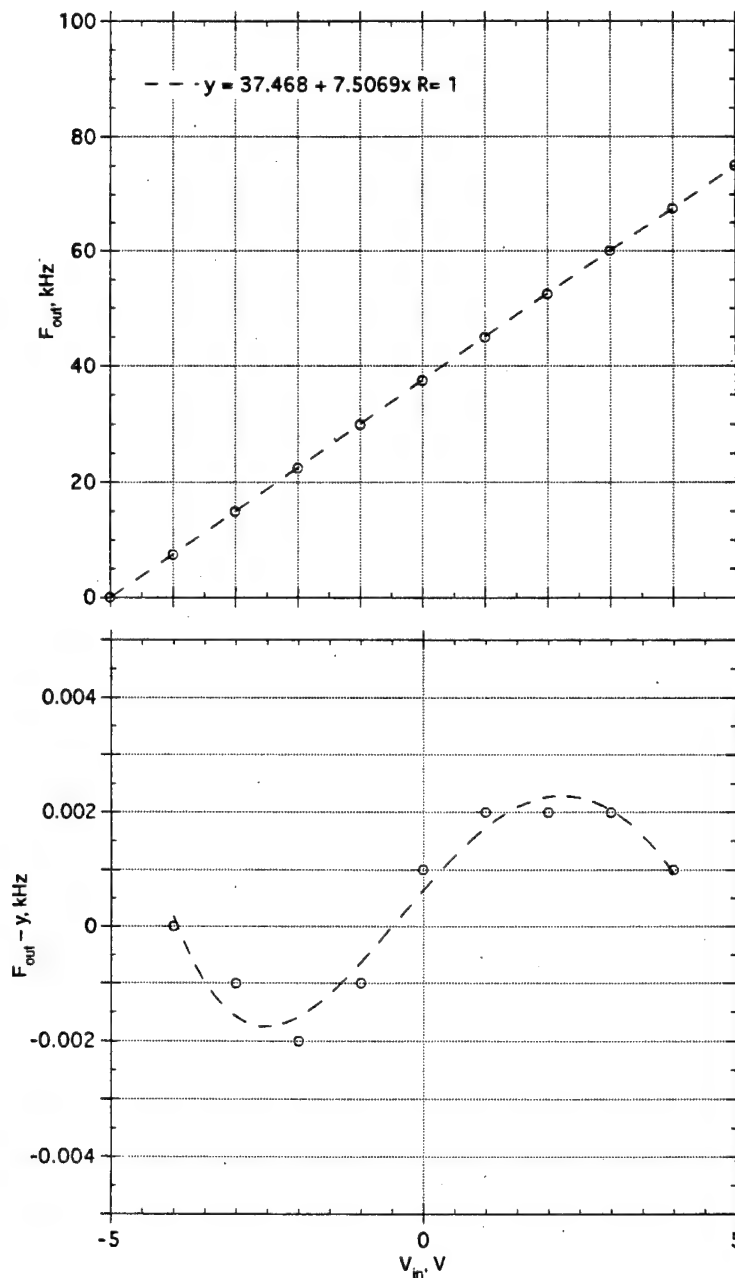


Figure 4.6. Straight-line transfer function of V/F converters (top) and deviation from a straight-line fit (bottom). The upper panel shows calibration data for one of the VFC 100 voltage-to-frequency converters used to FM encode the data for transmission over the fiber-optic cable link. The output frequency is linearly related to the input frequency. The fit to the data is represented by y , which is given at the upper left. The bottom panel graphs the difference between the best-fit straight line and the actual data as a function of input voltage. The worst-case deviation is 2 Hz out of 75 kHz, or 0.003% of full scale.

The four fiber-optic cables are bundled together with the two-conductor neoprene-jacketed cable that supplies the excitation current for the electromagnet coil. An outer sheath of braided plastic fiber provides protection against abrasion while the cable is being handled on deck. The overall diameter of the cable bundle and protective braid is about 0.7 in. In addition, a SpectraTM strength member with an outside diameter of 0.375 in. is attached to the cable bundle. This synthetic line has a working strength of 1000 lb, more than sufficient for either lifting and deploying the tripod or towing the instrument with the fiberglass fairing.

The power source for the underwater unit is a bipolar battery pack of plus and minus 15 V. The capacity of the battery pack is 4.5 A-h. The batteries are of the gelled lead-acid type. These were chosen for their reliability and relatively high energy density. They are easily recharged overnight. An underwater connector provides access to the battery leads for charging purposes. A special jumper plug on the connector is used to switch on the power to the internal electronics.

4.2.5 Pressure vessels, housings, and structures

The main pressure case for the underwater electronics is constructed of 6061-T6 aluminum. It has an outside diameter of 12.00 in., a wall thickness of 0.625 in., and an overall length of 15 in. The endcaps, also constructed of 6061-T6, are 1.90 in. thick. They seal with both a single radial O-ring and a facial O-ring. One endcap has a special penetrator which provides a continuous silver-wire feedthrough for the low-level electrode signals. The other endcap has an underwater connector which supports the fiber-optic cable interface. The fiber-optic cable drivers and receivers are potted in an aluminum tube which is attached to the back of a 24-pin underwater connector. The plastic optical fibers are permanently potted into the driver/receiver assembly, which operates at hydrostatic pressure. The aluminum case and stainless steel fasteners produce a significant amount of corrosion with associated corrosion currents. These currents are not significant when we use the oscillating magnetic field and synchronous demodulation. They are troublesome, however, when we use a permanent magnet for the exciting field and low-frequency ac-coupled amplifiers for making the measurements. This problem was alleviated somewhat by coating the housing with vinyl paint. In the future, this underwater housing will be changed to an all plastic design, perhaps one utilizing glass-filled Delrin.

Several tripods have been constructed to allow the underwater unit to operate at a fixed height off the bottom. The first tripod was constructed of solid steel rod 0.75 in. in diameter. The completed tripod with instrument attached is shown in Figure 4.7. The structure was extremely solid and relied on its mass to keep it from tipping over. During some deployments with this tripod, unexplained noise was present which we felt might be due to corrosion currents associated with the tripod itself. Consequently, the structure was coated with vinyl paint. Later, a second tripod was constructed, this time entirely of

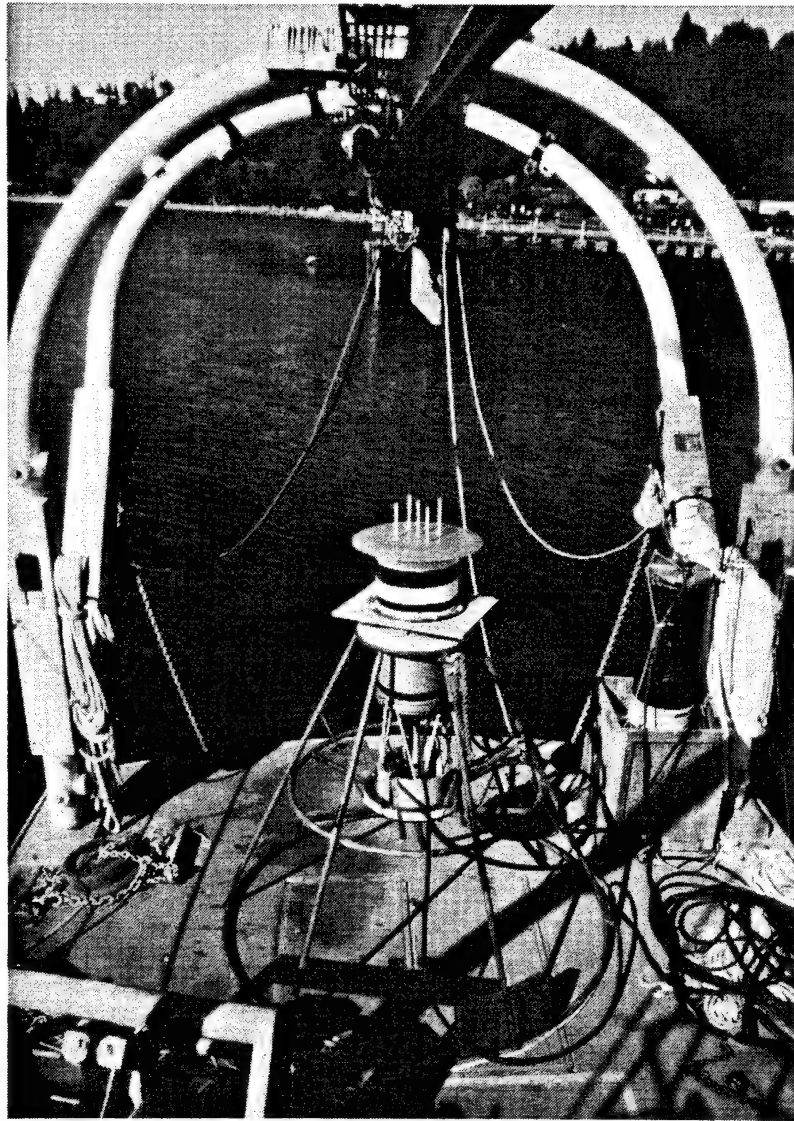


Figure 4.7. The first, all-steel tripod used to place the EMVM near the bottom. The tripod is shown with the fifth version of the EMVM mounted so that measurements of the vertical component of vorticity can be obtained.

composite glass and plastic materials. Joints were constructed with layed-up fiberglass reinforcements and fiberglass bolts. Granite curb blocks, each weighing 100 lb in air, were used at each of the three corners to provide restoring force against tip-over. Figure 4.8 shows this tripod with the instrument attached, sitting on the aft deck of the R/V *Miller*.

This sensor was used exclusively with the GW fairing described in Section 3.5.2. This fairing, previously shown in Figure 3.21, allows towing the sensor in a vertical

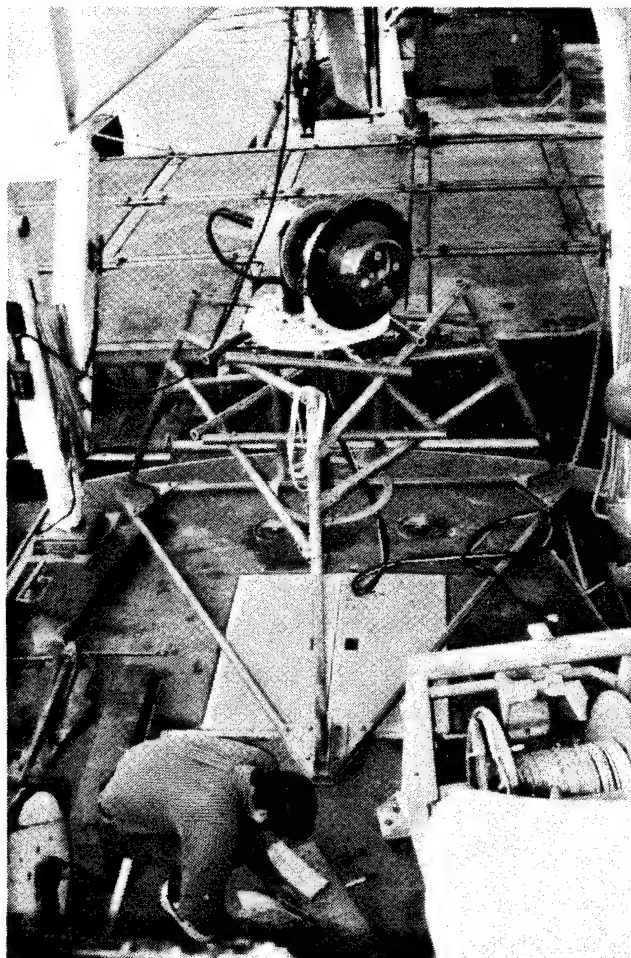


Figure 4.8. All-plastic tripod with fifth version of the EMVM attached. The tripod is sitting on the aft deck of the research vessel R/V *Miller*. The structure is made up entirely of fiberglass. The fasteners are glass-reinforced plastic. The ballast weights (not shown) were granite blocks that weighed about 150 lb in water. This construction technique was chosen to eliminate the generation of electric fields due to corrosion of the tripod.

upright position only. The size and shape of the fairing were dictated by the original underwater sensor and electronics, which were much larger. No provision was made to tow the sensor horizontally, since it was envisioned that the Seasoar tow body would supplant this fairing. However, this fairing remains in use to this date because it provides lower vehicle vibration levels at low (<2.5 kn) tow speeds.

4.2.6 Shipboard electronics

The EMVM electronics are separated into three main assemblies. The first, containing the battery-isolated preamplifiers and V/F converters, is in the small underwater housing previously described. What we now call the deck electronics was previously underwater with the preamplifiers. Now mounted on the deck, it performs the frequency

digitizing and digital data buffering and creates the asynchronous, bit-serial, Manchester-encoded data stream that is sent over a twisted pair to the computer interface. It also provides all the necessary timing signals and power drivers for driving the electromagnet. Several auxiliary sensors are housed with these electronics, including a triaxial force-balance-accelerometer set, an angular rate sensor, and a compass. A block diagram of the deck electronics is shown in Figure 4.2.

The data rate is adjustable via software programming of the timing generator; however, we have settled on using a basic data rate of two samples every 1.067 s. One of these samples is taken while the north of the applied magnetic field is pointed up; the other is taken when the field is reversed. Since an up and a down measurement are required to generate an estimate of vorticity or velocity, this yields a new data point every 1.067 s. The timing generator also provides a variable blanking period during which the FM data from the underwater unit are ignored. This is used to blank out the transients that occur when the magnetic field switches direction. The transients are produced in whatever residual loop area is left in the sensor wiring. After the blanking time, the counters used to digitize the FM data are gated on for an exact multiple of the 60-Hz line frequency period. This has the effect of integrating the signals over an n -cycle period of the local 60-Hz field. Signals present in the system at the 60-Hz line frequency are greatly rejected. This allows us to test the instrument in the laboratory where large 60-Hz electric fields are present. The same data rate applies to all data channels, of which there are 17 plus a synchronization word. The total is then 36 16-bit words every second. These data are applied to an asynchronous, serial Manchester adapter. These bit-serial data are clocked out over a twisted pair of wires at 100 kbit/s. The twisted-pair drivers and receivers for this serial link are transformer coupled to the line at each end, thereby reducing common-mode noise and grounding problems.

The computer interface consists of two parts: the serial Manchester decoder with 4096 word FIFO buffer, and a 16-bit parallel I/O interface with proper handshaking logic for an HP-9020 computer. The 4096-word FIFO provides roughly 100 s of data-buffering capacity in the computer interface. This may seem like an extreme amount; however, we originally anticipated having a data rate 15 times faster. The HP-9020 runs UNIX, which is not designed to be a real-time operating system. Consequently, there can be periods of up to several seconds when the computer is unable to service the data-acquisition task. The buffering allows the computer to be occupied with other tasks while the data are saved in the interface unit.

4.3 Performance Evaluation

4.3.1 Sensitivity and self-noise in APL test tank

Many tests have been conducted in which the sensor was operated underwater in a salt-water test tank measuring 6 ft \times 8 ft \times 4 ft deep. This tank is wooden framed with a fiberglass liner. It is electrically nonconducting and is isolated from ground by virtue of resting on a polyethylene plastic sheet 1/8 in. thick which in turn sits on a smooth, flat concrete floor. The tank is fitted with a movable carriage which can translate the full

length of the tank, one on each side of the 6-ft dimension. The plenums extend to the full depth of the tank. Each is drilled with 80 small holes in a regular pattern on its inner face. The interior volume of each plenum houses a very large silver/silver-chloride electrode which can be driven with up to 20 mA of current. This arrangement provides a uniform transverse electric field of known magnitude.

Figure 4.9 shows the noise level achieved in the test tank with the instrument submerged to the back of the splitter plate. No signals were being injected via the plenums. The water was extremely still, having been left undisturbed for several hours after the instrument was placed into the tank before data were collected. The upper panel shows the vorticity time series for 120 s of data. The rms variability of the signal over the 120-s window is $1.9 \times 10^{-3} \text{ s}^{-1}$. The largest part of the signal is a slow drift upward after 30 s into the test. The lower panel shows the power spectrum of vorticity for the same interval.

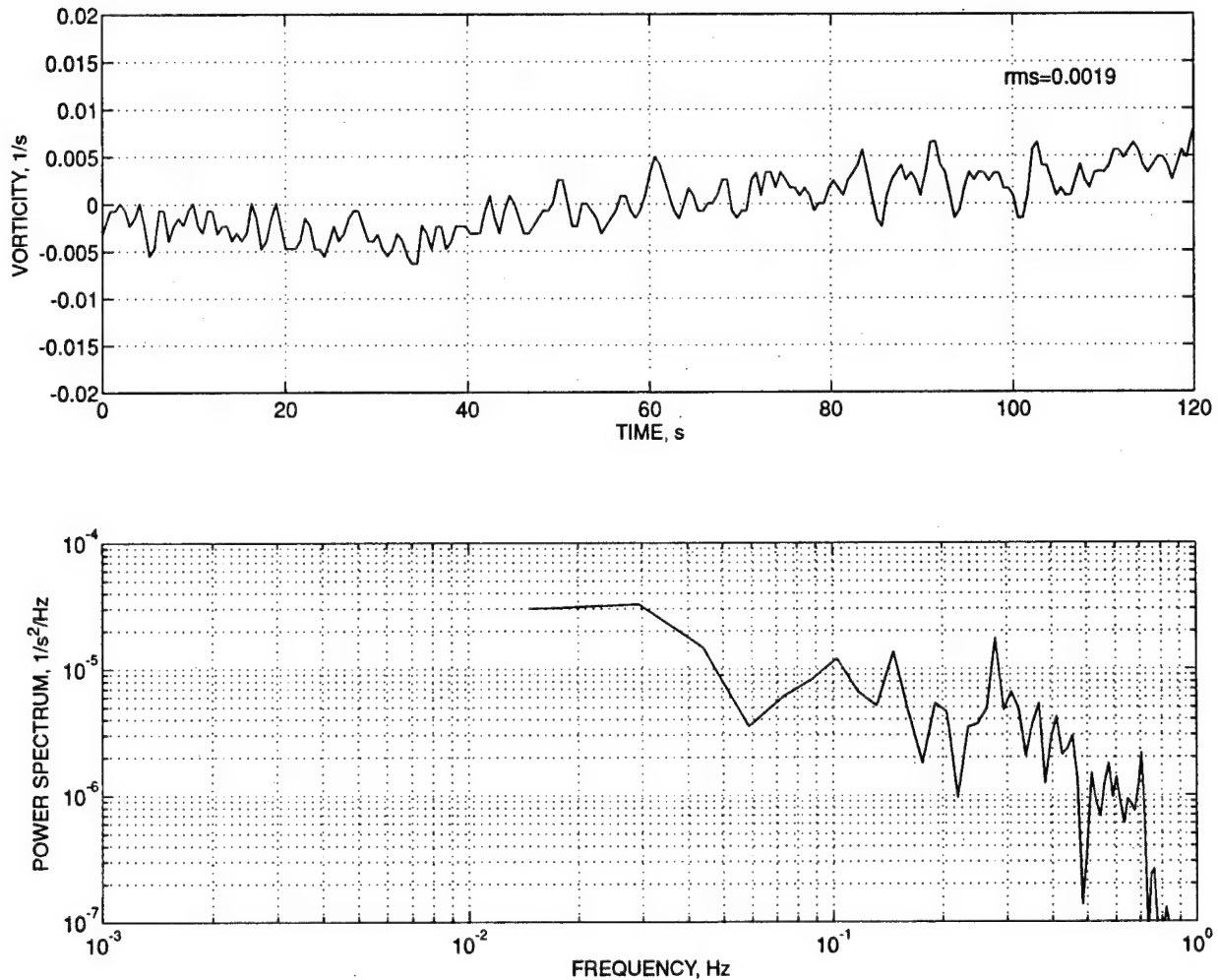


Figure 4.9. Fifth version EMVM noise levels in still water. The upper panel shows a time series of vorticity from the EMVM while it was operated in still water in an electrically isolated all-plastic test tank. The lower panel shows a power spectrum of the data from the upper panel.

4.3.2 Summary of low signals in Puget Sound experiments (upper bound on noise)

Several tests were conducted in Blakely Harbor, a small, shallow inlet in Bainbridge Island on Puget Sound. The inlet measures 0.4 n.mi. across at its mouth and tapers back to 0.1 n.mi. at a point 0.8 n.mi. inside the harbor. The depth is about 70 ft at the mouth and shallows up to 6 ft at a point 0.8 n.mi. inside the harbor. The bottom on the inner third of the harbor is smooth and sandy. Some of our quietest *in situ* data have been acquired at this location. Figure 4.10 shows a power spectrum of vorticity for data taken on 14 December 1990. The quietest 300 s of data from the ebb flow portion of the deployment were used. The mean velocity of water flowing past the tripod-mounted sensor during this time was 0.08 m/s. The vorticity signal level is two orders of magnitude greater than that observed in the still water of the test tank.

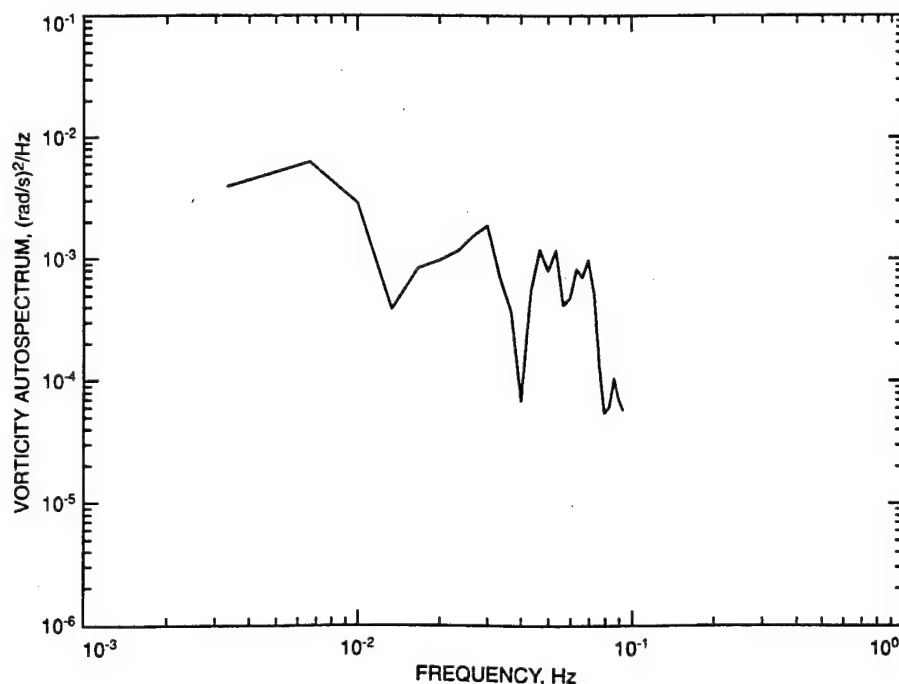


Figure 4.10. Power spectrum of vorticity data taken in a quiet location in Puget Sound on 14 December 1990. The raw data were filtered to remove the effects of intermittent spikes (similar to those shown later in Figure 5.2). The raw data were filtered with a median filter whose length was 10 points of the original raw-data time series. The filter window was then slid by five data points, and the 10-point median again calculated. The output median-filtered time series has a data rate of 1/5th the original sample rate. Since the original sample rate was 0.9375 Hz, the median-filtered data rate is 0.1875 Hz. This makes the Nyquist frequency for the spectrum of Figure 4.10 equal 9.375×10^{-2} Hz. The quietest 300-s portion of the ebb flow from a tripod-mounted deployment in Blakely Harbor was used. During this time, the mean flow past the sensor was 0.08 m/s. The spectral levels are two orders of magnitude greater than those observed when the instrument was operated in the still water of a test tank.

5. OBSERVATIONS OF VORTICITY IN PUGET SOUND

The present sensor system was used to observe background levels of natural vertical vorticity at various sites in Puget Sound during 1990 and 1991. (Earlier EMVM deployments were used to estimate instrument performance.) These observations were designed to study the strength and distribution of vorticity in strong tidal flow, in a protected harbor, and in the wake of an island or a promontory.

The principal measurement sites are shown in Figure 5.1. Point Jefferson is at the northeast entrance to the bight of Port Madison. Blakely Rock is on the east side of Bainbridge Island near the entrance to Blakely Harbor. Restoration Point and Decatur Reef are off the southeast extremity of Bainbridge Island. Toliva Shoal is in the middle of Puget Sound off Fox Island southwest of the Tacoma Narrows.

5.1 Point Jefferson

On 13 December 1990, the EMVM was deployed off Point Jefferson on a steel tripod which rested on a sandy bottom about 0.3 n.mi. offshore at a depth of 43 ft. The instrument was put on the bottom just after slack water at high tide, and about 2 hours of data were taken during the ebb flow. The flow was from the west, and the rms vorticity variability was quite high during the entire deployment. Figure 5.2 shows a representative time series for the 13 December 1990 deployment at Point Jefferson.

The data from this deployment (and the one the next day at Blakely Rock) were contaminated with random intermittent spikes. These spikes occurred relatively infrequently (one to two per minute) and mostly when the instrument was cold. It was later discovered that the cause of these spikes was an intermittent phase-lock condition between two or more of the V/F converters. A circuit utilizing newer V/F integrated circuits was designed, constructed, and used for the subsequent deployments off Point Jefferson during mid-February 1991. No spiking was observed at any time during these deployments.

For the February deployments, the EMVM was mounted on a steel tripod which rested on the bottom of Puget Sound at a depth of about 50 ft. Data were collected on three days for about 6.5 hours each day.

The first of the three deployments was on 7 February about 0.33 n.mi. offshore in water 45 ft deep. The instrument was put on the bottom just after slack water at high tide. About 6.5 hours of data were taken during the ebb flow. The flow was from the west, and the rms vorticity variability was quite high during the entire deployment.

The instrument was operated with the oscillating electromagnet field, and the sensor assembly consisted of an array of thin ceramic tubes filled with a gelled agarose and concentrated sodium-chloride solution. These were the smallest diameter tubes used to date and were only 0.10 in. in outside diameter.

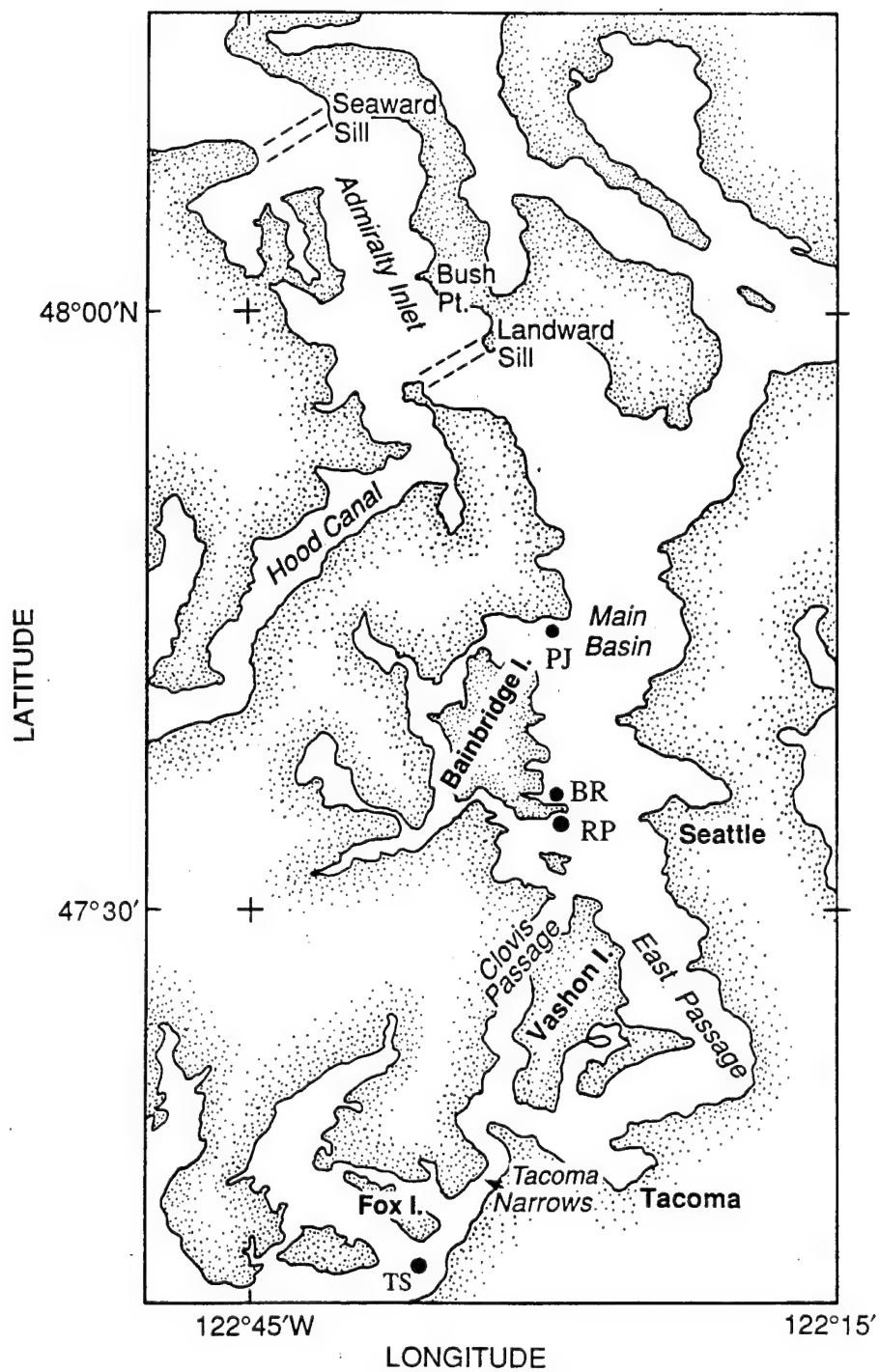


Figure 5.1. Map of Puget Sound with EMVM field operations marked as large dots. PJ = Point Jefferson; BR = Blakely Rock; RP = Restoration Point/Decatur Reef area; TS = Toliva Shoal.

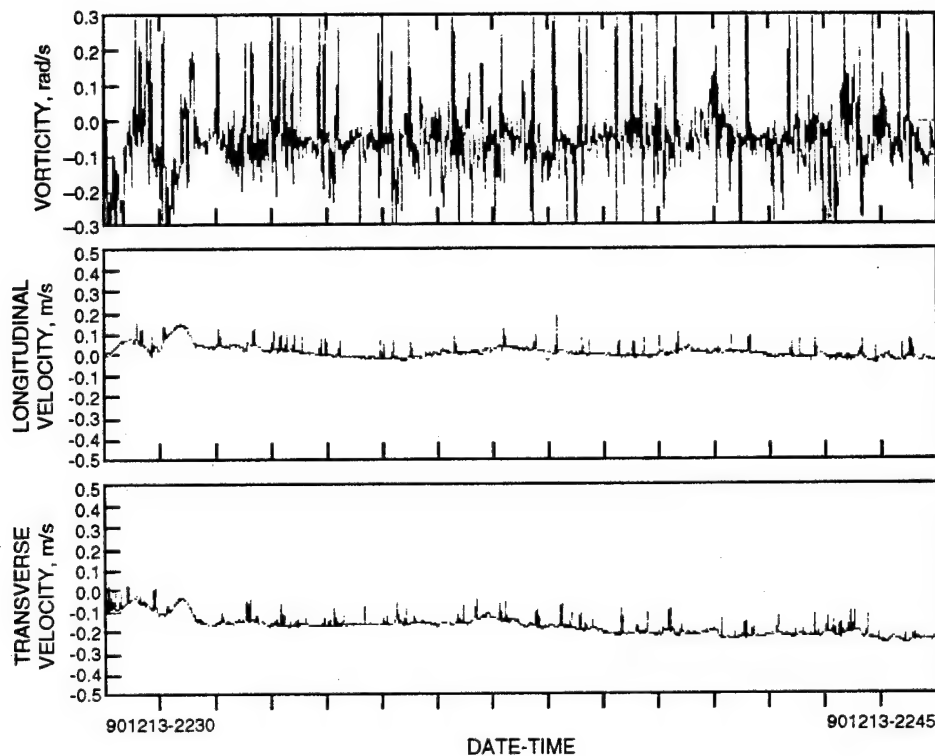


Figure 5.2. Time series of data from a deployment off Point Jefferson showing random intermittent spikes. The spiking was caused by a phase-lock condition between two or more of the V/F converters. The upper panel is vertical vorticity, the center panel is current direction (CW from north), and the bottom panel is current speed. Time scale is in two-digit units indicating from left to right, year, month, day - hour, minutes, seconds (UTC).

On 8 February, the instrument was deployed at nearly the same spot as the previous day and a depth of 38 ft. The instrument was deployed during slack water at high tide, and 6.5 hour of data were recorded mainly during the ebb flow from the west.

For this deployment, the sensor assembly was changed to one having no ceramic tubes. Instead, the measurement ports were flush with the large-diameter plastic plate separating the sensor head from the rest of the instrument.

The third deployment, on 11 February, was at the same location off Point Jefferson in 44 ft of water. During this deployment, the instrument was again operated with the ceramic tubes, but a permanent magnet was installed in place of the electromagnetic coil. The strength of the magnetic field generated at the sensor array by the permanent magnet was about three times the peak amplitude produced by the electromagnetic coil. About 4 hours of data were collected, starting at slack water at low tide and including about 3 hours of observations during the flood flow. The processing software was changed to accommodate the lack of signal chopping. The signals were ac coupled after the low-noise preamplifiers, providing a rolloff below 3×10^{-2} Hz.

Figure 5.3 compares the power spectra for the different magnet configurations. The solid line represents the spectrum produced from 2 hours of data taken when the electromagnet coil was energized. The dashed line represents 2 hours of data taken when the instrument was operated with the permanent magnet. Because the signal is not synchronously demodulated with the instrument in the permanent-magnet configuration, we expect a rolloff of the signal at a frequency of 0.03 Hz. For this comparison, an attempt was made to use data taken under similar environmental conditions. It is encouraging that the spectral levels are comparable over a wide range of frequencies, down to and including the roll-off point. Since there is no excess noise at low frequencies in the permanent-magnet data, we may be able to lower the roll-off frequency in the electronics without having problems with excess noise due to electrode drift. Lowering the low-frequency cut-off point in the electronics should be relatively easy and would increase the measurement bandwidth.

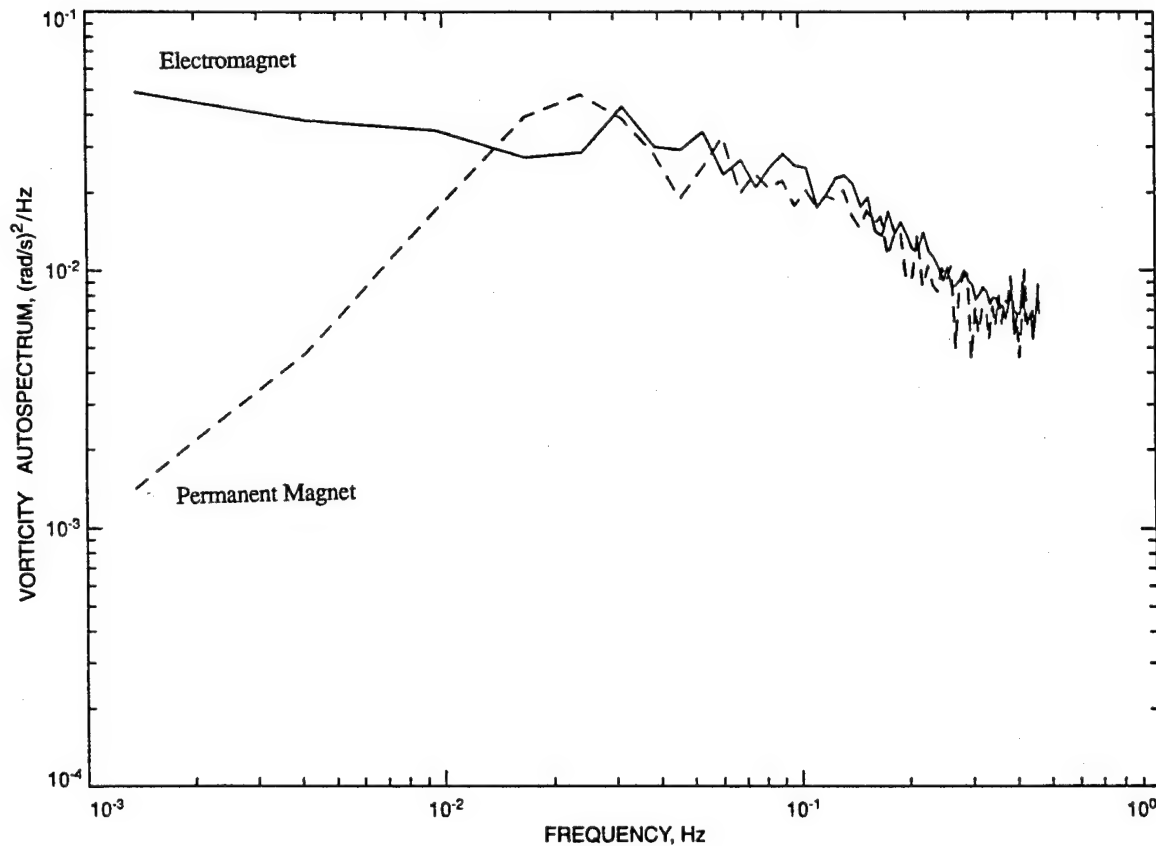


Figure 5.3. Comparison of spectra obtained during two different deployments of the EMVM on a tripod in Puget Sound. A different electronic configuration was used for each deployment. The solid line is the spectrum of vertical vorticity when an electromagnet was used. The dashed line is the spectrum when a permanent magnet and an electronic rolloff at 0.03 Hz were used.

Figure 5.4 compares the spectra obtained with the ceramic straws in place and with the straws removed and replaced with small orifices mounted flush with the splitter plate. Again, an attempt was made to use data taken under similar environmental conditions. The flush-mounted configuration seems to have excess energy at frequencies greater than 0.10 Hz. This may be due to fluctuations in the boundary layer flow. A flush-mounted sensor is desirable from the standpoint of mechanical integrity, but if the excess noise above 0.1 Hz is due to boundary layer fluctuations, then this configuration is unacceptable. More deployments will be needed to determine whether the spectra continue to exhibit high levels at 0.01 Hz and higher.

Figure 5.5 shows two spectra taken during the same deployment; the lower one was with the electromagnet turned off and the upper one with it turned on. There is a difference of nearly two orders of magnitude (in power) between the two. The spectral level of the lower trace is somewhat larger than had been observed *in situ* during previous deployments. We believe this is because the data used for this spectrum were taken just after the instrument reached the bottom, and the electrodes were still coming to equilibrium.

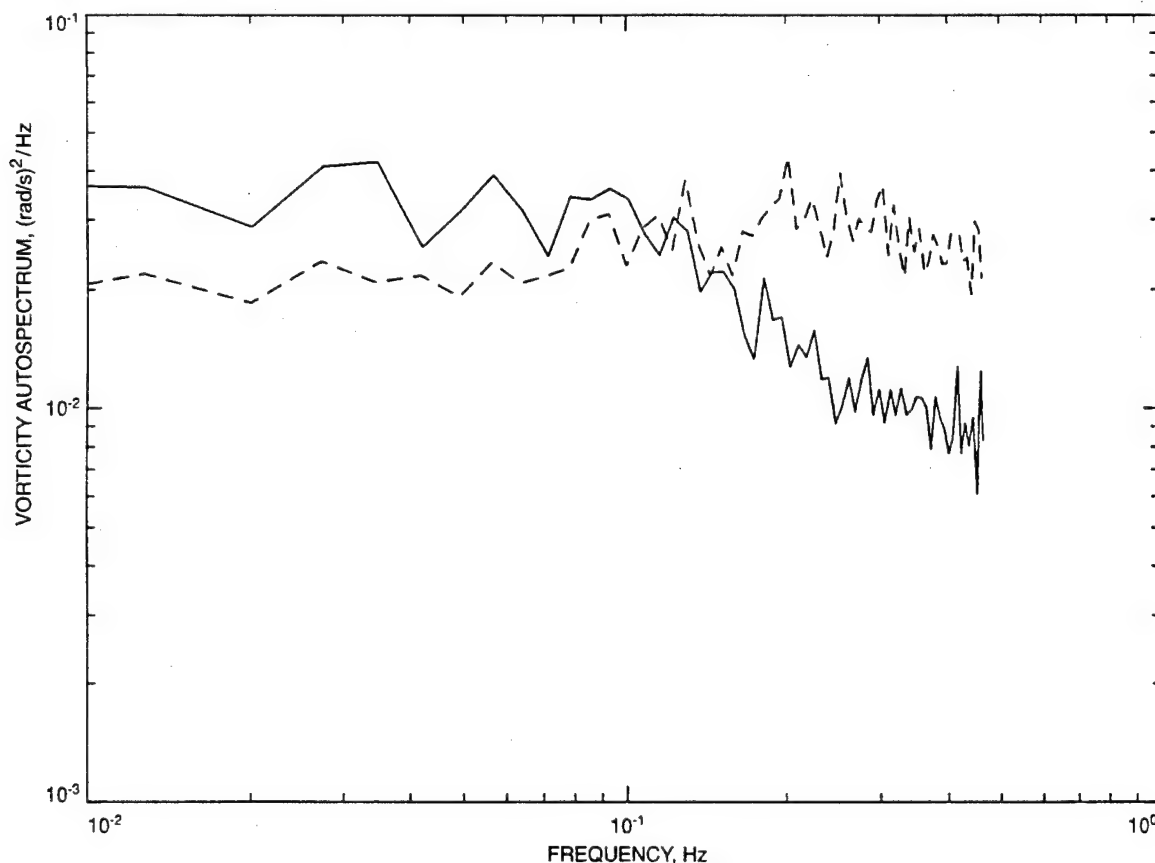


Figure 5.4. Comparison of spectra obtained from the EMVM when two different electrode port configurations were used: one flush mounted (dashed line) and one at the ends of ceramic straws (solid line).

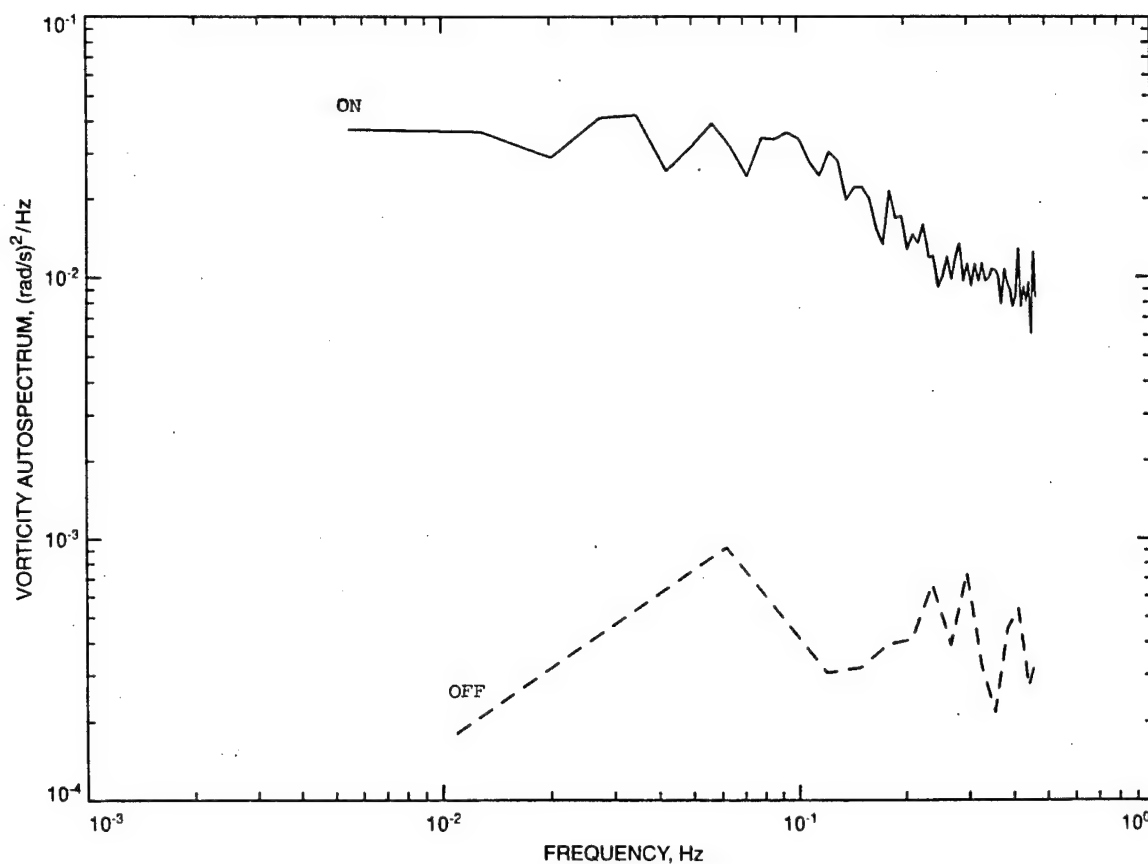


Figure 5.5. Comparison of spectra obtained from the EMVM with the electromagnet turned on and with it turned off.

5.2 Blakely Rock and Blakely Harbor

The EMVM was deployed 6 ft off the bottom on a tripod at a depth of 46 ft in Blakely Harbor, Bainbridge Island, on 14 December 1990. The purpose of this deployment was to obtain observations in waters less influenced by direct tidal flow than the measurements at Point Jefferson the previous day. The instrument was deployed during the flood tide, and the 4-hour record spans 1.5 hours before slack water at the high tide and 2.5 hours after. Both flood and ebb flows were observed, with velocities up to 0.18 m/s measured during the beginning of our observation of the flood flow. Figure 5.6 shows the entire 4-hour record. The upper panel shows the vorticity time series. The first 10 min of the record are quiet because a plastic shroud covered the sensor and protected it from motion of the ambient water. The mean vorticity during the shrouded operation is about 0.1 s^{-1} . This is due to an offset in the instrument and has not been removed. Divers removed the shroud *in situ* and calibrated the sensor by rotating it through a known angle several times. The rms vorticity was $1.6 \times 10^{-2} \text{ s}^{-1}$ during the flood flow and $8 \times 10^{-3} \text{ s}^{-1}$ during the later part of the ebb flow. Thus the rms vorticity observed during the flood flow is at least twice that of the ebb flow. During the flood flow, water is advected from the mouth of Blakely Harbor and Puget Sound where more activity is

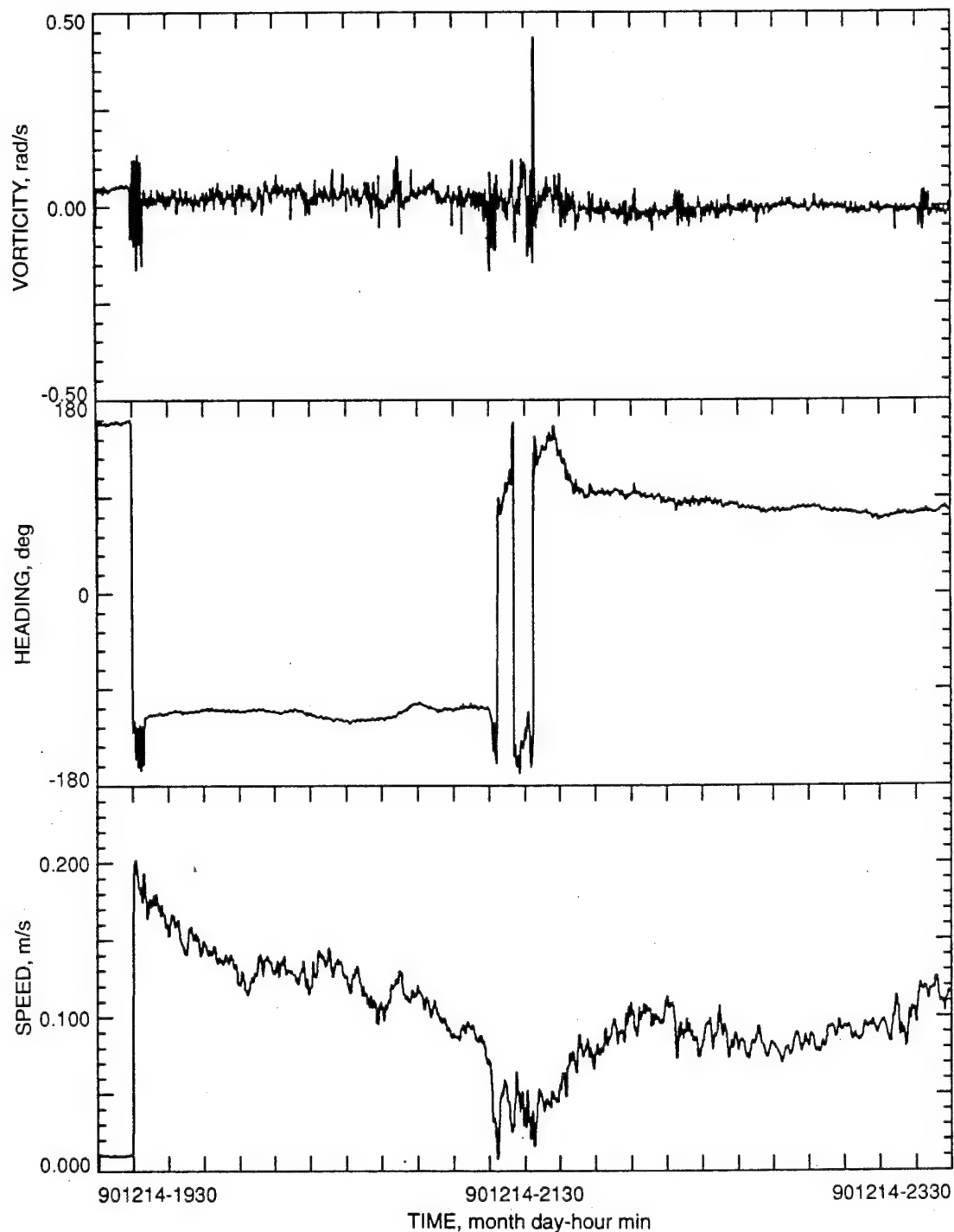


Figure 5.6. Data taken with the EMVM deployed on a tripod at a depth of 15 m in Blakely Harbor. The upper panel shows the vorticity time series for the first 4 hours of deployment. There was a flood flow during the first 2 hours which tapers off and becomes slack water at the high tide. The middle panel is the flow direction measured CW from north. The bottom panel shows the flow speed past the sensor. The flow shows a dramatic decrease at 2120 UTC near the middle of the record. The ebb flow slowly builds toward the later part of the record. The quietest part of the record occurs during the ebb flow, when water that was sitting in the inner reach of the harbor was flowing past the sensor.

expected. The middle panel shows the direction that the water was flowing with respect to the sensor head. The direction becomes quite variable during the 20 min or so of slack water at the middle of the record. The bottom panel shows the water velocity relative to the sensor. The highest velocity observed is 0.2 m/s at the beginning of the deployment during the flood flow. Although the tides cause flow into and out of the harbor, the flow was less energetic than that off Point Jefferson. The tripod provides the most stable platform for the instrument, and observations from it are thought to exhibit the lowest noise level. These observations are compared with later ones obtained by towing the EMVM in the harbor.

The EMVM was towed around Blakely Rock and Blakely Harbor for several days in mid-April 1991. The instrument was housed inside a fiberglass fairing with the sensor end protruding about 1 ft below the tow body. The instrument was towed behind the R/V *Miller* at low speeds (2.5 kn) and a depth of 25 to 30 ft. The tows were primarily in a straight line from within Blakely Harbor to a point within several hundred yards of Blakely Rock and out into the central portion of Puget Sound adjacent to Elliot Bay. The first tows, on 16 April 1991, were to the south of Blakely Rock, as we were observing during a flood flow (i.e., south-flowing current). The tows on 17 April were to the north of the rock, as we were observing during an ebb flow. During this series of deployments, a vehicle dynamics package intended to evaluate the Seasoar tow body was attached to the GW fairing for the EMVM. In addition, an Eagle 8 GPS receiver was installed on board R/V *Miller*, and position data were logged at a 1-Hz rate.

For the tows on 16 and 17 April, the EMVM was operated with the electromagnet and with ceramic sensor tubes 0.10 in. in diameter extending 2.5 in. beyond the splitter plate. These tubes were 1 in. shorter than in previous deployments. This change was made because the longer tubes were extremely fragile, often breaking after only 15 min of towing. Because the measurements made in February with the flush-mounted sensor ports produced higher noise levels, we decided to try an intermediate-length tube to gain durability without sacrificing noise performance. An *in situ* calibration was performed at the end of the second day of operations, in which we rotated the instrument while it was suspended from the overhead hoist off the aft end of R/V *Miller* while the vessel drifted slowly in Blakely Harbor. Even though we were not under way, there was an increase in the vorticity noise level, presumably because of interference from electric fields associated with the zinc anodes and the bronze propeller.

Figure 5.7 shows a time series of the vorticity data for the first 4 hours of towing near Blakely Rock on 16 April. The lower panel shows the vorticity corrected for yaw rate and bandpass filtered as a function of time. The upper panel shows the rms vorticity variability computed over 20-s windows. During the least active portions of the tow, the rms variability was slightly less than $5 \times 10^{-3} \text{ s}^{-1}$. This is slightly lower than what was achieved with the sensor mounted on a tripod moored at the bottom of Blakely Harbor. The quietest rms vorticity levels observed on the tripod during the 14 December 1990

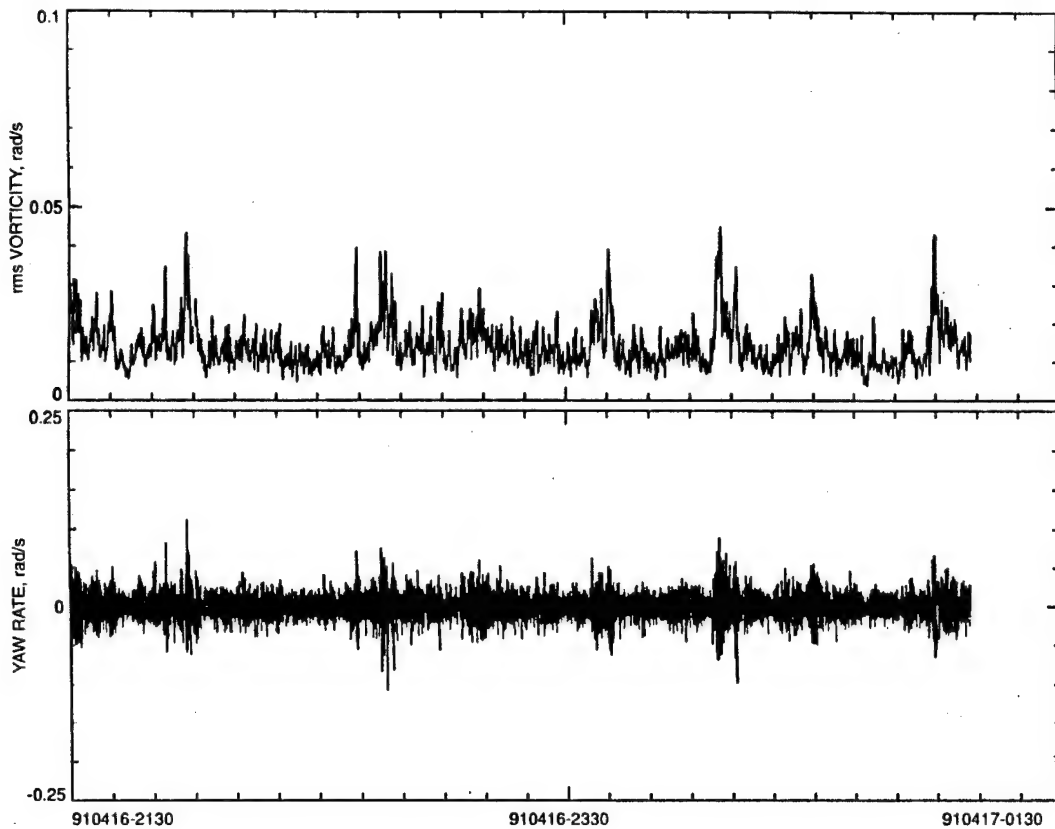


Figure 5.7. Data from the EMVM towed with the GW fairing on 16 April 1991 in the wake of Blakely Rock. The lower panel shows vorticity corrected for yaw rate and bandpass filtered as a function of time. The upper panel shows the rms vorticity computed over 20-s windows. There are several instances where the rms vorticity was $> 0.04 \text{ s}^{-1}$ while traversing the wake.

deployment were $8 \times 10^{-3} \text{ s}^{-1}$. Figure 5.7 shows six separate events when the rms variability is greater than $4 \times 10^{-2} \text{ s}^{-1}$. The most active event has an rms variability of $4.5 \times 10^{-2} \text{ s}^{-1}$. These events occurred when the sensor passed just south of Blakely Rock. The wake of the rocks was to the south, as we were towing during flood flow of the tidal cycle. Figure 5.8 shows the tide heights for Restoration Point on 16–18 April 1991. The heights at the times that we were towing have been highlighted.

Figures 5.9 through 5.16 show vorticity variance computed for 20-s intervals from data taken on 16 April. The vorticity variance is plotted as a variable-sized dot whose center corresponds to the latitude and longitude of the average position for that particular interval. The largest dots correspond to a vorticity variance of $3 \times 10^{-3} \text{ s}^{-2}$, the smallest dots to a variance $\leq 2 \times 10^{-5} \text{ s}^{-2}$. It can be seen from these plots that, in addition to the large spatial variability associated with Blakely Rock, there is a temporal variability which is not entirely explained by the variation in mean flow due to tidal forcing. In addition to the area just south of the rock, there is another area with elevated vorticity

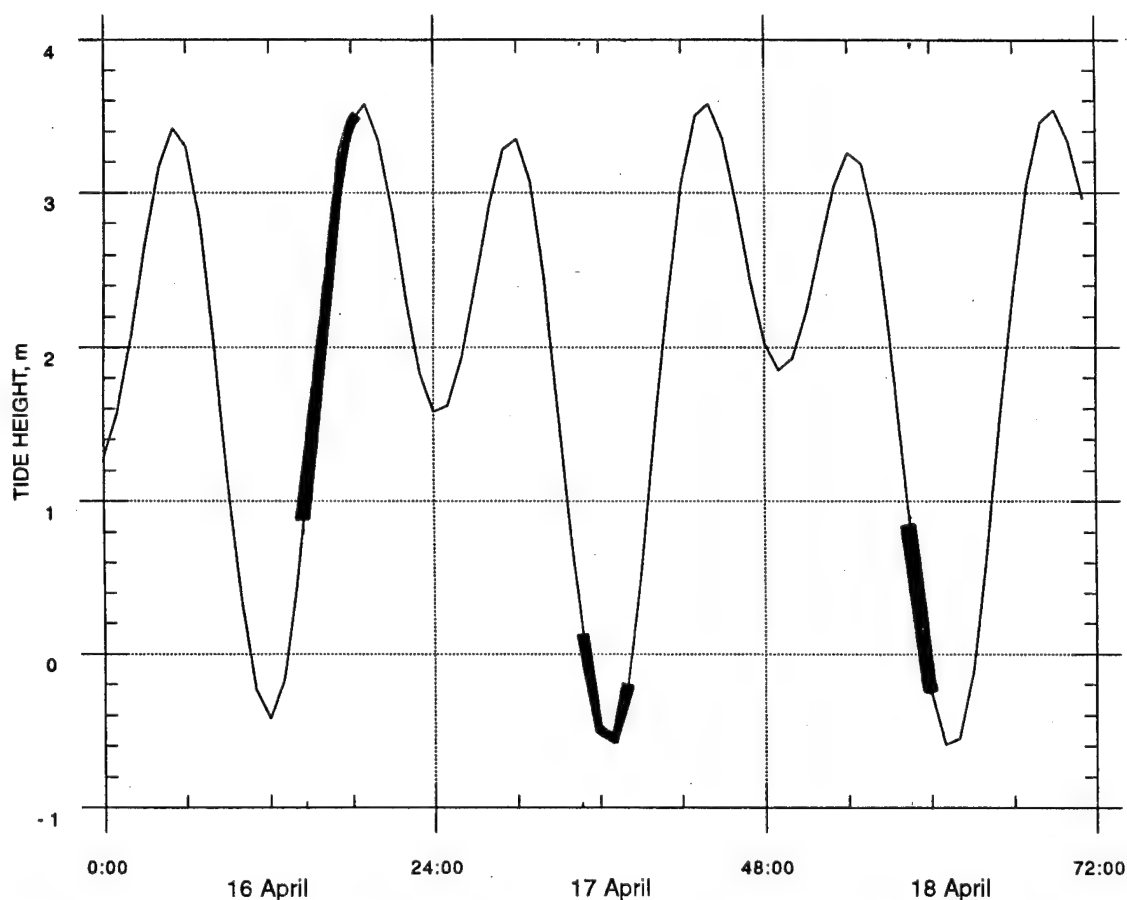


Figure 5.8. Tide heights at Restoration Point for 16–18 April 1991. Data for the times of the tows are highlighted.

levels between Blakely Rock and the entrance to Blakely Harbor (see Figures 5.9 and 5.16). The source may be Tyee Shoal 2 km to the north or the point just to the north of the entrance to Blakely Harbor.

Figure 5.17 shows the ensemble average of five vertical vorticity spectra taken when the sensor was passing through the wake of Blakely Rock. Also shown in dashed lines is the ensemble average of three spectra taken when the sensor was in deep water in the middle of Puget Sound. The spectra have similar shapes, but the spectrum for the lee of the rock is elevated by a factor of 3. The rolloff at small wavenumber (high frequency) is due to low-pass filtering during the processing, which runs a four-point weighted window filter through the time-series data.

Figure 5.18 shows similar time series data from the second day of towing. Again, there are several periods with elevated vorticity. These occurred during passage of the instrument through the lee of Blakely Rock. During this time series, the wake of the rock was to the north, as we were towing during the ebb flow of the tidal cycle. During the

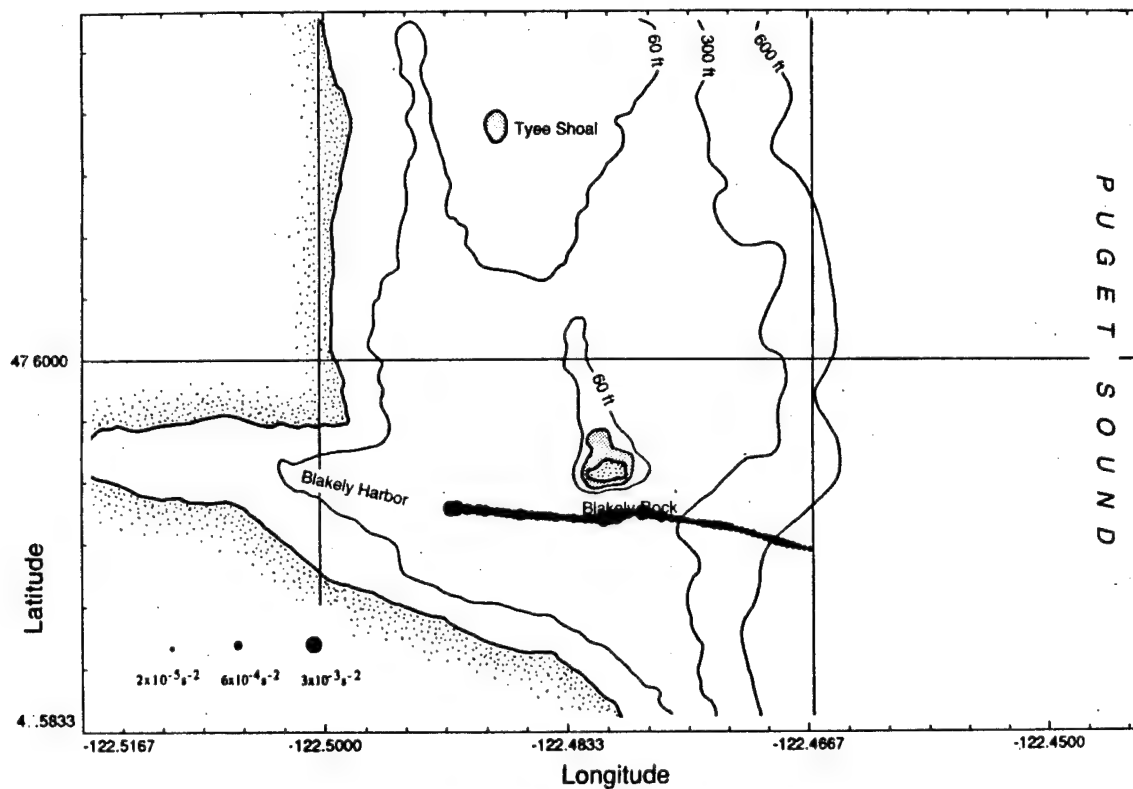


Figure 5.9. Vorticity variance along ship's track computed at 20-s intervals for data collected from 2120–2143 UTC on 16 April 1991. The dots represent variance between $3 \times 10^{-3} \text{ s}^{-2}$ and $2 \times 10^{-5} \text{ s}^{-2}$.

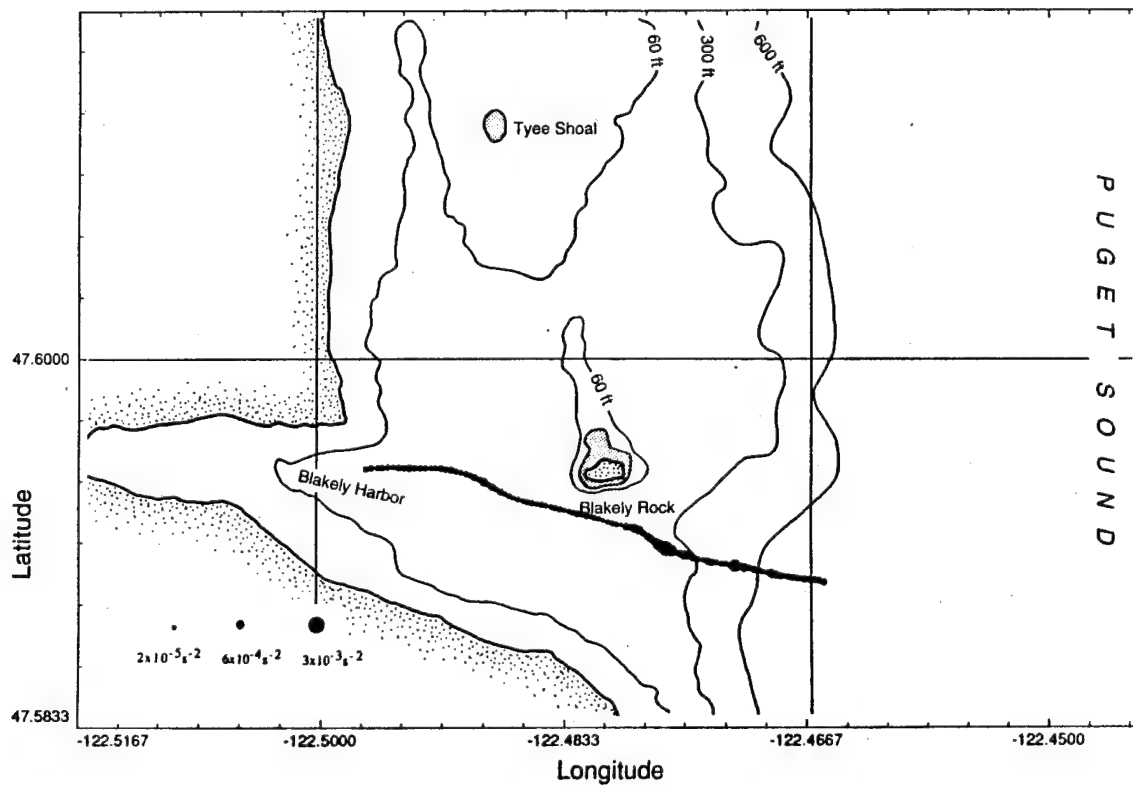


Figure 5.10. Vorticity variance along ship's track computed at 20-s intervals for data collected from 2146–2220 UTC on 16 April 1991.

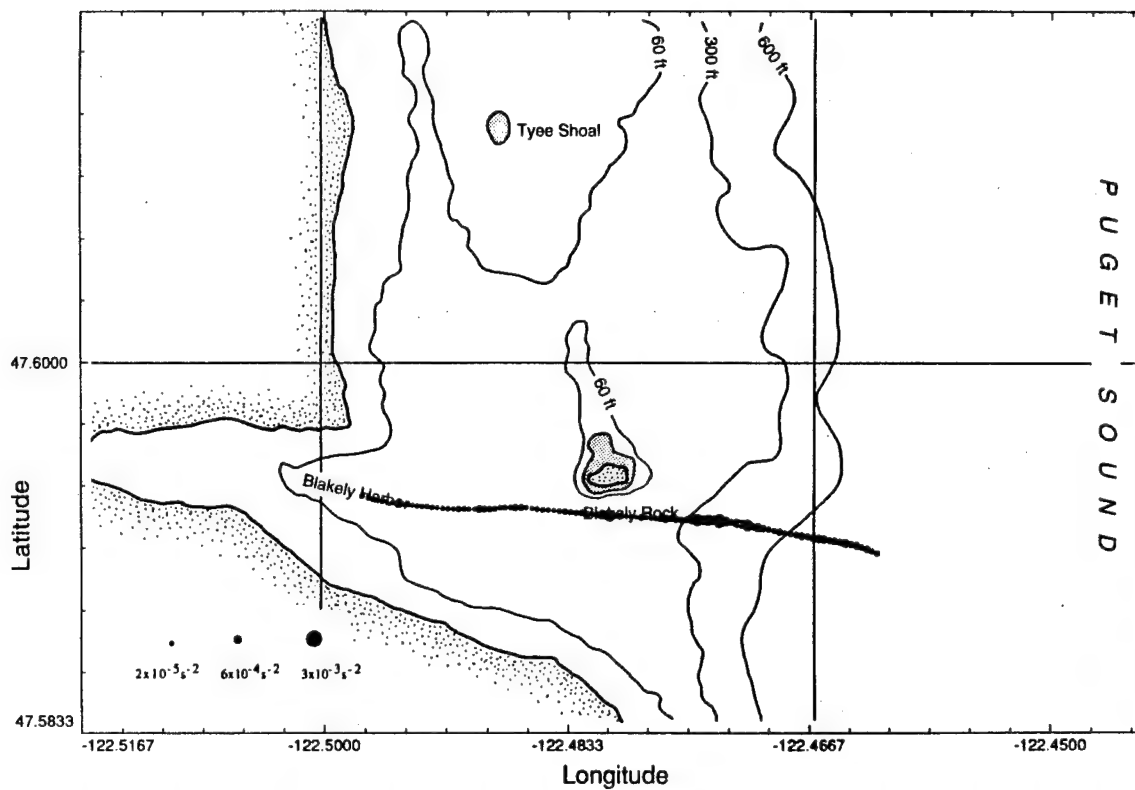


Figure 5.11. Vorticity variance along ship's track computed at 20-s intervals for data collected from 2223–2256 UTC on 16 April 1991.

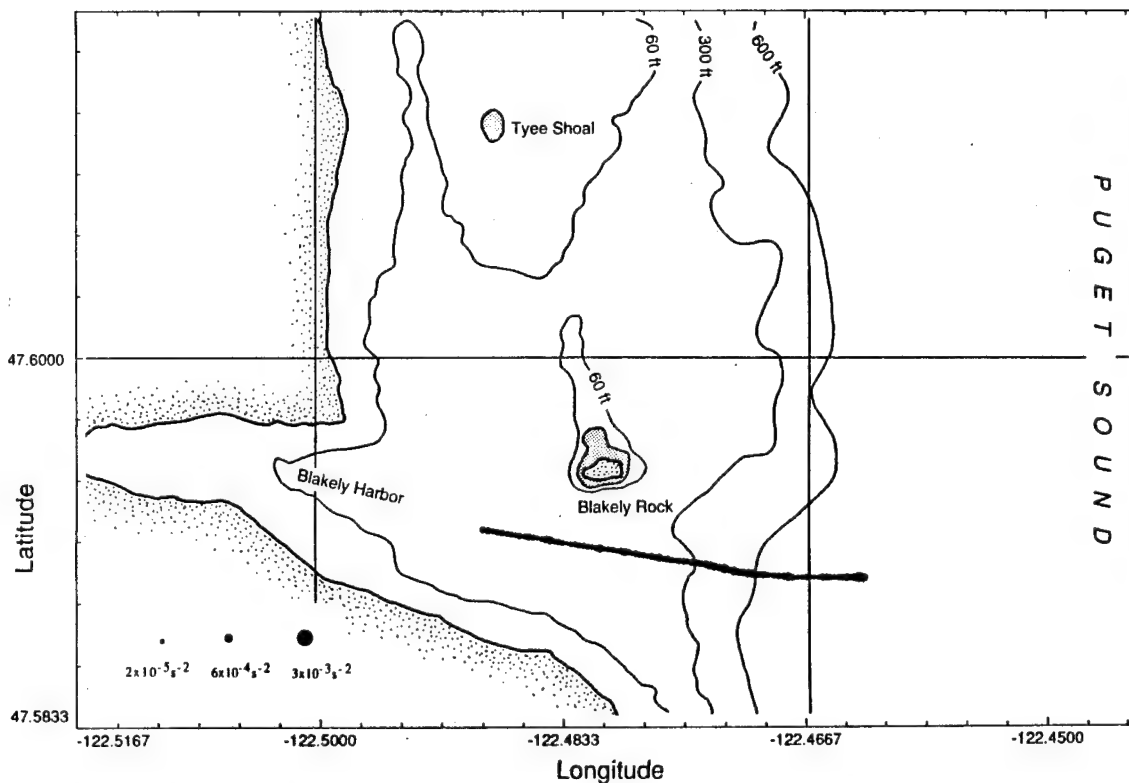


Figure 5.12. Vorticity variance along ship's track computed at 20-s intervals for data collected from 2258–2328 UTC on 16 April 1991.

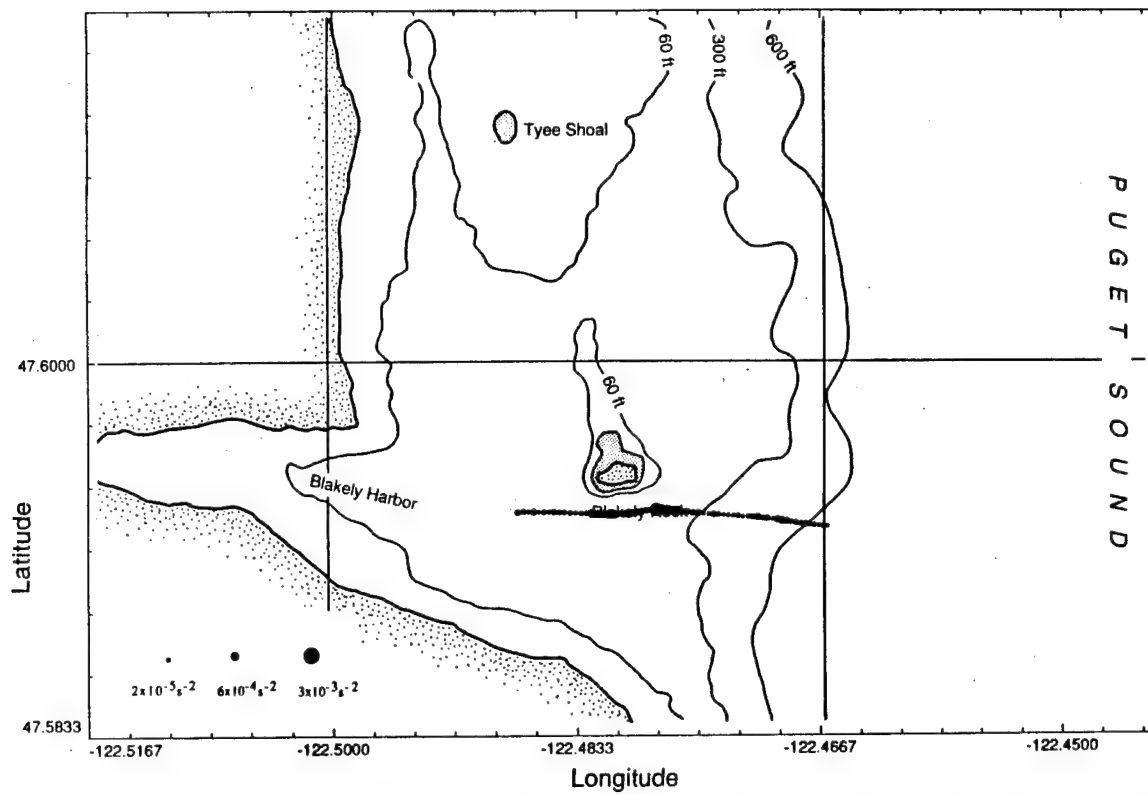


Figure 5.13. Vorticity variance along ship's track computed at 20-s intervals for data collected from 2331–2352 UTC on 16 April 1991.

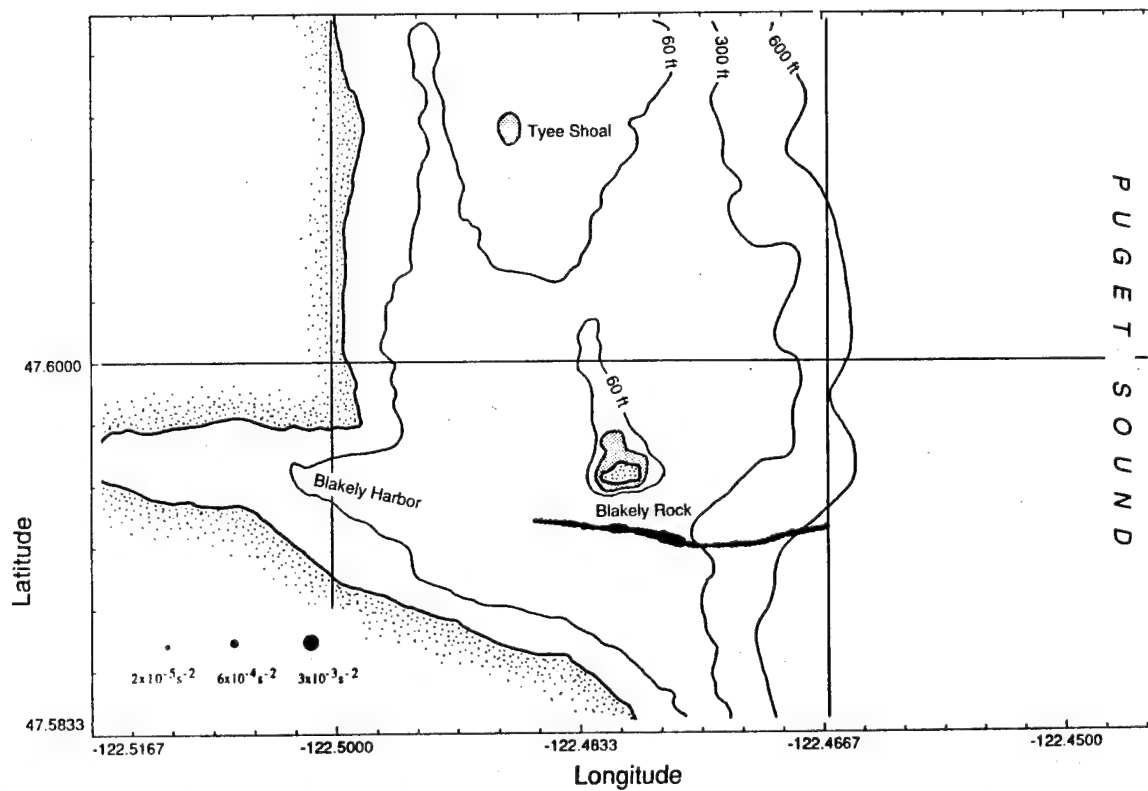


Figure 5.14. Vorticity variance along ship's track computed at 20-s intervals for data collected from 2355–0017 UTC on 16–17 April 1991.

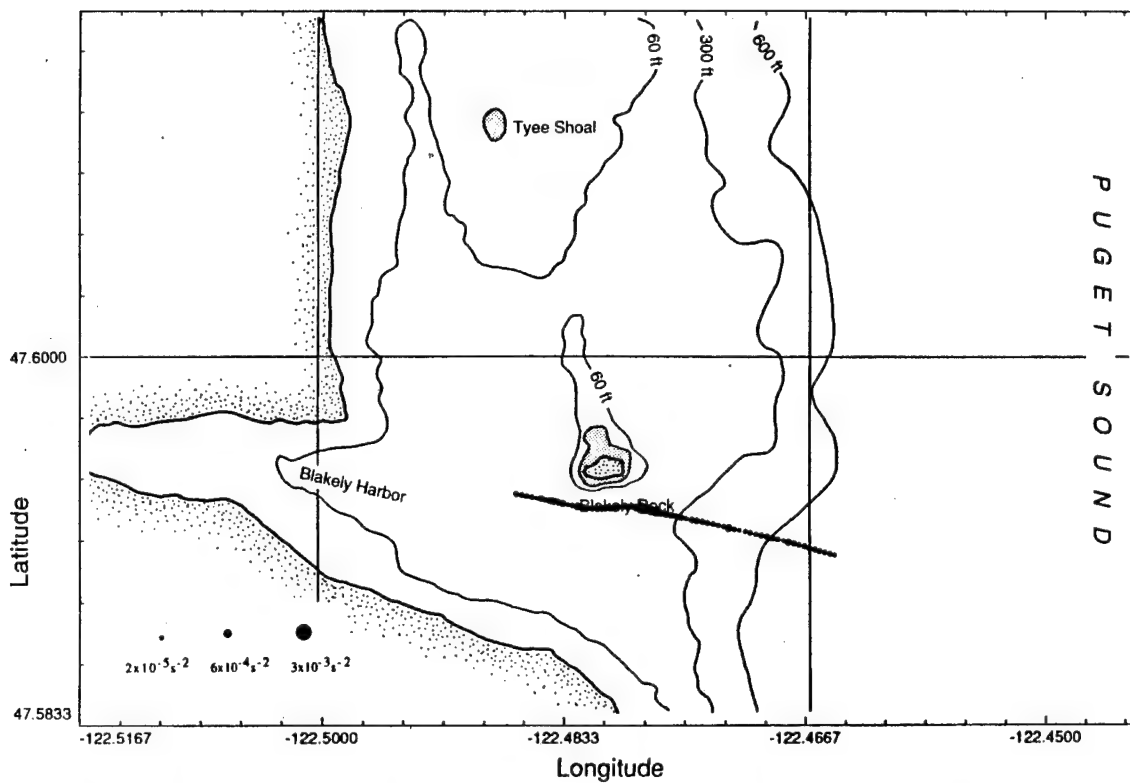


Figure 5.15. Vorticity variance along ship's track computed at 20-s intervals for data collected from 0020–0042 UTC on 17 April 1991.

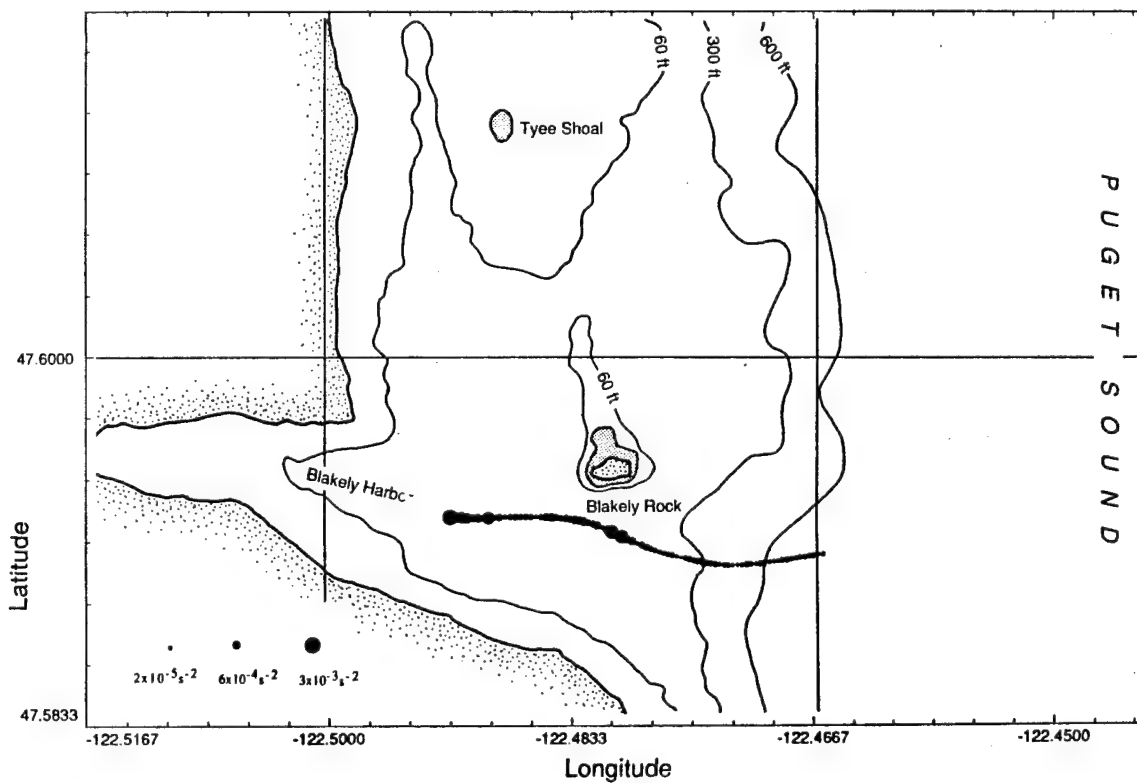


Figure 5.16. Vorticity variance along ship's track computed at 20-s intervals for data collected from 0044–0111 UTC on 17 April 1991.

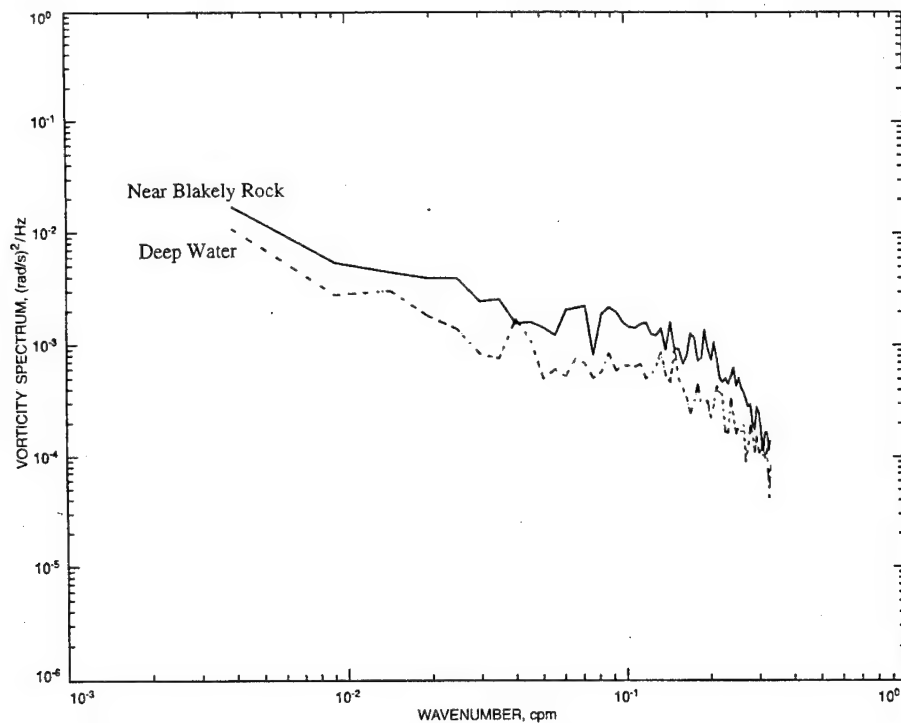


Figure 5.17. Comparison of vertical vorticity spectra from active and quiet regions of Puget Sound near Blakely Rock. Solid line: average of five spectra taken while towing the sensor through the wake of Blakely Rock. Dashed line: average of three spectra taken while towing the sensor in deep water in the middle of Puget Sound.

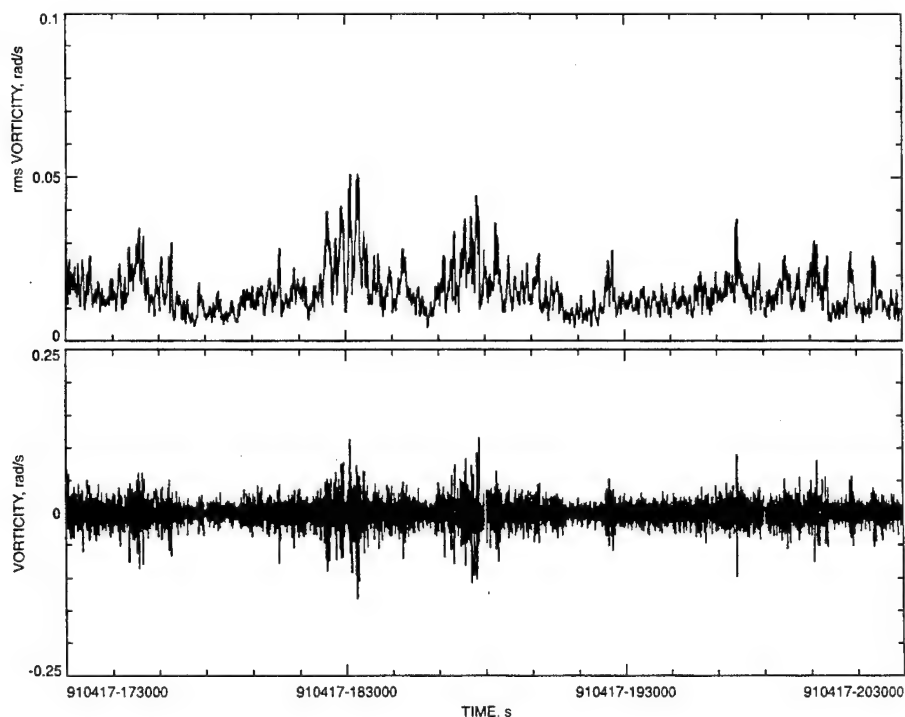


Figure 5.18. Time series of vertical vorticity on a tow with the GW fairing on 17 April 1991. The lower panel shows vorticity corrected for yaw rate and bandpass filtered as a function of time. The upper panel shows the variability in rms vorticity computed over 20-s windows.

later part of the tow, the flow became weak, and slack water occurred at about 2040 UTC. This corresponds with the quietest part of the record, which occurs at 2030 UTC. Figures 5.19 through 5.24 show vorticity variance for 20-s intervals of data from 17 April. Again, the size of the dots corresponds to the vorticity variance, and the average latitude and longitude of the 20-s interval determines the center of the dot. The highest vorticity levels were observed north and considerably east of Blakely Rock. It is difficult to attribute this active area to Blakely Rock because the area is so far to the east. The currents for this area are not well determined, however, so we cannot rule out the possibility of Blakely Rock as the source. There are also periodic elevated vorticity levels in the area between Blakely Rock and the mouth of Blakely Harbor. Some of this activity is apparently due to the promontory just to the north of the harbor entrance.

Figure 5.25 shows two spectra of vorticity data taken in Blakely Harbor. The solid line is the spectrum computed from data taken on 14 December 1990 when the sensor was mounted on a tripod resting on the bottom. The dashed line is the spectrum computed from data taken on 16 April 1991 when the sensor was being towed at a depth of 30 ft and a speed of approximately 2.5 kn. The spectra have been computed with respect to wavenumber, so effects of the speed of the sensor are accounted for.

In conclusion, the tests of the EMVM found clear evidence of environmental signals with rms amplitudes as great as $4.5 \times 10^{-2} \text{ s}^{-1}$. Blakely Rock seems to be the source for most but not all of the high-vorticity areas. The sporadic high levels observed away from the rock are probably due to distant promontories and shoals, vessel traffic, and biological activity. The data for a given area show a great deal of temporal variability, only some of which is correlated with the tidal cycle.

The EMVM was deployed again in Puget Sound on two consecutive days in mid-June 1991. The instrument was housed inside the GW fairing with the sensor end protruding about 1 ft below the tow body and was towed behind R/V *Miller* at low speeds (2.5 kn) and a depth of about 30 ft. The tows on both days were to the south of Blakely Rock, as we were observing during a flood flow. During this series of deployments, the vehicle dynamics package for Seasoar was attached to the GW fairing. In addition, an Eagle 8 GPS receiver was installed on board R/V *Miller*, and position data were logged at a 1-Hz rate.

The EMVM was operated with a permanent magnet and ceramic sensor tubes 0.10 in. in diameter extending 2.50 in. beyond the flow-splitting plate. An *in situ* calibration was performed at the beginning and end of each day of operations. The calibration consisted of rotating the instrument while it was suspended from the overhead hoist off the aft end of R/V *Miller* as the vessel was drifting slowly in Blakely Harbor.

Figure 5.26 shows a time series of vorticity data from the 4 hours of towing near Blakely Rock on 12 June. The lower panel shows vorticity corrected for yaw rate and bandpass filtered as a function of time. The upper panel shows the rms vorticity variability computed over 20-s windows. Although we use the term rms variability, we are actually calculating the standard deviation of the data about the mean over an interval of k points. The calculation we perform to yield the "rms" vorticity is

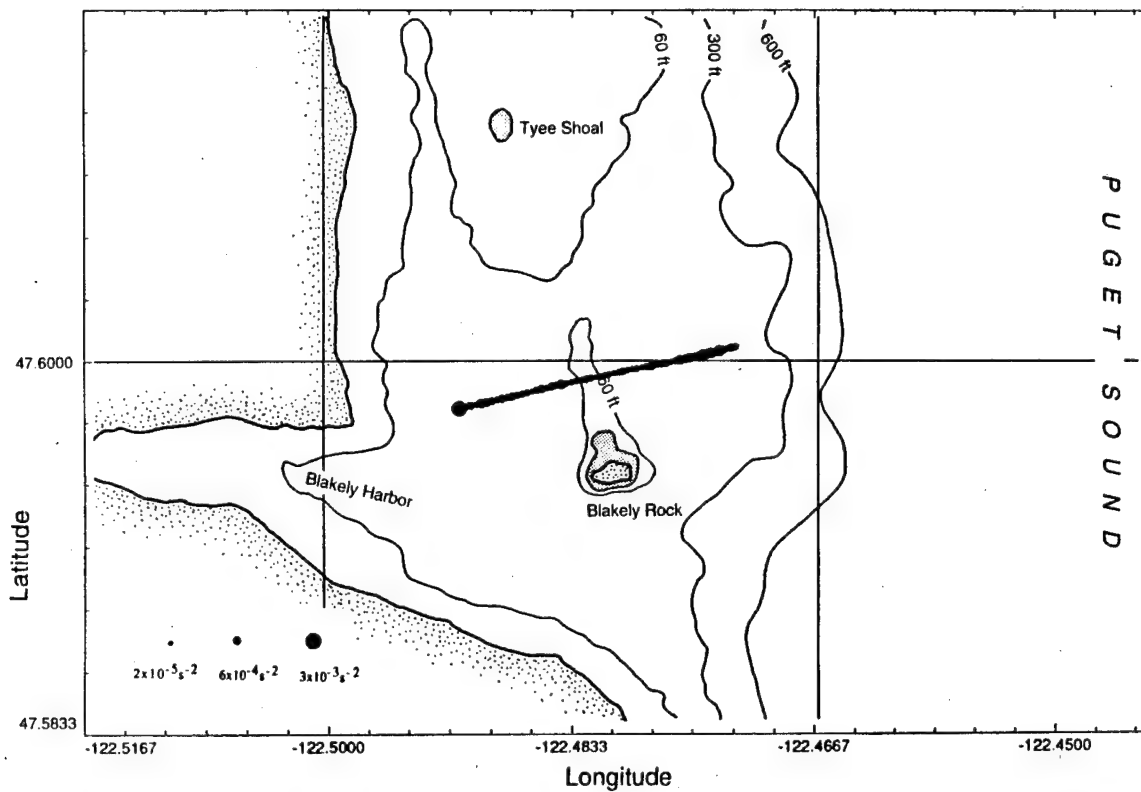


Figure 5.19. Vorticity variance along ship's track computed at 20-s intervals for data collected from 1728–1748 UTC on 17 April 1991. The size of the dots corresponds to vorticity variance, and the average latitude and longitude of the 20-s interval determines the center of the dot.

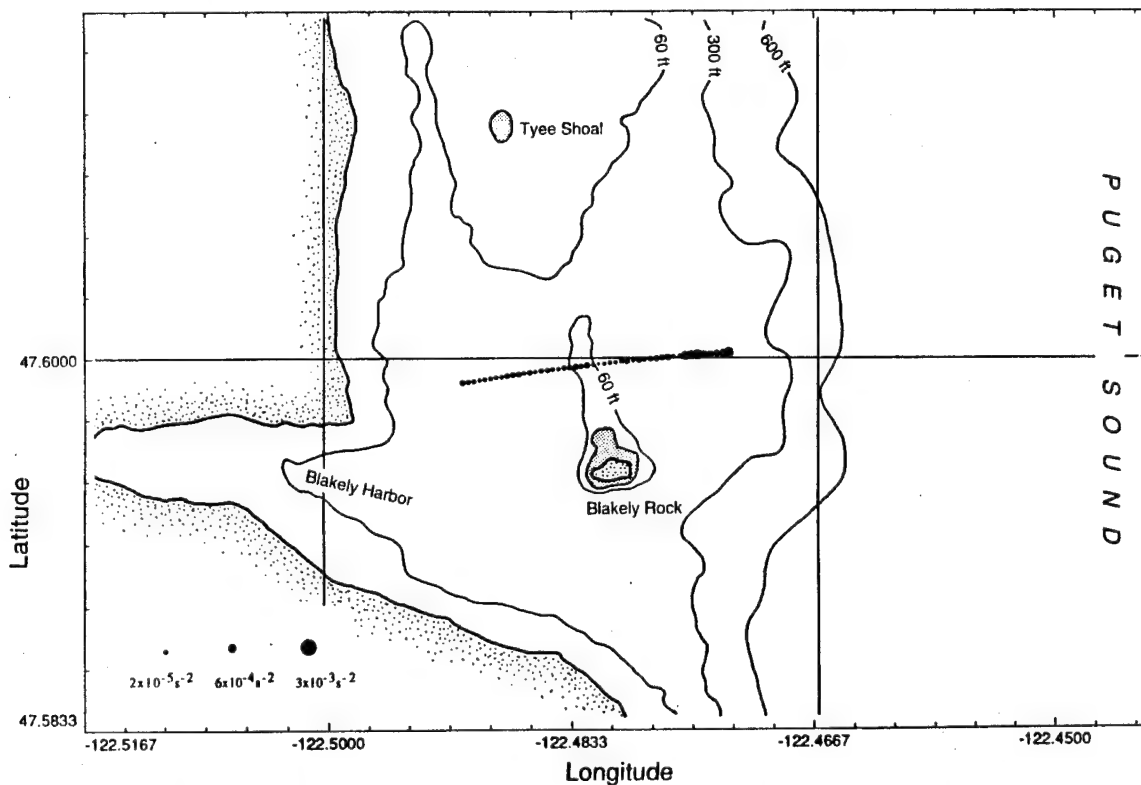


Figure 5.20. Vorticity variance along ship's track computed at 20-s intervals for data collected from 1750–1806 UTC on 17 April 1991.

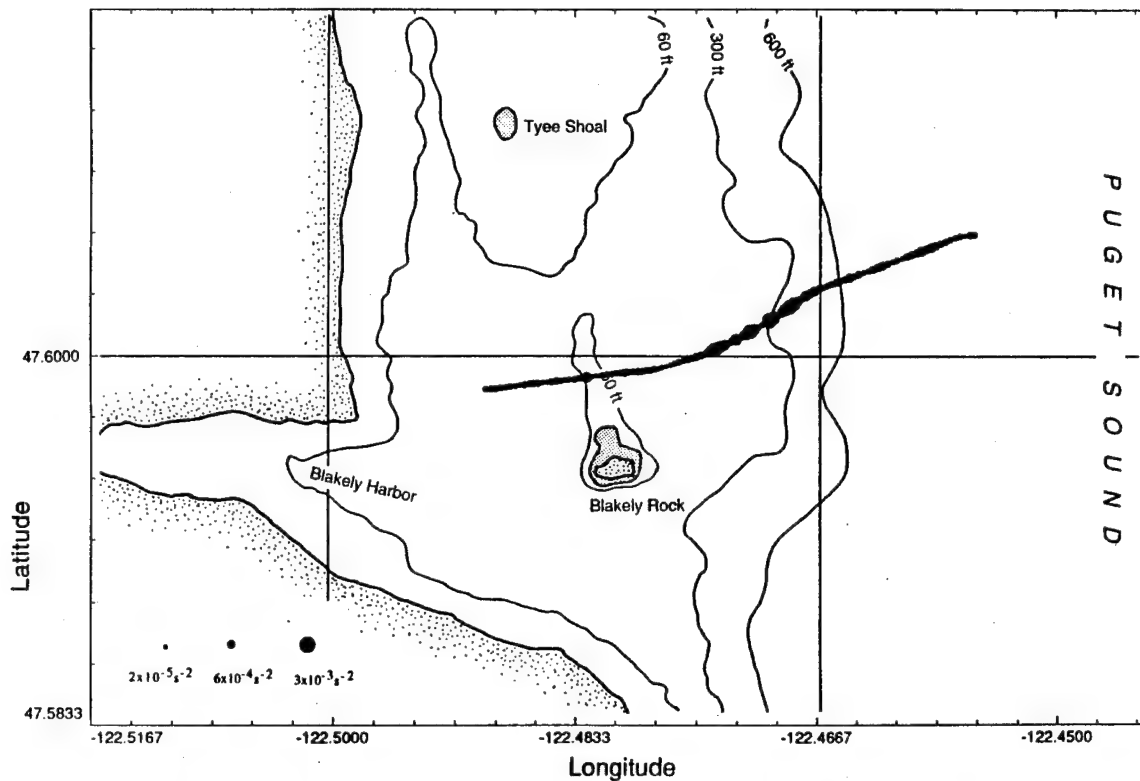


Figure 5.21. Vorticity variance along ship's track computed at 20-s intervals for data collected from 1808–1846 UTC on 17 April 1991.

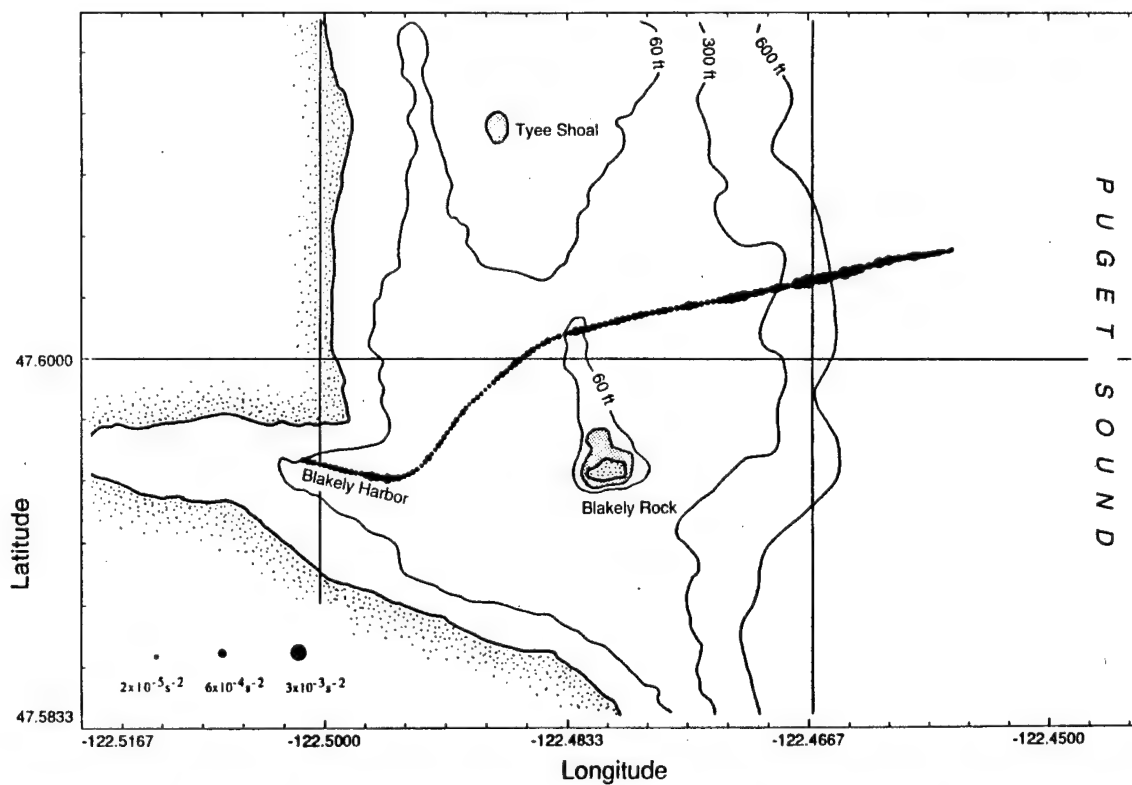


Figure 5.22. Vorticity variance along ship's track computed at 20-s intervals for data collected from 1848–1932 UTC on 17 April 1991.

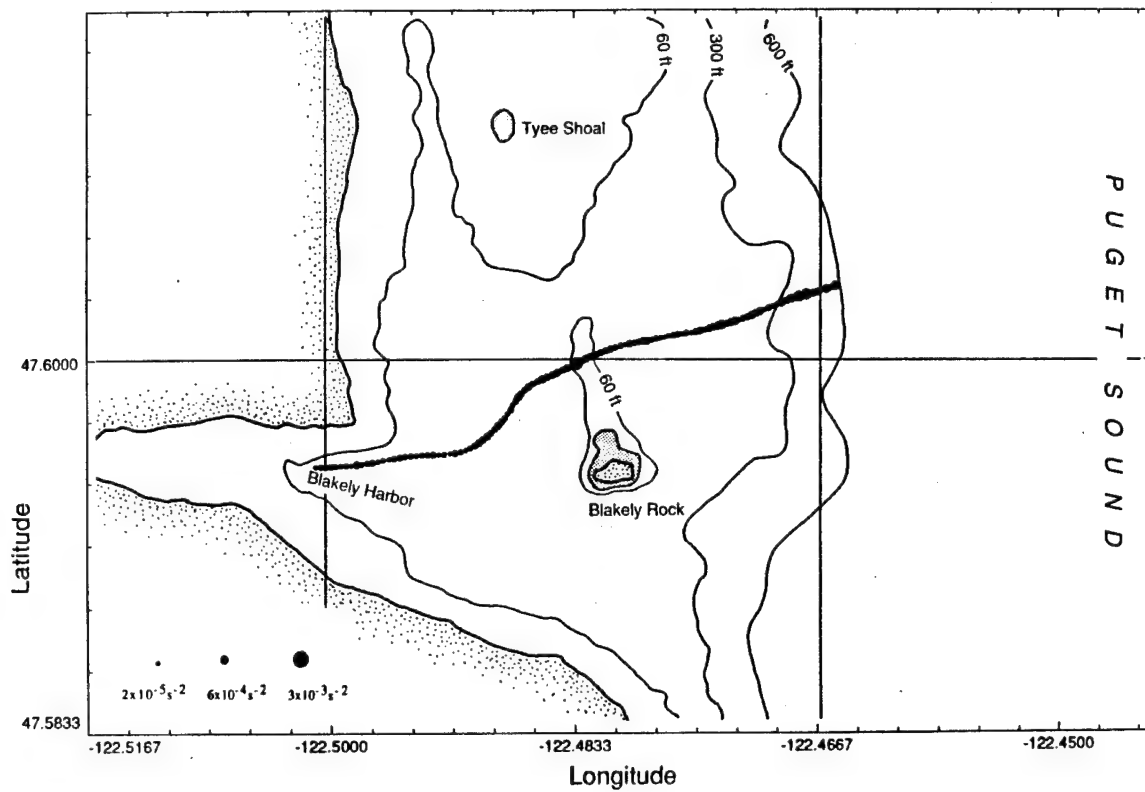


Figure 5.23. Vorticity variance along ship's track computed at 20-s intervals for data collected from 1935–2014 UTC on 17 April 1991.

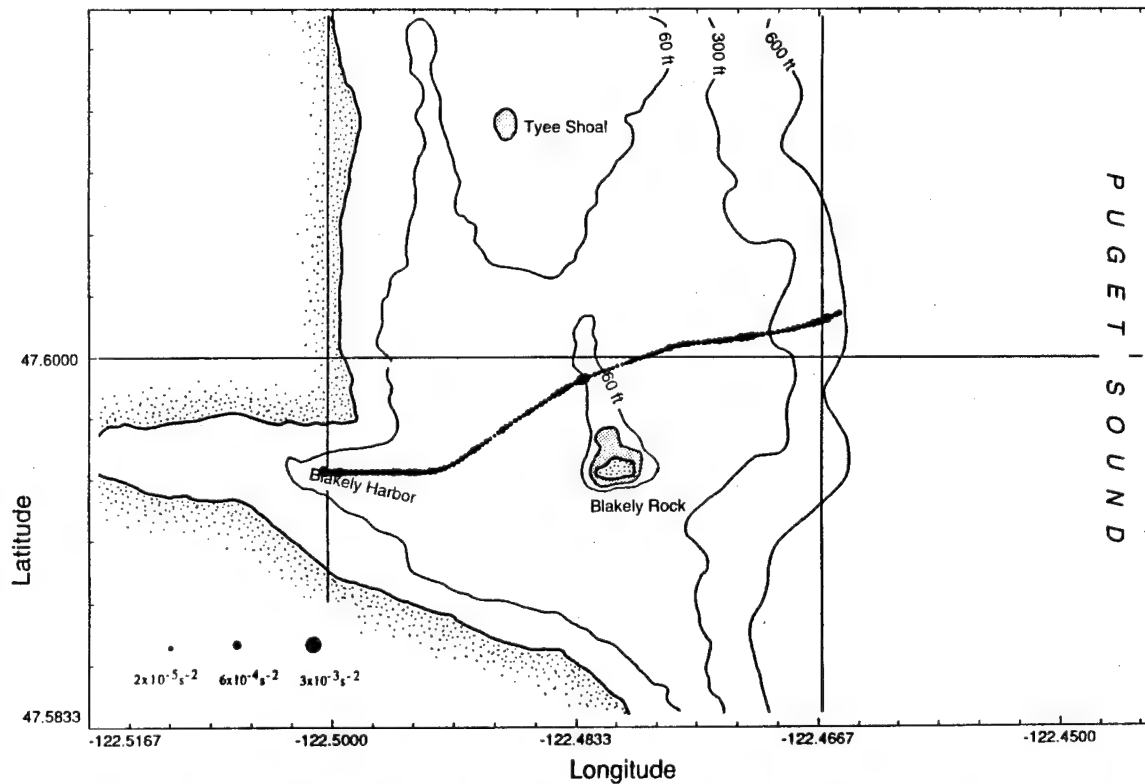


Figure 5.24. Vorticity variance along ship's track computed at 20-s intervals for data collected from 2017–2054 UTC on 17 April 1991.

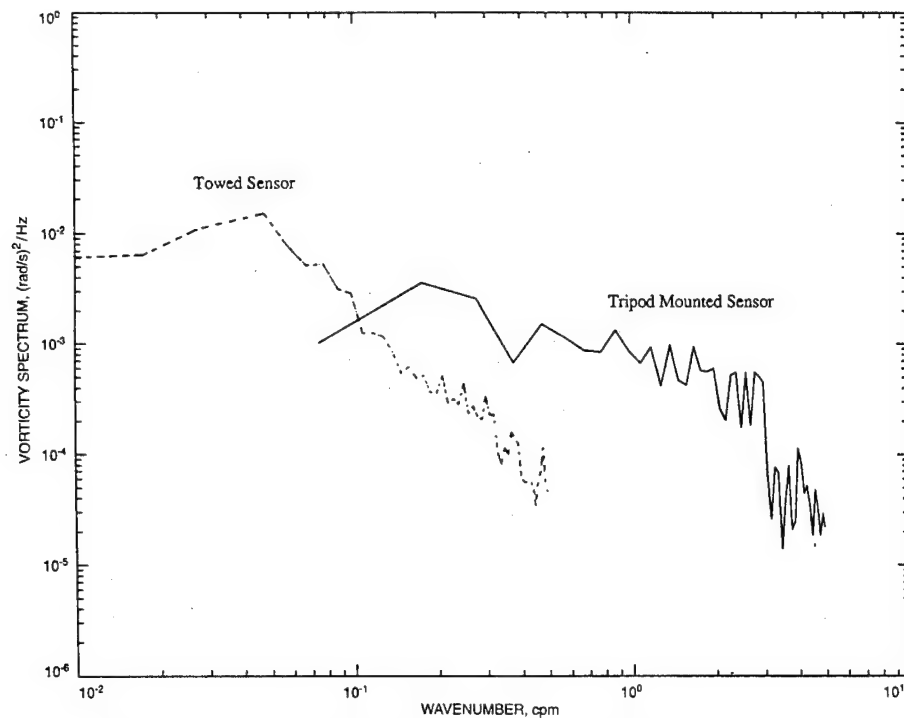


Figure 5.25. Two spectra of vertical vorticity data collected in Blakely Harbor. The solid line is the spectrum computed from data taken when the sensor was mounted on a tripod resting on the bottom. The dashed line is the spectrum computed from data collected while the sensor was towed at a depth of 30 ft at approximately 2.5 kn.

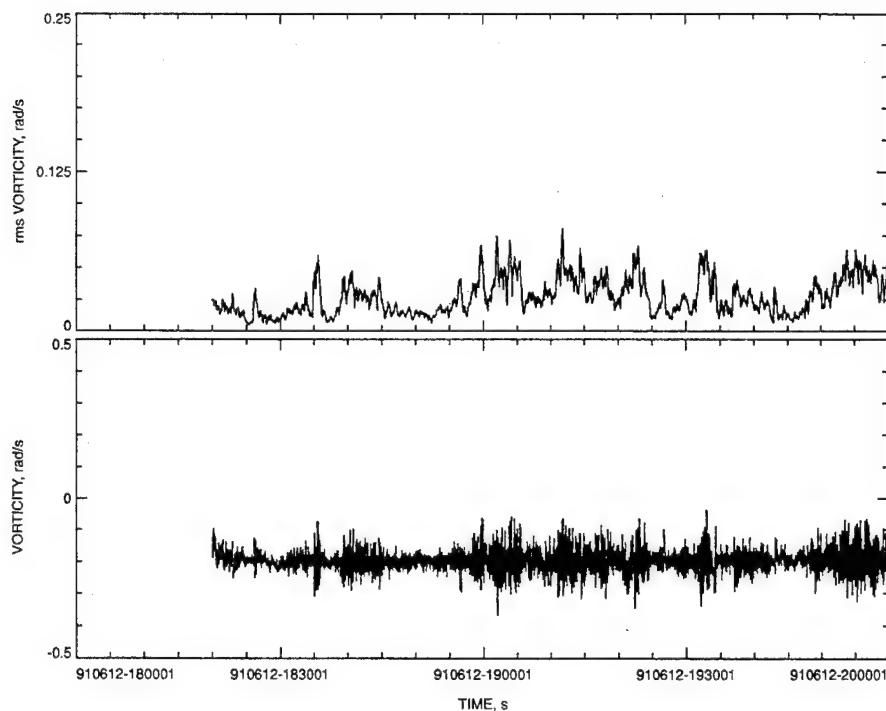


Figure 5.26. Time series data from a tow on 12 June 1991. The lower panel shows vertical vorticity corrected for yaw rate and bandpass filtered as a function of time. The upper panel shows the variability in rms vorticity computed over 20-s windows.

$$\text{rms vorticity} = \sqrt{\frac{\sum_{n=1}^k x_n^2 - k \bar{x}^2}{k-1}}, \quad (5.1)$$

where x and n are the individual vorticity measurements and \bar{x} is the mean of the vorticity measurements over the interval ($k = 20$ for a 20-s interval).

During the least active portions of the tow, the rms variability was slightly less than $5 \times 10^{-3} \text{ s}^{-1}$. This is slightly lower than what was achieved with the sensor mounted on a tripod moored at the bottom of Blakely Harbor on 14 December 1990. The quietest vorticity levels observed on the tripod during the 14 December deployment were $8 \times 10^{-3} \text{ s}^{-1}$ rms. Figure 5.26 shows nine separate events where there is a signal greater than $6 \times 10^{-2} \text{ s}^{-1}$ rms. The most active area has an rms variability of $8.3 \times 10^{-2} \text{ s}^{-1}$. These events occurred when the sensor passed just south of Blakely Rock. The wake of the rock was to the south, as we were towing during flood flow of the tidal cycle. Figure 5.27 shows the tide heights and average current for Restoration Point on 12–14 June 1991. The tow times have been highlighted. Figure 5.28 shows the vorticity variance computed for 20-s intervals for data taken on 12 June. The vorticity variance is plotted as a variable-sized dot whose center corresponds to the latitude and longitude of the average position for the particular interval. The legend in the lower left shows the correspondence of dot size to vorticity variance. In this case, vorticity variance is just the square of the rms vorticity signal levels computed over the 20-s window. We prefer plotting vorticity variance because it is more indicative of the power contained in the signal.

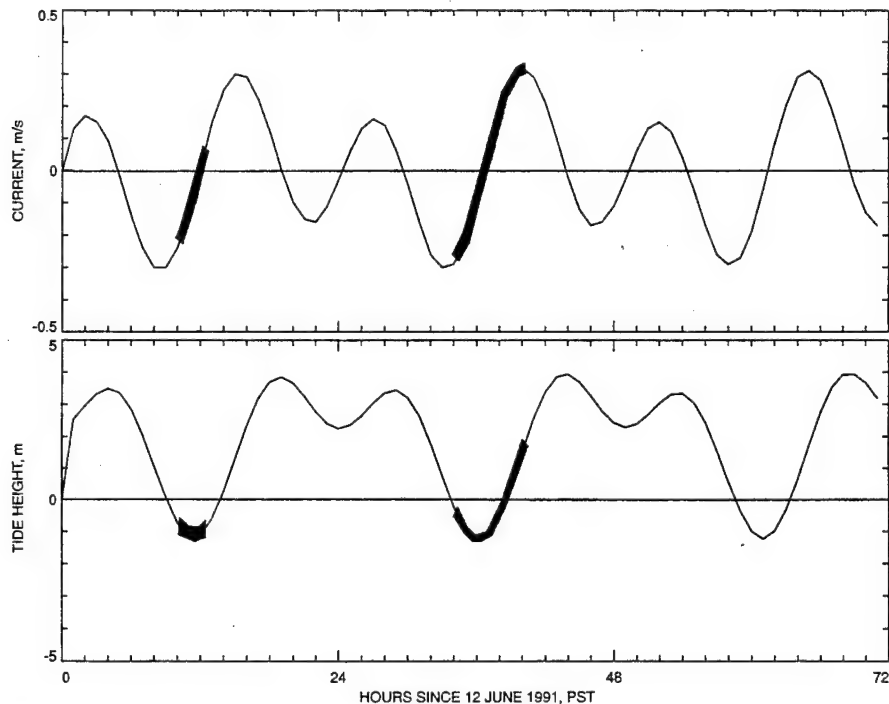


Figure 5.27. Tide heights and average current for Restoration Point on 12–14 June 1991. Tow times have been highlighted.

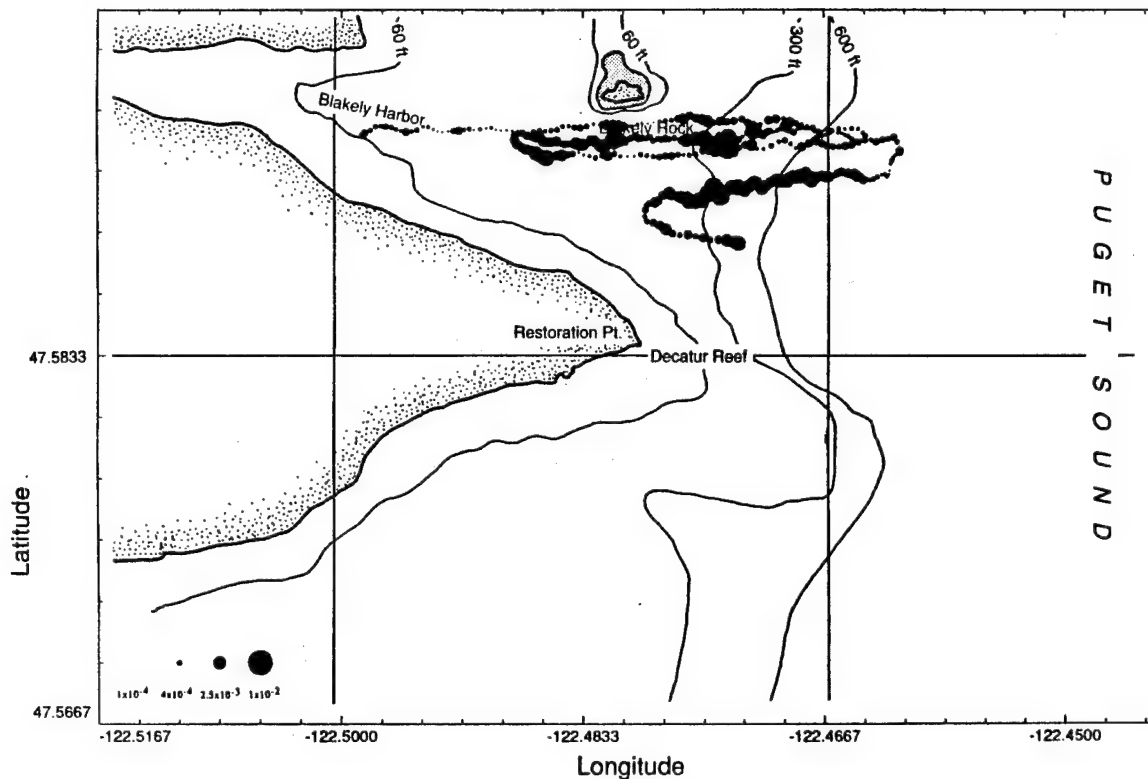


Figure 5.28. Vertical vorticity variance computed at 20-s intervals for data collected on 12 June 1991. The variance is plotted as a variable-sized dot whose center corresponds to the latitude and longitude of the average position for a particular interval. The legend in the lower left shows the correspondence of dot size to vorticity variance.

Figure 5.29 shows a similar time series of data from the second day of towing. Again, there are several periods with elevated vorticity levels. The most active has a signal level of $1.1 \times 10^{-1} \text{ s}^{-1}$ rms. Figures 5.30 and 5.31 show the vorticity variance (square of the rms vorticity over a 20-s interval) for data from 13 June. Figure 5.30 is for the first part of the tow when the flow was weak. (The surface flow seemed to increase as we towed farther south and around the mid-channel marker buoy. We could only estimate the flow based on the set taken by our vessel as we tried to steer an east/or/west course.) Figure 5.31 shows data taken later in the day when the flood flow was the greatest. Both Figures 5.30 and 5.31 show a shadow zone directly behind Blakely Rock where the vorticity level is low. The highest vorticity levels occur in two bands just south of Blakely Rock during the peak of the flood flow. One band is slightly to the west of the rock and the other is slightly to the east, areas where the water has flowed past the edge of the rock.

Figure 5.32 shows a blowup of one particular event in relation to signals observed during the entire day of towing. The upper panel shows rms vorticity levels for the entire deployment on 13 June. An arrow points to the signal that is expanded in time in the lower panel. This time series was taken as the EMVM passed through an active area just

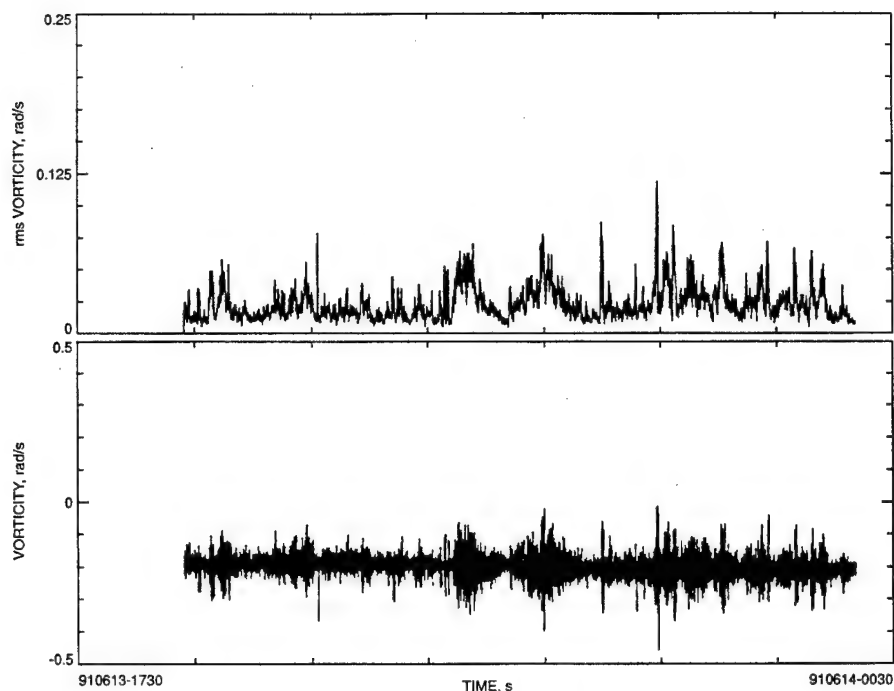


Figure 5.29. Time series data from a tow on 13 June 1991. The lower panel shows vertical vorticity corrected for yaw rate and bandpass filtered as a function of time. The upper panel shows the variability in rms vorticity computed over 20-s windows.

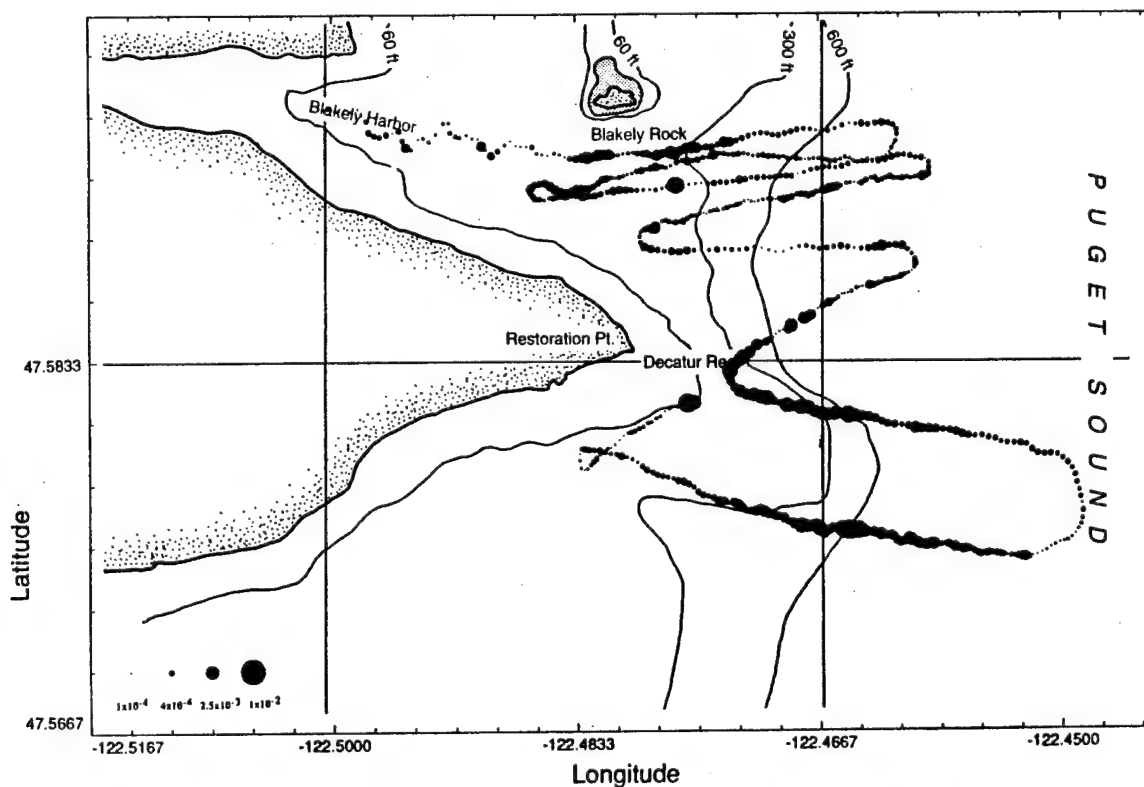


Figure 5.30. Vertical vorticity variance for data from 13 June 1991 taken during a time when the tidal flow was weak.

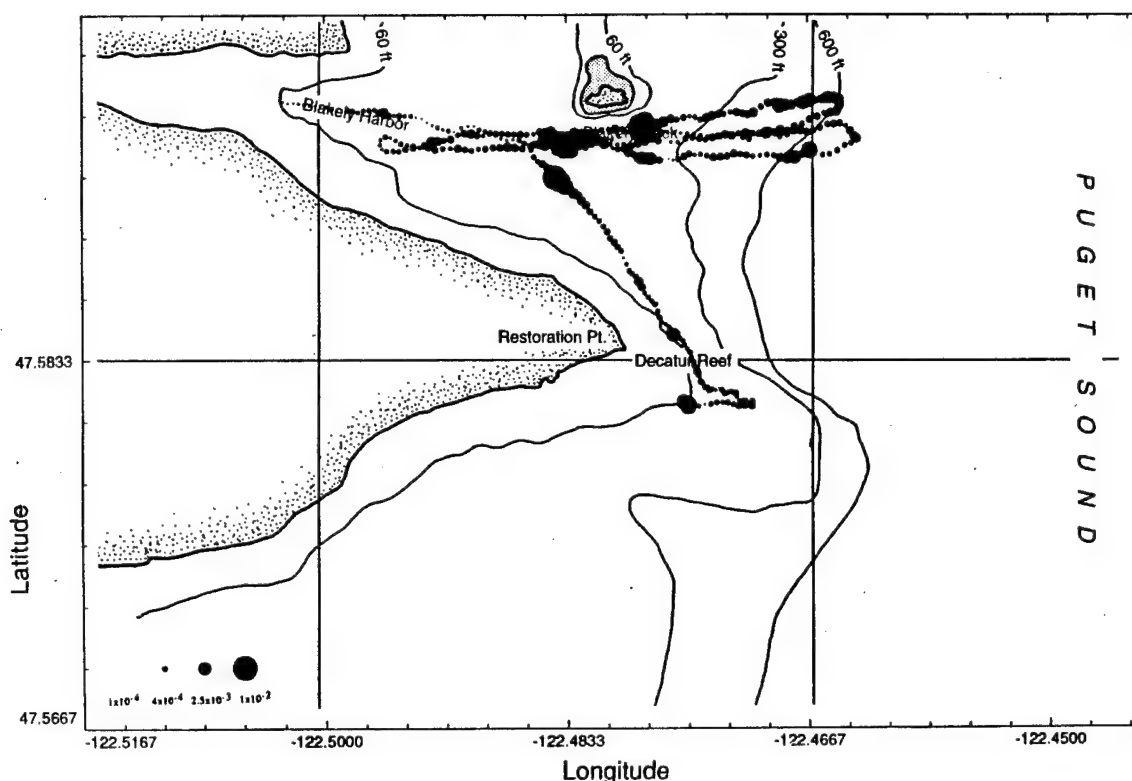


Figure 5.31. Vertical vorticity variance for data from 13 June 1991 taken during the time of maximum flood tide.

to the southeast of Restoration Point. This area corresponds to the large dot at the beginning of the track near Decatur Reef on Figure 5.31. The tow speed at this point was 1.2 m/s and the event spans a time period of 60 s. The physical extent of this feature is therefore about 70 m along the direction of the tow, which was perpendicular to the flow from the north.

In conclusion, the EMVM tests in June 1991 found clear evidence of environmental signals with rms amplitudes as great as $1.1 \times 10^{-1} \text{ s}^{-1}$. Blakely Rock and the point at the north of the entrance to Blakely Harbor seem to be the source for most of the vorticity observed in the area north of Restoration Point. Restoration Point also seems to be a source for vorticity observed in the area to its south. The data for a given area show a great deal of temporal variability, only some of which is correlated with the tidal cycle.

5.3 Restoration Point and Decatur Reef

In July 1991, the EMVM was deployed again for 2 days in Puget Sound. The instrument, equipped with the GW fairing, was towed behind R/V *Miller* at low speeds (2.5 kn) and a depth of about 30 ft. On both days, the tows were to the south of Restoration Point, just south of Blakely Rock, during a flood flow. During these tows, a vehicle dynamics package was attached to the instrument. In addition, an Eagle 4 GPS receiver was installed on board R/V *Miller*, and position data were logged at a 1-Hz rate.

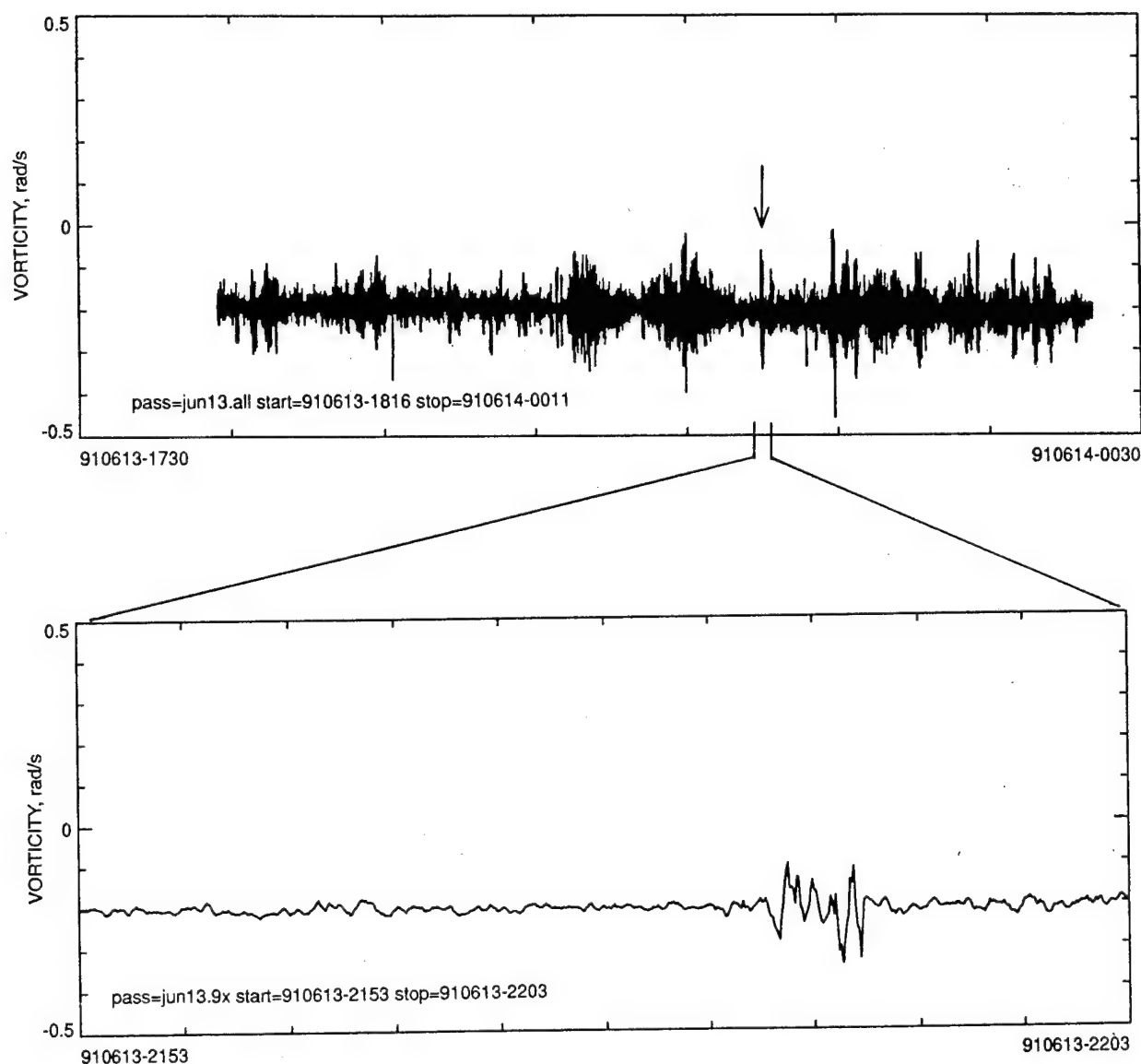


Figure 5.32. Blowup of one particular event in relation to signals observed during the entire day of towing. Upper panel shows the rms vertical vorticity signal levels for the entire deployment on 13 June 1991. Arrow points to the data segment that is expanded in time in the lower panel.

For these deployments, the EMVM was operated with a permanent magnet which provided an average field strength of 1.4×10^{-2} T (140 G) within the sensing volume. This is approximately three times the field strength of the previous electromagnet configuration. As in the June tests at Blakely Rock, the instrument was fitted with ceramic sensor tubes 0.10 in. in diameter extending 2.50 in. beyond the flow-splitting plate. The small-diameter tubes seemed to produce a lower level of self-induced noise, and the short length provided greater durability. The towing bridle was adjusted from the

June deployments to provide a pitched-up condition of about 7° , which seemed to give a lower background noise over a wider range of operating conditions, including ship heave and turning corners. An *in situ* calibration was performed at the beginning of each day of operations by rotating the instrument while it was suspended from the overhead hoist off the aft end of the R/V *Miller* as the vessel was slowly drifting.

Figure 5.33 shows a time series of the vorticity data for 10 July. The lower panel shows the vertical vorticity corrected for yaw rate and bandpass filtered as a function of time. The upper panel shows the rms vorticity variability computed over 20-s windows. During the least active portions of the tow, the rms vorticity variability was slightly less than $4.5 \times 10^{-3} \text{ s}^{-1}$. In the most active, it was $8 \times 10^{-2} \text{ s}^{-1}$. Figure 5.34 shows the tide heights and average current for Restoration Point on 10–12 July 1991. The tow times have been highlighted.

For this series of measurements, two 6-in.-diameter by 12-in.-long buoys with 4 ft by 8 ft "window shade" drogues suspended by a thin line to a depth of 25 ft were launched in areas of high activity near Restoration Point. To aid visibility, a small black flag was attached to the top of a 3-ft-high pole running through the center of each buoy.

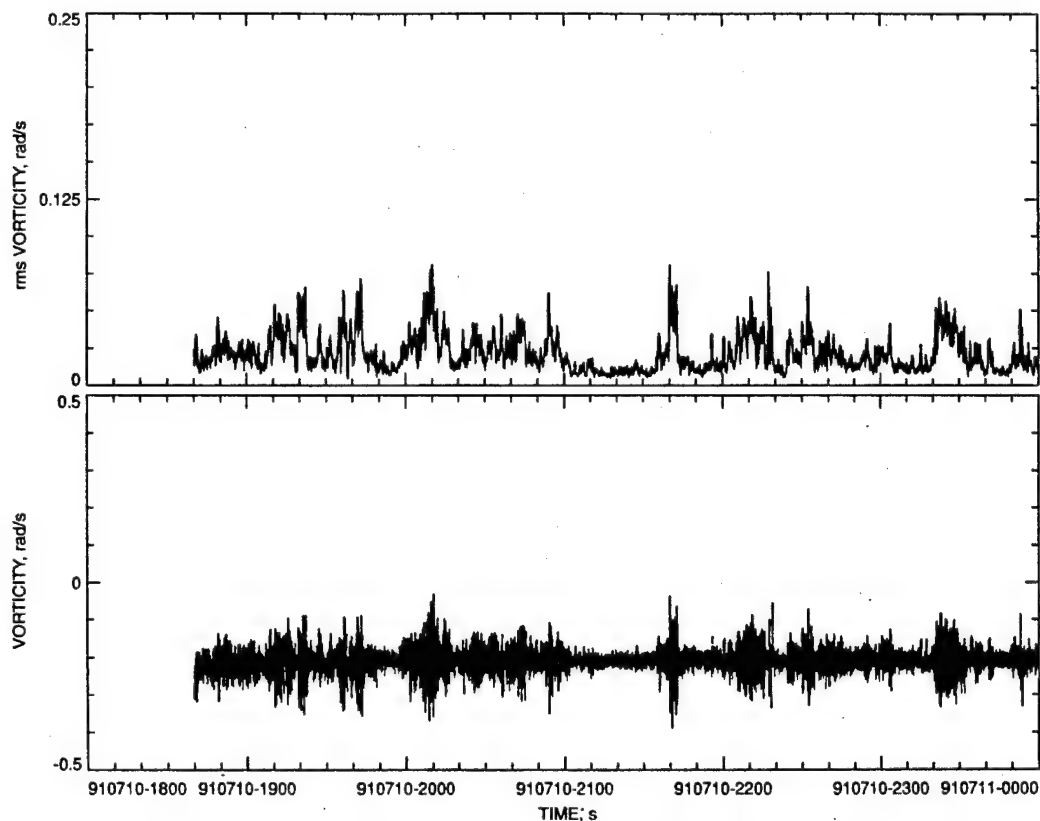


Figure 5.33. Time series of vertical vorticity data for 10 July 1991. Lower panel: Vorticity corrected for yaw rate and bandpass filtered as a function of time. Upper panel: variability in rms vorticity computed over 20-s windows.

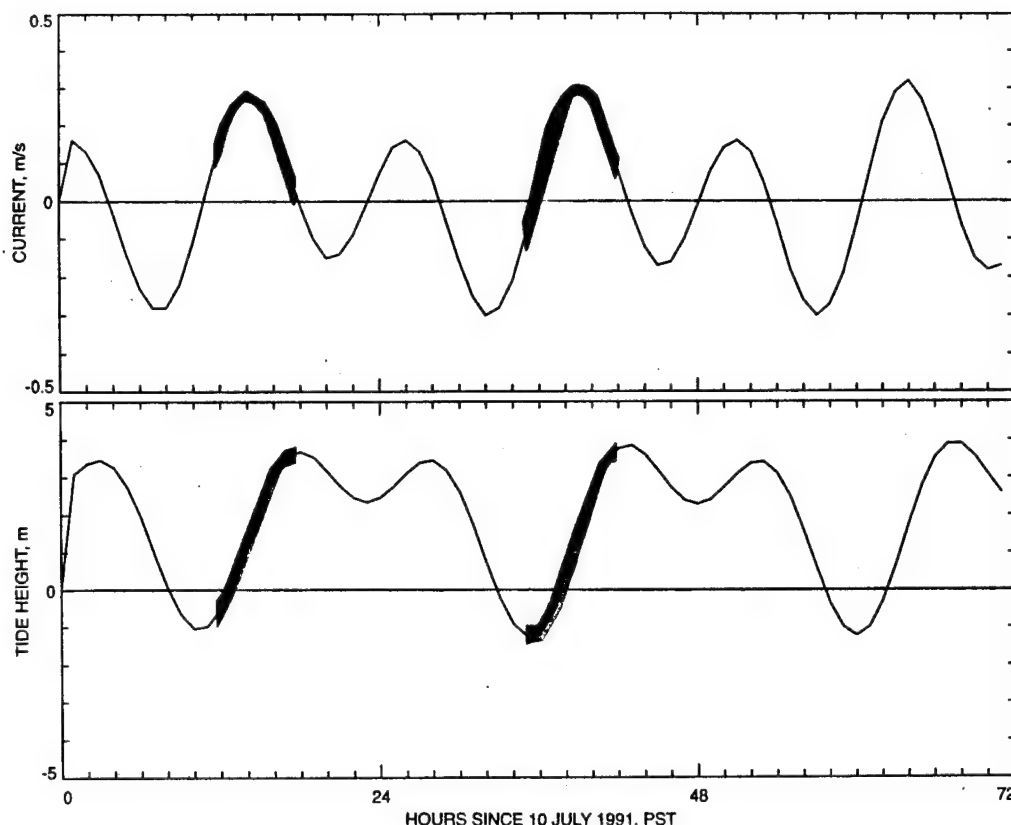


Figure 5.34. Tide heights and average currents for Restoration Point during 10–12 July 1991. Tow times have been highlighted.

The ship's track and the tracks of the two drogue buoys are shown in Figure 5.35. The positions of the boat are plotted every minute with an additional tick mark and time label every tenth minute. Four positions of the drogue buoys are also plotted. These four positions were calculated from a series of range and bearing measurements taken with the *Miller's* radar. The motion of the buoys should correspond closely to that of the water at a depth of 25 ft.

The average velocity for the two buoys was 0.84 kn. The average velocity between the first and second positions measured for buoy #2 was 1.17 kn, the highest observed. We placed buoy #1 in an area of moderate vorticity activity during our first westbound towing leg. It turned out that, as we progressed more to the west and closer to Restoration Point, the vertical vorticity signal levels increased. After towing through the area with the peak vorticity signal, we turned back to the east and deployed buoy #2 in a parcel of water that had much higher signal levels.

Figure 5.36 shows data from the first part of the day, when we tagged a piece of water with the drogue buoys and followed them as best we could by towing a serpentine course which brought the instrument alongside the buoys periodically. The highest vertical vorticity levels were observed in an area southeast of Restoration Point. This is the expected location for large vorticity signals given the velocities observed with the drogue

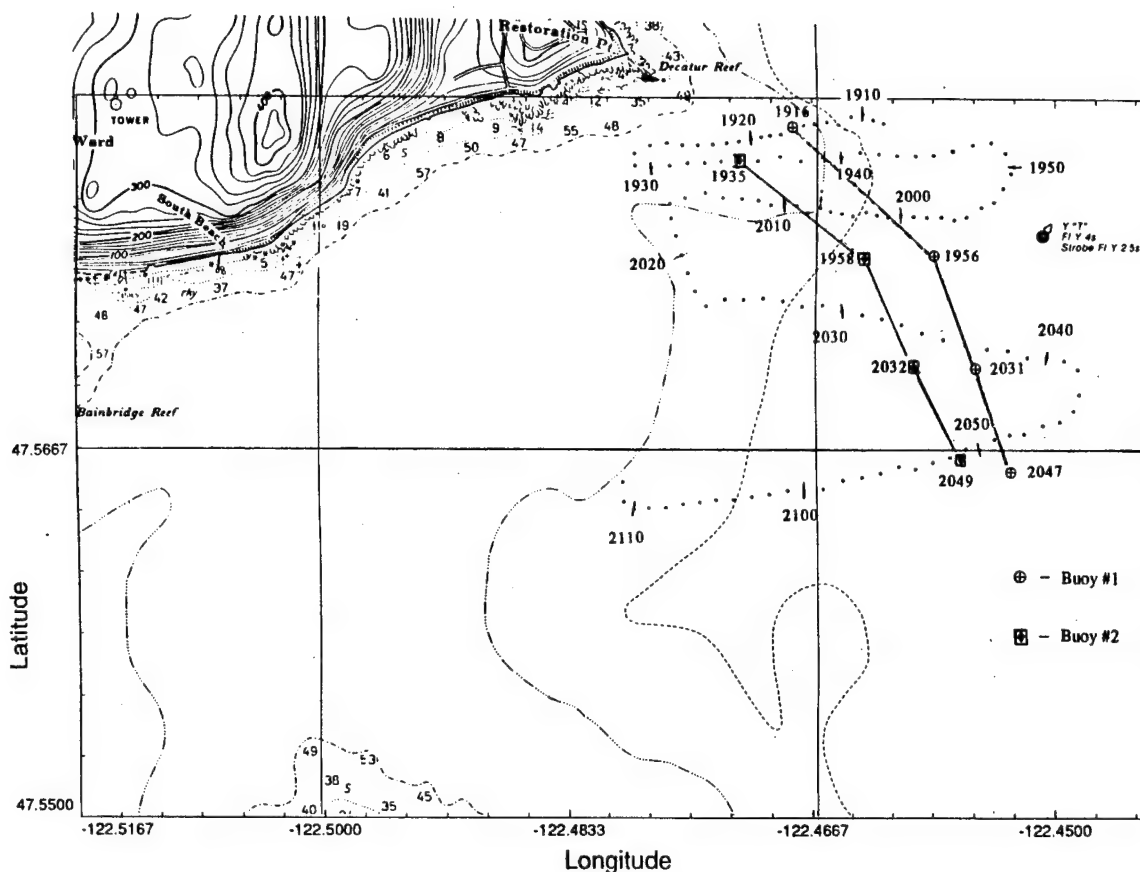


Figure 5.35. Ship's track (dots) and drogue buoy tracks (lines) in areas of high vertical vorticity activity near Restoration Point. The positions of R/V *Miller* are plotted every minute, with an additional tick mark and time label every tenth minute.

buoys. If we use the initial velocity vector of buoy #2 to extrapolate back to the source, we find that the parcel of water passed along the edge of Restoration Point and over Decatur Reef. It is interesting to note that we were able to observe the signature of the Decatur Reef source on our southernmost transect. The peak vorticity signal levels on this transect correlate well with our point of closest approach to buoy #2. At this time (2050 UTC), the parcel of water had been traveling for about 2 hours since its passage over Decatur Reef. The maximum vertical vorticity signal level decreased only slightly during this interval. We observed a maximum vorticity signal level of $6.4 \times 10^{-2} \text{ s}^{-1} \text{ rms}$ during our first transect near Restoration Point and a maximum signal level of $6.1 \times 10^{-2} \text{ s}^{-1} \text{ rms}$ during our southernmost transect 80 min later. What may be more significant is that the size of the area with high vertical vorticity signal levels seems to have decreased. During the passes near Restoration Point, the area with high vorticity signal levels was about 300 m across in the direction of the tow (east-west). During the southernmost transect 80 min later, the area with high vorticity signals was about 150 m across.

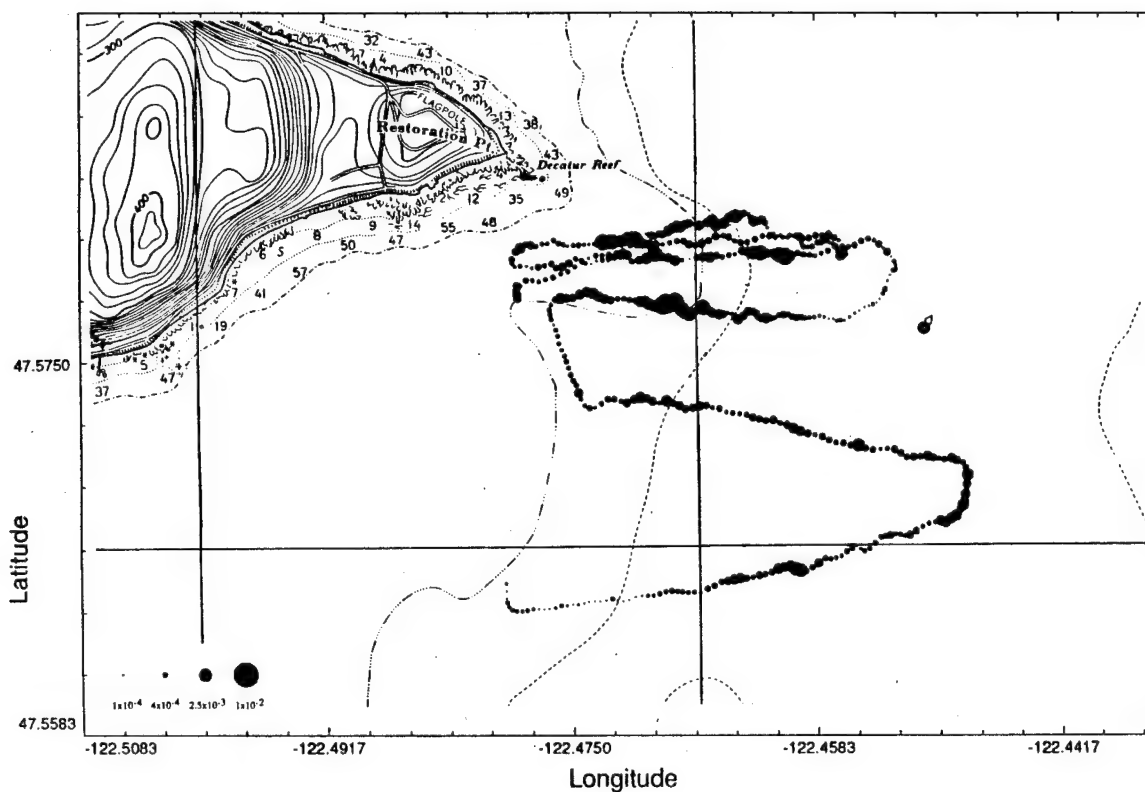


Figure 5.36. Vertical vorticity data from the first half of 10 July 1991. The variance is plotted as a variable-sized dot whose center corresponds to the latitude and longitude of the average position for a particular interval. The legend in the lower left shows the correspondence of dot size to vorticity variance.

During the second half of the day, we towed the EMVM through a pattern designed to map the vertical vorticity levels in the area just to the south of Restoration Point. For these transects, we decided to proceed farther to the west before turning back to an easterly course. These data were collected later in the tidal cycle near high tide when the current was decreasing. Figure 5.37 shows that the area with high signal levels to the north near Decatur Reef splits into two distinct bands. One curls back to the west around Restoration Point heading southwest, and the other heads out into the middle of Puget Sound to the southeast.

Results from the second day of towing on 11 June are shown in Figure 5.38. This day consisted of repeated transects both east and west along $47^{\circ}34'40''$ N latitude. The most active area during these transects has an rms level of $1.1 \times 10^{-1} \text{ s}^{-1}$ (over a 20-s interval). Figure 5.39 shows vorticity variance for 20-s intervals for data from 1 July. The highest vorticity levels are southeast of Restoration Point during the peak of the flood flow. Although closer to Decatur Reef, the presumed source, the area just south of the point shows lower vorticity signals. We believe this is because the mean flow is

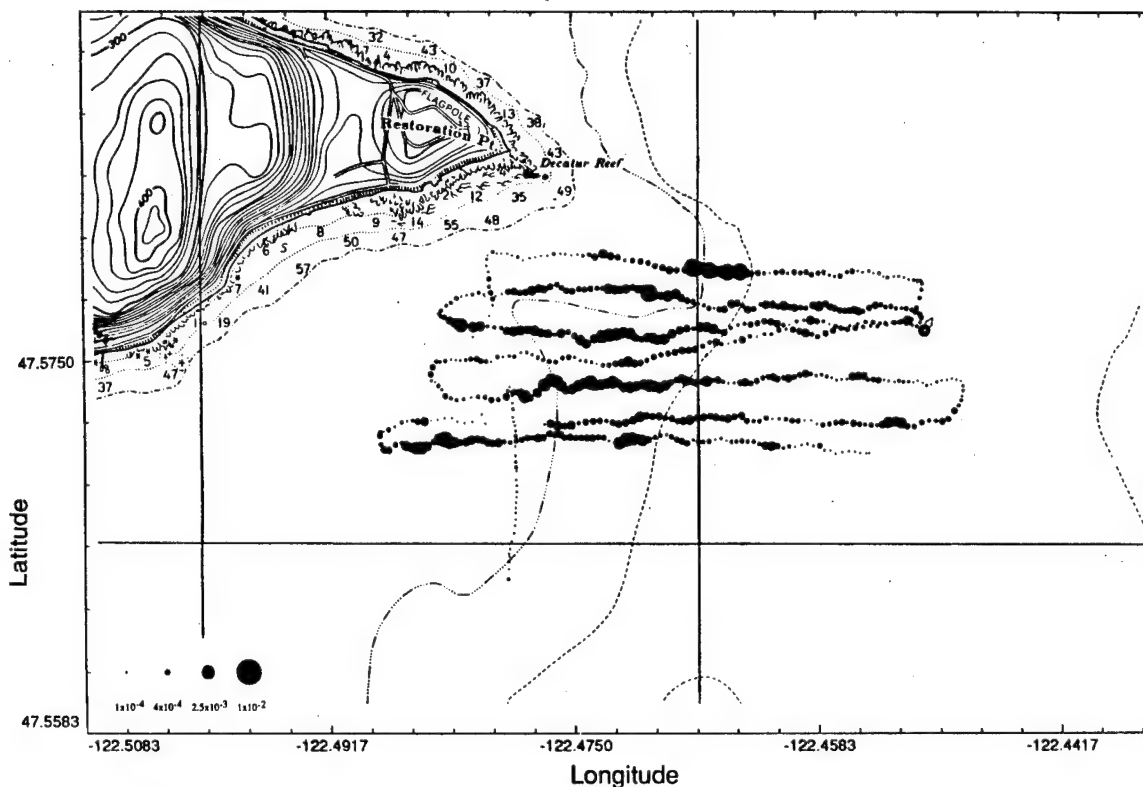


Figure 5.37. Vertical vorticity data from the second half of 10 July 1991. Note the two bands of high vorticity variance: one curling back to the west around Restoration Point, and one heading out into the middle of Puget Sound.

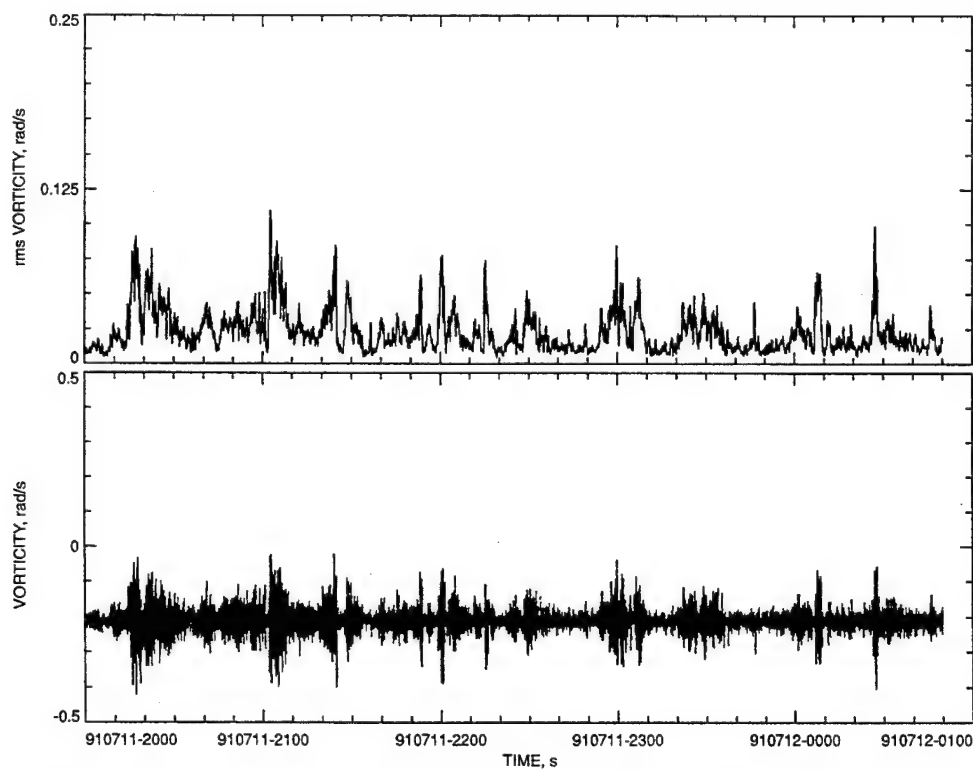


Figure 5.38. Time series of vertical vorticity data from 11 July 1991. The lower panel shows vorticity corrected for yaw rate and bandpass filtered as a function of time. The upper panel shows the variability in rms vorticity computed over 20-s windows.

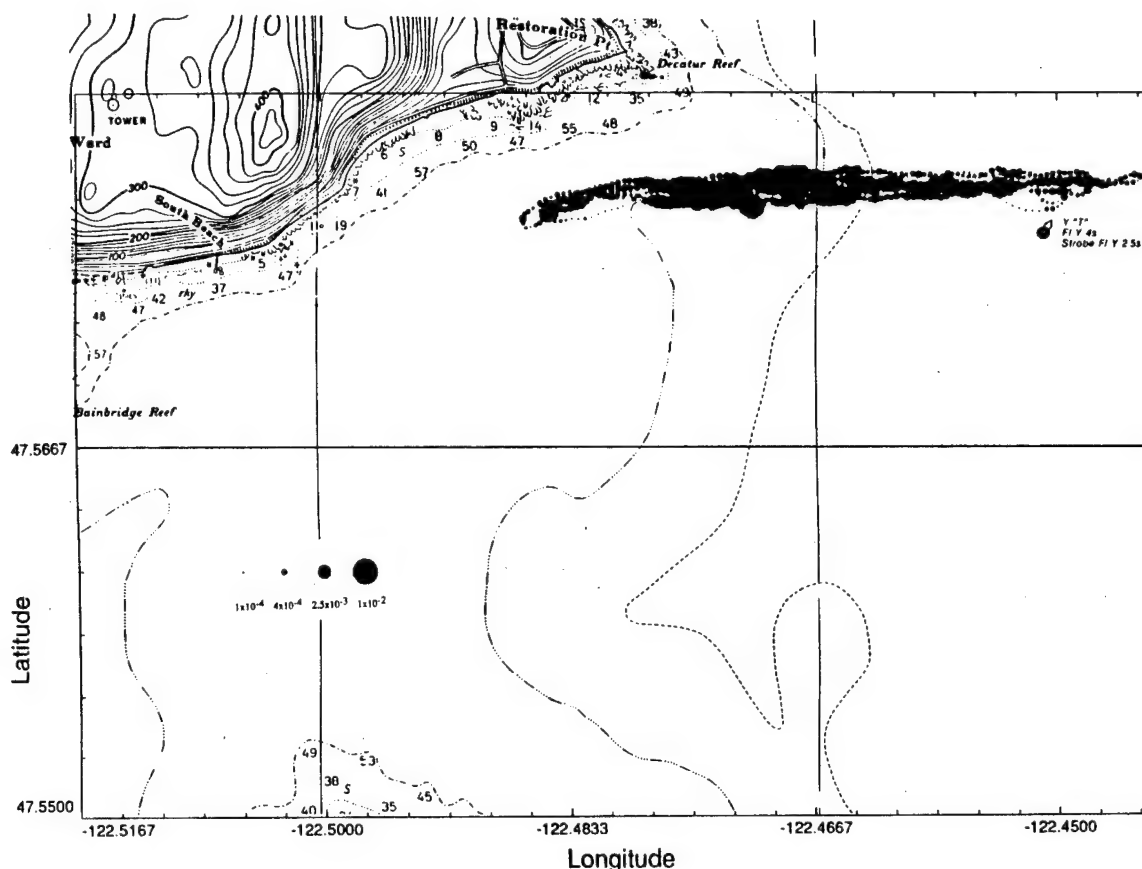


Figure 5.39. Vertical vorticity variance at 20-s intervals for data from 11 July 1991. The size of the dots corresponds to vorticity variance and the average latitude and longitude of the 20-s interval determines the center of the dot.

parallel with the shoreline to the north of the point, causing the vorticity signals to be advected the southeast. The water velocities measured with the drogue buoys the previous day near Restoration Point indicated just this type of water motion.

Figure 5.40 shows nine along-track plots of vertical vorticity taken as we passed back and forth along $47^{\circ}34'40''$ N just to the south of Restoration Point. The zero for the along-track axis is a point due south of Restoration Point. The earliest transect is shown at the top of the figure and the latest at the bottom. The start and stop times for each pass are printed on the plot. Figure 5.41 shows nine along-track plots of rms vorticity calculated for 20-s intervals. Again, the earliest transect is on the top. It can be seen from these plots that the area containing the highest vorticity signals shifts back and forth during the observing period.

Figure 5.42 shows the data from pass 1 (the top panel in Figure 5.41) formed into 100-m averages; that is, all the data within a 100-m band have been averaged together and displayed as a single point. The pass has been broken into 26 segments, and the average is plotted at the geometric center of each segment. (The first segment, for example,

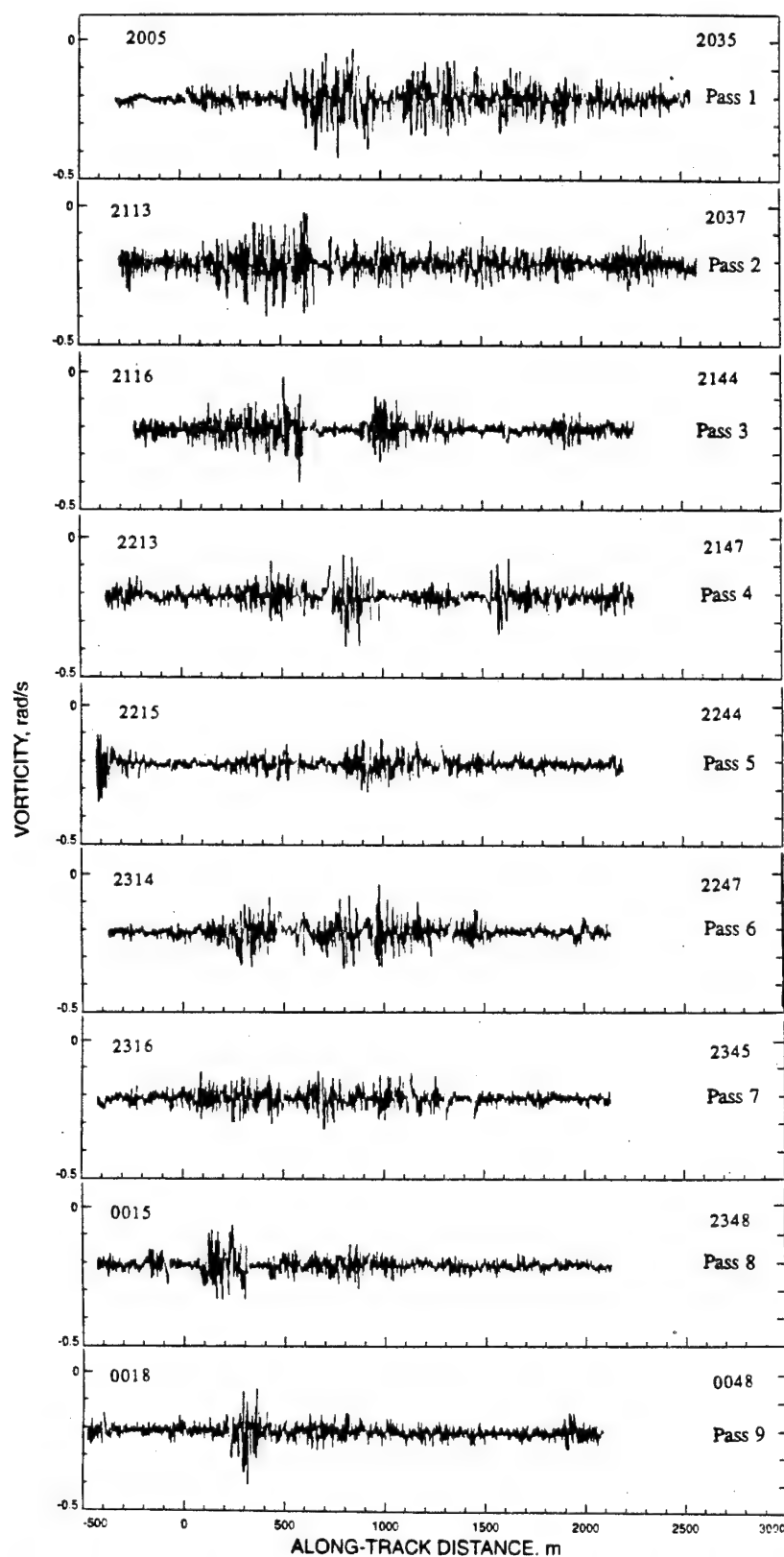


Figure 5.40. Nine along-track plots of vertical vorticity along a line just south of Restoration Point. The earliest transect is shown at the top, and the latest at the bottom; start and stop times are noted on each plot.

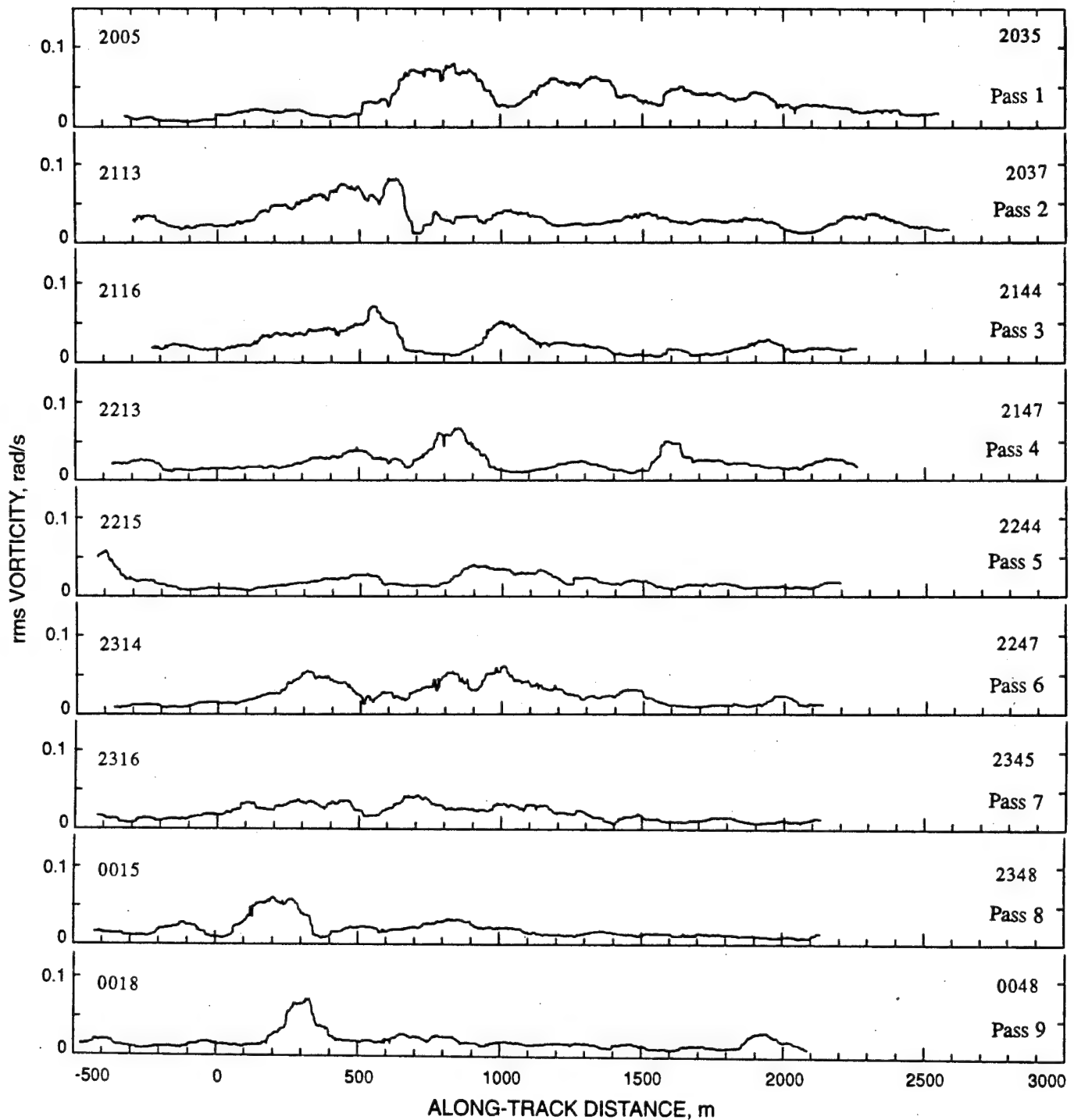


Figure 5.41. Nine along-track plots of rms vorticity calculated for 20-s intervals. The earliest transect is shown at the top, and the latest at the bottom; start and stop times are noted on each plot.

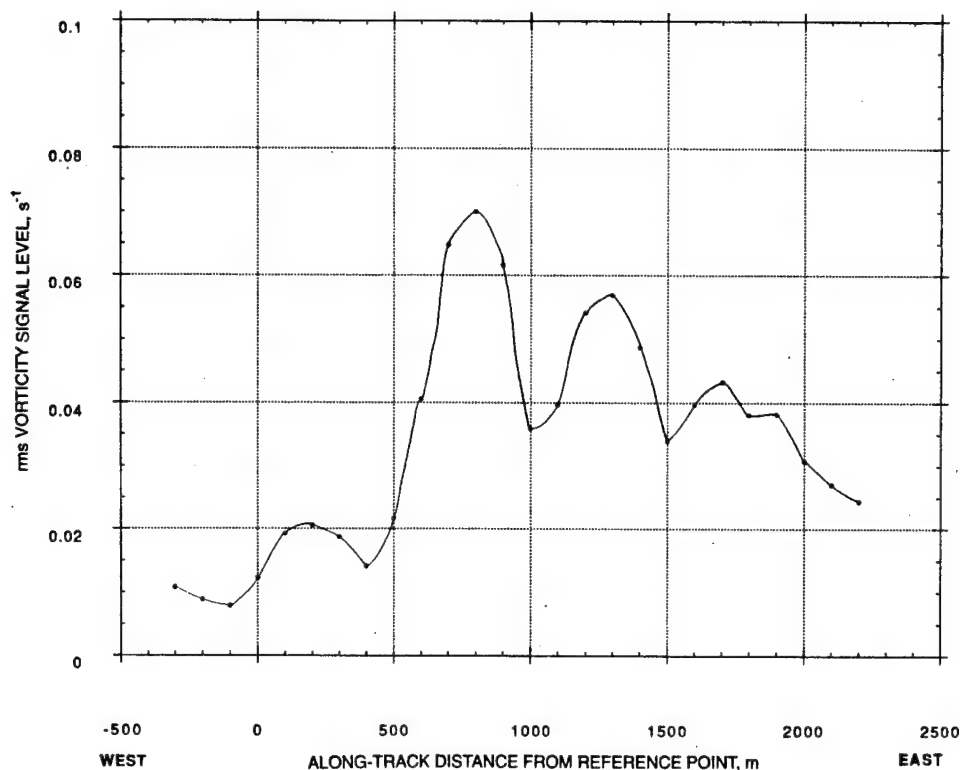


Figure 5.42. Data from pass 1 (top panel, Figure 5.39) formed into 100-m along-track averages and displayed as a single point.

runs from -550 m to -450 m, and the average is plotted at -500 m.) When this is done for all nine passes, the data for a particular segment can be plotted versus time (pass number). Figure 5.43 shows this type of time series for the 1000-m and 1100-m segments. The peak signal levels are observed during pass 6, whose median time is about 2300 UTC. This corresponds to 1500 PST, near the calculated time of maximum flow due to tidal forcing (see Figure 5.34). If we combine the data from all the 100-m segments and all nine passes, we can plot a three-dimensional map of vorticity signal levels relative to distance along-track and time. Figure 5.44 shows contours of equal rms vorticity signal levels versus distance (horizontal axis) and time (vertical axis). During passes 1, 2, and 3, the rms vorticity levels were high over a large portion of the tow track. Later during passes 8 and 9, the high vorticity signals were localized to a small area. The peak levels shifted to the west as time progressed.

In conclusion, the EMVM tows at Restoration Point and Decatur Reef found clear evidence of environmental signals with rms amplitudes as great as $1.1 \times 10^{-1} \text{ s}^{-1}$ over a 20-s interval. The locations of these large signals were consistent with Decatur Reef as the source and advection at the water velocities measured with the drogue buoys.

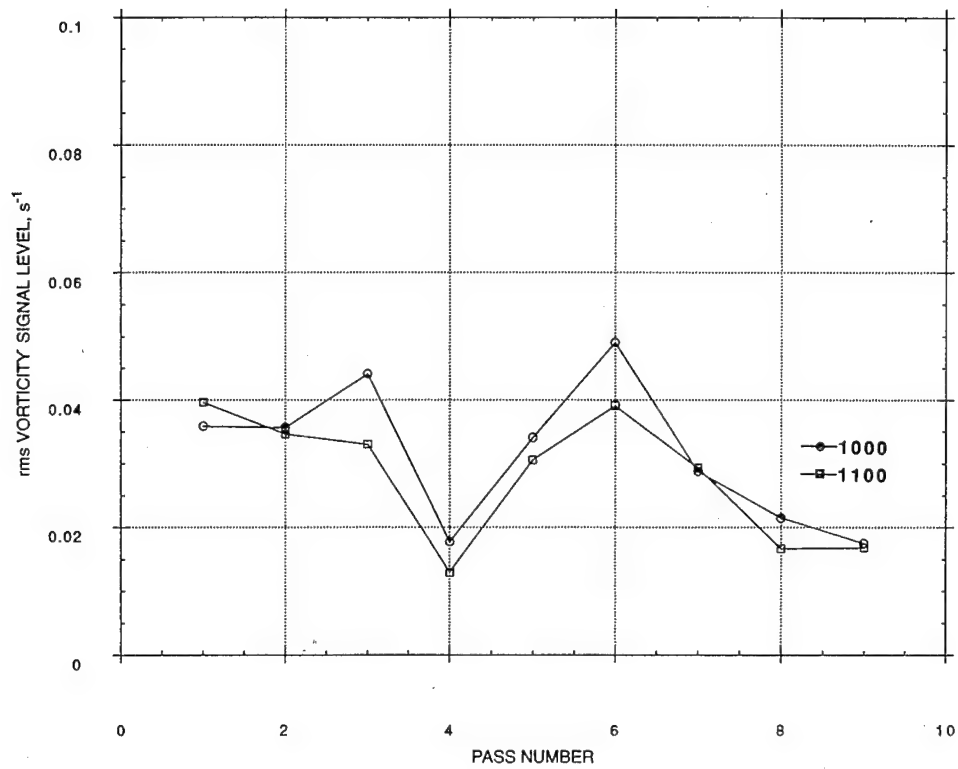


Figure 5.43. Vertical rms vorticity data from the 1000-m and 1100-m segments of Figure 5.39 plotted for each pass.

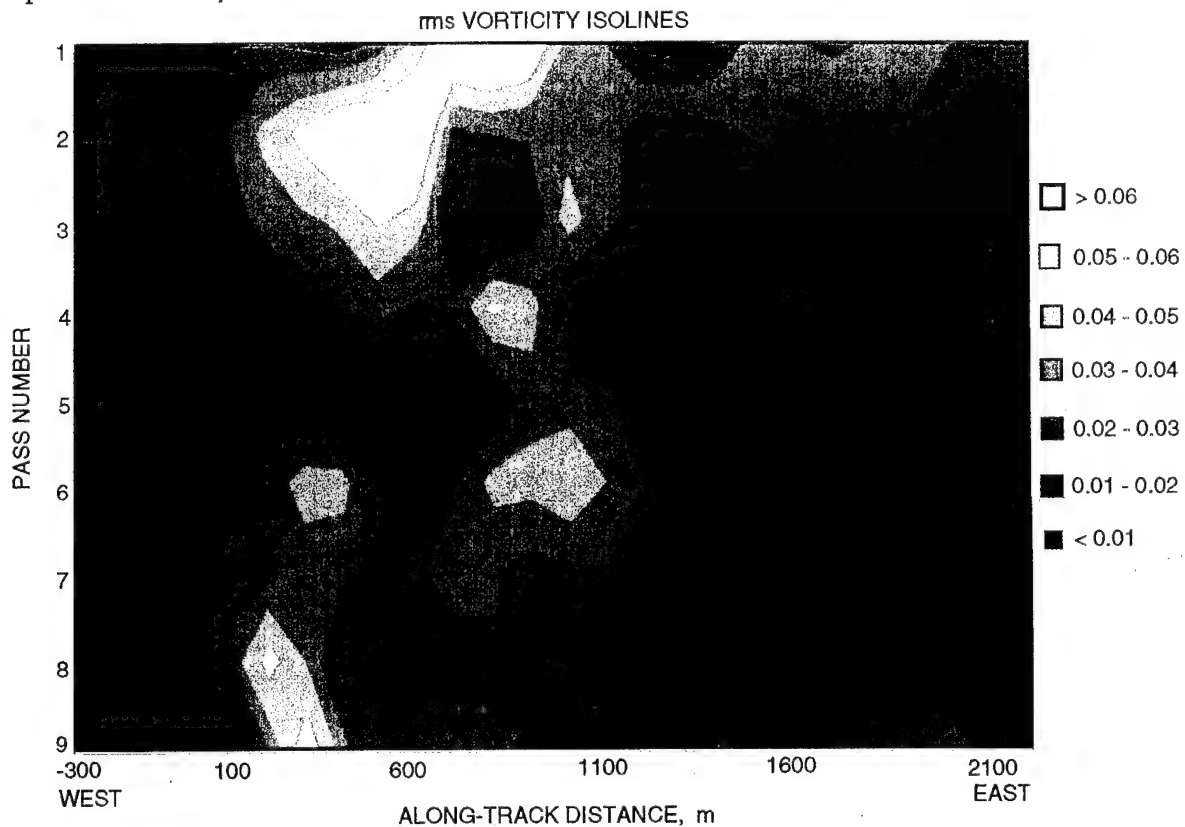


Figure 5.44. Contour plot of equal rms vertical vorticity versus distance (x) and time (y). Units of shading are seconds⁻¹.

5.4 Toliva Shoal

On 27–29 August 1991, the EMVM was deployed around Toliva Shoal in South Puget Sound. The instrument utilized the GW fiberglass fairing and was towed behind R/V *Miller* at low speeds (2.5 kn) and at a depth of about 30 ft. Toliva Shoal in the middle of Puget Sound just southwest of the Tacoma Narrows. Figure 5.1 shows the operating area in relation to the rest of Puget Sound. This underwater feature rises from a mean depth of 400 ft to within 20 ft of the surface. The center of the shoal is marked at the surface with a buoy. The tows were conducted during an ebb flow while circling the center of the shoal at a distance of about 0.25 n.mi. Figure 5.45 shows the track of the towing vessel. During these tows, a vehicle dynamics package was attached to the instrument. In addition, an Eagle 4 GPS receiver and two Megapulse 4000 LORAN receivers were installed on board R/V *Miller*, and position data were logged at a 1-Hz rate.

The permanent magnet (1.4×10^{-2} T) was again used. The towing configuration was the same as the previous deployments in Puget Sound in July.

Figure 5.46 shows a time series of the vertical vorticity data for 28 August. The lower panel depicts the rms vorticity corrected for yaw rate and bandpass filtered as a function of time. The upper panel shows the variance in vorticity computed over 20-s windows. During the least active portions of the tow, the vorticity variance was slightly less than $1.5 \times 10^{-5} \text{ s}^{-2}$ ($\text{rms} = 4 \times 10^{-3} \text{ s}^{-1}$). In the most active portions, the vorticity variance was $1.2 \times 10^{-3} \text{ s}^{-2}$. The time series is better understood by breaking it up into four sections, each corresponding to a "circle" of data acquired as we towed the instrument around Toliva Shoal.

Figures 5.47 through 5.50 show the vertical vorticity variance plotted as variable-sized dots whose centers are plotted at the latitude and longitude where the data were acquired. On the first two passes (Figures 5.47 and 5.48), we steered a constantly changing heading which produced a circular path with a radius of 0.25 n.mi. On the last two passes (Figures 5.49 and 5.50), we were trying to produce a box pattern with sides approximately 0.5 n.mi. long centered on the submerged shoal. The fourth circle was interrupted when the submerged sensor hit an unknown object and all five ceramic sensor tubes were sheared off at their bases. The data show both temporal and spatial variability; in general, however, the geographical location with the highest vorticity signal levels is to the northeast of the buoy marking the center of the shoal. This is consistent with the observing period being during ebb flow, when the bulk of the water that was flowing past (and over) Toliva Shoal was progressing up the main channel of Puget Sound just east of Fox Island. This set of conditions puts the area with highest vorticity signals directly in the wake of the shoal.

To investigate the azimuthal distribution of vorticity with respect to the center of Toliva Shoal, the data for the first three circles around the shoal were sorted into 7.5° bins. Using coordinate transformation algorithms, we transformed the latitude/longitude data into radial distance-vs-angle bins. The data were then sorted into 7.5° angle bins and averaged. Because the vessel's speed over ground was not constant owing to wind

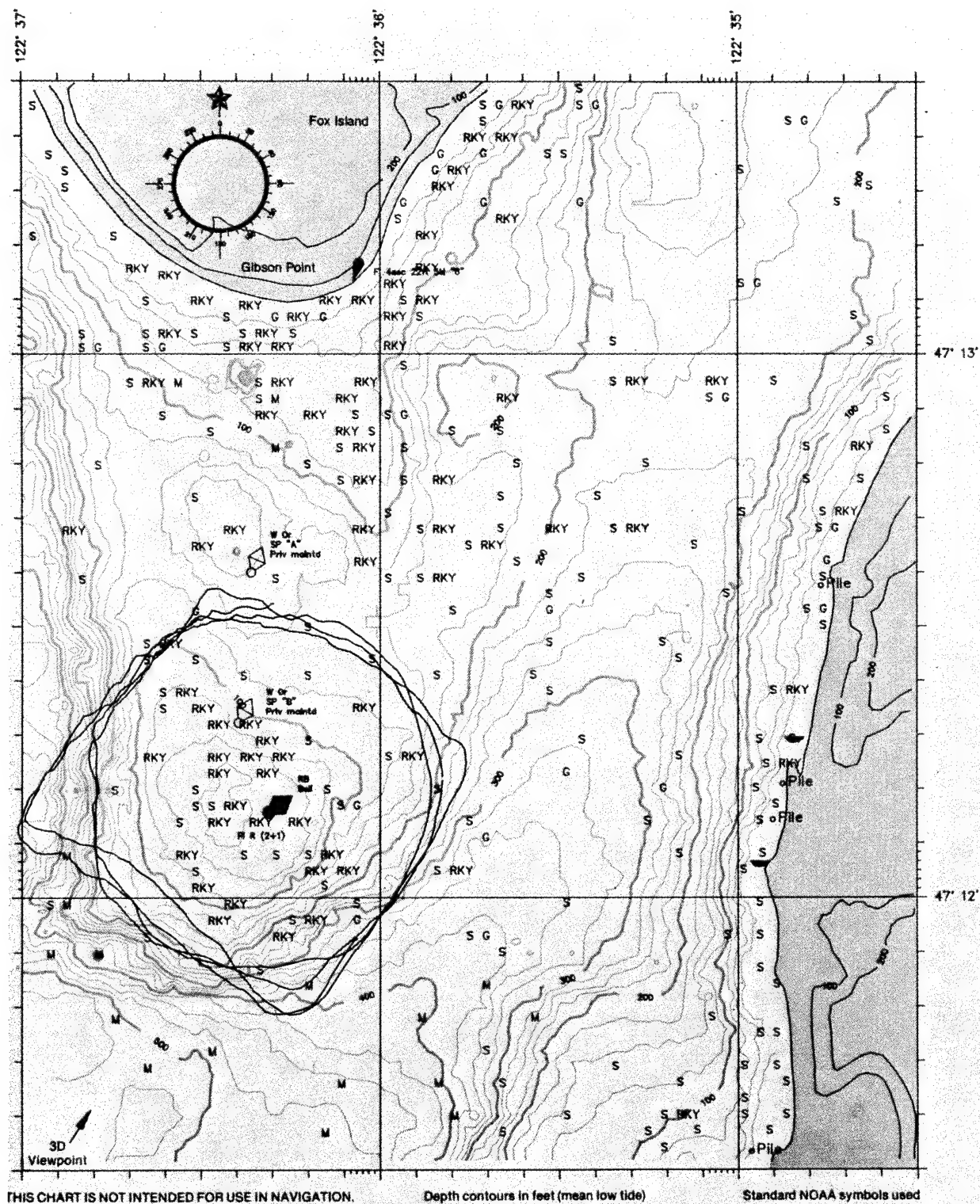


Figure 5.45. Ship's track around Toliva Shoal in Puget Sound in August 1991. The ship circumnavigated the shoal four times. Two of the circumnavigations were circles at a radius of 0.25 n.mi., and two were boxes with sides 0.5 n.mi. long and centered at 0.25 n.mi. from the shoal.

and currents, the number of data points in a given angle bin varied from a high of 20 to a low of 5. These binned and averaged vorticity variance data are shown in Figure 5.51. This plot confirms our hypothesis that the area with the highest vorticity signals is in the wake of the submerged feature. The area with the lowest vorticity was in the relatively undisturbed water coming from the south, where the nearest flow-disturbing feature (an island) was over 4 n.mi. away.

5.5 Horizontal

Two field tests were conducted in Puget Sound in which the vorticity sensor was operated horizontally, one on 24 February and one on 27 February 1992. For both tests, the vorticity sensor was attached to a fiberglass tripod sitting on the bottom at a depth of 15–20 ft. The EMVM obtained high-quality data during both deployments.

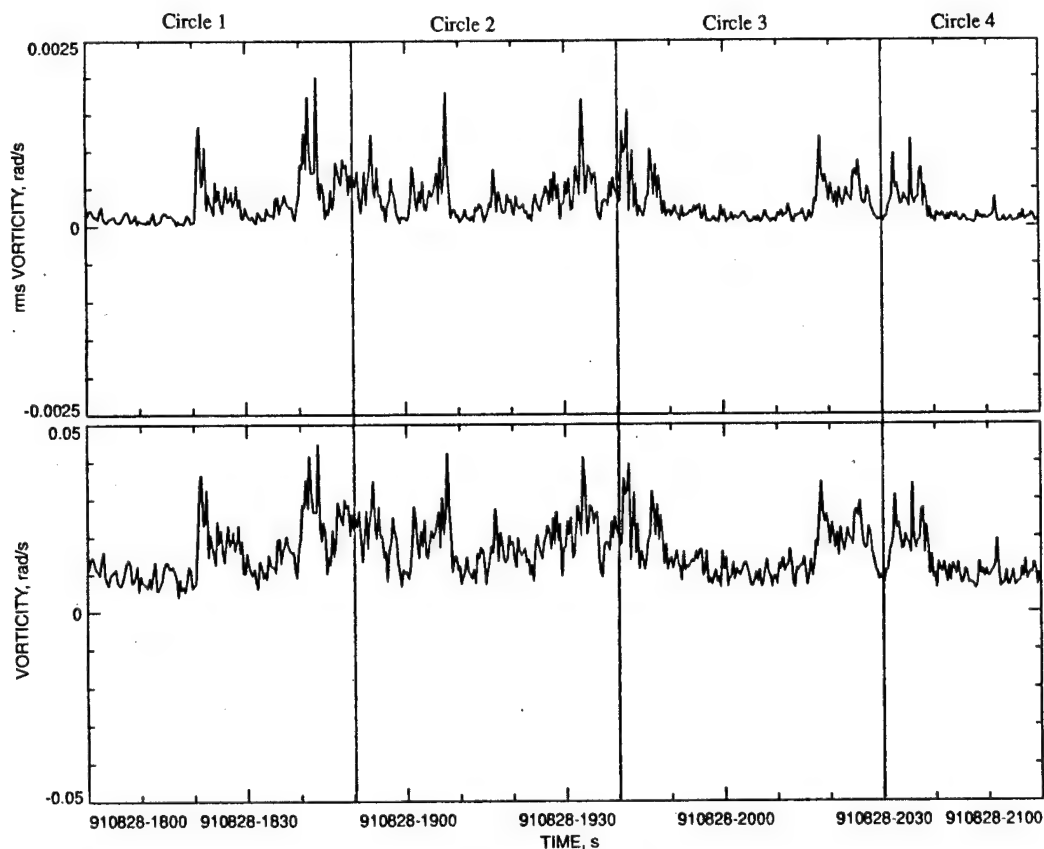


Figure 5.46. Time series of vertical vorticity data for 28 August 1991. The lower panel shows vorticity corrected for yaw rate and bandpass filtered as a function of time. The upper panel shows the variability in rms vorticity computed over 20-s windows. The circle the data come from is noted at the top.

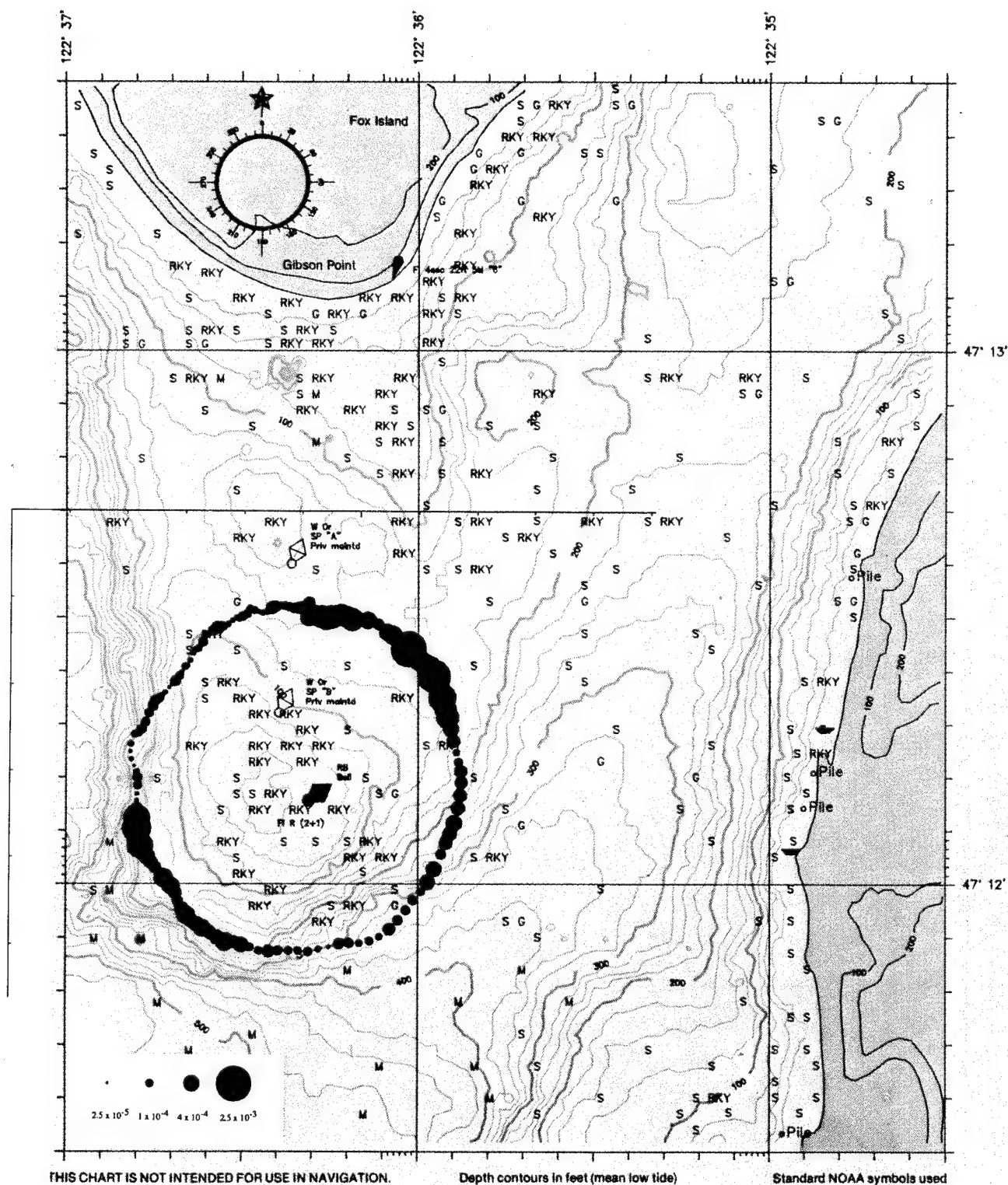


Figure 5.47. First circle of Toliva Shoal, 1800–1850 UTC. The size of the dots indicates the magnitude of the vertical vorticity variance (s^{-2}); the scale of the dots is shown in the lower left-hand corner.

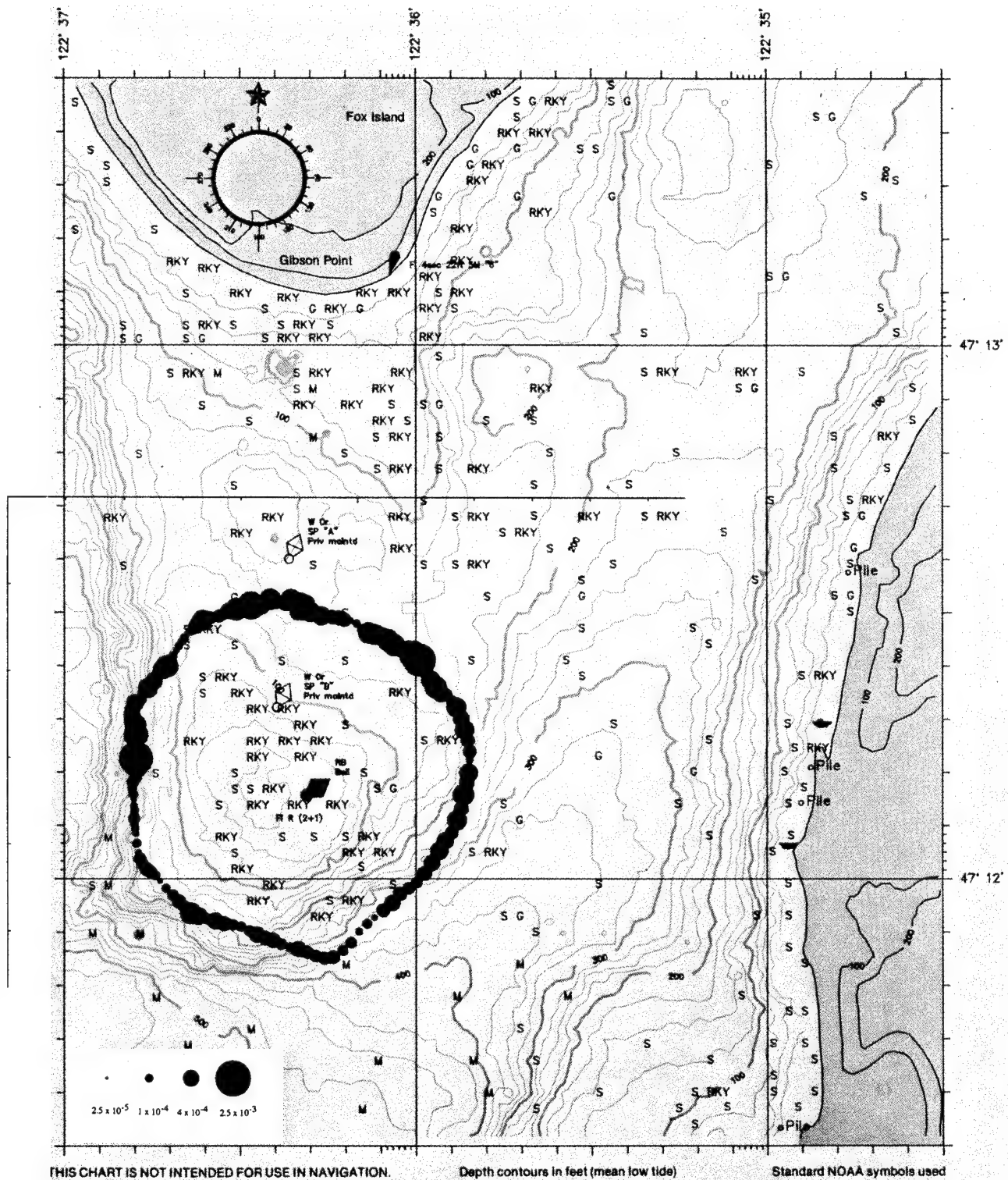


Figure 5.48. Second circumnavigation of Toliva Shoal, 1850–1940 UTC. The size of the dots indicates the magnitude of the vertical vorticity variance (s^{-2}); the scale of the dots is shown in the lower left-hand corner of the figure.

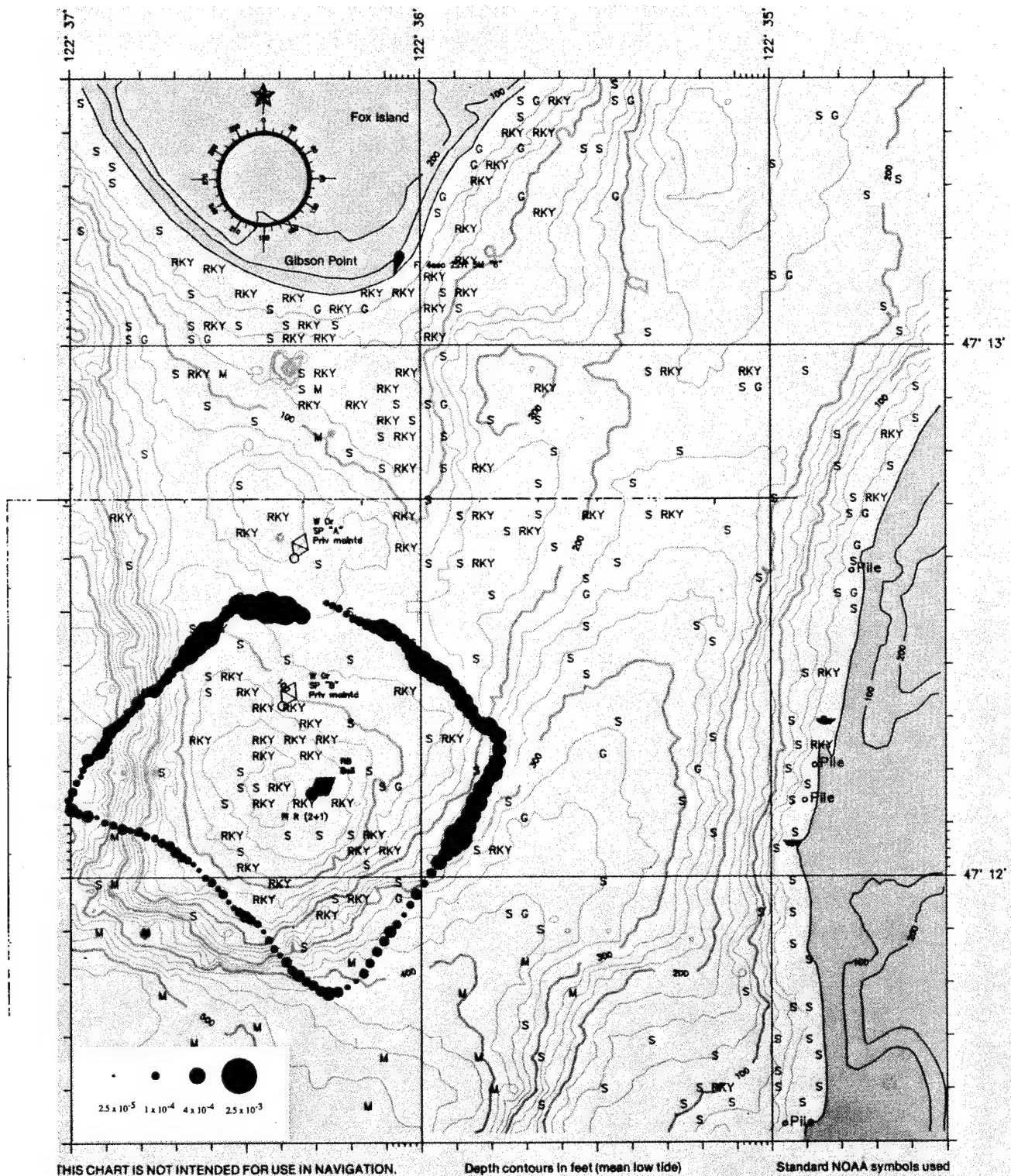


Figure 5.49. Third circumnavigation of Toliva Shoal, 1940–2030 UTC. The size of the dots indicates the magnitude of the vertical vorticity variance (s^{-2}); the scale of the dots is shown in the lower left-hand corner of the figure.

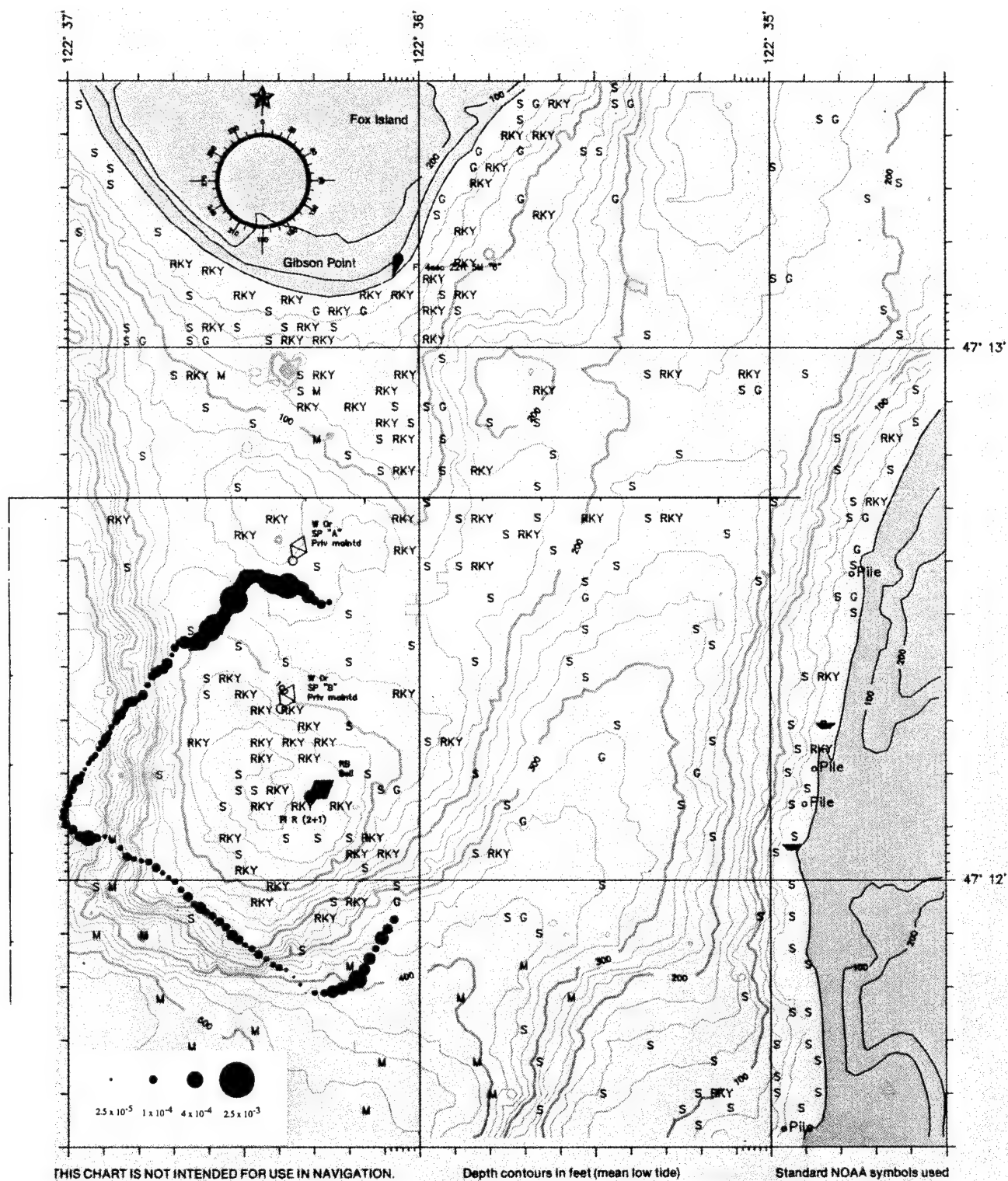


Figure 5.50. Fourth circumnavigation of Toliva Shoal, 2030–2106 UTC. The size of the dots indicates the magnitude of the vertical vorticity variance (s^{-2}); the scale of the dots is shown in the lower left-hand corner of the figure.

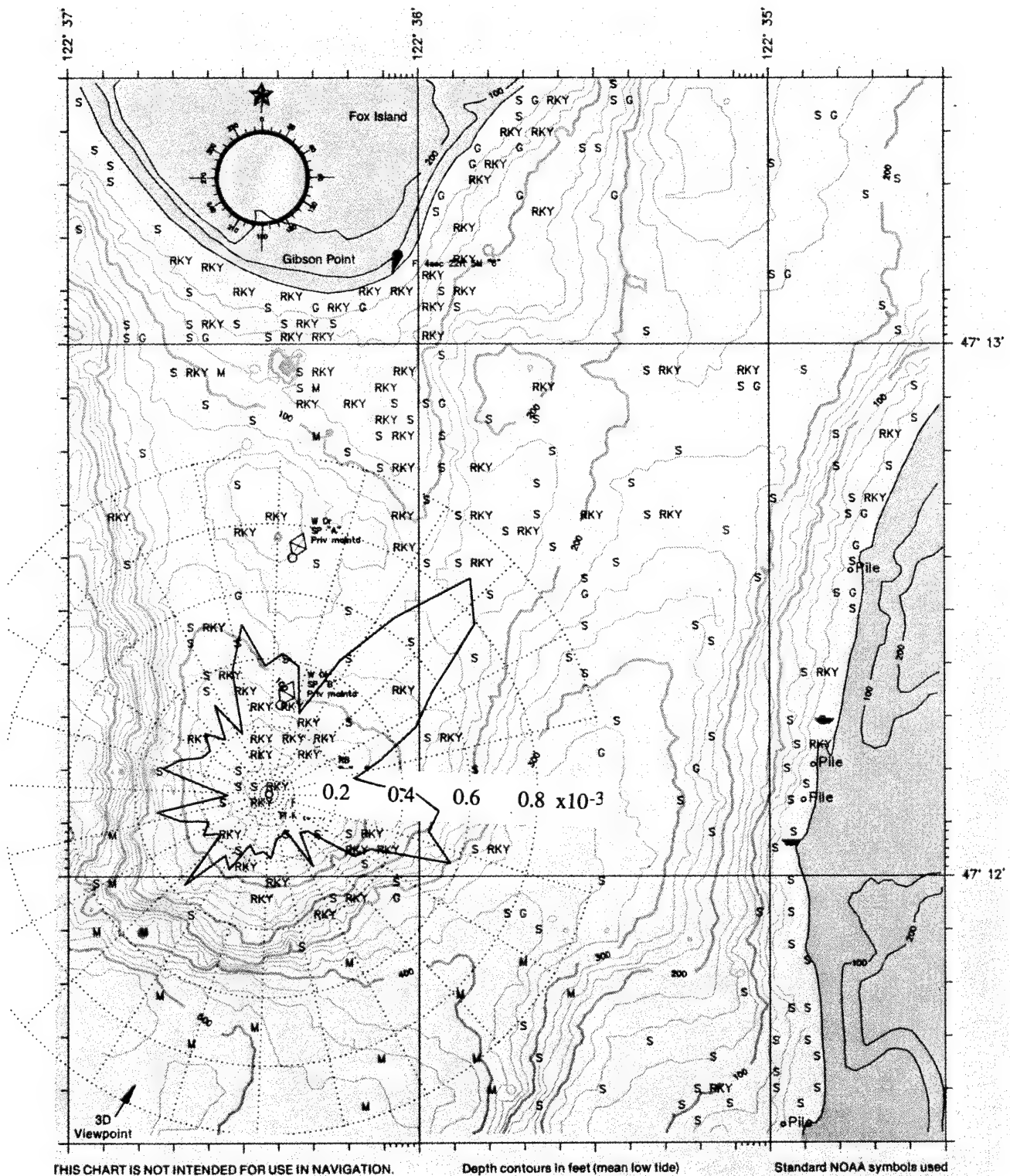


Figure 5.51. Azimuthal distribution of vertical vorticity variance (s^{-2}). Vorticity variance during the first three circumnavigations of Toliva Shoal was sorted into 7.5° bins and averaged. The radial distance indicates the magnitude of the vorticity variance according to the scale shown.

Small signals perturbing the measurements were noted during past experiments when the EMVM was operated from a steel tripod. A new tripod was constructed especially for these tests. It was made entirely of fiberglass and plastic so that electric fields due to the corrosion of dissimilar metals were not present. The new tripod allowed the vorticity sensor to pivot freely around the vertical axis.

During the experiments, the EMVM was operated horizontally. A large plastic vane and drag parachute attached to the sensor caused it to pivot about the vertical axis and remain aligned with the local flow, which had mean values of up to 0.4 m/s. Both deployments were conducted during a period that spanned the maximum ebb flow. The sensor, which was mounted at the top of the tripod, was submerged only 3–5 m below the surface, depending on the height of the tide.

Several interesting features were observed. During both experiments, large vorticity signals occurred when there were only small velocity signatures. Figure 5.52 shows a portion of the data recorded during the second deployment. The horizontal vorticity time series contains substantial signals with rms amplitudes of $3.2 \times 10^{-2} \text{ s}^{-1}$. There are no horizontal or vertical velocity signals that correlate well with the observed vorticity. There is also a patch of water near the middle of the record that has much a much lower vorticity variability, less than $5 \times 10^{-3} \text{ s}^{-1}$ rms. There is no apparent change in either the mean velocity or the rms variability of velocity. Likewise, there are large velocity sig-

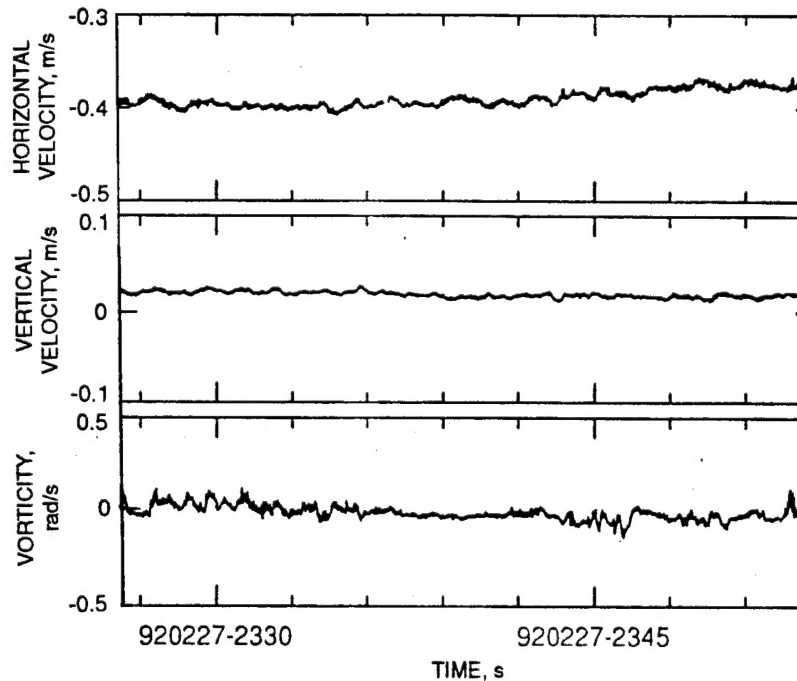


Figure 5.52. Data acquired with the EMVM sensor aligned so that the sensitive axis was horizontal. The top panel shows the horizontal velocity component measured along the local streamlines. The middle panel shows the vertical velocity component. The bottom panel shows the horizontal component of vorticity aligned perpendicular to the local streamlines and the vertical. There are substantial signals in vorticity that do not have corresponding signatures in velocity.

nals due to variations in the mean flow and surface waves without corresponding vorticity signals. During the second experiment, the EMVM measured horizontal velocities of up to 20 cm/s peak to peak due to surface waves from a large vessel passing nearby. Vertical velocities of up to 10 cm/s were simultaneously observed. This event is evident in Figure 5.53. The middle and upper panels show, respectively, the vertical and one component of the horizontal velocity field. The bottom panel shows the horizontal vorticity. The surface waves peak near 2315 UTC and appear as a high frequency on the record because of the time scale used for plotting. Visually, little of the signal appears present in the vorticity data. This is the expected result. A more sensitive analysis could be done using spectral techniques.

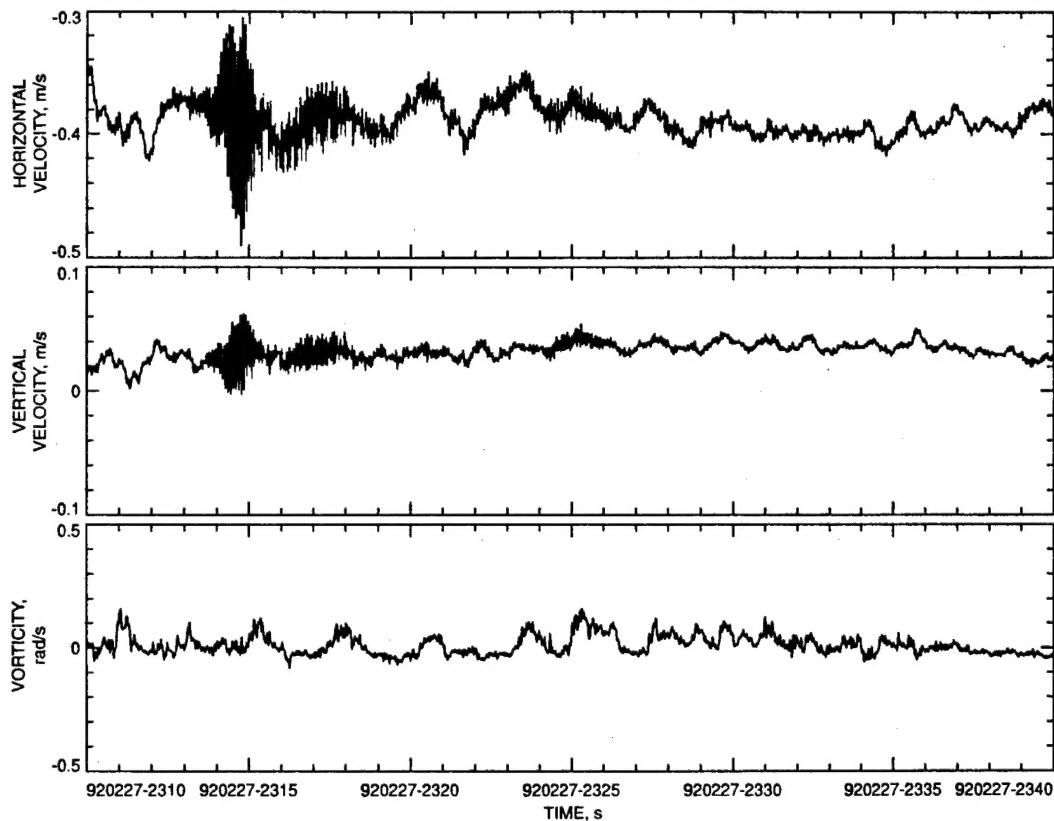


Figure 5.53. Data acquired with the EMVM sensor aligned so that the sensitive axis was horizontal. The uppermost panel shows the horizontal velocity component measured along local flow streamlines. The middle panel shows the vertical velocity component. The bottom panel shows the vorticity about an axis perpendicular to the local streamlines and the vertical. The high-frequency signals present in the first half of the record are due to the waves of a passing vessel. These surface gravity waves do not contain vorticity and therefore are not present in the vorticity data channel.

6. REFERENCES

- Baker, R. C., "On the electromagnetic vortex probe," *J. Phys. E: Sci. Instr.*, **4**, 99–101, 1971.
- Briscoe, M. G., "Preliminary results from the trimoored Internal Wave Experiment," *J. Geophys. Res.*, **80**, 3872–3884, 1975.
- Gargett, A. E., P. J. Hendricks, T. B. Sanford, T. R. Osborn, and A. J. Williams III, "A composite spectrum of vertical shear in the upper ocean," *J. Phys. Oceanogr.*, **11**, 1258–1271, 1981.
- Grossman, L. M., H. Li, and H. A. Einstein, "Turbulence in civil engineering: Investigations in liquid shear flow by electromagnetic induction," *Proc. Am. Soc. Civ. Eng. J. Hydr. Div.*, 1394-1–1394-15, 1957.
- Lin, J.-T., and Y.-H. Pao, "Wakes in stratified fluids," *Ann. Rev. Fluid Mech.*, **11**, 317–338, 1979.
- Müller, P., "Small-scale vortical motions," *Internal Waves and Small-Scale Turbulence: Proceedings, Hawaii Winter Workshop, University of Hawaii at Manoa, January 17–20, 1984*, P. Müller and R. Pujulet, eds. (Hawaii Institute of Geophysics, 1984), pp. 249–262, 1984.
- Müller, P., G. Holloway, F. Henyey, and N. Pomphrey, "Nonlinear interactions among internal gravity waves," *Rev. Geophys.*, **24**, 493–536, 1986.
- Saffman, P. G., "Dynamics of vorticity," *J. Fluid Mech.*, **106**, 49–58, 1981.
- Sanford, T. B., R. G. Drever, J. H. Dunlap, and E. A. D'Asaro, Design, Operation and Performance of an Expendable Temperature and Velocity Profiler (XTVP), APL-UW 8110, Applied Physics Laboratory, University of Washington, May 1982.
- Shercliff, J. A., *The Theory of Electromagnetic Flow-Measurement* (Cambridge University Press, Cambridge, 1962), 149 pp.
- Tsinober, A., E. Kit, and M. Teitel, "On the relevance of the potential-difference method for turbulence measurements," *J. Fluid Mech.*, **175**, 447–461, 1987.

REPORT DOCUMENTATION PAGEForm Approved
OPM No. 0704-0188

Public reporting burden for this collection of information is estimated to average 1 hour per response, including the time for reviewing instructions, searching existing data sources, gathering and maintaining the data needed, and reviewing the collection of information. Send comments regarding this burden estimate or any other aspect of this collection of information, including suggestions for reducing this burden, to Washington Headquarters Services, Directorate for Information Operations and Reports, 1215 Jefferson Davis Highway, Suite 1204, Arlington, VA 22202-4302, and to the Office of Information and Regulatory Affairs, Office of Management and Budget, Washington, DC 20503.

1. AGENCY USE ONLY (Leave blank)		2. REPORT DATE November 1995	3. REPORT TYPE AND DATES COVERED Technical	
4. TITLE AND SUBTITLE An Electromagnetic Vorticity Meter			5. FUNDING NUMBERS	
6. AUTHOR(S) Thomas B. Sanford, James A. Carlson, and Mark D. Prater				
7. PERFORMING ORGANIZATION NAME(S) AND ADDRESS(ES) Applied Physics Laboratory University of Washington 1013 NE 40th Street Seattle, WA 98105-6698			8. PERFORMING ORGANIZATION REPORT NUMBER APL-UW TR 9503	
9. SPONSORING / MONITORING AGENCY NAME(S) AND ADDRESS(ES) Tactical Oceanographic Warfare Support Program Office Naval Research Laboratory, Code 7410 Stennis Space Center, MS 39529-5004			10. SPONSORING / MONITORING AGENCY REPORT NUMBER	
11. SUPPLEMENTARY NOTES				
12a. DISTRIBUTION / AVAILABILITY STATEMENT Unlimited distribution.			12b. DISTRIBUTION CODE	
13. ABSTRACT (Maximum 200 words) The Electromagnetic Vorticity Meter (EMVM) directly measures small-scale vorticity in the ocean using the principles of electromagnetic induction. The scientific motivation for developing the EMVM, the design concept, and the theory of operation are discussed. Complete descriptions are given of the instrument's design, construction, and performance through several evolutions of the sensor, and extensive observations are presented of sensor performance during laboratory and field tests. The tests demonstrate a vorticity noise level of 10^{-3} s^{-1} .				
14. SUBJECT TERMS Motional induction, current meter, vorticity meter, vorticity			15. NUMBER OF PAGES 140	
			16. PRICE CODE	
17. SECURITY CLASSIFICATION OF REPORT Unclassified	18. SECURITY CLASSIFICATION OF THIS PAGE Unclassified	19. SECURITY CLASSIFICATION OF ABSTRACT Unclassified	20. LIMITATION OF ABSTRACT SAR	